Author:
Stacey, Jonathan

Title:
Composite compliant shell mechanisms
tailoring and characterisation

Composite Compliant Shell Mechanisms: Tailoring and Characterisation

University of Bristol

March 2021

Jonathan Paul Stacey

A dissertation submitted to the University of Bristol in accordance with the requirements for award of the degree of Doctor of Philosophy in the Faculty of Engineering, Department of Aerospace Engineering.

Word Count: 38000

Abstract

Compliant shell mechanisms are thin shell structures that transmit loads and motion via large elastic deflections. These have advantages over classical mechanisms by reducing the need for traditional joints, thereby reducing part count, friction, and backlash. By replacing designs that utilise discrete joints and moving parts, compliant mechanisms have found application in areas including deployable structures, medical support braces and morphing aerostructures.

Designing compliant shell mechanisms is not without challenges. Typically, these mechanisms need to achieve specific force-displacement responses, and their nonlinear nature means that these responses can be sensitive to small changes in design parameters. Inclusion of anisotropic composite materials expands their design space through selection of the composite laminate layup and prestress, potentially offering alternative routes for stiffness tailoring for restricted design cases. Therefore, understanding the theoretical and practical limits of what is possible in this design space is very valuable.

The research presented investigates several compliant shell structures and 1) explores the potential of combining mechanical and thermal prestress with composite laminate layup to tailor the response of compliant shell mechanisms, 2) develops analytical and numerical models to characterise and visualise their response, and 3) validates these models against manufactured prototypes. Different combinations of thermal and mechanical prestress are investigated, as well as the effects of various design parameters (thickness, geometry, fibre angles etc.) on compliant mechanism behaviour. Detailed finite element models are presented and validated against prototypes of prestressed composite tape springs and helical lattice structures. Eigenscrew characterisation of compliant mechanisms has also been applied to composite shells for the first time, giving new insight into the interplay between material stiffness and shell geometry in mechanism behaviour, via visualisation of compliance axes. These findings pave the way for future studies of robust design, fatigue life enhancement and optimum material selection for compliant shell mechanisms.

Dedication & Acknowledgements

Undertaking a PhD has been a personal goal for some years. This experience of facing up to the huge gaps in my knowledge and personal development has been very humbling and very rewarding. As well as expanding my technical abilities I have learnt much about myself, and I wish to thank those who have helped me.

Firstly I thank my supervisors Mark Schenk and Matt O'Donnell. Their dedication and attention to detail really inspire me to strive for the best. I have been incredibly fortunate to have had supervisors who have been so supportive and easy to get along with, and I am a far greater researcher and engineer as a result of their guidance. I also thank Carwyn Ward and Ian Hamerton for their advice and support when first encouraging me to consider a PhD, and all those in the Bristol Composites Institute who have supported me since. I thank Charles Kim at Bucknell University for hosting me in the US, and for continuing our collaboration afterwards, and also those in Just Herder's group at TU Delft who helped kick-off my research.

I thank Steve Grey, Dina Kanari and Anatoly Koptelov, who have been very good friends throughout my time in the ACCIS CDT. Collectively I think we kept each other more-or-less sane, and managed to have more than a few laughs while doing so. Great thanks are also in order for my friend Ellis Keeber who, as my housemate and sole human company during the height of the COVID-19 lockdown, did so much to keep me in good spirits. In addition, the support of Fr Rupert Allen and the community at the University Catholic Chaplaincy has been invaluable throughout my time in Bristol. I know many friendships I have made there are for life.

To my parents, siblings and grandparents: your loving friendship and encouragement is the foundation of all that I set out to do. When I have doubted myself, you have got me going again, and when times have been tough, you have provided space to rest. I am so grateful for all you do, and so proud to be part of such a family.

Finally I wish to acknowledge that none of this would have been possible if not by the grace of God. If I have achieved any small good thing during this time it has been through His guidance and by His gifts, and no words of thanks I can muster would be sufficient. I offer all this work, everything that I am, and everything that have back to my wonderful Lord who has given me so much.

Ad Majorem Dei Gloriam

Declaration

I declare that the work in this dissertation was carried out in accordance with the requirements of the University's *Regulations and Code of Practice for Research Degree Programmes* and that it has not been submitted for any other academic award. Except where indicated by specific reference in the text, the work is the candidate's own work. Work done in collaboration with, or with the assistance of, others, is indicated as such. Any views expressed in the dissertation are those of the author.

SIGNED:

DATE:

Contents

List of Figures

List of Tables

List of Publications

The following are lists of journal papers and conference contributions resulting from the work detailed in this thesis.

Journal Contributions

1. **Stacey J.P.**, O'Donnell M.P., Kim C.J., Schenk M., (2020), *From Shear Centre to Eigenwrenches*, Thin-Walled Structures, 161:107478

2. O'Donnell M.P., **Stacey J.P.**, Chenchiah I.V., Pirrera A., (2019), *Multiscale Tailoring of Helical Lattice Systems for Bespoke Thermoelasticity*, Journal of the Mechanics and Physics of Solids, 133:103704

3. **Stacey J.P.**, O'Donnell M.P., Schenk M. (2019), *Thermal Prestress in Composite Compliant Shell Mechanisms*, Journal of Mechanisms and Robotics, 11(2):020908

Conference Contributions

1. **Stacey J.P.**, O'Donnell M.P., Schenk M., Kim C.J. (2020), *Visualizing Compliance of Composite Shell Mechanisms*, ASME IDETC/CIE 2020, 16-19 August, St. Louis, MO, USA [**Paper, Presentation**]
   (Virtual conference due to COVID-19 pandemic)

2. **Stacey J.P.**, Schenk M., O'Donnell M.P. (2019), *Thermo-Elastic Composite Helical Lattices - Analysis, Manufacture and Testing*, 5th International Conference on Mechanics of Composites (MechComp2019), 1-4 July, Lisbon, Portugal [**Abstract, Presentation**]

3. **Stacey J.P.**, O'Donnell M.P., Schenk M. (2018), *Thermal Prestress in Composite Compliant Shell Mechanisms*, ASME IDETC/CIE 2018, 26-29 August, Québec City, Canada [**Paper, Poster, Presentation**]

Elements of these publications and contributions are reproduced in this thesis. Content from *"From Shear Centre to Eigenwrenches"* and *"Multiscale Tailoring of Helical Lattice Systems for Bespoke Thermoelasticity"* is reproduced in-line with Elsevier's retained author rights. Content from *"Thermal Prestress in Composite Compliant Shell Mechanisms"* (both the Journal of Mechanisms and Robotics paper, and the preceding ASME 2018 IDETC/CIE conference paper), and *"Visualising Compliance of Composite Shell Mechanisms"* is reproduced with the permission of the American Society of Mechanical Engineers (ASME) granted specifically for this thesis.

Elements of Chapter 1 and Chapter 2 were taken from a project overview written by this author and first published on the Bristol Composites Institute website in 2017 [224].

Nomenclature

Terms in bold text indicate vector or matrix quantities. Unless otherwise specified subscripts i and j refer to positions of terms within vectors or matrices.

Greek-Font Terms

α_{11}	Ply-level thermal expansion coefficient parallel to the fibre direction
α_{22}	Ply-level thermal expansion coefficient perpendicular to the fibre direction
$\boldsymbol{\alpha}$	Ply-level thermal expansion coefficients in vector form
β_{11}	Ply-level moisture expansion coefficient parallel to the fibre direction
β_{22}	Ply-level moisture expansion coefficient perpendicular to the fibre direction
β_i	Angle between F_{eq_i} and F_{m_i}
γ_{12}	Ply-level shear strains with respect to the fibre axes
γ^0_{xy}	Laminate/shell shear strains with respect to the laminate axes
$\boldsymbol{\gamma}_i$	Twist rotation components
δ_a	Twisting design parameter: D^*_{66}/D^*_{11}
δ_b	Twisting design parameter: D^*_{16}/D^*_{11}
δ_{eq_i}	Equivalent translation of a mechanism point of interest
δ_{h_i}	Translational displacements of a mechanism POI parallel to a twist axis
δ_{r_i}	Rotational displacements of a mechanism point of interest about a twist axis
$\delta_{\gamma r_i}$	Virtual displacement of a mechanism point of interest about a twist axis
δ_x	Deflection of a mechanism's point of interest in the global x-direction
δ_y	Deflection of a mechanism's point of interest in the global y-direction
δ_z	Deflection of a mechanism's point of interest in the global z-direction
$\boldsymbol{\delta}_i$	Twist translation components
ϵ_{11}	Ply-level direct strains parallel to the fibre direction
ϵ_{22}	Ply-level direct strains perpendicular to the fibre direction
ϵ^0_{xx}	Laminate/Shell direct strains parallel to the laminate x-axis
ϵ^0_{yy}	Laminate/Shell direct strains parallel to the laminate y-axis
$\boldsymbol{\epsilon}^{th}$	Ply-level thermal strains
$\boldsymbol{\epsilon}^{m}$	Ply-level moisture strains
ζ	Cross-sectional distance between the shear centre and centroid
θ	Fibre orientation angle

θ_x	Rotation of a mechanism's point of interest about the global x-direction
θ_y	Rotation of a mechanism's point of interest about the global y-direction
θ_z	Rotation of a mechanism's point of interest about the global z-direction
θ_C	Instantaneous twist angle of a tape spring about an underlying cylinder
θ_H	Wrap angle of the helical lattice strips on the cylindrical manufacturing tool
κ_{11}	Laminate/Shell curvature along the screw of a helical strip
κ_{22}	Laminate/Shell curvature perpendicular to the screw of a helical strip
κ_{12}	Laminate/Shell twist around the screw of a helical strip
κ_{xx}	Laminate/Shell curvature about the laminate x-axis
κ_{yy}	Laminate/Shell curvature about the laminate y-axis
κ_{xy}	Laminate/Shell twisting about with respect to the laminate axes
κ^0_{xx}	Helix manufactured curvature in the x-direction
κ^0_{yy}	Helix manufactured curvature in the y-direction
κ^0_{xy}	Helix manufactured twist
κ^G_{0y}	Gaussian curvature
$\boldsymbol{\kappa}^{th}$	Thermally-induced laminate/shell curvatures
$\boldsymbol{\kappa}_L$	Left-handed helix in-plane curvatures and twists
$\boldsymbol{\kappa}_R$	Right-handed helix in-plane curvatures and twists
λ_{1-14}	Tape spring strain energy partial derivative terms
$\boldsymbol{\lambda}_f$	Eigenvalues of the purely translational quadrant of $\boldsymbol{K}$
$\boldsymbol{\lambda}_\gamma$	Eigenvalues of the purely rotational quadrant of $\boldsymbol{C}$
μ	Mean value
ν	Isotropic Poisson's ratio
ν_{12}	Anisotropic Poisson's ratio ($\nu_{21} = \nu_{12}$)
ν_m	Poisson's ratio of the composite matrix material
ξ_{1-12}	Lamination parameters
Π	Helical lattice strain energy per unit cell
ρ	Material density
ρ_c	Composite density
ρ_w	Water density
σ	Standard deviation
σ_{11}	Ply-level direct stresses parallel to the fibre direction
σ_{22}	Ply-level direct stresses perpendicular to the fibre direction
σ_{xx}	Ply-level direct stresses parallel to the laminate x-axis
σ_{yy}	Ply-level direct stresses parallel to the laminate y-axis
τ_{12}	Ply-level shear stresses with respect to the fibre axes
τ_{xy}	Ply-level shear stresses with respect to the laminate axes
τ_L	Additional left-handed helix thermal response parameters
τ_R	Additional right-handed helix thermal response parameters

$\boldsymbol{\tau}_i$	Wrench angular torque components
ϕ	Half-angle enclosed by a tape spring cross-section
χ	Cross-sectional distance between the shear centre and mechanism POI
χ_i	Unification lengths ("RasT" approach)
$\boldsymbol{\chi}_L$	Left-handed helix thermal response parameters
$\boldsymbol{\chi}_R$	Right-handed helix thermal response parameters
ψ_i	Unification lengths ("TasR" approach)

Latin-Font Terms

$\tilde{a}_f$	Equivalent translational twist axis compliances ("RasT" approach)
$\tilde{a}_\gamma$	Equivalent translational wrench axis compliances ("TasR" approach)
$\boldsymbol{a}_f$	Wrench axis translational compliances
$\boldsymbol{a}_\gamma$	Twist axis rotational compliances
A	Cross-sectional area
A_{ij}	Laminate/Shell in-plane stiffness matrix terms
$\boldsymbol{A}$	Laminate/Shell in-plane stiffness matrix
b	Sinusoidal amplitude of the scoliosis brace mechanism
$\boldsymbol{b}_i$	Wrench location vector pitches
B_{ij}	Laminate/Shell extension-bending coupling matrix terms
$\boldsymbol{B}$	Laminate/Shell extension-bending coupling stiffness matrix
$\boldsymbol{B}^*$	Laminate/Shell partially-inverted coupling stiffness matrix
C	Cylinder curvature
$\boldsymbol{C}_t$	6x6 tangential compliance matrix of a mechanism point of interest
$\boldsymbol{C}_{1-4}$	3x3 tangential compliance matrix quadrants
d_i	Wrench torque-to-force ratio
D	Isotropic material flexural stiffness
D_{ij}	Laminate/Shell bending stiffness matrix terms
$\boldsymbol{D}$	Laminate/Shell bending stiffness matrix
$\boldsymbol{D}^*$	Laminate/Shell reduced bending stiffness matrix
E	Isotropic Young's modulus
E_{11}	Ply-level Young's modulus parallel to the fibre direction
E_{22}	Ply-level Young's modulus perpendicular to the fibre direction
$\boldsymbol{f}_i$	Wrench linear force components
F_{eq_i}	Equivalent virtual force at a mechanism point of interest
F_{m_i}	Virtual force applied around a twist axis that produces a moment M_i
F_x	Mechanism applied force in the global x-axis
F_y	Mechanism applied force in the global y-axis
F_z	Mechanism applied force in the global z-axis
G	Isotropic shear modulus

G_{12}	Ply-level shear modulus
h	Position of the top of a ply with respect to the laminate mid-plane
h_i	Twist pitches
H	Overall laminate/shell thickness
I_{xx}	Second moment of area about the x-axis
I_{yy}	Second moment of area about the y-axis
I_{xy}	Coupled second moment of area
$\boldsymbol{I}$	Identity matrix
J	Polar moment of area
k	Matrix condition number
$\boldsymbol{k}_f$	Wrench axis translational stiffnesses
$\boldsymbol{k}_\gamma$	Twist axis rotational stiffnesses
$\boldsymbol{K}_t$	6x6 tangential stiffness matrix of a mechanism point of interest
$\boldsymbol{K}_{1-4}$	3x3 tangential stiffness matrix quadrants
l	Side length of a helical lattice unit cell
L	Length of a cantilevered tape spring mechanism
L_{cool}	Length of cooled composite helical lattice
L_{hot}	Length of heated composite helical lattice
m	Laminate moisture content
M_i	Pure moment caused by rotation around a mechanism twist axis
M_x	Mechanism applied bending moment about the global x-axis
M_y	Mechanism applied bending moment about the global y-axis
M_z	Mechanism applied bending moment about the global z-axis
M_{xx}	Laminate/Shell bending moment about the laminate x-axis
M_{yy}	Laminate/Shell bending moment about the laminate y-axis
M_{xy}	Laminate/Shell twisting moment with respect to the laminate axes
$\boldsymbol{M}^{th}$	Laminate/Shell thermal residual bending moments
n	Number of repeating plies in a laminate
N	Number of individual helices of each handedness in a helical lattice
N_{xx}	Laminate/Shell direct stresses parallel to the laminate x-axis
N_{yy}	Laminate/Shell direct stresses parallel to the laminate y-axis
N_{xy}	Laminate/Shell shear stresses with respect to the laminate axes
$\boldsymbol{N}^{th}$	Laminate/Shell thermal residual direct stresses
p	Scoliosis brace mechanism helical pitch
$\boldsymbol{P}_i$	Schur complement partial terms
$\boldsymbol{Q}$	Lamina reduced stiffness matrix
$\bar{\boldsymbol{Q}}$	Lamina stiffness matrix
r	Tape spring cross-sectional arc radius
r_{H}	Internal radius of the flat helical scoliosis brace mechanism

r_{S}	Internal radius of the sinusoidal helical scoliosis brace mechanism
$\boldsymbol{r}_i$	Twist location vectors
R	Cylinder radius
S	Helix length along screw
S_s	Ply ultimate shear strength
t	Individual ply thickness
T	Temperature
T_{1-3}	An eigen-twist axis
$\boldsymbol{T}$	A generalised twist
$\boldsymbol{T}_\gamma$	An eigen-twist
$\hat{\boldsymbol{T}}_\gamma$	An eigen-twist (normalised)
$\boldsymbol{T}_f$	A twist induced from the application of an eigen-wrench
$\hat{\boldsymbol{T}}_f$	A twist induced from the application of an eigen-wrench (normalised)
$\boldsymbol{T}$	Lamina transformation matrix
u	Laminate/Shell height parameter
u_1	Range of helix angles for the scoliosis brace mechanism
u_2	Range of sinusoidal curvature angles for the scoliosis brace mechanism
U	Shell strain energy per unit area
$\hat{U}$	Shell strain energy per unit area (non-dimensionalised)
U_b	Shell bending strain energy density
U_s	Shell membrane strain energy density
U_{th}	Helical lattice thermal energy term
U_{1-5}	Material invariants
$\boldsymbol{v}_f$	Eigenvectors of the purely translational quadrant of $\boldsymbol{K}_t$
$\boldsymbol{v}_\gamma$	Eigenvectors of the purely rotational quadrant of $\boldsymbol{C}_t$
w	Width of a helical strip
w_{1-3}	An eigen-wrench axis
w_L	Left-handed helix width
w_R	Right-handed helix width
$\boldsymbol{w}$	A generalised wrench
$\boldsymbol{w}_f$	An eigen-wrench
$\hat{\boldsymbol{w}}_f$	An eigen-wrench (normalised)
$\boldsymbol{w}_\gamma$	A wrench induced from the application of an eigen-twist
$\hat{\boldsymbol{w}}_\gamma$	A wrench induced from the application of an eigen-twist (normalised)
W_{1-2}^{th}	Thermal material invariants
X_{cs}	Ply ultimate compressive strength parallel to the fibre direction
X_{ts}	Ply ultimate tensile strength parallel to the fibre direction
Y	Matrix reciprocal condition number
Y_{cs}	Ply ultimate compressive strength perpendicular to the fibre direction

Y_{ts}	Ply ultimate tensile strength perpendicular to the fibre direction
z	Distance between the mid-planes of an individual ply and the laminate

Chapter 1

Introduction

Compliant mechanisms are flexible devices used to transmit forces or motion via large elastic deformations. These have advantages over classical mechanisms (*i.e.* those comprised of rigid links connected by springs and hinges) by reducing the need to include and maintain discrete joints. A particular class of compliant mechanism, namely the compliant *shell* mechanism, utilises the spatial (*i.e.* 3D) bending and twisting of thin shell structures. Compliant shell mechanisms have found application in areas such as passive shell-based exoskeletons and medical supports [168], where shape and space constraints provide a challenging design space. A comparison between a classical compliant mechanism and a compliant shell mechanism in Figure 1.1 illustrates the ability to achieve equivalent functionality in a more constrained footprint.

Compliant shell mechanisms are similar in design and function to some morphing and deployable structures, as these also rely on elastic deformations of thin-walled shell structures to achieve large changes in shape. Applications are, for example, found in aerospace engineering where morphing wings are designed for improved aerodynamics [127] or deployable space structures are designed for compact stowage during launch [164]. Although the fields of compliant mechanisms and morphing and deployable structures are complementary, there has not been much overlap or collaboration in literature. The work in this thesis aims to bridge some of this gap.

Morphing and deployable structures increasingly utilise fibre reinforced composite materials to introduce novel functionality through a tailored laminate layup [128, 163] or to achieve large deformations through high allowable strains [164]. Thus, there is also great potential to enhance compliant shell mechanisms with these materials. Using composite systems such as carbon and glass fibre reinforced polymers provides a means to increase the stiffness and simultaneously reduce the weight of compliant shell mechanisms, as well as form shells with complex geometries. Furthermore inclusion of these materials offer new ways to tune the mechanism kinetics and kinematics, particularly through careful optimisation of the anisotropic mate-

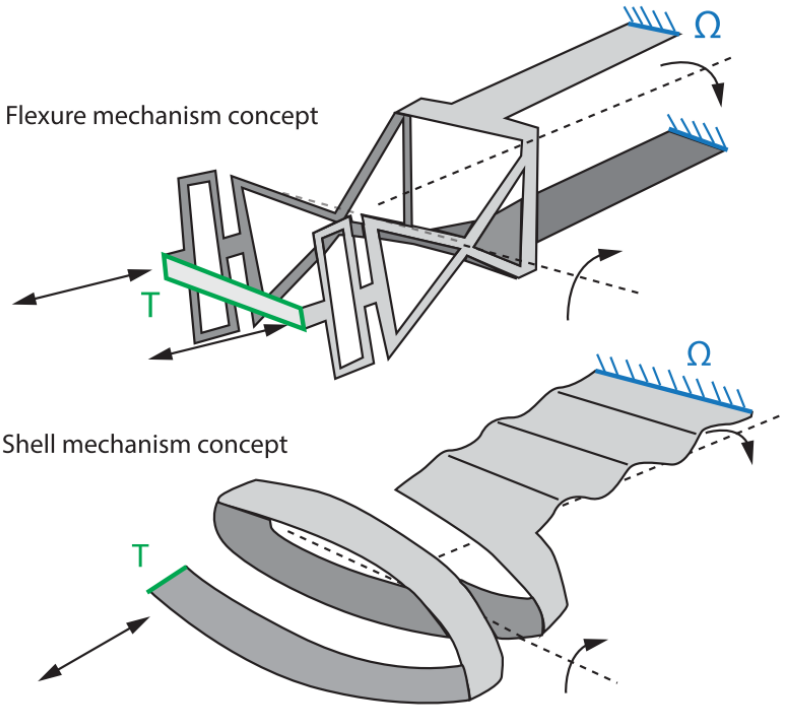

Figure 1.1: *Classical compliant mechanism and compliant shell mechanism concepts designed for the same kinematic requirements. Rotational axes are shown with dotted lines, with the fixed boundary, 'Ω', shown in blue and the translating region, 'T' shown in green. Reproduced from Ref [168].*

rial properties and by utilising a state of prestress in the laminate. Prestress can be applied to a shell mechanism via a mechanical load or assembling a mechanism in a post-buckled state, but also as a result of mismatches in thermal expansion coefficients. The anisotropic thermal properties of composite laminate materials therefore provide an additional means of tailoring the structural response. Figure 1.2 shows an example of shape changes that can occur in a flat plate with a cross-ply composite laminate lay-up where bistability is induced as a result of thermal prestress. Traditional compliant mechanisms achieve anisotropy of deformation typically via geometric choices, but including composite materials could enable anisotropic deformations via anisotropic materials, enabling compliant mechanisms with identical geometry to exhibit different behaviours. This approach has been almost completely unexplored in literature.

The use of composite materials in compliant shell mechanisms increases their design space. However, the increase in design complexity also results in a loss of design intuition. Furthermore, the nonlinear kinetic and kinematic response over large deformations of the compliant shell mechanism means that they can be sensitive to variations in geometry, material properties and prestress states. As well as this, a compliant composite shell mechanism would have to exhibit a specific force-displacement response through large deformations, and potentially maintain

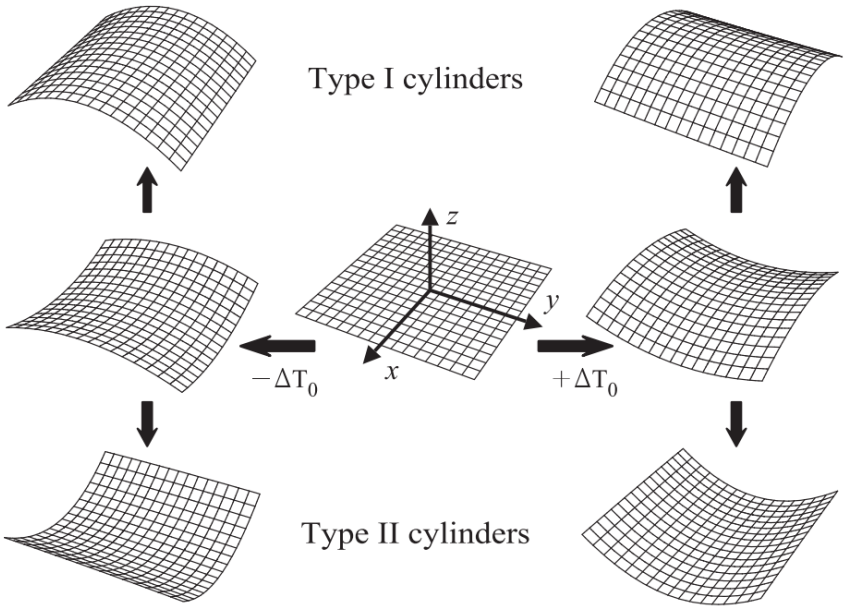

Figure 1.2: *Potential shape changes of an initially flat plate with a cross-ply laminate subject to uniform thermal loading. Reproduced from Ref [52].*

this for many cycles. However, polymeric materials traditionally used in composites can be susceptible to issues such as creep and stress relaxation. Addressing these issues requires advances in the design, analysis and manufacture of such composite compliant shells.

Successfully creating composite compliant mechanisms could thus be challenging, but developing new design, modelling and manufacturing techniques that provide intuitive insight into the compliant shell behaviour would be very valuable. The work in this thesis aims to do this, and thus enable an assessment of the potential benefits of compliant mechanisms made from composite materials and pave the way for additional collaboration between the fields of compliant mechanisms and morphing composite structures.

1.1 Project Objectives

The objectives of this project involve taking several shell structures as case studies and assessing the potential benefits to mechanism behaviour that the inclusion of tailored composites can bring. This will involve: i) exploring the potential of combining different means of tailoring composite compliant shell mechanisms (namely geometric, prestress and layup tailoring); ii) developing analytical and numerical models that can accurately and intuitively characterise the composite compliant mechanism behaviour; iii) assessing the design sensitivity and manufacturing feasibility of these tailored composite shells; and iv) bridging the gap between the

fields of compliant mechanisms design and composite structures design by applying mechanisms characterisation frameworks to composite compliant shells.

The project aims to investigate different combinations of thermal and mechanical prestress in these shells via analytical, numerical and experimental approaches, as well as the effects of various design parameters (thickness, layup, fibre angles etc.) on compliant mechanism behaviour. Material systems used are those that are well-characterised and representative of typical high-performance fibre reinforced polymer composites. Specifically this will involve the analysis and manufacture of two representative composite compliant shell mechanisms with different behaviours and types of prestress. The first case study involves simple geometry shells (singly-curved 'tape-springs') with thermal prestress. The second, while still a constrained geometry, is a more complex system (helical lattices) with thermal and mechanical prestress. The third case study considers more general 3D shells (*e.g.* a scoliosis brace) with more general displacements, and the ways to characterise and visualise compliance behaviour in general cases where material anisotropy is included.

1.2 Thesis Structure

Chapter 2 provides a review of academic literature and background concepts relevant to this project. Current state of the art of compliant mechanism design approaches are compared, and the particularities of compliant *shell* mechanisms are introduced. The parallels with shape-changing composite structures are then discussed, firstly with explanations of in-plane and out-of-plane coupling phenomena (and the mathematical framework for evaluating laminate properties), and then by categorising existing morphing composite structures according to whether they are mono-stable or multi-stable, and active or passive. After comparisons are drawn between these structures, a discussion of the use of prestress to tailor composites is presented, highlighting the methods for achieving prestress and novel low- and zero-stiffness behaviours that can be achieved as a result. The review ends with an overview of the key areas of behavioural uncertainties common in prestressed composite shells.

Chapter 3 presents an investigation into the potential of using thermal prestress in a composite material to radically change the passive behaviour of a simple singly-curved shell known as a tape spring. An existing analytical tape spring structural model is extended with thermal prestress effects, and energy landscapes of the torsional behaviour of such a structure are compared to finite-element models and prototype measurements. In addition, a brief analytical exploration of zero torsional stiffness is presented. The analytical models enable physical insight to be gained about the tape spring behaviour, and it is shown that while large shape-changes can be achieved with purely thermal prestress, this effect cannot be relied on its own to

tailor for complex behaviours (in this case, zero torsion stiffness).

To expand the potential design space for tailored behaviours, thermal and mechanical prestressing techniques are combined in Chapter 4 to enable extreme behaviour in an actuated composite helical lattice structure. Detailed finite element simulations are presented which must model the assembly process of the helical lattice in order to accurately capture the mechanical and thermal prestress required for its functionality. Numerical and analytical results are successfully compared with experimental measurements from precisely manufactured prototypes. The models presented in this chapter demonstrate the large potential in using multiple types of prestress to establish complex behaviours in a compliant structure, and the corresponding prototype - demonstrating a large negative thermal expansion helical lattice for the first time - illustrates that such mechanisms are feasible to manufacture and use.

Next, a design methodology suitable for assessing the stiffness characteristics of general shell geometries is considered in Chapter 5. A modelling approach developed in the field of mechanisms and robotics is extended to composite compliant shell mechanisms for the first time. An explanation of the eigen-decomposition technique is presented, and new links to classical structural mechanics concepts are shown analytically for the case of a cantilevered tape spring. A visualisation framework for general compliant shell mechanisms is presented and applied to simple composite tape springs of different geometry and fibre orientations. A composite scoliosis brace mechanism is investigated in Chapter 6 as a case study for this mechanism characterisation technique, and to assess the potential of inclusion of composite materials in improving a complex compliant shell mechanism design. As well as demonstrating mathematical links between two complementary fields of design, this characterisation technique is shown to give intuitive insight into what are usually non-intuitive deformations of composite compliant mechanisms, and highlight where designs become dominated by geometric effects, material properties, or a combination of the two.

Overall project conclusions are presented in Chapter 7, and potential avenues of future work are discussed.

Chapter 2

Background & Concepts

This chapter presents a broad overview of key research in the fields of compliant mechanism design and composite morphing shell structures, and details some fundamentals of composite laminate theory used in this thesis. This project seeks to explore the benefits of including composite materials in compliant shell mechanisms, and so this chapter specifically looks at compliant mechanism design techniques and the parallels between compliant mechanisms and morphing composites. Composite behaviour at a laminate level is also outlined, as well as design implications of prestress and behavioural uncertainties in composite shells. Some content presented in this chapter was initially detailed in an Exploratory Project (XP) internal report produced during this PhD [225].

2.1 Compliant Mechanisms

Compliant mechanisms are structures that transmit forces and motion via large scale elastic deformations, contrasting with rigid links and joints used in traditional mechanisms [95]. This mechanism design approach does limit their stiffness and motion ranges to what is achievable from the elasticity of the material and geometry, and this can include unwanted 'parasitic' responses [243]. While this can make compliant mechanisms challenging to design, they possess the significant advantage of lacking friction, mechanical backlash and need for lubrication, as well as reducing system maintenance requirements and part counts.

Compliant mechanisms are therefore frequently used where lubrication and maintenance is not possible, such as in spacecraft mechanisms [164] or in medical devices [168]. Precision devices that required backlash-free responses (such as microelectromechanical systems (MEMS)) also benefit from the use of compliant mechanisms [122]. Traditional structural design often seeks greater stiffnesses and strengths, but there are some applications where compliance can be exploited. Such examples include "gravity balancing" devices that match the weight of the mechanism and

any loading with the elastic forces in the structure [9, 195]. Additionally, the desire for greater energy efficiency has made compliant design an attractive option to help enable load alleviation and reduce turbulent flow across wings and aerostructures [127].

Tailoring the compliance of a structure is not a modern phenomenon however, with numerous examples of compliant mechanisms used throughout human history. Chariot designs from ancient Egypt have been shown to utilise multi-functional compliant components, with poles connecting the chariot to the horse's yolk tuned to act as both leaf springs, and torsional springs [205]. In addition to this many variations of composite bow (see Figure 2.1) have been used historically in hunting and warfare which have used combinations of woods, horn and sinew to deliberately enhance the performance of compressive and flexural regions of the bow, enabling bows to become smaller and shoot arrows faster and further [154]. Even early aircraft control surfaces were designed to be compliant structures, with perhaps the most famous example being the warping wings of the Wright brothers' 1902 glider and their subsequent "Wright Flyer" of 1903 [119].

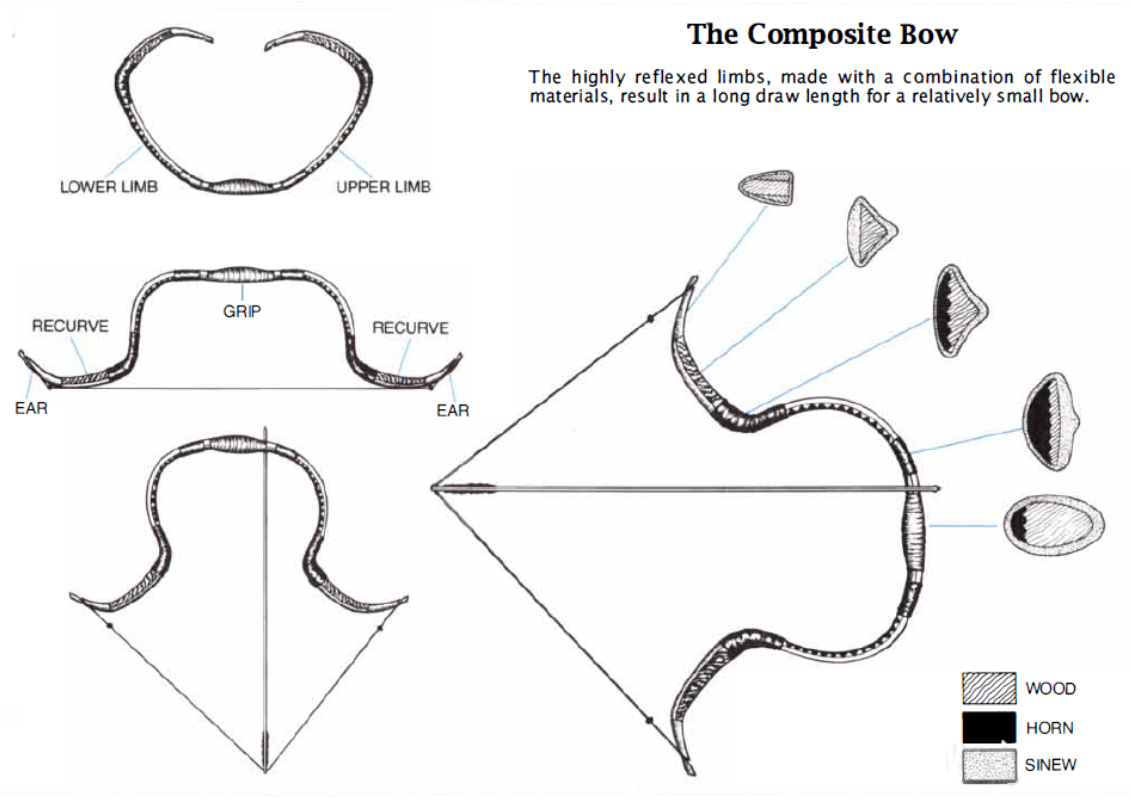

Figure 2.1: *Illustration of the regions and cross-sections of the composite bow, highlighting material choices and placement that enhanced the possible distance that arrows could be drawn. Reproduced from Ref [154].*

2.1.1 Design Frameworks

Many of the ancient examples of compliant structures were developed over long periods of time as a result of trial and error. Modern approaches for the design of compliant mechanisms focus on matching a set of mathematical requirements to improve design efficiency. In their review of such methods, Gallego and Herder [71] identify three main approaches for compliant mechanism design: kinematic approaches, structural optimisation techniques, and building-block approaches.

Kinematic Approaches

In this approach designs are sought that match a series of kinematic requirements. The main kinematic approaches are the Freedom and Constraints Topologies (FACT), and rigid-body-replacement methods. The FACT approach developed by Hopkins and Culpepper sets about identifying the mechanism requirements in terms of degrees of freedom, identifying the corresponding constraint space and then selecting topologies from this constraint space to generate an early-stage mechanism design [90–92]. Figure 2.2 shows an example where a mechanism with a single rotational degree of freedom is required (shown by the red line), and the corresponding constraint space consists of planes intersecting this line (shown by the blue lines). Next, designs can be selected that correspond to geometry permitted by the constraint space, with one example mechanism shown consisting of two blade flexures perpendicular to the flexure axis, and another consisting of four blade flexures aligned with the rotation axis. This approach is very effective for rapidly generating initial mechanism concepts, but only provides initial shapes and topologies to the designer. Some examples of mechanisms designed using the FACT approach can be found in Refs [93, 94, 257, 258].

In contrast, the rigid-body-replacement approaches focus on designing mechanisms by approximating a compliant mechanism as a series of rigid links connected by springs (*i.e.* a conventional rigid body mechanism) of appropriate stiffness [204]. This can simply involve the replacement of discrete hinges with equivalent flexible elements [96] by inspection or by using a pseudo-rigid-body model. A pseudo-rigid-body model considers flexible members as torsion springs attached to rigid links, as shown in the example in Figure 2.3. Kota *et al.* also promoted the idea of mechanisms with distributed compliance (*i.e.* where the entire structure is compliant to some degree) for improved reliability and performance [122]. While Kota *et al.* initially used optimisation processes to determine topologies for distributed compliance, rigid-body-replacement methods provide a simple way of incorporation of distributed compliance into designs [232]. The advantages of this approach are that the design process is simplified, with the closed-form displacement and force

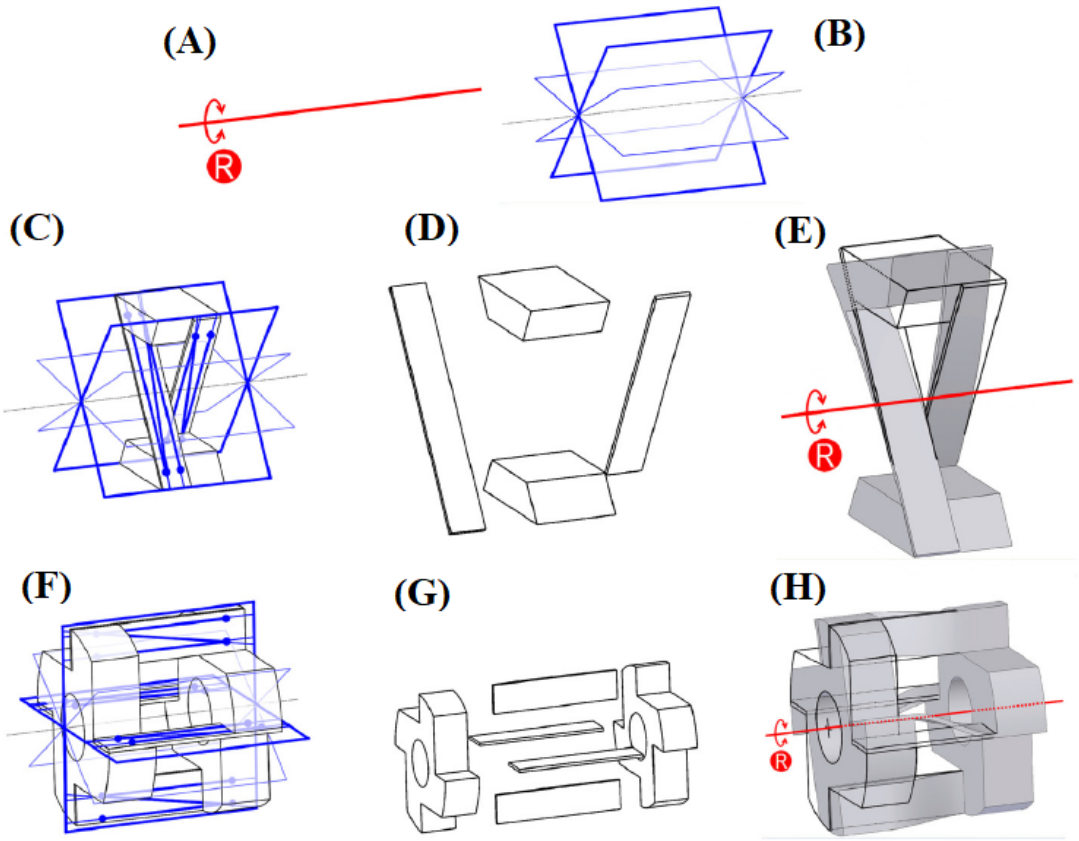

Figure 2.2: *An illustration of the use of the FACT design approach for a single degree of rotation mechanism, adapted from Ref [92]. Image (A) shows a mechanism's required freedom space, while image (B) shows the corresponding constraint space. Images (C-E) illustrate the selection of a mechanism utilising two blade flexures. Images (F-H) illustrate the selection of a mechanism utilising four blade flexures. Reproduced from Ref [92].*

equations from the models being beneficial for allowing the designer to conduct parameter sensitivity analyses [161]. The limitation of this approach is that it relies on knowledge of the design of conventional rigid body mechanisms, so limits application to existing mechanisms designers. Some examples of mechanisms designed using rigid-body replacement approaches can be found in Refs [115, 153, 182, 200].

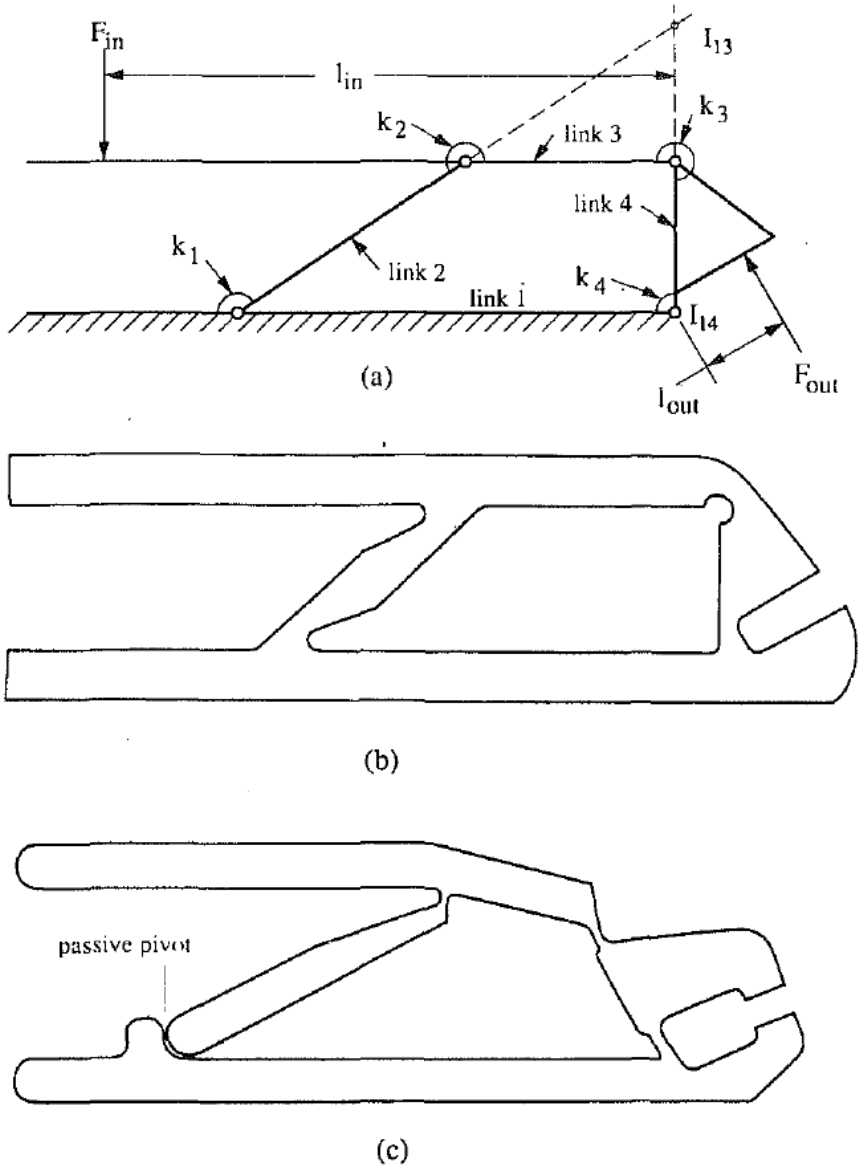

Figure 2.3: *A compliant gripper (a) modelled as a rigid body mechanism using the pseudo-rigid-body model to express the flexible members as torsion springs attached to rigid links, (b) the original compliant design, and (c) the compliant design found via the pseudo-rigid body method. Reproduced from Ref [96].*

Structural Optimisation Techniques

These techniques utilise mathematical optimisations to identify mechanisms that satisfy a given objective function. They are very popular, with many examples of optimisation-based compliant mechanisms (*e.g.* Refs [19, 20, 68, 99, 146, 172, 181, 220]). Radaelli and Herder highlighted the general difficulty in designing compliant mechanisms due to the coupling between the kinetics and kinematics, presenting shape-optimisation methods as a design solution [193, 194]. These optimisation techniques provide a method for generating complete designs directly from a set of requirements contained within a cost function, but do not grant the designer any physical insight into the behaviour of the resulting mechanism. The designer must instead be relied upon to generate suitable cost functions and use suitable optimisation algorithms if the resulting mechanism is to be feasible.

Building-Block Approaches

Building-block approaches combine multiple well-characterised mechanisms together to achieve a desired response. The kinematic and optimisation approaches provide pathways for designing compliant mechanisms that are tailored for specific responses, but these procedures have limitations for the designer insofar as providing only limited intuitive insight into the mechanism behaviour, requiring detailed understanding of classical rigid-body mechanism design, or necessitating further analysis to reach a complete design (*i.e.* not just a mechanism topology). Techniques that allow the generation of complete mechanism designs and provide more intuitive insight into the responses of compliant mechanisms are thus desirable, and the building-block design approach proposed by Kim *et al.* aims to do this [109, 112, 113]. Kim noted that rigid-body replacement methods are often reliant on initial 'seed' mechanisms, and while optimisation strategies generate designs straight from requirements, they are highly sensitive to the cost function definitions and algorithms used [113]. The idea behind the building block approach is to build a library of standard, well-characterised compliant mechanisms and develop an analytical framework and series of simple design rules that can aid a designer in choosing and combining these simple mechanisms (in series or in parallel) into suitable complex mechanisms for given problems [111].

The mechanisms in the library can be characterised by considering each with respect to a single point of interest (POI) on the mechanism, *e.g.* similar to an end effector on a robotic arm. The principal degrees of freedom of the POI could then be found, *i.e.* the three principal translational directions and rotational axes (as well as their associated compliances). Kim's chosen method for identifying these degrees of freedom is to decompose the POI stiffness matrix into a series of 'eigentwists' (rep-

resenting principal rotational degrees of freedom) and 'eigenwrenches' (representing principal translational degrees of freedom). This eigen-decomposition technique was developed by Likpin and Patterson [142–145,179,180], and is explored in further detail in Chapters 5 and 6, and Refs [226, 229] that resulted from the work therein. Huang and Schimmels also investigate this eigen-decomposition, providing commentary on the physical interpretation of the translational cases [98]. Some examples of mechanisms designed using this technique can be seen in Refs [88,110,121,123,138]. Once found, these principal degrees of freedom can be visualised, usually with compliance ellipsoids (3D ellipsoids with principal dimensions and orientations that correspond to the principal eigenscrew magnitudes and directions of the mechanism) or by plotting the eigenscrew axes in 3D space and comparing magnitudes of the compliances of each degree of freedom [137,138,171].

2.1.2 Shell and Spatial Mechanisms

Much work in the field of compliant mechanisms has focused on the design of planar mechanisms. A more recent development has been that of compliant shell mechanisms, which are compliant mechanisms that achieve large force-displacement responses by utilising thin-walled structures that can bend and twist in three dimensions. Compliant shell mechanisms can achieve equivalent functionality to planar mechanisms, but in a more constrained footprint. Seffen defined compliant shell mechanisms to be those with corrugations connected by folds or hinges (*e.g.* origami mechanisms) [214], but herein Farshad's more general definition of a shell mechanism being a spatially-curved thin-walled structure is used [64].

Some interesting examples of topology-optimised compliant shell mechanisms have been designed by Radaelli *et al.*, including gravity balancers [194, 195] and a carbon fibre leaf spring [193]. Morsch *et al.* also developed a novel compliant joint that uses leaf spring shell mechanisms combined with planar flexures, but this time using the pseudo-rigid-body model approach coupled with an optimiser to reach a design [163].

The building block design approach and eigenscrew decomposition framework discussed in Section 2.1.1 has also proved effective for designing shell mechanisms. Of particular note is the work of Nijssen *et al.* who highlighted that design of shell mechanisms can become difficult without a standard characterisation method due to their spatial nature, and presented a library of compliant shells to act as building blocks [168, 169] as shown in Figure 2.4. This library was developed to help with the design of a scoliosis brace where multiple correctional constraints are needed to be applied to the patient [168, 170]. The kinetic requirements of the patient could be identified in terms of translational and rotational stiffnesses,

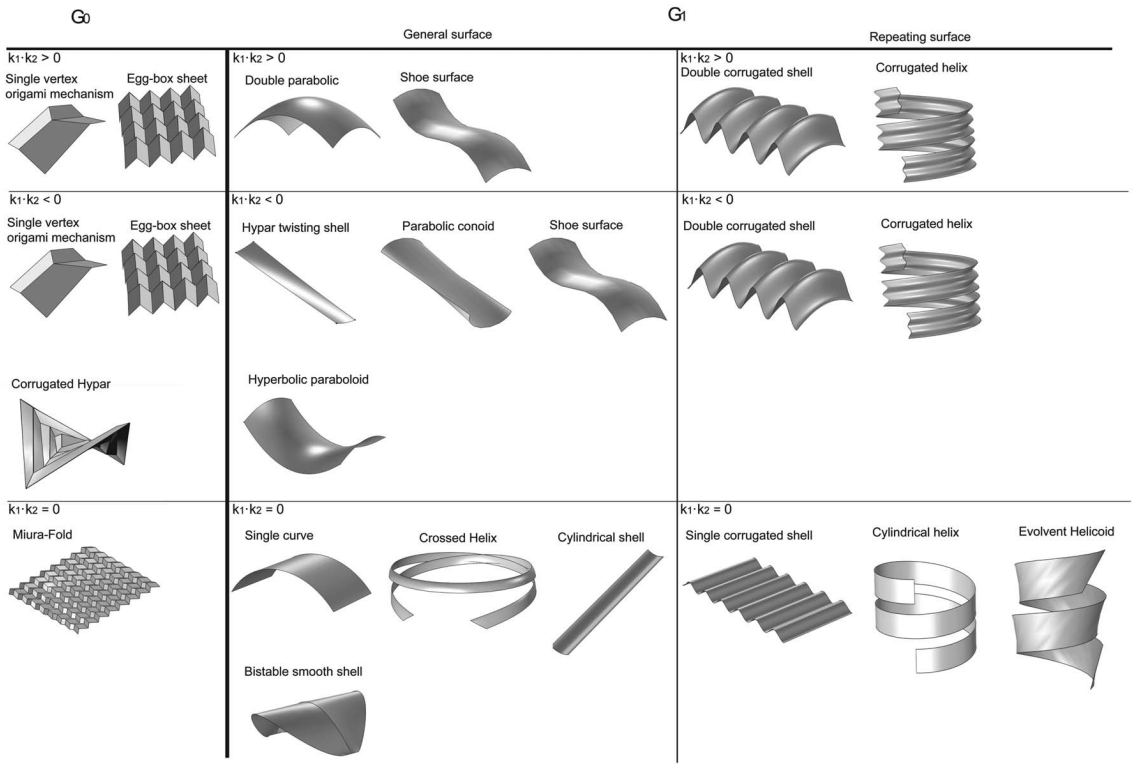

Figure 2.4: *Nijssen's library of compliant shell mechanism building blocks, including several origami mechanisms. G terms refer to whether geometry curves meet at join line (G^0) or have the same tangent direction at the join line (G^1) and κ terms refer to the principal curvatures. Reproduced from Ref [169].*

and suitable compliant shell mechanisms could be used to achieve these. While Nijssen characterised the library using compliance ellipsoids [169] (see Figure 2.5a), Leemans developed it further by creating framework to unify the units of compliance between the rotational and translational degrees of freedom, allowing them to be directly compared to give each building block a compliance ranking of its degrees of freedom [137, 138] (see Figure 2.5b).

The state of the art in compliant mechanism design includes a wide range of methods for determining detailed mechanism shapes and topologies, as well as methods for characterising and comparing complex mechanism behaviours. In contrast, less focus has been applied to material choices for such structures (despite careful choice and placement of material playing a large role in historical designs), which could further expand the available compliant mechanism design space.

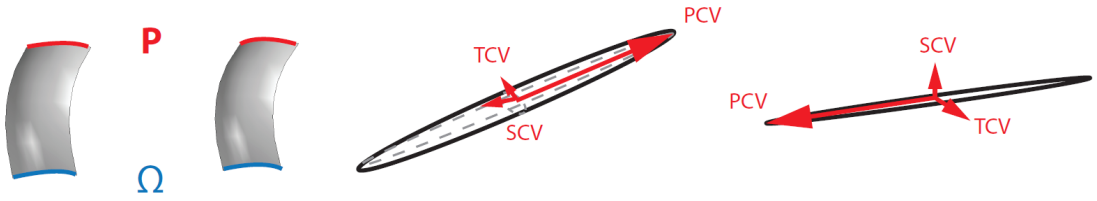

(a) *Double parabolic shell characterised with compliance ellipsoids, adapted from Ref [168]*

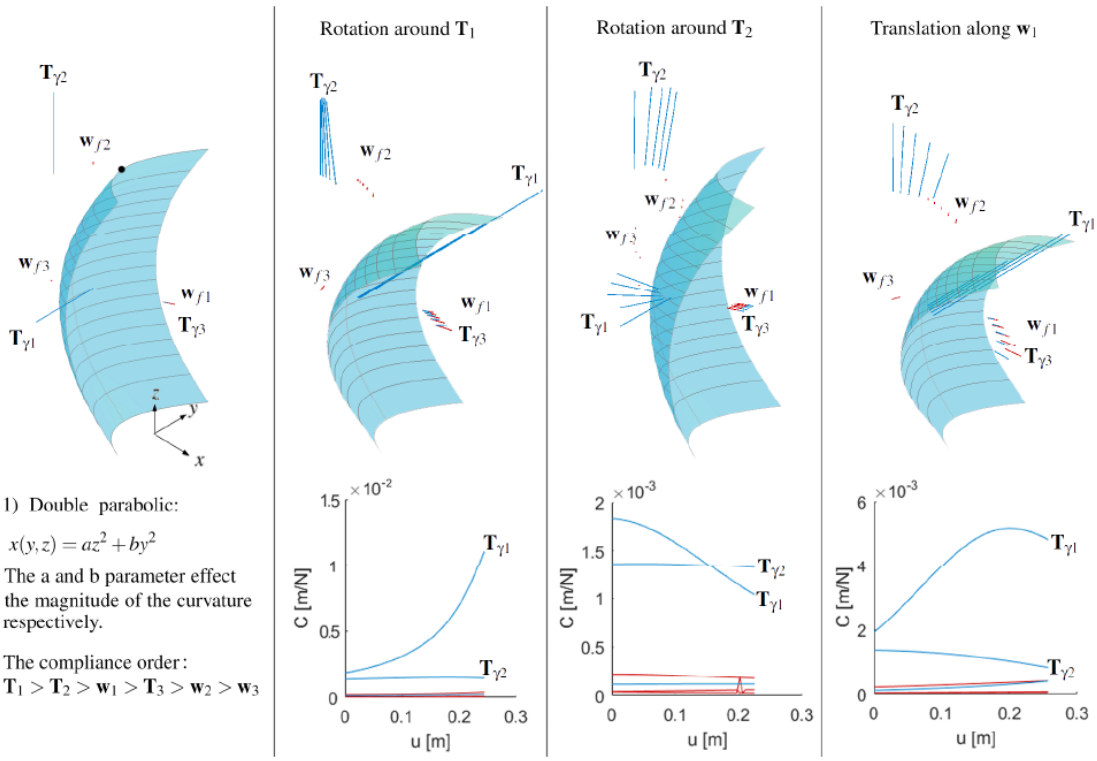

(b) *Double parabolic shell characterised with unified eigenscrews, adapted from Ref [139]*

Figure 2.5: *Comparison of compliance characterisation visualisation approaches for a double parabolic shell mechanism building block*

2.2 Composite Laminate Materials

In parallel to developments in compliant shell mechanisms, aerospace engineers have created shape-changing shell structures using anisotropic fibre reinforced composite materials. Composite materials often exhibit high specific properties, and can provide this high stiffness in an anisotropic manner by changing the orientations of the reinforcing fibres, enabling shells of the same geometry to deform differently and in novel manners that couple bending, twisting and extensional deformations [126]. Such anisotropic tailoring could include varying the fibre layup across the structure or prestressing the composite laminates. In addition, composite materials lend themselves to geometric optimisation as they can readily be formed into complex geometries with the shape and material created at the same time during manufacture. Application areas of interest have included morphing wings for aircraft [237], deployable structures for spacecraft [164] and aerodynamically-optimised wind turbine blades [128].

Huang and Schimmels noted that elastic members that couple translational and rotational components are required to be able to build mechanisms with any arbitrary stiffness matrix, suggesting tailored composites could be key for advanced mechanism design [97]. Despite this, almost all of the research in the field of compliant shell mechanisms has focused on isotropic shells. A couple of examples of anisotropic compliant mechanisms exist in literature, but these are only planar mechanisms. Both Li *et al.* [140] and Tong *et al.* [240] developed topology optimisation processes for composite mechanisms, highlighting that composite anisotropy could enable improved performance, with Tong *et al.* even investigating the potential of using composites with varying fibre angles. All of this work was entirely numerical however, with no manufacturing methods presented, and no consideration given for spatial composite shell mechanisms. It seems that the use of composites in the design of compliant mechanisms is currently under-utilised, which is surprising given their potential benefits, and this is something this thesis aims to address.

2.2.1 Classical Laminate Analysis (CLA)

Before reviewing the state of the art examples of morphing and deployable composite shells it is worth outlining some of the key aspects of Classical Laminate Analysis (CLA). The following subsection gives a brief overview of the mathematics required to evaluate the stiffness of composite laminates, as well as the composite material properties used throughout the work in this thesis; for full details of CLA the reader is directed to Refs [104, 167].

ABD Matrices

Evaluating effective shell-level stiffness properties is more complex when composite materials are included. Individual plies are stacked together to form a laminate, and the contributions of the different materials, fibre directions, and their distance (and ordering) from a reference plane (typically the shell mid-plane) must be taken into account. Composite Laminate Analysis (CLA) defines the $\boldsymbol{A}$, $\boldsymbol{B}$ and $\boldsymbol{D}$ matrices as the in-plane, coupling (between in-plane and out-of-plane) and bending stiffness matrices of the laminate [104, 167].

For these matrices to be valid, CLA relies on several key assumptions [100]: 1) displacements are continuous through the laminate thickness; 2) the laminate cross-sections remain plane and perpendicular (Kirchoff-Love hypothesis); 3) the strain-displacement relationship is linear; 4) the constituent materials are linear-elastic; and 5) the through-thickness stresses are small relative to the in-plane stresses (*i.e.* assume a state of plane stress). If these conditions apply, then ply-level stiffnesses can be expressed using the reduced stiffness matrix $\boldsymbol{Q}$, which links the ply-level stresses (σ / τ terms) to the ply-level strains (ϵ and γ terms),

$$\begin{bmatrix}\sigma_{11}\\ \sigma_{22}\\ \tau_{12}\end{bmatrix} = \boldsymbol{Q}\begin{bmatrix}\epsilon_{11}\\ \epsilon_{22}\\ \gamma_{12}\end{bmatrix} = \begin{bmatrix}Q_{11} & Q_{12} & 0\\ Q_{21} & Q_{22} & 0\\ 0 & 0 & G_{12}\end{bmatrix}\begin{bmatrix}\epsilon_{11}\\ \epsilon_{22}\\ \gamma_{12}\end{bmatrix}, \tag{2.1}$$

where

$$\begin{aligned} Q_{11} &= \frac{E_{11}}{1-\nu_{12}\nu_{21}},\\ Q_{12} = Q_{21} &= \frac{\nu_{12}E_{22}}{1-\nu_{12}\nu_{21}},\\ Q_{22} &= \frac{E_{22}}{1-\nu_{12}\nu_{21}}. \end{aligned}$$

Here E_{11} and E_{22} refer to the in-plane stiffness parallel to and perpendicular to the fibre direction respectively, G_{12} refers to the shear modulus, and ν_{12} and ν_{21} refer to the Poisson's ratios.

To take into account the orientation of the fibres in each ply (the angle θ), the transformation matrix $\boldsymbol{T}$, defined as,

$$\begin{bmatrix}\sigma_{11}\\ \sigma_{22}\\ \tau_{12}\end{bmatrix} = \boldsymbol{T}\begin{bmatrix}\sigma_{xx}\\ \sigma_{yy}\\ \tau_{xy}\end{bmatrix} = \begin{bmatrix}\cos^2\theta & \sin^2\theta & 2\sin\theta\cos\theta\\ \sin^2\theta & \cos^2\theta & -2\sin\theta\cos\theta\\ -\sin\theta\cos\theta & \sin\theta\cos\theta & \left(\cos^2\theta-\sin^2\theta\right)\end{bmatrix}\begin{bmatrix}\sigma_{xx}\\ \sigma_{yy}\\ \tau_{xy}\end{bmatrix}, \tag{2.2}$$

(where numeric subscripts refer to fibre axes, and alphabetic subscripts refer to global axes) can be used to convert the reduced stiffness matrix $\boldsymbol{Q}$, into the lamina

transformed stiffness matrix $\bar{\boldsymbol{Q}}$, defined as,

$$\bar{\boldsymbol{Q}} = \boldsymbol{T}^{-1}\boldsymbol{Q}\boldsymbol{R}\boldsymbol{T}\boldsymbol{R}^{-1}, \tag{2.3}$$

where $\boldsymbol{R}$ is the Reuter matrix

$$\boldsymbol{R} = \begin{bmatrix} 1 & 0 & 0 \\ 0 & 1 & 0 \\ 0 & 0 & 2 \end{bmatrix}, \tag{2.4}$$

which is included so that the strain transformation can be written elegantly when using an engineering definition of strain (*i.e.* $\epsilon_{12} = \frac{1}{2}\gamma_{12}$). Using this lamina stiffness matrix, the $\boldsymbol{ABD}$ matrices can be constructed by summing the stiffness contributions of each ply:

$$A_{ij} = \sum_{k=1}^{n} \left[\bar{Q}_{ij}\right]_k \left(h_k - h_{k-1}\right), \tag{2.5}$$

$$B_{ij} = \frac{1}{2}\sum_{k=1}^{n} \left[\bar{Q}_{ij}\right]_k \left(h_k^2 - h_{k-1}^2\right), \tag{2.6}$$

and

$$D_{ij} = \frac{1}{3}\sum_{k=1}^{n} \left[\bar{Q}_{ij}\right]_k \left(h_k^3 - h_{k-1}^3\right), \tag{2.7}$$

where i and j refer to the positions of the terms in the matrix, k is the ply index (with the first ply being $k = 1$), and h_k being the position of the top of ply k with respect to the laminate reference plane. Together the $\boldsymbol{ABD}$ matrices link the laminate-level loads and bending moments (N and M terms respectively) to the reference plane strains and curvatures (ϵ^0 / γ^0 and κ terms):

$$\left[\begin{array}{c} N_{xx} \\ N_{yy} \\ N_{xy} \\ \hline M_{xx} \\ M_{yy} \\ M_{xy} \end{array}\right] = \left[\begin{array}{c|c} \boldsymbol{A} & \boldsymbol{B} \\ \hline \boldsymbol{B} & \boldsymbol{D} \end{array}\right] \left[\begin{array}{c} \epsilon^0_{xx} \\ \epsilon^0_{yy} \\ \gamma^0_{xy} \\ \hline \kappa_{xx} \\ \kappa_{yy} \\ \kappa_{xy} \end{array}\right] = \left[\begin{array}{ccc|ccc} A_{11} & A_{12} & A_{16} & B_{11} & B_{12} & B_{16} \\ A_{12} & A_{22} & A_{26} & B_{12} & B_{22} & B_{26} \\ A_{16} & A_{26} & A_{66} & B_{16} & B_{26} & B_{66} \\ \hline B_{11} & B_{12} & B_{16} & D_{11} & D_{12} & D_{16} \\ B_{12} & B_{22} & B_{26} & D_{12} & D_{22} & D_{26} \\ B_{16} & B_{26} & B_{66} & D_{16} & D_{26} & D_{66} \end{array}\right] \left[\begin{array}{c} \epsilon^0_{xx} \\ \epsilon^0_{yy} \\ \gamma^0_{xy} \\ \hline \kappa_{xx} \\ \kappa_{yy} \\ \kappa_{xy} \end{array}\right] \tag{2.8}$$

When a laminate possesses a non-zero $\boldsymbol{B}$ matrix, in-plane (thermal) strains can cause out-of-plane curvature changes, *i.e.* (thermal) warping. The reduced bending stiffness matrix

$$\boldsymbol{D}^* = \boldsymbol{D} - \boldsymbol{B}^T\boldsymbol{A}^{-1}\boldsymbol{B}. \tag{2.9}$$

accounts for the contribution of non-zero $\boldsymbol{B}$ matrices to the bending stiffness. It is used in the calculation of the flexural strain energy.

Material Invariants & Lamination Parameters

Another useful concept for the analysis of composite structures are lamination parameters, first proposed by Tsai [241]. These allow the stiffness of any (non-hybrid) composite layup to be represented using at most twelve continuous parameters (ξ_1 to ξ_{12}) and a thickness, h. In addition, they allow the $\boldsymbol{ABD}$ matrix terms to be expressed as linear functions:

$$\begin{bmatrix} A_{11} \\ A_{12} \\ A_{22} \\ A_{66} \\ A_{16} \\ A_{26} \end{bmatrix} = h \begin{bmatrix} 1 & \xi_1 & \xi_2 & 0 & 0 \\ 0 & 0 & -\xi_2 & 1 & 0 \\ 1 & -\xi_1 & \xi_2 & 0 & 0 \\ 0 & 0 & -\xi_2 & 0 & 1 \\ 0 & \frac{\xi_3}{2} & \xi_4 & 0 & 0 \\ 0 & \frac{\xi_3}{2} & -\xi_4 & 0 & 0 \end{bmatrix} \begin{bmatrix} U_1 \\ U_2 \\ U_3 \\ U_4 \\ U_5 \end{bmatrix}, \tag{2.10}$$

$$\begin{bmatrix} B_{11} \\ B_{12} \\ B_{22} \\ B_{66} \\ B_{16} \\ B_{26} \end{bmatrix} = \frac{h^2}{4} \begin{bmatrix} 0 & \xi_5 & \xi_6 & 0 & 0 \\ 0 & 0 & -\xi_6 & 0 & 0 \\ 0 & -\xi_5 & \xi_6 & 0 & 0 \\ 0 & 0 & -\xi_6 & 0 & 0 \\ 0 & \frac{\xi_7}{2} & \xi_8 & 0 & 0 \\ 0 & \frac{\xi_7}{2} & -\xi_8 & 0 & 0 \end{bmatrix} \begin{bmatrix} U_1 \\ U_2 \\ U_3 \\ U_4 \\ U_5 \end{bmatrix}, \tag{2.11}$$

$$\begin{bmatrix} D_{11} \\ D_{12} \\ D_{22} \\ D_{66} \\ D_{16} \\ D_{26} \end{bmatrix} = \frac{h^3}{12} \begin{bmatrix} 1 & \xi_9 & \xi_{10} & 0 & 0 \\ 0 & 0 & -\xi_{10} & 1 & 0 \\ 1 & -\xi_9 & \xi_{10} & 0 & 0 \\ 0 & 0 & -\xi_{10} & 0 & 1 \\ 0 & \frac{\xi_{11}}{2} & \xi_{12} & 0 & 0 \\ 0 & \frac{\xi_{11}}{2} & -\xi_{12} & 0 & 0 \end{bmatrix} \begin{bmatrix} U_1 \\ U_2 \\ U_3 \\ U_4 \\ U_5 \end{bmatrix}. \tag{2.12}$$

of material invariants U_1 to U_5, which are linear combinations of the reduced stiffness matrix terms, Q_{ij}, as follows [241]:

$$U_1 = \frac{1}{8}(3Q_{11} + 3Q_{22} + 2Q_{12} + 4Q_{66}) \tag{2.13}$$

$$U_2 = \frac{1}{2}(Q_{11} - Q_{22}) \tag{2.14}$$

$$U_3 = \frac{1}{8}(Q_{11} + Q_{22} - 2Q_{12} - 4Q_{66}) \tag{2.15}$$

$$U_4 = \frac{1}{8}(Q_{11} + Q_{22} + 6Q_{12} - 4Q_{66}) \tag{2.16}$$

$$U_5 = \frac{1}{8}(Q_{11} + Q_{22} - 2Q_{12} + 4Q_{66}) \tag{2.17}$$

The lamination parameters themselves (ξ_1 to ξ_{12}) are then defined. Using a similar notation to that used by Fukunaga in Ref [69]:

$$\begin{bmatrix}\xi_1 & \xi_2 & \xi_3 & \xi_4\end{bmatrix} = \frac{1}{2}\int_{-1}^{1}\begin{bmatrix}\cos 2\theta & \cos 4\theta & \sin 2\theta & \sin 4\theta\end{bmatrix} du \tag{2.18}$$

$$\begin{bmatrix}\xi_5 & \xi_6 & \xi_7 & \xi_8\end{bmatrix} = \int_{-1}^{1}\begin{bmatrix}\cos 2\theta & \cos 4\theta & \sin 2\theta & \sin 4\theta\end{bmatrix} u du \tag{2.19}$$

$$\begin{bmatrix}\xi_9 & \xi_{10} & \xi_{11} & \xi_{12}\end{bmatrix} = \frac{3}{2}\int_{-1}^{1}\begin{bmatrix}\cos 2\theta & \cos 4\theta & \sin 2\theta & \sin 4\theta\end{bmatrix} u^2 du \tag{2.20}$$

where θ represents the fibre angle of a unidirectional ply, and $u = 2z/t$, with z referring to the distance away from the laminate reference plane, and t the individual ply thickness. Lamination parameters are another way to sum the contributions of the fibre angles to the laminate stiffness through the thickness of the laminate, and can act as elegant laminate design parameters. These linear ABD expressions, and being able to describe any laminate in terms of only twelve parameters and a thickness, can simplify equations used in composites analysis and are particularly beneficial for optimisation problems as their design space is convex. A few examples of composite design using lamination parameters can be found in Refs [105,107,162].

Composite Material Properties

In this thesis two composite material systems are considered for the analysis and prototyping of various case studies, with both chosen due to their well-documented properties and ease of availability. Firstly a higher-stiffness system utilising unidirectional Hexcel IM7 carbon fibres and 8552 epoxy resin matrix was used in initial studies of a tape spring mechanism (Chapter 3) and helical lattice structures (Chapter 4). Nominal material properties relevant for this work are noted in Table 2.1 based on values from Refs [24, 87, 197]. Here α_{11} and α_{22} refer to the coefficients of thermal expansion parallel to and perpendicular to the fibre direction respectively, t refers to the cured ply thickness, and ρ refers to the laminate density. Additionally, the terms X_t and X_c refer to the ultimate tensile and compressive strengths of an IM7-8552 ply along the fibre direction, Y_t and Y_c refer to the ultimate tensile and compressive strengths perpendicular to the fibre direction, and S refers to the ultimate shear strength.

Later work considers composite compliant mechanisms for medical support applications and uses generic properties for a lower-stiffness system with unidirectional E-Glass fibres and an epoxy matrix. The material properties relevant for this work are listed in Table 2.2. Here the terms are the same as for Table 2.1, with the additional term H referring to the total thickness of the cured laminate (*i.e.* the sum of the thicknesses of all individual plies).

Table 2.1: *Material Data IM7-8552 [24, 87, 197]*

$E_{11} = 161$ GPa	$\alpha_{11} = -0.1 \cdot 10^{-6}$ K^{-1}	$X_{ts} = 2326.2$ MPa
$E_{22} = 11.38$ GPa	$\alpha_{22} = 31 \cdot 10^{-6}$ K^{-1}	$X_{cs} = 1200.1$ MPa
$G_{12} = 5.17$ GPa	$t = 0.131$ mm	$Y_{cs} = 62.3$ MPa
$\nu_{12} = 0.32$	$\rho = 1.57 \cdot 10^{3}$ kg/m^{3}	$Y_{cs} = 199.8$ MPa
		$S_s = 92.3$ MPa

Table 2.2: *Material Data E-Glass - Epoxy [37]*

$E_{11} = 41$ GPa	$\alpha_{11} = 7.0 \cdot 10^{-6}$ K^{-1}
$E_{22} = 10.4$ GPa	$\alpha_{22} = 26 \cdot 10^{-6}$ K^{-1}
$E_{11}/E_{22} = 3.9$	$\nu_{12} = 0.28$
$G_{12} = 4.3$ GPa	$H = 0.5$ mm

2.3 Classifying Morphing Composite Shells

Morphing structures are those in which the structural shape is designed to change between different functional states. This can also include deployable structures, *i.e.* those where one state is a compact, stowed configuration, and the other is a much larger operational configuration. Ways to classify the many different configurations and behaviour of morphing composite structures in the literature is by considering the actuation and stability states of the morphing shell:

- **Active or Passive Structures.** Is the shape change determined entirely by the structure stiffness and the external loading (*i.e.* a classical flexure element), or is it controlled by some stimuli input by the user, *e.g.* thermal, piezoelectric or shape-memory actuators?
- **Mono- or Multi-Stable Structures.** Does the structure possess one reference 'undeformed' state, or are non-linear buckling or rapid shape-changes included in the design?

2.3.1 Passive Monostable Shells

While not the most common type of morphing composite in the literature, passive monostable shells have been an area of interest for deployable structures. In particular tape springs (open-section cylindrical shell structures with a single curvature about the shell longitudinal axis) have been investigated as deployable devices due to their ability to be folded and stowed in an unstable state that can be released when deployment is required. Initially studied by Rimrott [198], Seffen *et al.* detailed the deployment behaviour of such structures, presenting two ways in which tape springs can be stowed: coiled or folded (as shown in Figure 2.6) [216, 217]. In these studies Seffen showed that the development of an elastic fold is a propagating instability

with constant bending moments existing on either side of the fold, and presented analytical models for coiled and locally-folded tape springs. While traditionally these deployable shell structures were metallic structures, Yee *et al.* demonstrated the potential of using composite tape springs to reduce mass and reduce thermal expansion coefficients [256].

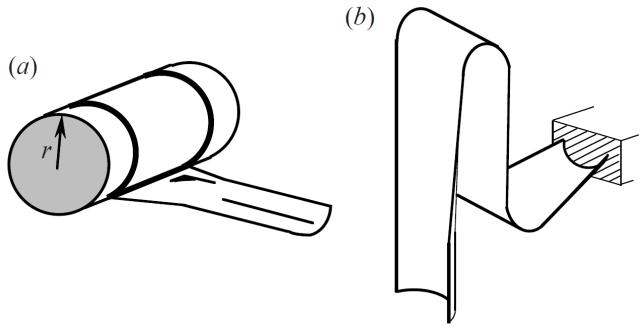

Figure 2.6: *Two configurations for stowing deployable tape springs: (a) coiled and (b) locally-folded. Reproduced from Ref [216].*

Another folded deployable composite shell structure is the slit-tube hinge (sometimes also referred to as a tape spring hinge) most famously used for the antenna on the MARSIS experiment onboard the Mars Express spacecraft [148]. This class of structure is a development of the folded tape spring, with slits cut into a hollow tube to enable a discrete hinge to form in the manner of folded tape springs (as shown in Figure 2.7). Yee and Pellegrino extended existing analytical models to include composite materials and conducted strain measurement studies for this class of structure [184, 255], noting that woven composite booms are more suitable for surviving high strain deployments. Mallikarachchi and Pellegrino conducted a design study of a double-hinged boom with a focus on assessing the boom sensitivity to deployment failure [147].

This concept of using a cut-out slit to develop a folded shell structure was later used by Lachenal *et al.* for a folding wing concept, although the effect of the slit

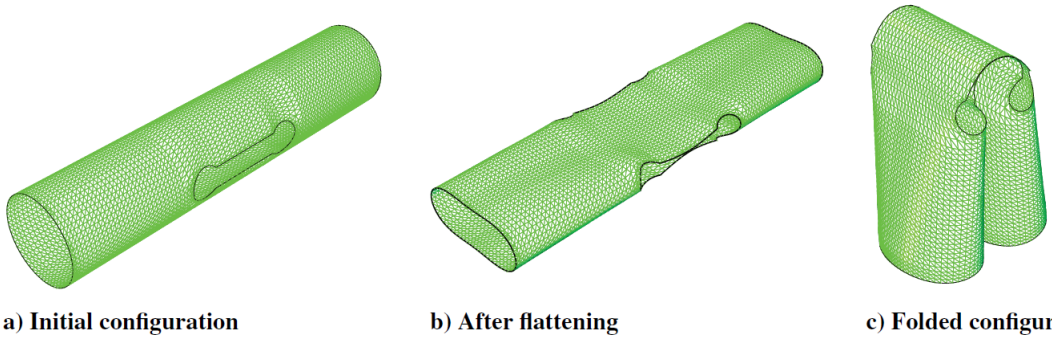

Figure 2.7: *Folding sequence of a composite slit-tube hinge. Reproduced from Ref [147].*

on aerodynamic performance was not investigated [132]. A further variation of the deploying hinge was presented by Sarkovsky *et al.* using multi-matrix composites, with more flexible matrix materials used at hinge locations instead of cutting holes into the tube [202, 203].

2.3.2 Passive Multistable Shells

Tape Springs

Tape springs were also found to be capable of exhibiting bistable behaviours that could be exploited for morphing purposes, and have received significant research interest as a result. First developed by Daton-Lovett, these tape springs differed from previous monostable metallic designs by utilising an anti-symmetric composite laminate to cause the tape spring to become stable in its coiled configuration and its deployed configuration [40]. Iqbal and Pellegrino presented an energy-based analytical model to describe the main folding behaviour of these structures and carried out finite element simulations to predict radii values and highlight structural nonlinearities [101]. Galletly and Guest presented two further analytical models for bistable composite tubes based on beams and shells, showing that shell edge effects can have a significant impact on shell equilibrium states [72, 73]. Pellegrino *et al.* showed that this bistability could also be incorporated into any material tape spring by mechanically prestressing it [106, 183]. Building on this bistability work, Seffen and Guest showed that same-sense prestressing could be used to generate a neutrally stable isotropic shell structure (*i.e.* one where minimal, if any, load is required for deformation), or a bistable orthotropic shell structure, as well as novel configurations where neutral and bistable behaviour could exist together [215].

One of the most popular application areas for these composite tape springs is in bistable booms for small satellites, and examples of these can be seen in Refs [33, 66, 102, 165]. More recent developments have included investigations by Wang *et al.* into the folding behaviour of bistable tape springs, which mapped out the bending and buckling processes that occur [248, 249], and new bistable forms developed by Knott *et al.* that include double curvatures and stable helical configurations [117, 118].

Helical Shells

Helical shell structures have also been of interest for tailored multistable morphing. Lachenal *et al.* presented a twisting structure comprised of two prestressed composite strips connected in parallel by rigid spokes where changing the layup could allow stable twisted states to be tailored [130]. A diagram of this is shown in Figure 2.8, and similar structures were presented in Refs [7, 26, 28, 149]. Later Lachenal *et al.* applied this concept to make a bistable composite twisting I-beam [129].

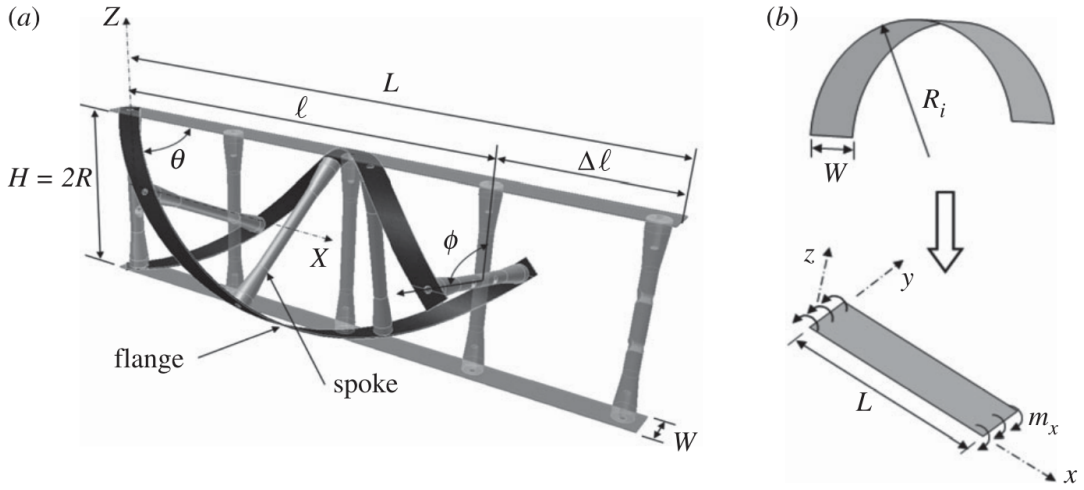

Figure 2.8: *Illustration of Lachenal's ladder-type morphing composite helix (a) showing the structure in its straight and twisted configurations, and (b) showing the generation of prestress by flattening initially-curved strips. Reproduced from Ref [130].*

Other helical morphing composites were considered in bistable lattice configurations, initially presented by Pirrera *et al.* [187] (non-helical multistable composite lattices also exist [36]), and is shown in Figure 2.9. Other work with these helices has involved stiffness tailoring for novel thermal behaviour (see Chapter 4 and Ref [175]), as well as combining them to create coupled non-linear structures [49]. Pirrera's initial helix model using 1D rods was refined by McHale *et al.* to include the effects of shell transverse curvatures and thermal effects [27, 155, 156]. Analytical analysis of these structures could be done in an elegant manner by introducing the assumption that the helical strips remain on an underlying cylinder, and such models are compared to numerical and experimental results in Chapter 4. Both classes of lattice structure show good examples of how geometry, composite layup and prestress can be used to configure the multistable states of a structure, and further structural tailoring can be achieved by combining multiple such helices [49, 157].

Aerodynamic Surfaces

Multi-stability has also been considered for shape-changing composite aero-surfaces, with Diaconu *et al.* presenting three bistable aerofoil sections utilising prestressed composite skins on the trailing edge [48]. These sections could undergo large deformations, but lacked load-carrying capacity. Kuder *et al.* presented an alternative morphing aerofoil with internal bistable flexures that was more suitable for aerodynamic loading [124, 125]. Daynes *et al.* demonstrated the feasibility of flow-dependant bistability in the design of an air inlet where the prestressed composite laminate could be tailored to change states at a pre-determined flow state [45].

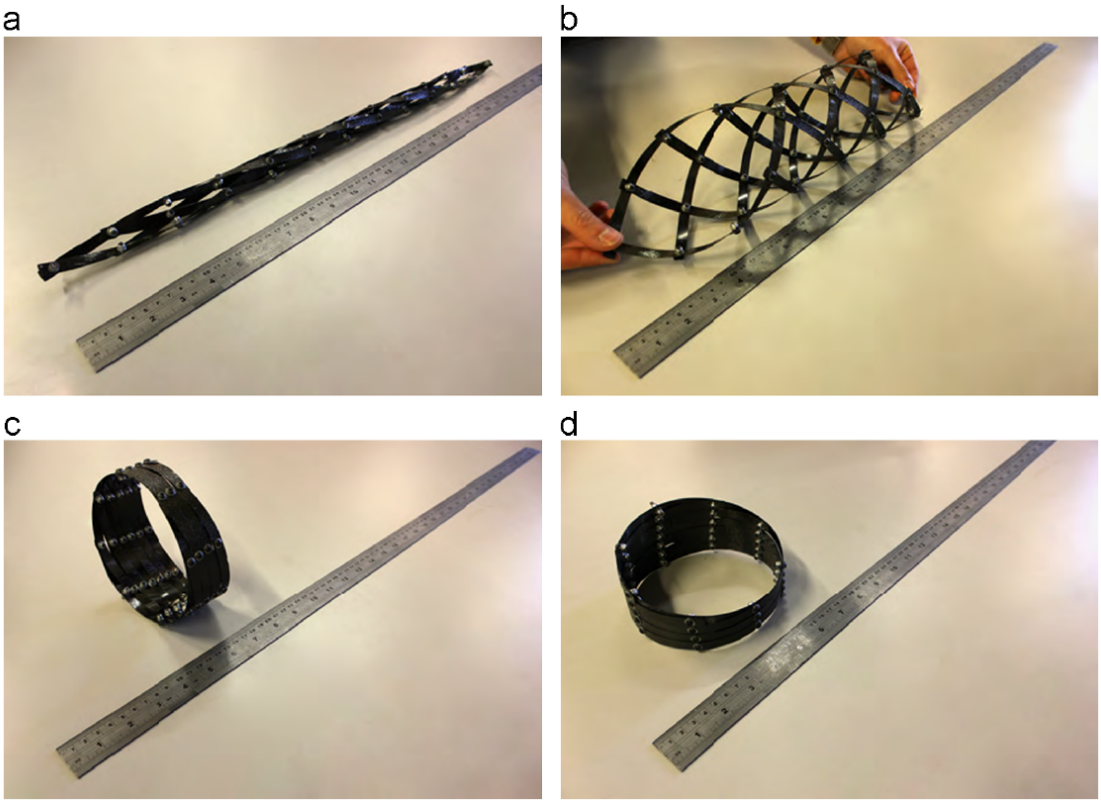

Figure 2.9: *Photographs of Pirrera's bistable composite helical lattice prototype showing (a) the stable extended state, (b) an unstable transition state, and (c,d) the stable contracted state. Reproduced from Ref [187].*

General Shells

Multi-stability has also been investigated in detail for general geometries of shells [133], and for shells with arbitrary laminates [11], illustrating the vast potential for tailoring shell structures. Seffen showed that bistability could be achieved in thin shells by choosing only material properties and an initial shell shape (*i.e.* without any prestressing of the shell) [213], and Vidoli *et al.* expanded this to demonstrate tristability [246]. More general multistable behaviour has been investigated for corrugated shells [173], and in surfaces created by connecting multiple bistable laminated shells [34, 35].

Attention has also been given to thermal contributions to multistability in shells. This has been investigated in shells containing unsymmetric laminates [38, 152, 185], shells that were mechanically prestressed [42], shells where novel variable fibre angle manufacturing technologies were used [178], shells that utilise hybrid laminates [43], and shells that were initially curved [53, 136]. In later work, Daynes and Weaver focused on laminates that became multistable due to expansion coefficient differences, showing that inducing mechanical prestress could counter hygro-thermal effects, increase achievable deflections, and maintain high stiffnesses [44]. Brinkmeyer *et al.* showed how the use of hybrid laminates with viscoelastic behaviours could enable a time-dependant bistability [15, 16].

Whereas in previous cases simplified analytical models were feasible for capturing complex behaviour (*e.g.* the helical lattice structure [187]), a variety of semi-analytical and numerical techniques have been presented for modelling the behaviour of general multistable shells. These include energy minimisation of the assumed plate curvatures to identify stable states [38, 41], using higher-order polynomials techniques to model displacements accurately [134, 186], using assumptions of uniform or quadratic curvature for quick computation of the Föppl-von Karman equations for the large deformations of plates [85], and using generalised path-following algorithms with finite-element solvers to identify the stability sensitivities to various design parameters [79, 80].

A variety of different behaviours have been shown in literature for passive shell structures with a range of geometries, materials and stress states. This demonstrates the significant potential for tailoring the responses of shell structures.

2.3.3 Active Monostable Shells

While self-deploying and multistable structures have been shown to be tailorable, some applications have required more control of the shell deformation, typically in the form of a controlled actuator. For monostable shell structures multiple methods of actuation have been demonstrated in literature. Yang *et al.* incorporated Shape

Memory Alloys (SMAs) that return to a reference shape under a predefined thermal load into a composite wing structure to enable smooth camber change [252]. Bilgen *et al.* also developed a smooth variable-camber aerofoil, but by using macro-fibre actuation: a series of piezoelectric ceramic fibres embedded into a polymer matrix [12]. Steeves *et al.* used a piezoelectric layer to actuate (and thus correct shape errors in) an ultra-thin composite mirror for a space telescope [230]. Johannisson *et al.* demonstrated the potential of electro-chemical actuation by embedding carbon fibres in a structural battery electrolyte matrix (shown in Figure 2.10) to create a device similar to a bi-metallic strip, where two layers of this composite were insulated from each other and lithium ions allowed to flow from one to the other, causing the discharging layer to contract and the charging layer to expand [103].

Many active monostable shells have also been developed using elastomeric matrix composites to create 'soft' mechanisms. Chillara *et al.* demonstrate a pneumatically-actuated shell comprised of a rigid constraint layers, hollow 'fluidic' layers (to be actuated) and prestressed fibre reinforced elastomeric layers [31]. Several prototype soft composite structures have been developed that are actuated using SMA wires where bend-twist coupled deflection of cantilever beams has been sought using anisotropic effects from material and actuator placement [2, 199, 222]. SMA-actuated monostable composite shells have also been developed there for smart prosthetic [114] and automotive applications [86]. While elastomeric matrices offer greater mechanism deflections, their reduced stiffness means their ability to transmit or resist loads is limited.

2.3.4 Active Multistable Shells

Actuation has also been used to control the multistable behaviour of mechanisms, typically in low-power systems used to snap between different stable states. Pollard *et al.* present a deployable truss structure made from composite tape springs and embedded SMA flexures, where the SMAs are included to allow the boom to pack down tighter while still being able to deploy [188]. Murphey *et al.* also use nickel-titanium SMAs to control the shape of a tape spring structure; their tape spring had a stress state and layup tailored to enable it to be neutrally-stable (see Figure 2.11), *i.e.* every deformation state of the coiled tape spring was stable, creating a multistable structure with infinite stable states [166].

Murphey *et al.* also proposed using a piezoelectric film to actuate the tape spring as it was shown to be slightly less sensitive to manufacturing imperfections (the neutrally-stable behaviour was very difficult to produce). Other active mechanisms have considered using piezoelectric actuation to snap a bistable [135, 189, 210] or multistable [65] plate between its to stable states.

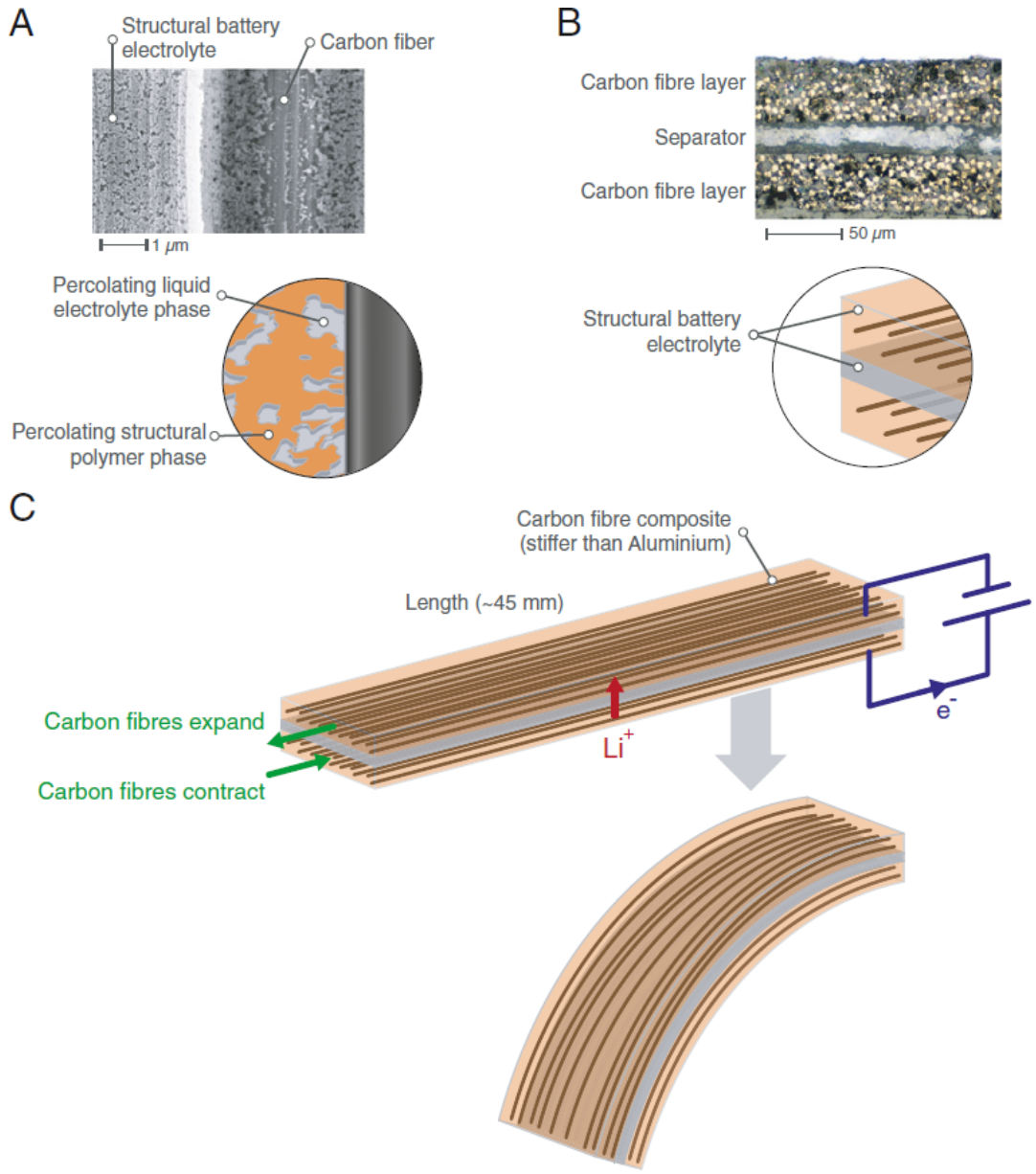

Figure 2.10: *Electro-active mechanism comprised of carbon fibres in a structural battery electrolyte matrix that allows the movement of lithium ions. (A) shows the matrix phases and interface, (B) shows the mechanism cross-section, and (C) shows the shape change resulting from the expansion and contraction of the layers as the lithium ions discharge. Reproduced from Ref [103].*

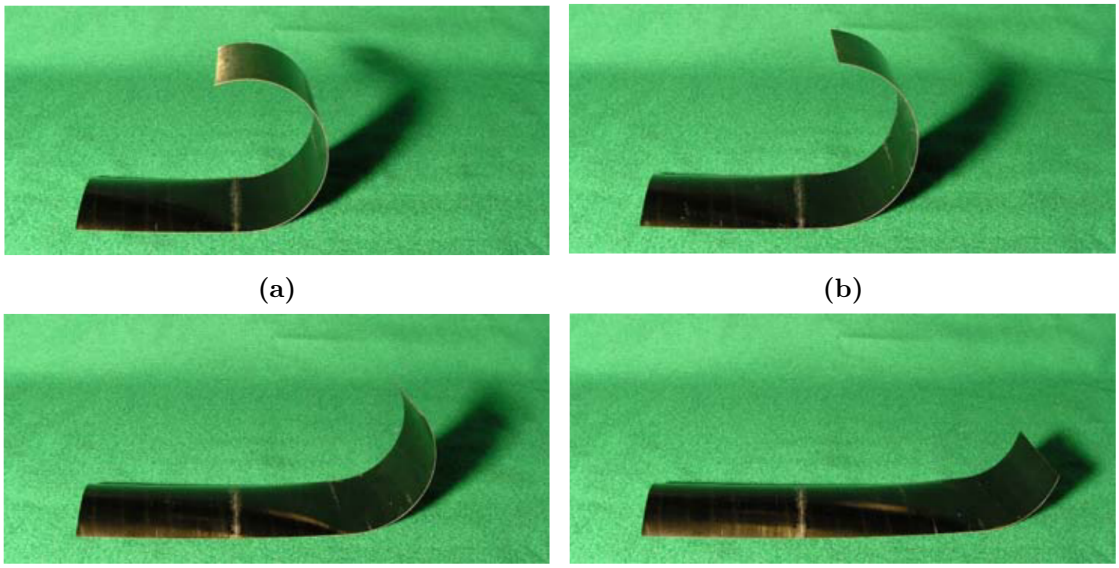

Figure 2.11: *Photographs of various states of deployment of the neutrally-stable tape spring developed by Murphey at al.. Reproduced from Ref [166].*

Due to material anisotropy and residual stresses often left after curing, thermal actuation has also been used to enable shape change in composite shells. Giddings *et al.* investigated the shape changes of a bistable curved composite shell when heated and considered the effects of ply thickness variations and resin pockets [74], while Eckstein *et al.* and Zhang *et al.* have investigated the stable shapes of multistable composite shells with temperature-dependant material properties [52, 259]. Eckstein *et al.* also considered the effects of high temperature morphing using hybrid laminates and metal matrix composites where the mismatches between thermal expansion coefficients can be more extreme (hence granting more tailoring potential) than in classical polymer matrix composites [54, 55].

The use of thermal actuation of a composite structure is explored in this thesis in Chapter 4, but the variety of geometric controls for both active and passive morphing composite structures seen in literature demonstrate that other actuation routes are possible.

2.4 Prestressed Composite Shells

Novel behaviour in compliant shell structures is governed not just by geometry and material properties, but also by specific stress states within the material. Inclusion of prestress offers significant scope for expanding the design space of shell structures, and has been present in a wide variety of the shape-changing composite devices in the literature (*e.g.* Refs [15, 41–44, 130, 149, 152]), and is a prerequisite for novel behaviours such as neutral stability [215].

2.4.1 Techniques for Inducing Prestress

A wide range of techniques exist for imparting prestress into a composite shell structure, and these generally fall into one of three categories: mechanical prestress, thermal prestress and viscoelastic prestress. Including these can enable a re-distribution of the shell internal strain energy during deformations towards a novel functionality.

Mechanical Prestress

Often mechanical prestress involves bending or buckling a structural member before locking it into the mechanism assembly, in order to tailor its geometric stiffness contribution to the structure. As previously mentioned, helical lattices have been used to enable novel structural behaviours, and Lachenal *et al.* flattened curved cured composite strips to create a lattice structure with embedded bending moments that induced bistable twisting behaviour [131]. This kind of mechanical prestress has been used to 'statically balance' mechanisms - ensuring they remain in fixed positions with no loading. Hoetmer *et al.* used a buckled beam to impart negative stiffness into a gripper mechanism to balance other elements with positive stiffnesses [89], and Radaelli *et al.* using prestressed torsion bars to balance an inverted pendulum [192]. Composite patches can also be used to prestress structures, with Chillara *et al.* showing how prestressed elastomeric composites could be bonded to an isotropic shell to induce bistability [30]. Another method for mechanical prestress was shown by Kebadze *et al.* who used mechanical rolling of an isotropic metallic shell in specific directions to impart desired residual bending moments and membrane stresses that would balance the induced energies caused during deformation of the shell. An analytical model for the shell strain energies was presented, which assumed that the shell rotates around an underlying cylinder [106], and a prototype of such a zero torsional stiffness device was shown by Guest *et al.* [81] (see Figure 2.12).

Thermal Prestress

Several examples of passive and active composite structures included prestress from the mismatch of thermal expansion coefficients in the composite layup. These thermal residual stresses have been investigated in composite structures, as they are a by-product of composite manufacture due to high temperature curing processes, and when combined with unsymmetric layups they can generate out-of-plane twisting and warping. A good example of this can be seen in Ref [52], where the potential thermally-induced shape changes of a cross-ply laminate are shown (see Figure 1.2 in Chapter 1). Laser forming can also be used to impart prestress in metallic structures, and has been modelled by Yanjin *et al.* [254]. It is worth noting that thermal prestress can be difficult to control as changes in the environmental conditions will

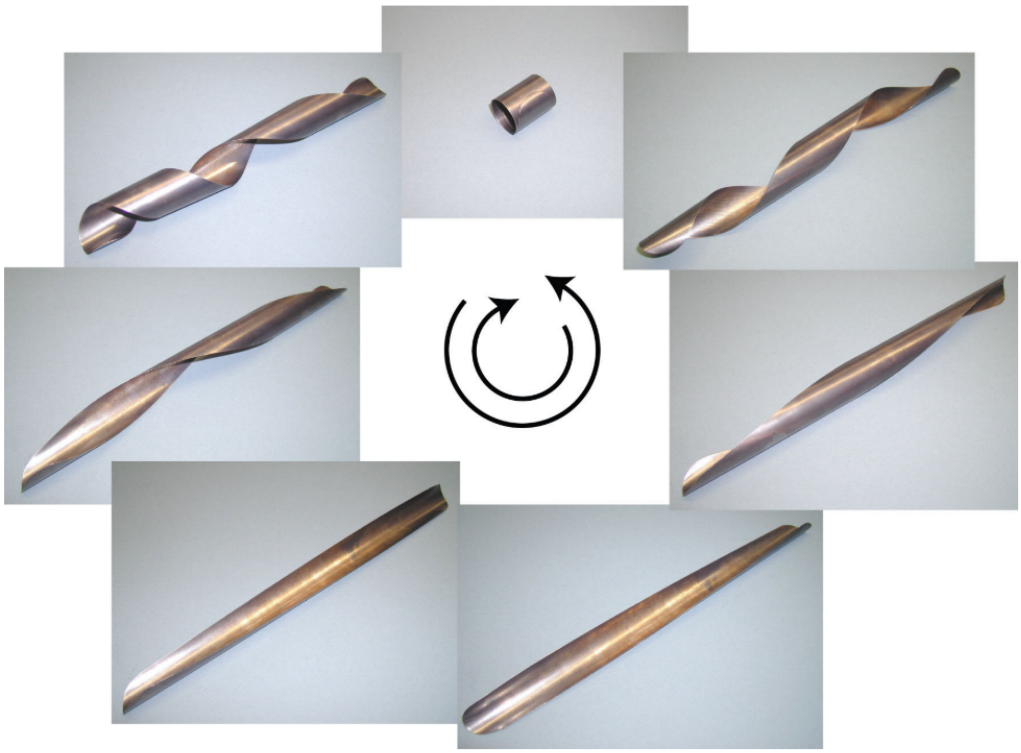

Figure 2.12: *Different deformation states of a copper-beryllium tape spring that was mechanically-prestressed to generate zero torsional stiffness behaviour. Reproduced from Ref [81].*

affect the thermal prestress. In their review of composite prestressed structures Daynes *et al.* stated that hygrothermal variability and low stiffnesses often warranted the need for additional mechanical prestressing of structures where thermal prestress had been used to induce multistability [44]. Furthermore, it has also been demonstrated that symmetric composite laminates can be made bistable using prestressing techniques and thermal loading [42,53], illustrating the potential benefits of combining thermal and mechanical prestress. Thermal prestress is explored in this thesis for tailoring the torsion of tape springs in Chapter 3, and in Refs [227, 228] based on the work therein.

Viscoelastic Prestress

The third most common form of prestress is via pre-loading viscoelastic materials (usually polymeric reinforcing fibres or constituent composite matrix) to include a time-dependent stress state in the shell. Fancey *et al.* investigated the potential of using viscoelastically stretched nylon 6,6 fibres in polymer composites as a mode of prestress [60], showing them to offer improved flexural stiffness [63] and impact energy absorption [61], and noting that these properties are maintained over many years. Manufacturing such composites is challenging, however, with stress needing

to be applied to the fibres during cure. Additionally, the lifespan of viscoelastic behaviour was not assessed for mechanisms where large deflections over many cycles may cause stress relaxation. Work by Brinkmeyer *et al.* and Wang *et al.* has shown that this sort of stress relaxation may be beneficial, with viscoelastic prestress enabling time-dependant multistable behaviour, where mechanisms snap between states after a sufficient period of stress relaxation has passed [17,247]. Burgoyne and Alwis noted that the viscoelastic behaviour of aramid fibres can be complex, with regions of linear and nonlinear behaviour that depend on stress levels, indicating that care must be taken if viscoelasticity is used to target a specific mechanism behaviour [21].

2.4.2 Developing Zero Stiffness Behaviour

While prestressed compliant mechanisms are potentially challenging to design and make, one of their most interesting potential benefits is the ability to enable the creation of structures that exhibit zero stiffness in certain degrees of freedom [215]. Also known as neutral stability, such structures require little to no energy input to achieve a deflection, adopting whatever deflected configuration they are left in [206]. As such these mechanisms are beneficial in applications where only small actuation forces can be provided (demonstrated nicely in the piezoelectrically-actuated rotating cylindrical shell from Hamouche *et al.* [84]), and can also be used as a way of isolating a system from vibrations. In practice, real mechanisms are unlikely to be 'truly' zero stiffness as there will always be small material or geometric variations in the shell that cause a favouring of one equilibrium state [234]. Nonetheless several examples of 'practical' zero stiffness shell mechanisms exist, where residual forces are so small that frictional or other forces can hold the structure in place.

Classical zero stiffness mechanisms have relied on the interaction of multiple members to achieve an overall neutrally stable response. Elements with negative stiffnesses (often generated via mechanical prestressing, *e.g.* a buckled beam) could cancel out the responses of elements with positive stiffnesses (rods, springs etc.) [206]. These combinations of springs and connecting beams can enable energy-free adjustments of mechanism responses, and some of these devices have been used in gravity balancing mechanisms [9, 195] and tensegrity structures [207].

Examples of zero stiffness tape springs have been introduced previously, and these also rely on energy balances. The copper-beryllium prototype of Guest *et al.* (shown in Figure 2.12) relied on an energy exchange occurred between bending moments and membrane stresses of the shell in such a way that the shell could rotate around an underlying cylinder and remain stable at any twist angle [81]. This behaviour is not limited to isotropic materials however: several examples of

zero-stiffness composite shells exist in literature. Murphey and Pellegrino's earliest example involved the bonding together of two singly-curved cross-ply laminates in an opposite sense so that the deformed shapes were maintained by the balance of residual stress in each laminate [166]. The approach of Schultz *et al.* was materials-based, utilising specific angle plain-weave fabrics and a novel matrix to eliminate moment resultants that would usually occur during deflection [209].

Other techniques have involved modifying the laminates of multistable helical structures, where inherent restrictions in curvature changes during twisting can enable zero torsional stiffness for specific fibre angles [130]. Another morphing aerostructure from Lachenal *et al.* became neutrally stable due to the interactions of the skin and prestressed elements (akin to the spring-balanced systems) [127]. Doornebal also conducted initial investigations into tailoring layup and thermal prestress to achieve zero stiffness twisting of a singly-curved composite shell but, while identifying some theoretical regions of twist ranges that could be practically zero stiffness, was unable to experimentally observe this behaviour [50].

2.5 Behavioural Uncertainties in Composite Shells

Issues with successfully manufacturing a practical zero stiffness shell highlight a broader challenge of working with thin composite shells. Shell structures can be highly sensitive to variations in their geometry, and using composite material also presents challenges in terms of controlling variations such as fibre misalignments, thickness variations, regions of resin-richness and cure temperature gradients [141, 191, 196]. Statistical techniques such as Monte Carlo simulations are often used to get 'averaged' properties for laminated structures [56, 223, 244].

Fibre Misalignment

Early investigations into fibre misalignment predicted reductions in Young's modulus of single-angle unidirectional fibre composites of up to 20% [10, 116], although these were for thick laminates with large fibre misalignments of approximately $\pm 10^\circ$. Steeves and Pellegrino showed that using manual layup techniques fibre misalignments would be in the order of $1.9^\circ - 2.2^\circ$, although these misalignments exacerbate twisting deformation modes in contrast to laminate thickness and cure variations that can exacerbate inextensional bending deformation modes [231]. Arao *et al.* showed that fibre misalignments could be reduced to a standard deviation of $\pm 0.4^\circ$ when an expert laminator made the laminates, but that this still caused out-of-plane warping in cross-ply, symmetric and quasi-isotropic laminates due to moisture absorption. It was suggested to increase the number of plies (*i.e.* to use thin ply

systems) to counteract this [5,6], a technique also employed by designers of precision composite mirrors [253].

Laminate Thicknesses & Resin-Richness

Giddings *et al.* used finite element methods to show that ply thickness changes (and resin-rich regions) can alter expected laminate curvatures, and through-thickness shear stresses can cause local curvature reversal [74]. In their review of manufacturing uncertainties, Mesogitis *et al.* highlighted the importance of fibre volume fraction - the ratio of fibre to overall composite volume - noting that a 6% change in volume fraction could cause a 5% change in the spring-in angle of a curved composite plate, suggesting control of resin content is important for composite compliant shell mechanisms that are highly reliant on geometric stiffness for their behaviour [160]. This is especially relevant for thin composite laminates since the flexural stiffness is determined by the thickness cubed (see Equation 2.12).

Moisture Ingress & Stress Relaxation

Brampton *et al.* considered the impacts of manufacturing process variations specifically on thin morphing composites. As well as showing that shell curvatures could vary approximately ±2% for a ±5% deviation in Young's modulus (longitudinal or transverse) or cure temperature, and ±5% for a ±5% change in laminate thickness, they noted that a 5% increase moisture absorption could reduce curvatures by almost 90% [13]. This correlated with work by Etches *et al.* who also noted that post-cure moisture uptake in polymer matrices can significantly change snap-through loads of bistable composites, as well as change their geometries [57]. Telford considered moisture effects in detail, reporting reductions in residual stresses of over 70% in saturated laminates [235], highlighting a potential problem if prestress is to be used to find novel behaviours in composite compliant shell mechanisms.

Although moisture absorption can be quite a fast process, prestressed shells are susceptible to long term behaviour changes as well. Brinkmeyer *et al.* showed significant latency and increases in deployment time for bistable structures that had been stowed for a long period of time, suggesting time-dependent material relaxation [14]. Prestress in viscoelastic composites reduces over time due to creep in the matrix [62,63]. The design of prestressed composite compliant shell mechanisms is therefore likely to require both short-term and long-term analyses of behaviour.

Fatigue

The importance of the fatigue life of a compliant mechanism varies depending on the mechanism application and functional requirements. Many compliant mechanisms

are required to undergo cyclic loading for many cycles, but stress levels during each cycle can remain low if the mechanism stiffness and deflections are small. A good example of such a mechanism is the mirco-scriber developed by Cannon *et al.* [25]. Here, three compliant mechanisms connect to a scribe head to provide small forces to the substrate material and maintain alignment of the scribe tip, and the fatigue life is estimated to be more than five hundred million cycles. However, for compliant mechanisms where energy storage is a key function - such as leaf-spring suspension devices - fatigue failure can become the design-limiting factor due stress levels within the mechanism becoming very high as a result of high loads and tight space requirements [3]. It is also worth noting that designing a structure to be compliant can actually help increase its fatigue life. A prime example of this is in wind turbine blades, where tailored composite laminates cause the structure to deform in ways that reduce gust loads that limit the fatigue life of the blades [127].

As well as enabling this sort of stiffness tailoring, composites are often used in compliant structures because their fatigue behaviour is considered to be very good. Indeed, Potter investigated the fatigue performance of snapping bistable composite plates and observed very little damage in test specimens after two million cycles (moisture absorption over this period had a greater effect on the performance) [190]. It has also been shown that building laminates using ultra-thin plies (*i.e.* ply densities of $30gm^{-2}$) can further improve the fatigue performance of composite structures, with these laminates showing significantly slower damage growth and more brittle failure modes than equivalent laminates with regular ply thicknesses (*i.e.* ply densities of $300gm^{-2}$) [4, 221, 242].

2.6 Final Remarks

Compliant mechanisms and morphing structures have found application in a wide range of areas, from deployable spacecraft structures to medical support devices and shape-changing aircraft. Designing compliant mechanisms that can accurately undergo a large spatial deformation is a non trivial-process. Mechanism design frameworks such as the building-block method built on an eigenscrew decomposition of the stiffness matrix can offer greater and more intuitive insight into the physical behaviour of such shell mechanisms, and this eigenscrew characterisation framework is investigated in Chapters 5 and 6.

Compliant shell mechanisms in particular offer great potential for collaboration between mechanisms engineers and composites engineers, as coupling offered by the material anisotropy of composite shell may enable shape-changing structures. In spite of potential manufacturing challenges such as fibre misalignment, thickness variation and moisture ingress, composite materials offer more routes to tailor the

shell behaviour than isotropic shells. This is due to the ease of forming more complex geometries, the different material combinations available and novel routes for tailoring the shell stiffness and state of prestress, and the potential of these additional design freedoms are worth investigating.

Efforts to combine intuitive compliant mechanism design techniques with the enhanced design freedom afforded by composite materials may enable the development of composite compliant mechanisms that exhibit novel behaviours. In particular, the use of prestress has been demonstrated to enable novel behaviours, with mechanical, thermal or viscoelastic prestress the most commonly used in complex composite morphing structures. An initial step in development of composite compliant shell mechanisms may therefore be to evaluate the limits to which prestress can affect the behaviour of a simple passive compliant mechanism.

Chapter 3

Prestressed Passive Structures: Tape Springs

The stiffness response of compliant mechanisms is dependant on the geometry, material and stress state of the mechanism. By prestressing a mechanism during its manufacture the stiffness behaviour in different degrees of freedom can be tailored. Many avenues exist to include prestress in a structure [50], but one such method of tailoring highly suited to composites is to use thermal residual stresses. This is because thermal residual stresses are an integral part of composite manufacture as the structure cools down after typically a high temperature curing process.

One of the most extreme behaviours that can be achieved by utilising prestress is that of zero stiffness (also known as neutral stability). In certain applications of compliant mechanisms it may be helpful if behaviour in one degree of freedom could be zero stiffness behaviour. For example, a medical support brace need not be restrictive to the patient in directions of bodily movement that do not need rehabilitating: if only upper body sagittal bending support is needed, then it would be advantageous to leave other degrees of freedom unhindered. Shell structures with zero torsional stiffness were demonstrated by Guest and Pellegrino [81]. They used rollers to mechanically-prestress copper-beryllium strips, thereby inducing a precise residual moment within the shell which enabled zero-stiffness torsional behaviour. Guest and Pellegrino used the analogy of a heated bimetallic disk (*i.e.* thermally-prestressed) to help explain the zero stiffness behaviour of their shell.

This chapter details the preliminary investigative work to evaluate the potential of using such thermal prestress to tailor the stiffnesses of certain deformation modes in a simple composite compliant shell mechanism, with a view to understanding how extreme any reduction in stiffness would be.

Work in this chapter was presented at ASME IDETC 2018 (Québec City, Canada) [227], and published in a subsequent special issue of the Journal of Mechanisms and Robotics [228]. In addition, some content presented in this chapter was ini-

tially detailed in an Exploratory Project (XP) internal report produced during this PhD [225]. As such this chapter is based primarily on these sources where the author was the prime contributor to the literature reviews, analytical and numerical modelling, manufacturing and experimentation.

3.1 Introduction

This chapter focuses on using thermal prestress to reduce torsional stiffness within composite tape springs, and to evaluate the feasibility of generating zero torsional stiffness tape springs using such prestress.

Tape springs are simple shell structures with a single curvature existing about a principal axis *i.e.* the curvatures $\kappa_{xx} = \kappa_{xy} = 0$, and $\kappa_{yy} = 1/R$, where R is the radius of the cylindrical tool used to manufacture the tape spring (see Figure 3.1 for details). Due to their simple geometry they are easy to manufacture and have well-understood mechanical behaviour, making them a suitable compliance shell mechanism for preliminary study. They are a class of structures that have been investigated previously as compliant mechanisms [81, 82], and have demonstrated bistability [215] and zero stiffness capabilities [81, 166, 209], making them an attractive choice for mechanism designers seeking a range of behaviours from a geometrically-simple design. In classical mechanisms, multiple members would be required to enable such behaviour [9, 163, 206]. The analytical behaviour of tape springs is thus well-understood and, being singly-curved, they lend themselves to manufacture with composites as the cylinder axis can be readily used as a datum for ply angles.

This work builds on the analytical model by Guest and Pellegrino [82], which assumes that the tape spring shell is inextensional (valid for thin shells which require far more energy to stretch in-plane than to bend out-of-plane [211]), and that the shell curvature is uniform across its mid-surface. From these assumptions it follows that deformation of the tape spring is kinematically constrained to the surface of an underlying cylinder. It is worth noting here that this model only captures the simple torsional deformation behaviour of a tape spring, *i.e.* behaviour where the cylinder constraint remains valid throughout deformation. One area of significant research is that of the tape spring 'hinge' or 'fold', which separates a tape spring into three distinct regions: two 'straight' sections, the hinge, and two transition regions. These folds are instrumental in the design of some deployable structures and break the cylindrical constraint of Guest and Pellegrino's model. The reader is directed to Refs [23, 203, 212, 217, 248] for further analysis pertaining to these hinged tape spring architectures.

The model is extended by incorporating the thermal prestress introduced in

composite laminate materials, and it is demonstrated that the extended tape spring model correlates well with FE models and manufactured samples, and that thermal prestress can be used to reduce torsional stiffness in a simple cross-ply tape spring. The feasibility of creating zero torsional stiffness composite tape springs is briefly explored mathematically.

The chapter is structured as follows. First, the extended analytical formulation is presented, including rationale behind material selection, derivation of the strain energy equation and comparisons of energy landscapes and stability states. Next, two sections detail validation work: FE modelling and the manufacture of sample tape springs. The results of each approach are discussed and compared before final conclusions are presented.

3.2 Analytical Model

The first stage of the investigation was to select a suitable analytical model, material system and layup for the tape spring mechanisms that could be effectively thermally-prestressed.

3.2.1 Material and Layup Selection

To ascertain the potential of thermally prestressed composite compliant mechanisms, a layup and material configuration was selected which would exhibit the maximum thermally-induced bending moments per unit thickness. A cross-ply laminate configuration – where the fibres in the bottom half of the laminate lie perpendicular to those in the upper half – was therefore selected. Wider ranges of composite laminate layups are beyond the scope of the current work.

By placing fibres at 90° to the longitudinal axis on the inner surface of the tape spring the bending moments produced upon cooling are similar to those produced by mechanically prestressed isotropic tape springs [81]. The stacking sequence notation is positive radial outwards *e.g.* $[90_n/0_n]$, where n represents the number of repeating plies. The thermal residual strains in such cross-ply laminates (caused by the laminate cooling down post-cure) produce a 'coiling-up' moment, M_{xx}^{th}, in the longitudinal direction, and an 'opening-out' moment, M_{yy}^{th}, in the hoop direction (see Figure 3.1).

Carbon fibre composites were chosen due to their high specific stiffness and low creep characteristics relative to glass and aramid fibre reinforcements, as well as their suitable thermal expansion properties. Hexcel IM7-8552 was used as a benchmark composite material due to its general availability and well-characterised properties [24, 87, 197, 201]; see Table 2.1 in Chapter 2.

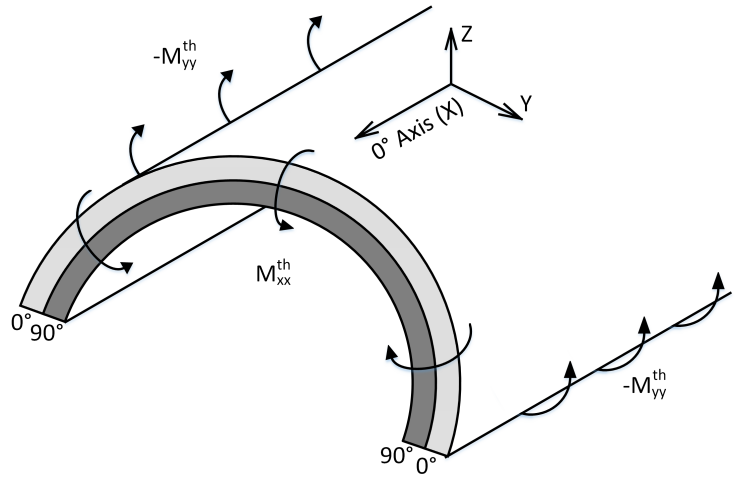

Figure 3.1: *Post-cure thermal strains produce a 'coiling-up' moment, M_{xx}^{th}, in the longitudinal direction, and an 'opening-out' moment, M_{yy}^{th}, in the hoop direction*

3.2.2 Elastic Strain Energy

In this work, the effect of thermal prestress on the energy landscape of anisotropic composite tape springs is considered. Following the approach of Guest and Pellegrino [82] (which includes standard shell assumptions and neglects membrane strains), the strain energy per unit area, U, stored in the tape spring is

$$U = \frac{1}{2}(\Delta\boldsymbol{\kappa}^T \boldsymbol{D}^* \Delta\boldsymbol{\kappa}), \tag{3.1}$$

where $\boldsymbol{D}^*$ is the laminate's reduced bending stiffness matrix (see Chapter 2 for definitions of CLA terms). The strain energy equation is non-dimensionalised as

$$\hat{U} = U\frac{R^2}{D_{11}^*}, \tag{3.2}$$

using the manufacture tooling radius, R, and the reduced bending stiffness term, D_{11}^* [82].

In the Guest and Pellegrino model, an inextensional tape spring shell element (with manufactured curvature $\boldsymbol{\kappa}_y$) is rotated around an underlying cylinder to investigate the curvature changes, $\Delta\boldsymbol{\kappa}$, that occur during twist. The modification made in this work is that change in curvature, $\Delta\boldsymbol{\kappa}$, is measured with respect to a thermally-warped element with curvatures $\boldsymbol{\kappa}_{\text{warped}}$, rather than an element with only manufactured curvature $\boldsymbol{\kappa}_y$, *i.e.*

$$\Delta\boldsymbol{\kappa} = \boldsymbol{\kappa}_{\text{cylinder}} - \boldsymbol{\kappa}_{\text{warped}}. \tag{3.3}$$

Thus, the strain energy calculated is that required to conform the warped element

to the reference underlying cylinder assumed by the model ($\boldsymbol{\kappa}_{\text{cylinder}}$).

The curvature of the tape spring on the underlying cylinder is based on a Mohr's circle of curvature

$$\boldsymbol{\kappa}_{\text{cylinder}} = \frac{C}{2}\begin{bmatrix} 1-\cos(2\theta_C) \\ 1+\cos(2\theta_C) \\ 2\sin(2\theta_C) \end{bmatrix}, \tag{3.4}$$

where θ_C refers to the twist angle, and C the curvature of an underlying cylinder (as shown in Figure 3.2 [81]). These two terms are the generalised degrees of freedom for the tape spring model. It is important to note that for this model to remain valid, the post-cure tape spring geometry must approximately conform to an underlying cylinder.

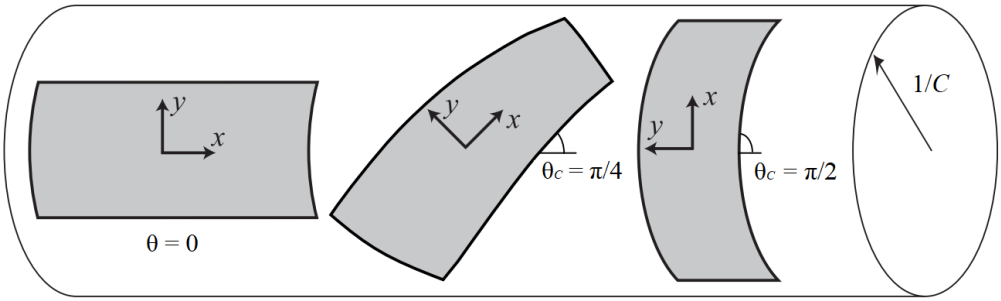

Figure 3.2: *Definition of tape spring geometric terms illustrating the underlying cylinder concept. Adapted from Ref. [81]*

The curvature of the thermally warped tape spring (*i.e.* the origin state) is defined as

$$\boldsymbol{\kappa}_{\text{warped}} = \boldsymbol{\kappa}_y + \Delta\boldsymbol{\kappa}^{th} = \begin{bmatrix} 0 \\ 1/R \\ 0 \end{bmatrix} + \Delta\boldsymbol{\kappa}^{th}, \tag{3.5}$$

where the thermal curvature changes during cooling from manufacture, $\Delta\boldsymbol{\kappa}^{th}$ are added to the manufacture tooling radius.

The changes in curvature of an anisotropic plate due to thermally-induced bending moments ($\boldsymbol{M}^{th}$) and in-plane forces ($\boldsymbol{N}^{th}$) [250] can be evaluated as

$$\Delta\boldsymbol{\kappa}^{th} = \begin{bmatrix} \Delta\kappa_{xx}^{th} \\ \Delta\kappa_{yy}^{th} \\ \Delta\kappa_{xy}^{th} \end{bmatrix} = \Delta T(\boldsymbol{D}^*)^{-1}(\boldsymbol{M}^{th} - \boldsymbol{B}\boldsymbol{A}^{-1}\boldsymbol{N}^{th}). \tag{3.6}$$

The thermal moments $\boldsymbol{M}^{th}$ and in-plane forces $\boldsymbol{N}^{th}$ per degree Celsius [47] are

given as

$$\boldsymbol{M}^{th} = \begin{bmatrix} M_{xx}^{th} \\ M_{yy}^{th} \\ M_{xy}^{th} \end{bmatrix} = \frac{H^2}{8} \begin{bmatrix} W_2^{th}\xi_5 \\ -W_2^{th}\xi_5 \\ W_2^{th}\xi_7 \end{bmatrix}, \tag{3.7}$$

and

$$\boldsymbol{N}^{th} = \begin{bmatrix} N_{xx}^{th} \\ N_{yy}^{th} \\ N_{xy}^{th} \end{bmatrix} = \frac{H}{2} \begin{bmatrix} W_1^{th} + W_2^{th}\xi_1 \\ W_1^{th} - W_2^{th}\xi_1 \\ W_2^{th}\xi_3 \end{bmatrix}. \tag{3.8}$$

The ξ_i terms refer to lamination parameters [241] (see Chapter 2 for a full definition), which allow the stiffness of any (non-hybrid) composite layup to be represented using at most 12 continuous parameters. Using this approach it is possible to gain physical insight into the underlying behaviour of the system without having to consider specific layups. In particular, using such an approach is valuable when trying to tailor designs to obtain an optimised configuration (for an example see Ref [70]). Lamination parameter definitions can be conveniently rearranged,

$$\xi_1 = \frac{(A_{11} - A_{22})}{2U_2H}, \quad \xi_3 = \frac{(A_{16} + A_{26})}{U_2H}, \quad \xi_5 = \frac{2(B_{11} - B_{22})}{U_2H^2}, \quad \xi_7 = \frac{4(B_{16} + B_{26})}{U_2H^2},$$

with material invariant U_2, as well as thermal material invariants W_1^{th} and W_2^{th} [241, 250]

$$\begin{aligned} W_1^{th} &= \alpha_{11}Q_{11} + (\alpha_{11} + \alpha_{22})Q_{12} + \alpha_{22}Q_{22}, \\ W_2^{th} &= \alpha_{11}Q_{11} + (\alpha_{22} - \alpha_{11})Q_{12} + \alpha_{22}Q_{22}, \end{aligned}$$

where H is the laminate thickness, α the coefficients of thermal expansion, and the Q terms refer to the terms of the reduced ply stiffness matrix (also see Chapter 2 for full definitions).

3.2.3 Equilibrium and Stability Analysis

Equilibrium configurations of the anisotropic tape spring in the twisting domain are identified by stationary points of the strain energy, *i.e.*

$$\frac{\partial U}{\partial \theta_C} = \frac{C}{4R}(\lambda_1 \sin(2\theta_C) + \lambda_2 \cos(2\theta_C) + \lambda_3 \sin(4\theta_C) + \lambda_4 \cos(4\theta_C)) = 0, \tag{3.9}$$

$$\begin{aligned} \frac{\partial U}{\partial C} = \frac{1}{R}\Big(&\lambda_5 + \lambda_6 \cos^2(\theta_C) + \lambda_7 \cos^4(\theta_C) + \lambda_8 \sin(2\theta_C) + \lambda_9 \sin^2(2\theta_C)... \\ &+ \frac{\lambda_4}{2} \sin(2\theta_C)\cos^2(\theta_C)\Big) = 0, \end{aligned} \tag{3.10}$$

where

$$\begin{aligned}
\lambda_1 &= 4(D^*_{22} - D^*_{12}) + 2CR(D^*_{11} - D^*_{22}) + 4R(\Delta\kappa^{th}_{xx}(D^*_{12} - D^*_{11})... \\
&\quad + \Delta\kappa^{th}_{yy}(D^*_{22} - D^*_{12}) + \Delta\kappa^{th}_{xy}(D^*_{26} - D^*_{16})), \\
\lambda_2 &= 4CR(D^*_{16} + D^*_{26}) - 8R(\Delta\kappa^{th}_{xx}D^*_{16} + (\Delta\kappa^{th}_{yy} + 1/R)D^*_{26} + \Delta\kappa^{th}_{xy}D^*_{66}), \\
\lambda_3 &= CR(4D^*_{66} + 2D^*_{12} - D^*_{22} - D^*_{11}), \qquad \lambda_4 = 4CR(D^*_{26} - D^*_{16}), \\
\lambda_5 &= CRD^*_{11} - D^*_{12} - R(D^*_{11}\Delta\kappa^{th}_{xx} + D^*_{12}\Delta\kappa^{th}_{yy} + D^*_{16}\Delta\kappa^{th}_{xy}), \\
\lambda_6 &= (D^*_{12} - D^*_{22}) + 2CR(D^*_{12} - D^*_{11}) + R(\Delta\kappa_{xx}(D^*_{11} - D^*_{12})... \\
&\quad + \Delta\kappa_{yy}(D^*_{12} - D^*_{22}) + \Delta\kappa_{xy}(D^*_{16} - D^*_{26})), \\
\lambda_7 &= CR(D^*_{11} + D^*_{22} - 2D^*_{12}), \\
\lambda_8 &= 2CRD^*_{16} - D^*_{26} - R(D^*_{16}\Delta\kappa_{xx} + D^*_{26}\Delta\kappa_{yy} + D^*_{66}\Delta\kappa_{xy}), \\
\lambda_9 &= CRD^*_{66}.
\end{aligned}$$

See Equations 2.9 and 3.6 for definitions of $\boldsymbol{D}^*$ and $\Delta\boldsymbol{\kappa}^{th}$ terms respectively.

The Hessian matrix of the strain energy provides a stiffness matrix for the tape spring, with respect to generalised degrees of freedom θ_C (which describes the twisted configuration of the tape spring) and C (the radius of the underlying cylinder that the tape spring assumes). A negative determinant of the Hessian indicates that the system is unstable, as one of the eigenvalues is negative. Conversely, a positive determinant can indicate a stable system (provided that it is not the product of two negative eigenvalues). The determinant of the Hessian matrix is,

$$\begin{aligned}
|\boldsymbol{H}(U)| &= \begin{vmatrix} \frac{\partial^2 U}{\partial\theta_C^2} & \frac{\partial^2 U}{\partial\theta_C\partial C} \\ \frac{\partial^2 U}{\partial\theta_C\partial C} & \frac{\partial^2 U}{\partial C^2} \end{vmatrix}... \\
&= \frac{\partial^2 U}{\partial\theta_C^2}\frac{\partial^2 U}{\partial C^2} - \frac{\partial^2 U}{\partial\theta_C\partial C}\frac{\partial^2 U}{\partial C\partial\theta_C},
\end{aligned} \tag{3.11}$$

where the individual terms are,

$$\frac{\partial^2 U}{\partial\theta_C^2} = \frac{C}{2R}(\lambda_1\cos(2\theta_C) - \lambda_2\sin(2\theta_C) + 2\lambda_3\cos(4\theta_C) - 2\lambda_4\sin(4\theta_C)), \tag{3.12}$$

$$\begin{aligned}
\frac{\partial^2 U}{\partial C^2} &= D^*_{11} + 2D^*_{16}\sin(2\theta_C) + D^*_{66}\sin^2(2\theta_C) + \lambda_{10}\cos^2(\theta_C) + \lambda_{11}\cos^4(\theta_C)... \\
&\quad + \lambda_{12}\sin(2\theta_C)\cos^2(\theta_C),
\end{aligned} \tag{3.13}$$

$$\frac{\partial^2 U}{\partial\theta_C\partial C} = \frac{1}{2R}(\lambda_{13}\sin(2\theta_C) + \lambda_{14}\cos(2\theta_C) + \lambda_3\sin(4\theta_C) + \lambda_4\cos(4\theta_C), \tag{3.14}$$

Table 3.1: *Predicted tape spring equilibrium states*

Figure	Curvature (mm^{-1})	Twist Angle, θ_C (°)	Determinant, $\lvert\boldsymbol{H}(U)\rvert$	Stability
3.3a	1.11	90.0	-11.7	Unstable
3.3a	26.3	0.0	77.6	Stable
3.3b	8.58	90.0	-56.4	Unstable
3.3b	18.8	0.0	-19.8	Unstable
3.3b	20.8	21.9	37.4	Stable
3.3b	20.8	158.0	38.2	Stable
3.3c	8.58	91.3	-56.3	Unstable
3.3c	18.8	1.8	-19.5	Unstable
3.3c	20.4	21.9	33.9	Stable
3.3c	21.2	158.2	59.2	Stable

with

$$\lambda_{10} = 2(D^*_{12} - D^*_{11}), \qquad \lambda_{11} = \frac{\lambda_7}{CR}, \qquad \lambda_{12} = \frac{\lambda_4}{2CR},$$
$$\lambda_{13} = 2(D^*_{22} - D^*_{12}) + 2CR(D^*_{11} - D^*_{22}) + 2R(\Delta\kappa^{th}_{xx}(D^*_{12} - D^*_{11})...$$
$$+ \Delta\kappa^{th}_{yy}(D^*_{22} - D^*_{12}) + \Delta\kappa^{th}_{xy}(D^*_{26} - D^*_{16})),$$
$$\lambda_{14} = 4CR(D^*_{16} + D^*_{26}) - 4R(\Delta\kappa^{th}_{xx}D^*_{16} + (\Delta\kappa^{th}_{yy} + 1/R)D^*_{26} + \Delta\kappa^{th}_{xy}D^*_{66}).$$

Table 3.1 details the equilibrium conditions predicted for the $[90_2/0_2]$ tape spring in Figure 3.3. Initial guesses for the equilibria were identified via visual inspection of the energy landscapes, and the equations were then solved numerically using the MATLAB function `fsolve`.

A zero-stiffness structure will exhibit no change in internal strain energy U throughout the designed mode of deformation (*i.e.* θ_C or C), and will thus be in constant equilibrium and thus be neutrally stable for all desired deformations. Guest *et al.* [81] describe a zero torsional stiffness tape spring using an isotropic material and mechanically introduced prestress. For prestressed composite tape springs the system is governed by coupled nonlinear equations for $\partial U/\partial\theta_C = 0$ and $\partial^2 U/\partial\theta_C^2 = 0$, even when simplified for cross-ply laminates where $D^*_{16} = D^*_{26} = 0$. A full exploration of the design space to find robust zero torsional stiffness (in terms of material selection, lay-up and manufacturability) is beyond the scope of the current investigation.

Alternatively, the combination of multiple prestressed laminates could be used to achieve overall mechanism zero-stiffness. Combining prestressed structural elements has been used to create mechanisms with overall zero-stiffness (*e.g.* the joint in Ref [163]), and this approach can be applied to shell mechanisms. Bonding multiple prestressed tape springs together is one way of achieving this (see previous work

by Murphey and Pellegrino [166]) although this would be at the cost of increased manufacturing complexity. Other mechanism geometries, prestressing techniques (*e.g.* mechanical, moisture etc.) and constituent materials may yield zero-stiffness responses more easily, but these lie outside the scope of this work.

3.2.4 Energy Landscapes

In order to illustrate the effects of including thermal prestress a comparison of the energetic landscapes are presented. Figure 3.3 shows polar plots of non-dimensional strain energy $\hat{U}$ (see Equation 3.2 for the normalisation) as a function of tape spring twist, $2\theta_C$, and underlying cylinder curvature, C. The tape spring is a $[90_2/0_2]$ IM7-8552 composite laminate shell with a manufactured radius of 38 mm. A change in temperature, ΔT, of -155°C models the cool down from a typical 180°C cure to room temperature [87].

Figure 3.3a shows the energy landscape for a cross-ply tape spring with no thermal prestress: it is monostable with a low energy ($\hat{U}$<0.1) twisting region of approximately ±20°. The low energy twist behaviour is due to the open cross-section of the tape spring. Figure 3.3b shows the effect of a thermally-induced prestress: the structure becomes bistable, with an unstable zero twist configuration (i.e. no equilibrium when the $C = 1/R$). The low-energy twisting region increases to approximately ±45°, illustrating the potential for using thermal prestress to reduce the torsional stiffness of thin shell composite structures. Figure 3.3c shows the effect of fibre misalignment on the thermally prestressed shells. A misalignment of 2° in the inner two plies causes a slight rotation of the energy landscape; as a result, the manufactured configuration ($\theta_C = 0$) is no longer in equilibrium, and the structure will favour one twisted mode. While the energy landscape is different, the location of equilibria and the range of the low energy twisting region are similar to the non-misaligned tape spring.

3.3 Finite Element Model

To support the results from the analytical energy landscapes, Finite Element (FE) analyses were conducted in Abaqus/Standard 2016.

3.3.1 Modelling Approach

Slender tape springs (600 mm long, with enclosed angles of 180°) were meshed using S4R shell elements for a range of radius values. A mesh refinement study compared the cross-sectional curvature at the centre of the post-warped, untwisted tape springs. Mesh target sizes of between 8×8 mm and 1×1 mm were considered,

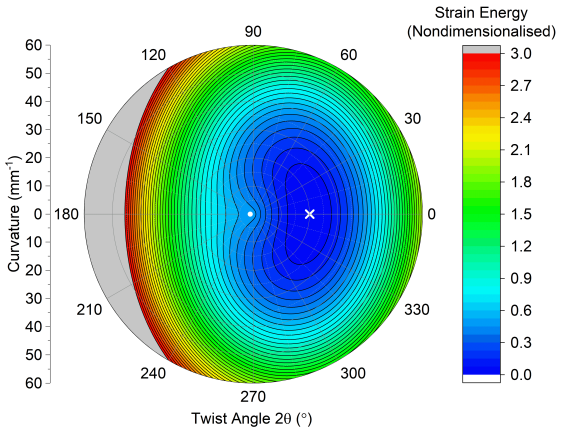

(a) *No thermal prestress, layup* $[90_2/0_2]$

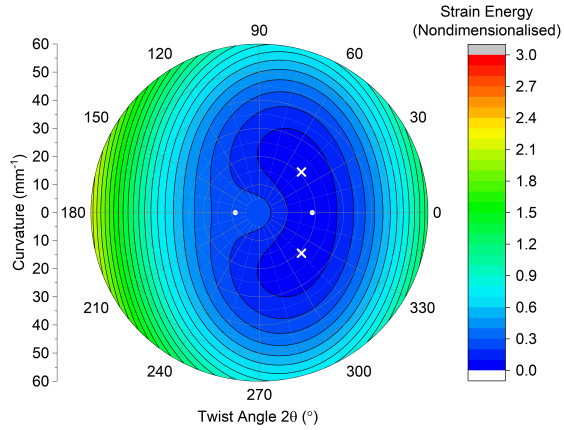

(b) *Thermal prestress, layup* $[90_2/0_2]$

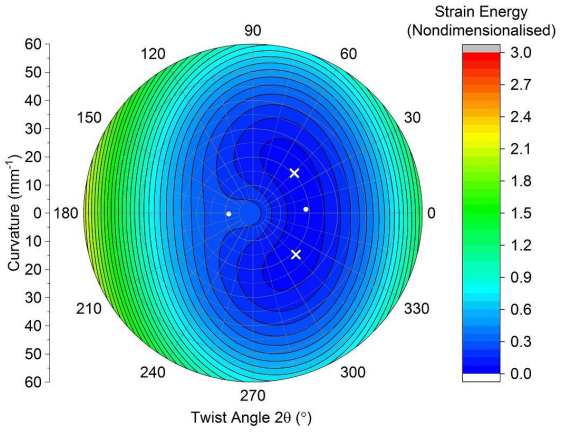

(c) *Thermal prestress, misaligned layup* $[88_2/0_2]$

Figure 3.3: *Polar plots of nondimensional energy* $\hat{U}$ *as a function of tape spring twist,* $2\theta_C$*, on the angular axis and cylinder curvature,* C*, on the radial axis. Contours are plotted for* $\hat{U}$ *values between 0.0 to 3.0 inclusive with intervals of 0.1. All tape springs have a manufactured radius of* $R = 38$ *mm. Points labelled with a cross indicate the stable state(s), and dots indicate unstable equilibria.*

and a final mesh size of 5×5 mm was selected, as the calculated curvature converged to within 0.10% of the analysis with a 1×1 mm mesh density. A fully-fixed boundary condition was applied to the central node, and general geometrically nonlinear static analyses were conducted. The post-cure cooling process which generates the thermal prestress and resulting warp was modelled by applying two ambient temperature fields to the entire tape spring as 'Predefined Field' variables. The two temperatures modelled were (i) the expected cure temperature (180°C), and (ii) the assumed room temperature (25°C), to give $\Delta T = -155$°C. An example of the resulting deformed shape is shown in Figure 3.4a. For each model the deformed nodal coordinates were exported as a point cloud so that the tape spring twist angle and radius of underlying cylinder could be measured.

3.3.2 Twisted Configurations

The warped shape shown in Figure 3.4a exists in a zero-twist configuration. The curling effects seen at the ends are due to residual moments from the thermal prestress. A prestressed $[90_n/0_n]$ cross-ply tape spring in this configuration corresponds to the unstable zero-twist equilibrium point in Figure 3.3b. The model possesses geometric and material symmetry, and thus cannot automatically bifurcate to a twisted configuration. In order to break this symmetry and let the model bifurcate to a preferred stable configuration, a small fibre misalignment was applied to each 90° ply in the laminate until a twisted structure was produced (-2° for the 38 mm radius springs; -5° for the 50 mm radius spring). Energy landscapes of tape springs with fibre misalignment (see example Figure 3.3c) were considered sufficiently similar to those without (see Table 3.1), that direct comparisons could be drawn between the 'misaligned' FE models and the other investigative approaches. An example twisted structure prediction can be seen in Figure 3.4b.

3.4 Prototype Manufacture

Prototype composite tape spring mechanisms were then manufactured to validate the analytical and FE models.

3.4.1 Design Curvature

The upper limit on the manufactured radius R is determined by the requirement that the warped tape spring nominally conforms to a cylindrical configuration. This is violated when the calculated thermally induced curvature $\Delta\kappa_y^{th}$ is equal to the manufacturing tooling curvature $1/R$. For an IM7-8552 [90/0] cross-ply laminate, this equates to a tooling radius of approximately 55 mm, and represents the limit

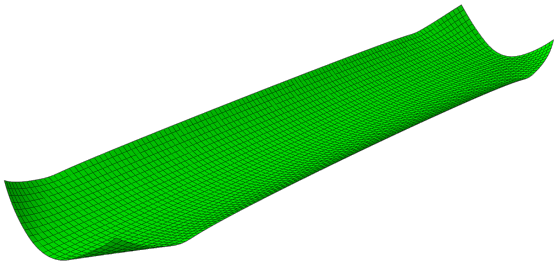

(a) *Unstable untwisted shape*

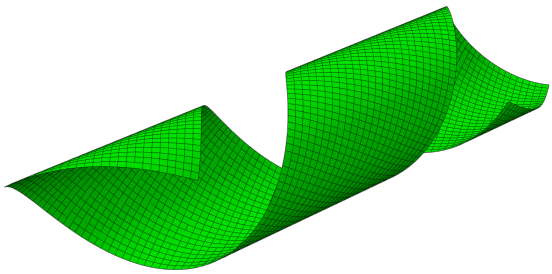

(b) *Stable twisted shape*

Figure 3.4: *FE predictions of the stable and unstable post-warp tape spring shapes for a [$90_2/0_2$] layup with tool radius $R = 38$ mm.*

at which the warped tape spring is cylindrical (and the analytical model is valid). Therefore, steel tooling of radius 38 mm and 50 mm was selected for ply layup to ensure that manufactured tape springs were within this limit. A naming convention of the form $RXXTn$ describes each sample, where XX refers to the manufactured tool radius (mm) and n refers to the layup $[90_n/0_n]$.

3.4.2 Manufacturing Process

A manual layup and vacuum-bagging process was used before curing the samples in an autoclave. Plies of pre-impregnated (prepreg) carbon fibre (IM7-8552) were laid-down to create rectangular plates with a $[90_n/0_n]$ layup. The resulting laminates were placed on steel tubes to provide the design curvature, with the 0° fibre direction aligned with the tube cylindrical axis. The inner 90° plies were separated from the tool surface by a layer of release film. A heat gun was used periodically to increase the prepreg tackiness and encourage adhesion to the tool surface. Once the layup was complete, an envelope bag was constructed around the tube, and a vacuum was applied to consolidate the plies on the tool. The samples were cured at 7 bar pressure and 180°C in an autoclave. The cured tape springs were allowed to cool down to ambient temperature before being released from their vacuum bags (to minimise moisture uptake from the atmosphere that could affect twisted geometry as a result of the laminate having a non-zero $\boldsymbol{B}$ matrix). Once cooled, the samples

were de-bagged and mass readings were immediately taken to establish a nominally zero-moisture benchmark, and geometric measurements were conducted within 24 hours so that measurements would be taken on samples with the least amount of moisture-related warping as possible.

3.4.3 Profile Measurement

The geometric information of the shell mechanisms was recorded using a FARO Edge ScanArm® optical measurement device and associated CAM2 Measure 10.7 software. This device consists of a laser scanning probe mounted upon a moveable arm, and generates a 'cloud' of XYZ data points of complex geometries. Point clouds were also generated from the deformed nodal positions of the FE models, to enable comparison with the manufactured prototypes.

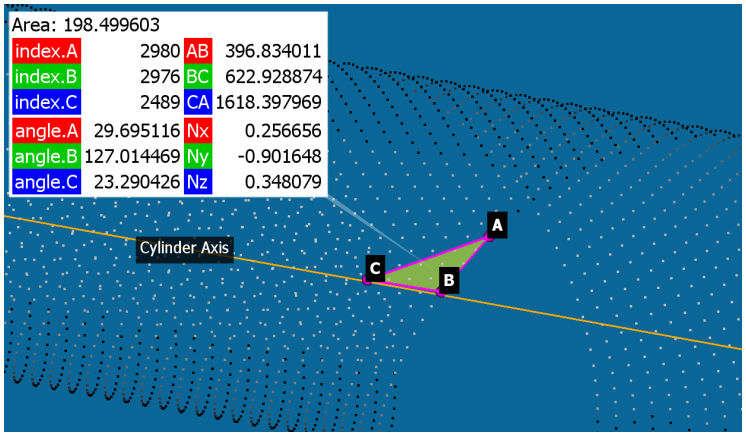

(a) *Twist angle measurement*

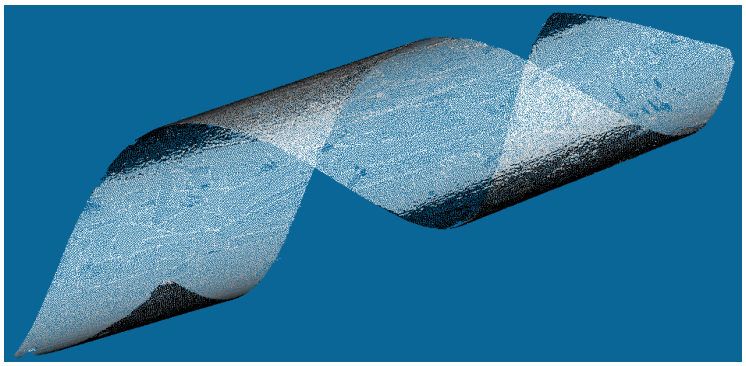

(b) *Sample R38T1 point cloud*

Figure 3.5: *Example point cloud analysis images*

The first parameter used for validation was the helical twist angle, defined as the angle of orientation of the twisted shell with respect to the length-wise axis of an underlying cylinder. This angle was measured by analysing the sample point clouds using the software CloudCompare [76]; see Figure 3.5a. The second parameter, underlying curvature, is directly measured from a cylinder fitted to the measured

Table 3.2: *Overall tape spring twist angles and underlying cylinder radii*

		Manufacture		Helix Radius, R, (mm)			Twist Angle, θ_C, (°)		
Sample	Layup	Radius (mm)	ΔT (°C)	Theory	FE	Experiment	Theory	FE	Experiment
R38T2	$[90_2/0_2]$	38	-162.7	48.1	50.6	50.9	22	21.8	16.9
R38T2 (+1 wk)	$[90_2/0_2]$	38	-162.7	48.1	-	47.4	22	-	6.0
R38T1	[90/0]	38	-163.9	48.1	47.3	55.5	55	53.0	47.8
R50T1	[90/0]	50	-164.6	63.3	-	80	87	-	90

cloud via the RANSAC Shape Detection algorithm inbuilt in CloudCompare [208]. The same procedures were applied to both the experimentally measured point clouds and those extracted from the FE analysis. FE and experimental results for the same tape spring can be seen in Figure 3.4b and Figure 3.5b respectively. The difference in twist direction is due to the arbitrary choice of fibre angle misalignment direction in the FE model. After FE-predicted geometries and manufactured sample geometries had been recorded, comparisons could be made between all three approaches to verify the analytical energy landscapes.

3.5 Results & Discussion

Comparisons between the calculated stable twisted configurations, using the methodology from Section 3.2, and the measured twist angles and helix cylinder radii are presented in Table 3.2; the corresponding energy plots for each sample are shown in Figure 3.6. Experimental results for R50T1 were from visual inspection and not point cloud measurement due to the shell being almost completely coiled post-cure and thus impractical for laser scanning. Table 3.2 shows good agreement between the analytical and FE models for both twist angles (range within 2°) and helix radii (range within 3 mm), as well as with the experimental results. The discrepancies could be attributed to manufacturing sensitivity of thin-shell composites, a higher ΔT observed in the manufactured samples, as well moisture ingress between manufacture and measurement.

Interestingly, after one week the measured twist angle of the R38T2 sample reduced by approximately 65%. Figure 3.7b shows the manufactured R50T1 sample after a week-long exposure to the ambient environment: the reduction in twist angle (and extension in length) is clearly visible compared to Figure 3.7a. It is hypothesised this is due to viscoelastic relaxation and moisture ingress, and their 'relaxation' effects on the laminate strains. These moisture effects can be captured analytically in a similar manner to thermal strains [57, 235]. Where thermal strains

$$\boldsymbol{\epsilon}^{th} = \boldsymbol{\alpha}\Delta T, \tag{3.15}$$

are a function of the coefficients of thermal expansion, α and the temperature change ΔT, the moisture strains

$$\boldsymbol{\epsilon}^m = \boldsymbol{\beta} m, \tag{3.16}$$

are a function of the moisture expansion coefficients, β, and the equilibrium moisture content of the laminate, m. For unidirectional laminates the moisture expansion coefficients

$$\beta_{11} = 0, \tag{3.17}$$

and

$$\beta_{22} = \frac{\rho_c}{\rho_w} \frac{(1 + \nu_m)}{3}, \tag{3.18}$$

are negligible in the direction of the stiff fibres, and functions of the composite and water densities, ρ_c and ρ_w respectively, and the Poisson's ratio of the composite matrix that absorbs the moisture, ν_m, in the 'matrix' direction [1]. As ΔT is negative in the case of post-cure cooling, the thermal and moisture strains are of opposite signs, meaning that these moisture contributions would correspond to an effective 'temperature increase', thereby reducing the size of the low stiffness twisting region in our tape springs.

This relaxation occurred rapidly, likely due to the laminates being so thin. The bistable samples tended to favour one twist direction within a few hours of being cured (in contradiction to energy landscape predictions in Figure 3.6), potentially accentuating any fibre misalignment effects from manufacturing. Time-dependant relaxation is likely a highly-nonlinear effect that is not captured by the analytical model, but is an important design consideration for any device comprised of thin-shell composites and should be modelled.

Storing samples in a desiccator mitigates against moisture effects. Quantifying the degree of recovery from moisture effects, as well as the impact of moisture on design spaces, is critical in the design of such thin shell composite mechanisms. While controlling temperature during manufacture is possible, controlling the usage temperature and ambient moisture is much more challenging. A composite compliant shell mechanism relying on thermal prestress will therefore behave differently depending on its environment conditions, and some degree of active thermal control may be necessary depending on the application and required mechanical responses.

Finally, it was possible to induce non-cylindrical stable shapes with R50T1 by manually twisting and buckling the sample. One such configuration can be seen in Figure 3.7c, highlighting the limitation of assuming that the underlying deformed shell structure is cylindrical. If a general approach for designing composite compliant shells is to be realised, then a less geometrically-restrictive model is required.

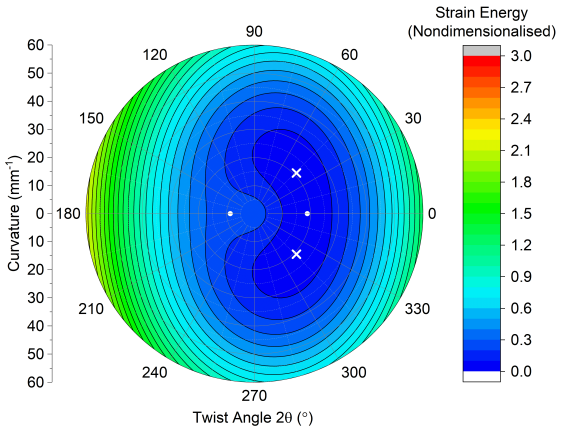

(a) *Sample R38T2*

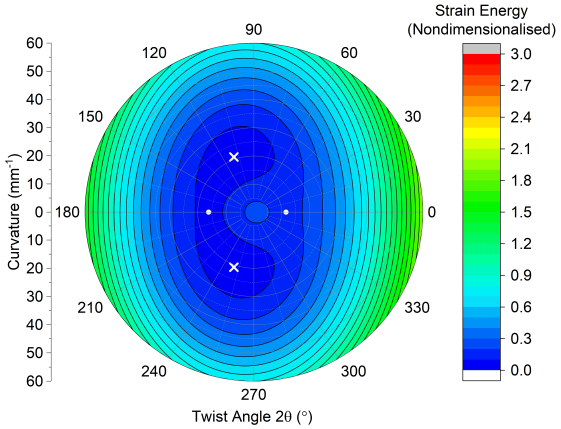

(b) *Sample R38T1*

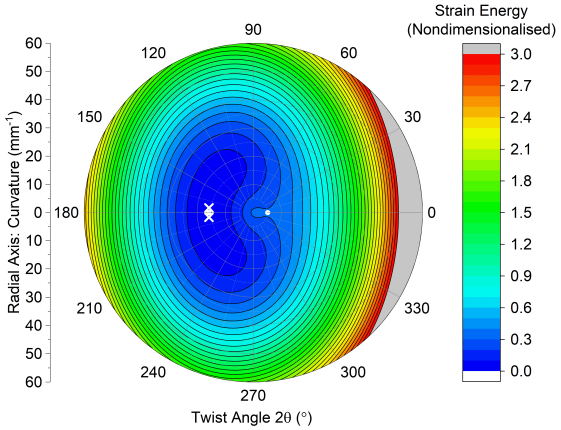

(c) *Sample R50T1*

Figure 3.6: *Polar plots of nondimensional energy $\hat{U}$ as a function of tape spring twist, $2\theta_C$, on the angular axis and cylinder curvature, C, on the radial axis. Contours are plotted for $\hat{U}$ values between 0.0 to 3.0 inclusive with intervals of 0.1. All plots predict unstable on-tool configurations, with (a) and (b) being clear bistable twisted structures, and (c) almost a monostable coiled structure. Points indicated by a cross represent stable state(s) and dots indicate unstable equilibria.*

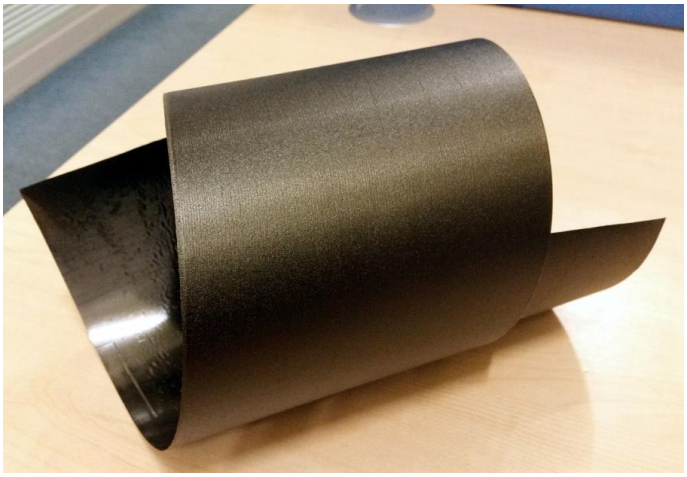

(a) *Original monostable configuration immediately after curing*

(b) *Extended monostable configuration after approximately 1 week in ambient office conditions*

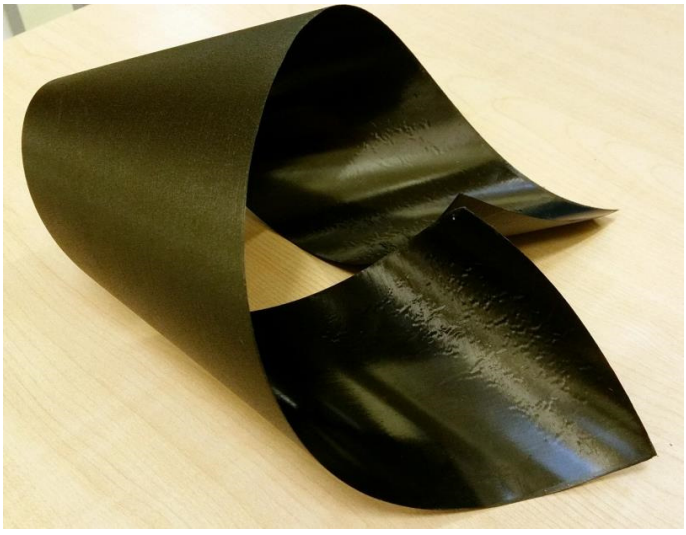

(c) *Stable configuration not predicted by either model*

Figure 3.7: *Photos of sample R50T1 showing stable shape configurations*

3.6 Final Remarks

An extension of an existing composite tape spring model [82] incorporating thermal effects has been presented, as well as finite element simulations and experimental samples of tape springs of different thickness and manufactured radius. All approaches were shown to have good agreement in predicting the tape spring twisted states. Very good agreement for helical twist angle and radius was shown between theoretical and FE predictions, with experimental results indicating that these structures are sensitive to manufacturing variations.

Potentially significant changes in geometry and behaviour can occur in thermally-prestressed thin composite shells, and it is important to incorporate thermal effects into the design and analysis of compliant or multistable structures. These effects can be utilised however, as shown in our example of using residual thermal stresses in a cross-ply composite cylindrical shell to increase the range of twist angles that can be achieved at low ($\hat{U} \leq 0.1$) levels of internal strain energy. This demonstrates the potential of exploiting thermal prestress in composite materials to tailor the mechanical properties of compliant mechanisms in ways not available to isotropic materials, and incorporate additional functionality into said mechanisms.

The feasibility of a composite tape spring with zero torsional stiffness has also been discussed. A zero torsional stiffness tape spring system has been shown to be governed by a set of coupled nonlinear equations, even for cross-ply laminates where D^*_{16} and D^*_{26} effects are removed. Further work is required to more generally quantify the limits of stiffness reduction achievable using thermal prestress in unidirectional-ply tape springs.

Several other design-influencing factors have been identified, including temperature control, viscoelastic effects, moisture-driven behaviour changes and experimental measurement methods. Moisture effects were shown to cause significant geometry changes in the thin shell structures over short periods of time, further reinforcing the need to model hygro-thermal effects as suggested by the literature [235, 236]. These factors must be addressed for practical thermally prestressed composite shell mechanisms to be realised that have useful lifespans. Each presents interesting avenues for further study: shell-based exoskeletons must provide sufficient support on cold and hot days, as well as dry and wet ones, and there should be minimal reduction in mechanism performance over many cycles and long periods of use. Future areas of work include refinement of measurement methods, measuring shape recovery by drying samples, and investigations into any long term viscoelastic relaxation.

3.7 Next Steps

In summary, the work in this chapter set out to assess the feasibility of tailoring the stiffness of a simple shell using thermal prestress. While achieving zero stiffness behaviour proved to be non-trivial for the designs investigated, it was shown that thermal prestress could be used to significantly change specific aspects of the behaviour of a simple compliant composite structure. This raises two main questions:

1. Unknown thermal and moisture environments could unfavourably affect mechanism responses. Could we harness this to tailor for active thermal effects, *i.e.* could a novel behaviour be found by actively heating and cooling a thermally-prestressed structure?

2. What potential is there for expanding the design space using other forms of prestress, *e.g.* mechanical?

Imparting a mechanical prestress to a composite structure could be done quite simply by ensuring a difference between the manufactured and operational curvatures, and could be used alongside thermal prestress to tailor behaviour. The next chapter will explore prestress effects in a thermally-active structure.

Chapter 4

Prestressed Active Structures: Helical Lattices

In the previous chapter it was shown that thermal prestress could significantly change the strain energy landscapes and stable states of thin-shell composite structures. Thermal prestress was only investigated in terms of the changes it could engender in the passive behaviour of one, geometrically-simple compliant member. In this chapter we exploit thermal prestress for actuation by considering a more geometrically-complex arrangement of shells. Helical lattice structures comprised of multiple composite helical ribbons combined with mechanical joints (see Figure 4.1) were selected as a case study to see whether interactions between thermal and mechanical prestress could be utilised to create novel structures with thermally-dependant behaviour, specifically negative thermal expansion.

Work in this chapter was presented at MechComp5 (Lisbon, Portugal). In addition, part of the work detailed in this chapter was published in a paper in the Journal of the Mechanics and Physics of Solids [175]. This chapter includes elements from this author's contribution to that paper - namely FE studies and prototype demonstrations - as well as additional studies and implementation details.

4.1 Introduction

Helical structures occur throughout nature, and often coincide with some shape-changing or snap-through mechanism [59, 83, 174]. One biological structure that has attracted a lot of attention from engineers and scientists is that of the rapidly-contracting molecular mechanism in the tail sheath of virus bacteriophage T4, and elasticity models have been developed for the complex behaviour of these sorts of protein arrays [67]. Inspired by this virus, Pirrera *et al.* developed a macroscopic lattice structure that tried to mimic the snap-through behaviour of the molecular

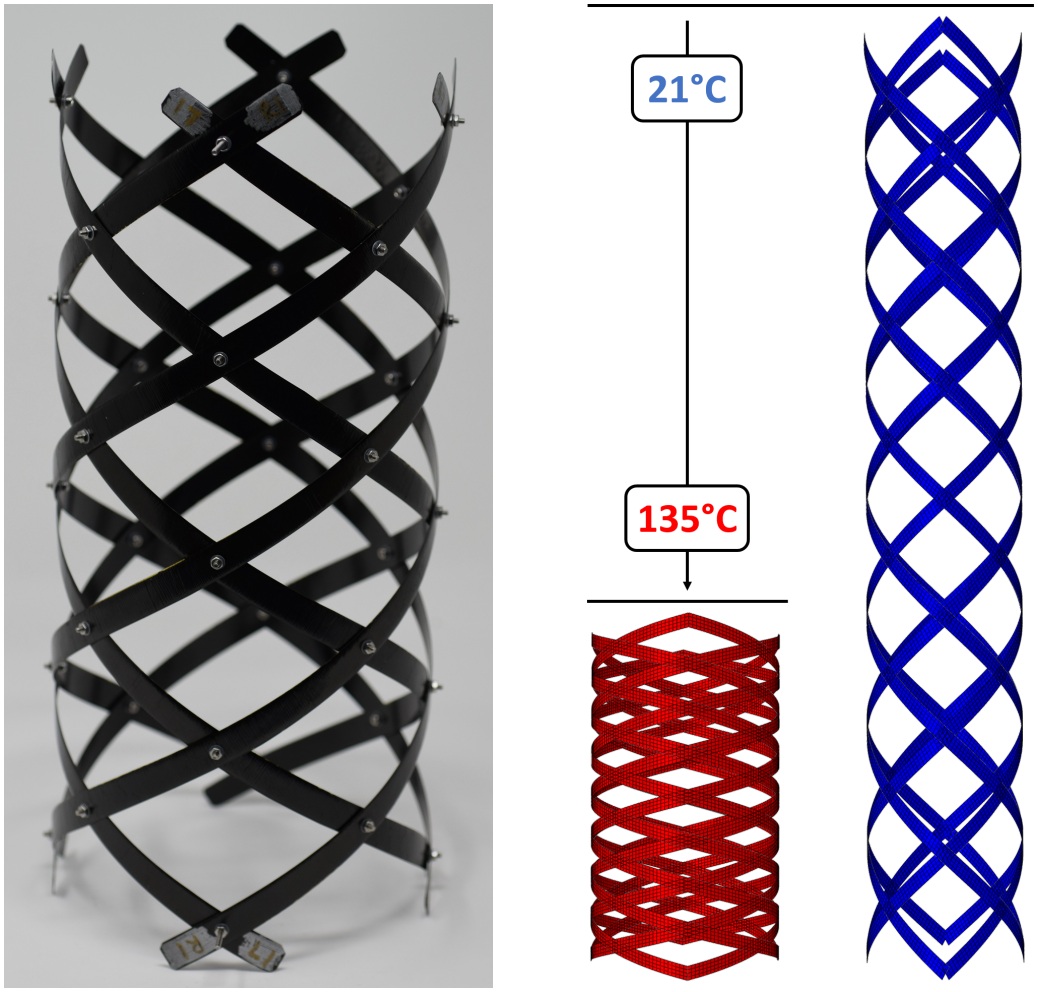

(a) *Photograph of a prototype composite helical lattice*

(b) *Illustration of a large negative thermal expansion lattice concept*

Figure 4.1: *The tuned cylindrical composite helical lattice concept. Left and right-handed helices are combined with mechanical joints at their intersections. Mechanical prestress is included by assembling the lattice at a different cylinder radius to that used to manufacture each helix. Using non-symmetric layups and applying a difference in temperature can induce local curvature changes that cause the lattice to extend or contract.*

mechanism with composite helices [187]. By utilising prestress, geometry and composite layup in helical configurations, they construct a bi-stable prototype with axial and radial strains in excess of those produced by bacteriophage T4, as well as demonstrate mathematically that there exist design spaces where such phenomena can be realised. Once the internal energy states and stability sensitivities are understood, other forms of lattice structure can be envisaged, for instance a structure where the stability configuration is temperature-dependent (*e.g.* via non-symmetric composite laminates), which can enable thermal actuation of snap-through behaviour.

For the physical demonstrators in literature, individual composite helices are assembled together into a lattice and pantograph-like motion is achieved by assigning hinge connectors at locations where the individual strips overlap each other. The lattice assembly constrains the helices to lie on a cylinder, and the interplay between mechanical prestress (provided by having a difference between helix manufactured radii and the lattice assembly radius) and helix geometry achieves tailorable nonlinear extension and contraction of the lattice (including multi-stable behaviour). Including thermal prestress (provided by an unsymmetric layup and a change in temperature) means that thermal strains will cause changes in the helix curvatures which, in-turn, cause the lattice to extend or contract axially. Work to combine such novel lattices into a hierarchical structure as a method to inspire the development of new materials has also been proposed [49, 176], but there only exists a handful of examples that have actually been prototyped [27, 155–157, 177], leaving manufacturing processes and sensitivities not fully understood.

This chapter details work carried out to model, manufacture and test a helical lattice that exhibits novel behaviour. The few existing lattice prototypes in literature often focused on bistable deployment, so a new behaviour unseen in literature was targeted: a lattice that exhibits very large negative coefficients of thermal expansion (CTEs). New high-fidelity FE models are presented, as well as higher-quality manufacturing techniques and experimental validation of predicted responses. Figure 4.1a shows a photo of the prototypes lattice structure, and Figure 4.1b shows an illustration of the negative CTE concept.

The chapter starts by presenting an analytical model for helical lattice structures from literature, followed by experimental results for a lattice design found using this model. Next, the initial analytical predictions and experimental results are compared against an enhanced analytical model from literature, before a finite-element approach to lattice modelling is discussed. After this some lattice design uncertainties and sensitivities are explored based on experimental measurements and FE simulations. The chapter ends by showing a couple of alternative lattice designs to illustrate the range of different behaviour achievable with combined thermal and mechanical prestress, before final conclusions are presented.

4.2 Analytical Model - 1D Beam

As the lattice is cylindrical (a developable surface) it can be represented on a flat plane (see Figure 4.2), and by considering this planar lattice geometry as a series of unit cells, Pirrera *et al.* developed the first analytical model for a helical lattice structure. In their energy-based formulation the behaviour of the entire lattice could be described by understanding how one of these unit cells behaves [187]. They assumed the following:

- The lattice is comprised of effectively 1D helical beams, *i.e.* the helices have longitudinal curvature (and twist as they conform to the underlying cylinder), but have no curvature across their width;
- The helices have frictionless hinges where helices intersect;
- The change in length of each helical strip is negligible;
- The entire lattice remains on a cylinder (whose radius and height can change) throughout extension.

This model was expanded by O'Donnell *et al.* [175] to include thermal effects from anisotropic materials, resulting in an expression for lattice strain energy per unit cell (*i.e.* each enclosed quadrilateral "cell" as seen in the planar lattice) as:

$$\begin{aligned}\frac{N}{2\pi}\Pi =& \frac{l}{2}(w_R\boldsymbol{\kappa}_R^T\boldsymbol{D}^*\boldsymbol{\kappa}_R + w_L\boldsymbol{\kappa}_L^T\boldsymbol{D}^*\boldsymbol{\kappa}_L) - \\ & l(w_R\boldsymbol{\chi}_R^T\boldsymbol{D}^*\boldsymbol{\kappa}_R + w_L\boldsymbol{\chi}_L^T\boldsymbol{D}^*\boldsymbol{\kappa}_L)\Delta T + \\ & \frac{l}{2}(w_R\tau_R + w_L\tau_L)(\Delta T)^2\end{aligned} \tag{4.1}$$

where Π is the strain energy per unit cell, l relates to the side length of each unit cell ($2\pi l/N$, see Figure 4.2), $\boldsymbol{\kappa}$ are the helix in-plane curvatures and twists, $\boldsymbol{D}^*$ is the reduced bending stiffness matrix (see Eqn. 2.9), and ΔT is the temperature difference from cure. In addition to these, N refers to the number of pairs of helices (*i.e.* $N = 4$ if there are four right-handed and four left-handed helices), and the w term is the strip width, and though this is present the 1D assumption of no transverse curvatures still applies. The "R" and "L" subscripts refer to whether the helix in question is right or left-handed. The $\boldsymbol{\chi}$ and τ terms are thermal response parameters [175]

$$\boldsymbol{\chi} = [\boldsymbol{B}^*]^T\boldsymbol{N}^{th} + \boldsymbol{M}^{th}, \tag{4.2}$$

and

$$\tau = U_{th} - [\boldsymbol{N}^{th}]^T\boldsymbol{A}^{-1}\boldsymbol{N}^{th}. \tag{4.3}$$

Here $\boldsymbol{N}^{th}$ and $\boldsymbol{M}^{th}$ refer to the thermal residual stresses and moments respectively, the $\boldsymbol{B}^*$ matrix is the partially inverted form of the $\boldsymbol{B}$ matrix

$$\boldsymbol{B^*} = -\boldsymbol{A}^{-1}\boldsymbol{B}, \tag{4.4}$$

and U_{th} is thermal energy term defined as

$$U_{th} = \sum_k \int_{z_k}^{z_{k+1}} [\boldsymbol{\alpha}^k]^T \bar{\boldsymbol{Q}}^k \boldsymbol{\alpha}^k dz, \tag{4.5}$$

where $\boldsymbol{\alpha}$ refers to the ply-level coefficients of thermal expansion, $\bar{\boldsymbol{Q}}$ is the lamina stiffness matrix, z refers to the mid-plane height of each ply, and k is an indicator for the ply in question.

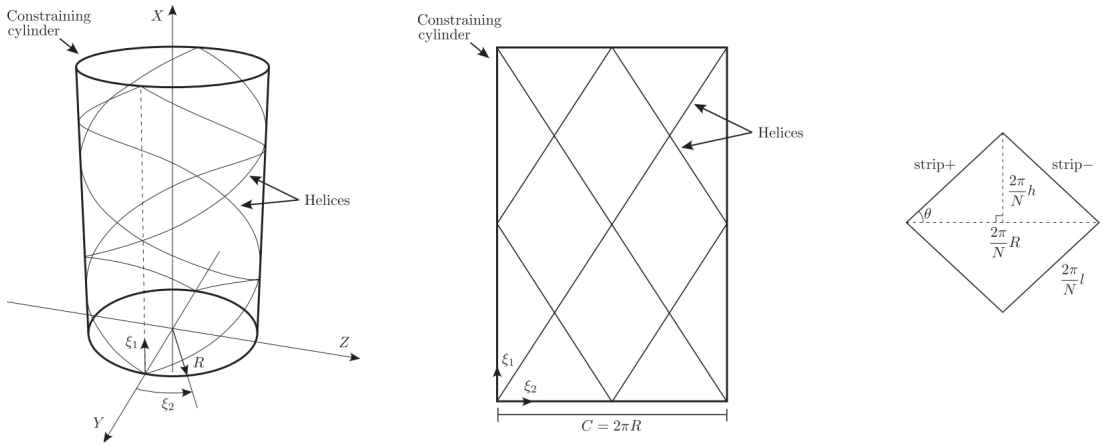

(a) A cylindrical lattice. (b) Planar projection of lattice. (c) Rhomboidal unit cell.

Figure 4.2: *Representations of the lattice geometry (a) as a 3D cylinder, (b) developed onto a 2D plane, and (c) the individual unit cell. Reproduced from Ref [175]. "strip+" and "strip-" in (c) refer to whether the helices making the unit cell have a positive or negative tool angle θ.*

By investigating the 1D extensional lattice energies from this analytical model, designs were sought to maximise negative thermal expansion along the lattice cylindrical axis while minimising the complexity of manufacture and modelling. The design space was reduced by only considering lattices that used eight helices in total: four right-handed helices, and four left-handed helices. In addition to this the layups of the right-handed and left-handed helices were chosen to be four plies only and mirror each other (*i.e.* where the right-hand helix had a ply of orientation $+\theta$ (with the zero direction defined as the helix screw direction - see Figure 4.3), the left-hand helix had a ply with orientation of $-\theta$).

Designs that included mechanical prestress were investigated analytically and in FE models (some are detailed at the end of this chapter) but early prototypes proved difficult to assemble successfully due to the high strains induced during mechani-

Table 4.1: *Lattice Prototype Design Details*

Parameter	Right-Handed Helices	Left-Handed Helices
Tool Cylinder Radius (R)	76 mm	76 mm
Tool Cylinder Wrap Angle (θ_H)	+15°	-15°
Distance Between Bolt Joints (l)	62 mm	62 mm
Helix Width (w)	10 mm	10 mm
Ply Thickness (t)	0.1177 mm	0.1177 mm
Layup	[-15 -70 -35 90]	[15 70 35 90]

cal prestressing leading to failure. As the project focus was primarily exploring the thermal prestress lattice design space it was decided not to include any mechanical prestress effects (*i.e.* the helices' cure-temperature geometry would be the lattice assembly geometry). This would reduce the material stress during assembly, minimising delamination risks in each prototype.

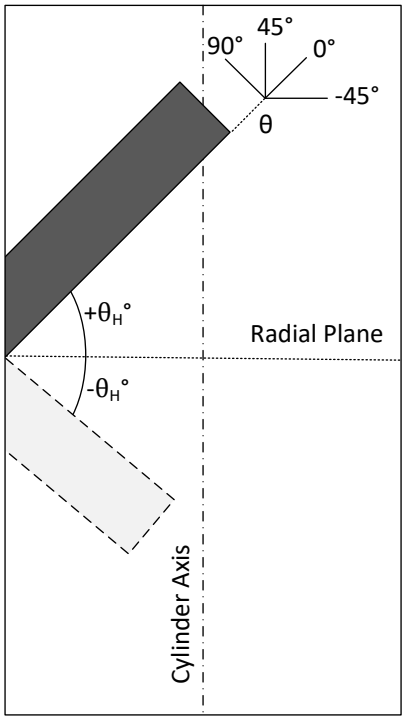

Figure 4.3: *Diagram of strip layup and tool angle orientation definitions. θ defines the fibre angle, with the helix line as the zero fibre angle. θ_H defines the angle at which the helical strips are wrapped around the cylindrical manufacturing tool, with the cylinder's radial plane as the zero angle.*

Thermally-active helix layups were generated using a genetic algorithm MATLAB optimiser [150] to ensure that as the lattice heated it contracted. Cost functions were designed to maximise the difference between the equilibrium lengths of the heated (L_{hot}) and cooled (L_{cool}) lattices:

$$\text{cost} = -\left(L_{\text{cool}} - L_{\text{hot}}\right). \tag{4.6}$$

The optimiser chose the four ply orientations (to the nearest 5°) and stacking sequence for given manufacturing parameters (tool radius, distance between bolts, tool angle *etc.*), and presented an energy landscape for each design showing how the calculated equilibrium lengths changed with temperature. IM7-8552 was the chosen material as it has well understood thermal and mechanical properties (see Table 2.1 in Chapter 2) [87, 197]. A Tsai-Wu failure criterion was also added to the optimiser check the feasibility of surviving the large deformations required during assembly and testing, using strength values from Ref [24].

The genetic algorithm optimiser was run with various weightings applied to the (L_{hot}) and (L_{cool}) terms in a trial-and-error approach to find the greatest negative thermal expansion design. The final design was chosen via manual inspection of the predicted performances while taking into account their manufacturing suitability *i.e.* was there suitable tooling available and were the predicted stresses below the failure limits. The design parameters for the final prototype are listed in Table 4.1. Figure 4.3 shows the layup and tool angle definitions used during this work. The underlined number in each layup represents the ply in contact with the tool surface during cure.

Figure 4.4 shows the predicted energy landscape and behaviour for this design using the 1D beam model. The energy landscapes are normalised by dividing them by their maximum value. Figure 4.4a shows the room temperature (20 °C) energy landscape for the lattice (cure temperature was 180 °C), which can be seen to exhibit monostable behaviour with a stable length of 408 mm. The location of this monostable point is designed to change with temperature, making the lattice smoothly extend as the applied temperature is decreased, as seen in Figure 4.4b.

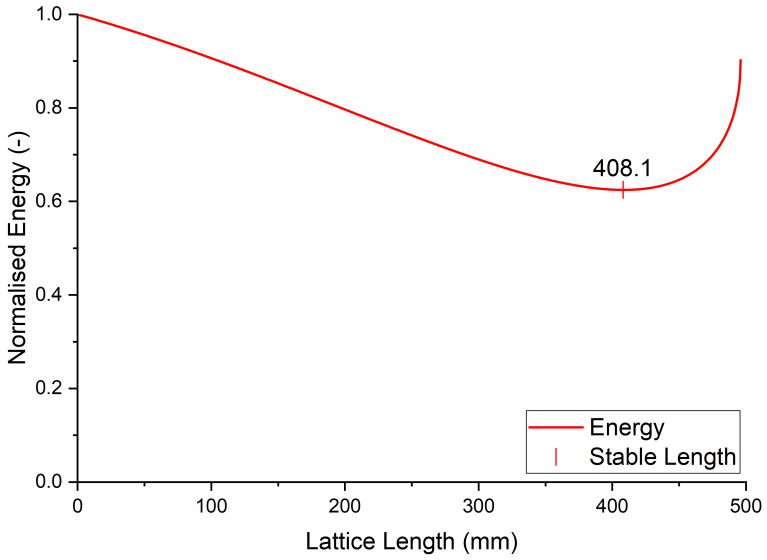

(a) *Lattice room temperature energy landscape*

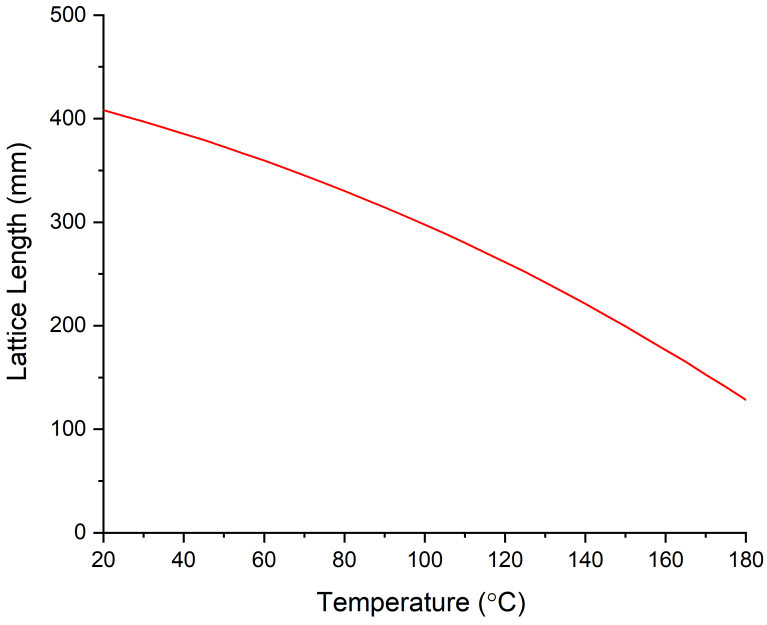

(b) *Lattice negative thermal expansion behaviour*

Figure 4.4: *Behaviour for the negative thermal expansion helical lattice as predicted by the 1D analytical model*

4.3 Experimental Investigations

Helical lattice prototypes were constructed and tested with the aims of refining the quality of existing manufacturing methods, providing a way to inform parameters for FE models (*e.g* hinge friction and average ply thickness) and validating the predicted behaviours from the analytical and numerical models.

4.3.1 Prototype Manufacture

This subsection details the steps for manufacturing composite helical lattices.

1. **Cylindrical Tool Preparation.** Two layers (for redundancy) of release film are wrapped around a clean cylindrical tool, before a cork datum is applied at the design tool angle (a simple sheet of paper cut at the right angle can help) which ensures the laminates are wrapped into helices correctly (see Figure 4.5a).

2. **Laying-Up the Helices.** The helices are laid-up as flat laminates and then wrapped onto the cylindrical tool. To avoid misalignment and poor edge quality of the high aspect ratio laminates two L-shaped try squares are used to create a slot in which the prepreg strips can sit during layup (see Figure 4.5b). A thin piece of double-sided tape placed at the bottom of the slot can hold the first plies steady during manual layup.

3. **Wrapping the Helices.** Laminates can struggle to stick to cold cylindrical metal surfaces, so a heat gun is used to evenly warm the laminate (making the resin tackier) prior to wrapping it on the tool. No one area should be heated for more than approximately ten seconds, as this may begin to cure the surface of the prepreg. The strips can then be easily applied to the tool, using the pre-placed cork datum to ensure correct wrap angle (see Figure 4.5b). Laminates are wrapped next to each other to ensure correct tool angles, as shown in Figure 4.5c, although including a 5 mm spacing between each laminate will allow a small amount of resin-runoff, which makes the helices easy to separate once cured and reduces the chance of them fracturing.

4. **Vacuum Bag and Curing.** A layer of release film and a layer of breather material must be wrapped-around the strips, and it is also recommended that a layer of silicone sheeting is placed on top of this to improve surface finishes and mitigate excessive thickness undulations. When not using a silicone layer it was found that significant ply thickness variations could occur, and the results of this investigation can be found in Appendix A: Helical Lattice Ply-Level Thickness Measurements. The vacuum bag must be wrapped around

the entire tool and have a protruding 'overhang' segment where the valves can be placed without the risk of them tearing the bag under pressure (see Figure 4.5e). The cylinder is placed on a flat tool plate covered in a layer of breather to protect the underside of the vacuum bag, and raising the cylinder off the tool plate using I-beam segments (also wrapped in breather material) can protect the laminates underneath.

5. **Finishing and Assembly.** The lattices are cured as per the manufacturer's instructions at 7 bar pressure and 180 °C. Once cured, helix edges are wet-sanded using silicon carbide grit paper to remove excess resin run-off. Nine holes are then be drilled periodically along the length of each helix using 2 mm diameter diamond-coated drill bits. A drill jig (see Figure 4.5f) was used to flatten small sections of the helices so as not to over-strain and damage them during drilling. The helices are then bolted together into a cylindrical lattice, with two nylon washers (each 0.3 mm thick) placed between the helices at each bolt joint to minimise contact friction. Once manufactured, prototypes are stored in controlled environmental conditions (20 °C and 16 % humidity) to limit moisture ingress.

4.3.2 Prototype Testing

This subsection details the tests carried out to verify the predicted behaviours of the helical lattice prototypes. Two series of tests were conducted to experimentally verify the behaviour of the prototype lattice. Firstly tests were conducted to observe the axial extension of the optimised lattice with varying temperature. To avoid surface friction effects during actuation, the lattice was suspended horizontally in an oven with 17 cm steel wires connected to the bolts at the ends of the lattice. The lattice was heated to 135 °C, and then allowed to cool to ambient room temperature. While cooling, lattice temperature was measured directly using a K-type thermocouple placed on the surface at the centre of the lattice, and displacements were captured using a digital single-lens reflex (DSLR) camera. A forward-looking infra-red camera (FLIR® T650) was used to qualitatively verify even heating across the lattice (see Figure 4.6, reproduced from [175]). Displacement values (defined as the distance between the bolts at opposite ends the lattice) were obtained via video post-processing using Tracker software [18].

A second series of tests were conducted to measure the force-displacement response at room temperature. The lattice was suspended vertically in a Shimadzu EZ-LX HS universal test machine with loops of high strength cotton thread connected to the bolts at the ends of the lattice (see Figure 4.7a). A 500 N load cell recorded axial force, and a 150 mm extension (at 50 mm per minute) was applied,

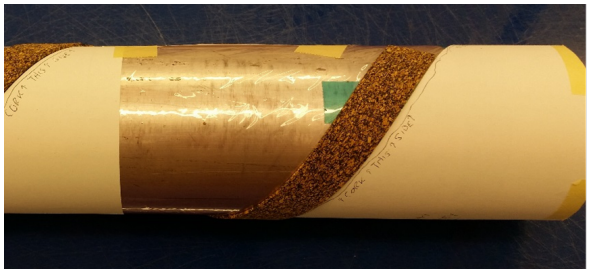

(a) *Cork edging and guide wrapped on cylinder*

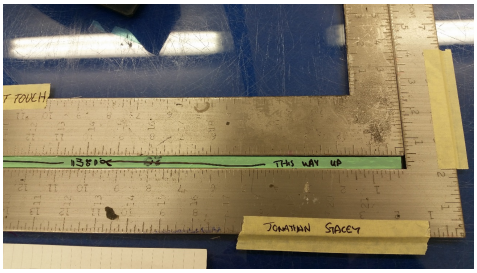

(b) *L-shaped try squares used to aid layup*

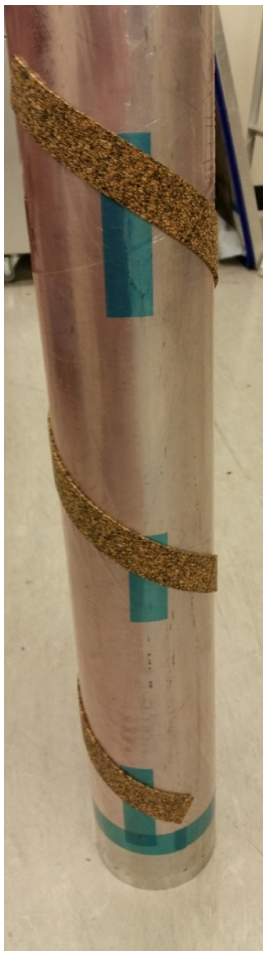

(c) *Cork datum placed at desired angle*

(d) *Flat strips wrapped around cylinder*

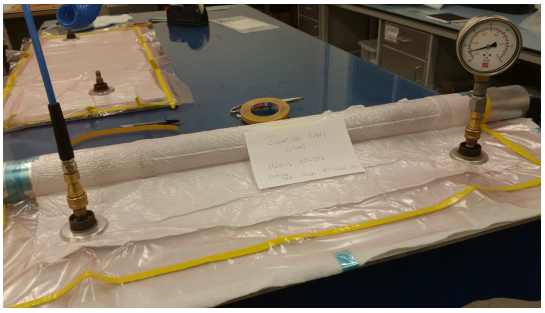

(e) *Envelope vacuum bag (with overhang)*

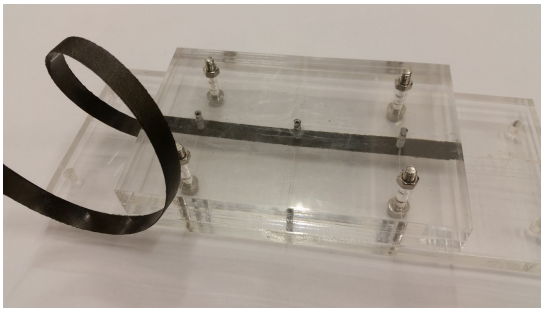

(f) *Drilling jig for partially-flattened helix*

Figure 4.5: *Key steps in the manufacture of helices for the composite lattice mechanism*

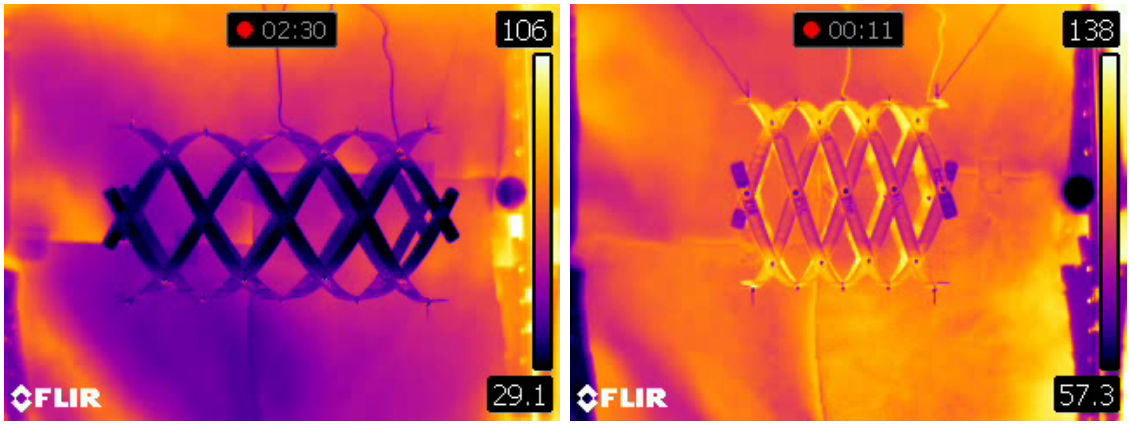

(a) *Lattice shown as extended when cooled* **(b)** *Lattice contracted when heated*

Figure 4.6: *Heat maps from FLIR camera showing even temperature distributions during lattice prototype testing, with colour scale in °C*

with displacements measured using a DSLR camera and video post-processing in a manner similar to the initial oven tests.

A third series of smaller tests was conducted to refine values used in the FE models. One set of tests investigated bolt joint friction. Four identical flat strips of four-ply IM7-8552 laminate (cured in the same manner as the lattice helices) were combined using three bolt joints identical to those used in the lattice, effectively creating a 2-bar linkage (see Figure 4.7b). The two ends of this linkage were clamped in a Shimadzu EZ-LX HS universal test machine with a 50 N load cell, and cross-head displacements and forces were measured. Two bolt joints were left loose, with the central bolt remaining tight under the assumption that all observed force would be from this hinge's friction. Hinge frictions were reported as frictional moments in Nmm, with the maximum and minimum values (measured as 7.29 Nmm and 1.23 Nmm respectively) used to refine FE models.

Prototyping the helical lattice structures can be a challenging process. Some mechanically-prestressed designs could not be assembled successfully, which was due to delaminations in the vicinity of the bolt holes. To gain an understanding of manufacturing variability, a study of the ply-level thickness distributions and volume fractions was also carried out to quantify laminate variations and further improve the manufacturing process. In particular this resulted in the use of silicone sheeting in the bagging and curing of the helices to control ply thicknesses (full results this study are presented in Appendix A: Helical Lattice Ply-Level Thickness Measurements).

(a) *Photograph of the lattice suspended configuration for measuring the force-displacement behaviour. Cotton loops attached the lattice to rods mounted in the test machine grips.*

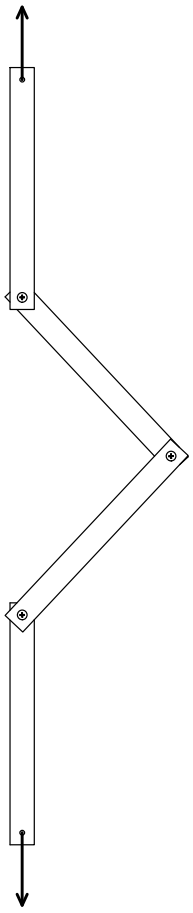

(b) *Diagram showing the 2-bar linkage setup for measuring hinge friction. The two vertical links were clamped in the test machine with the arrows indicating the applied load.*

Figure 4.7: *Tensile testing configurations used to determine lattice behaviours*

4.3.3 Experimental Results

Figure 4.8 shows the experimental measurements compared against the predictions from the 1D analytical beam model. The average experimental trend is shown in black, with the full range of measurements shown within the light grey region. By differentiating the energy landscape with respect to lattice length, a force response can be computed from the analytical model.

It can be seen that in both Figure 4.8a and Figure 4.8b that while general designed behaviour has been demonstrated (*i.e.* the lattice exhibits novel negative thermal expansion), there is a significant discrepancy between the analytical model predictions and the prototype. Firstly this could be the result of a systematic error when suspending the lattice in the oven, as the prototype had very low axial stiffness and was easy to unintentionally compress when handled causing an erroneous reduction in the room-temperature lattice length of approximately up to 30 mm. In addition it was also likely that the assumptions of the 1D beam model did not match well with the lattice prototype. It was not possible to manufacture helices that were as narrow as they were thick meaning the helices were more like 2D shells than 1D beams, and other work has shown that transverse curvatures (neglected in the 1D model) can have a significant contribution to lattice behaviour [156].

4.4 Analytical Model - 2D Shells vs 1D Beams

At the time this work was carried out, researchers at the University of Limerick independently expanded on the original lattice 1D analytical beam model by including membrane strains, $\boldsymbol{\epsilon}$, and the 2D effects of transverse curvature κ_{yy} [156]. Using this model, McHale *et al.* showed that for some lattice designs, ignoring transverse and membrane effects could give energy landscapes with incorrect stability predictions *i.e.* false bistability or monostability. This model was then applied to thermally-sensitive designs by choosing non-symmetric laminates where $\boldsymbol{B} \neq 0$, and then integrating along the length of each helix to find the strain energy [155]:

$$\Pi = \frac{N}{2} \int_S \left\{ \begin{bmatrix} \boldsymbol{\epsilon}^0 \\ \boldsymbol{\Delta\kappa} \end{bmatrix}^T \begin{bmatrix} \boldsymbol{A} & \boldsymbol{B} \\ \boldsymbol{B} & \boldsymbol{D} \end{bmatrix} \begin{bmatrix} \boldsymbol{\epsilon}^0 \\ \boldsymbol{\Delta\kappa} \end{bmatrix} - \begin{bmatrix} \boldsymbol{N}^{th} \\ \boldsymbol{M}^{th} \end{bmatrix}^T \begin{bmatrix} \boldsymbol{\epsilon}^0 \\ \boldsymbol{\Delta\kappa} \end{bmatrix} \right\} dS. \tag{4.7}$$

Again here Π refers to the lattice strain energy, $\boldsymbol{\epsilon}^0$ and $\boldsymbol{\Delta\kappa}$ refer to the membrane strains and changes in helix curvatures respectively, $\boldsymbol{A}$, $\boldsymbol{B}$ and $\boldsymbol{D}$ are the laminate stiffness matrices, $\boldsymbol{N}^{th}$ and $\boldsymbol{M}^{th}$ refer to the thermal residual strains and bending moments, and S is the helix length term.

McHale *et al.* included transverse curvature effects by solving a boundary value

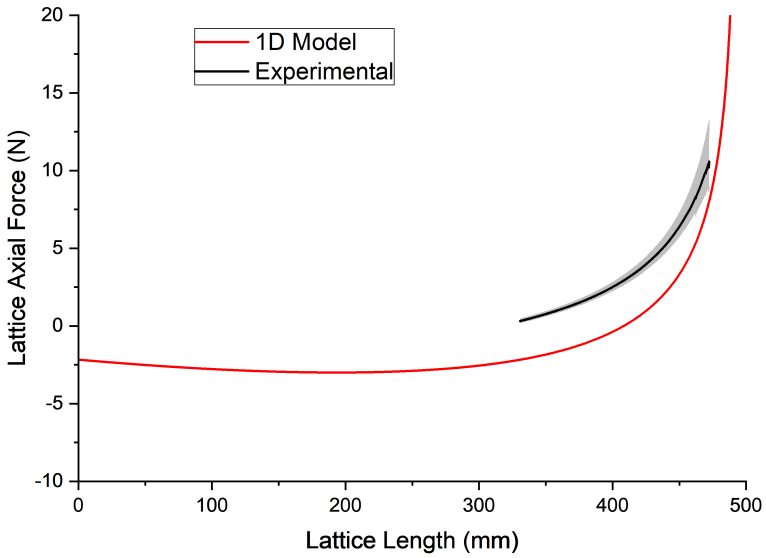

(a) *Experimental and 1D analytical force-extension behaviour*

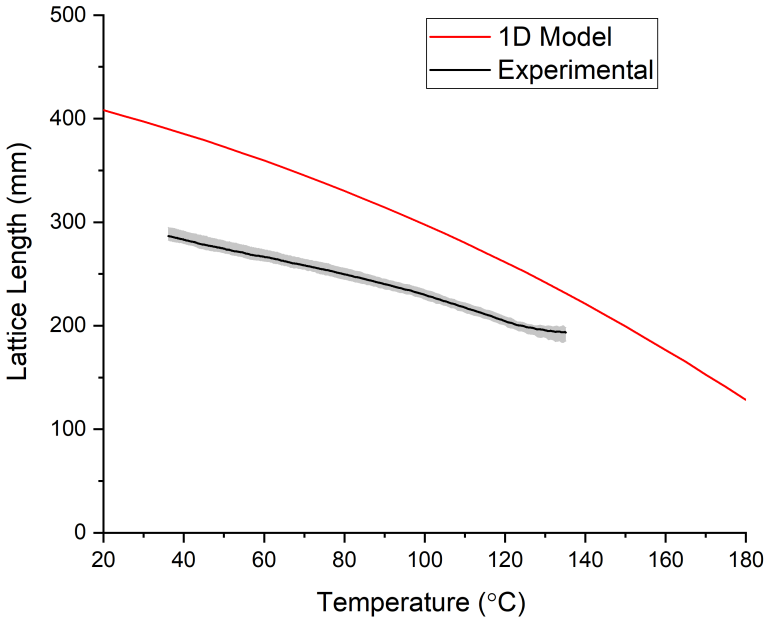

(b) *Experimental and 1D analytical temperature-extension behaviour*

Figure 4.8: *Comparison of prototype lattice behaviour with predictions from the 1D analytical beam model*

problem presented by Giomi and Mahadevan [75]. Here they assume that all physical quantities are constant in the x-direction (as the strips are assumed to be infinitely long), κ_{xx} and κ_{xy} are are constant in x and y and that there are no applied forces on the strip edges. Under these assumptions combining the general constitutive stress-strain relations with expressions for moment equilibrium and strain compatibility leads to the following fourth-order governing differential equation [75]

$$\begin{aligned}(A_{11}^* D_{22}^* + (B_{21}^*)^2)\frac{\partial^4 M_{yy}}{\partial y^4} + 2B_{21}^*\kappa_{xx}\frac{\partial^2 M_{yy}}{\partial y^2} + \kappa_{xx}^2 M_{yy} = \\ \kappa_{xx}(D_{22}^*(\kappa_{xx}^0\kappa_{yy}^0 - (\kappa_{xy}^0)^2 + \kappa_{xy}^2) + ... \\ \kappa_{xx}(D_{12}^*(\kappa_{xx} - \kappa_{xx}^0) + ... \\ D_{26}^*(\kappa_{xy} - \kappa_{xy}^0) - D_{22}^*\kappa_{yy}^0)),\end{aligned} \tag{4.8}$$

where the $\boldsymbol{A}^*$ terms refer to inverse $\boldsymbol{A}$ matrix terms, the κ^0 terms refer to the as-manufactured shell curvatures and κ terms refer to the instantaneous shell curvatures. Note that in Ref. [156] simplified versions of these equations presented that neglects $\boldsymbol{B}$ matrix contributions.

As there are no forces or torques applied to the strip edges this means

$$\frac{\partial M_{yy}}{\partial y} = M_{yy} = 0, \quad \text{at} \quad y = \pm\frac{W}{2}, \tag{4.9}$$

where w refers to the width of the individual helices.

Solving this boundary value problem gives an expression for the induced transverse curvature change, $\Delta\kappa_{yy}^I$ (required for the expression $\Delta\kappa_{yy} = \kappa_{yy}^0 + \Delta\kappa_{yy}^I$) as

$$\begin{aligned}\Delta\kappa_{yy}^I = \kappa_{0y}^G + (C_1 + B_{21}^* C_1')\cosh(k_1 y)\cos(k_2 y)... \\ + (C_2 - B_{21}^* C_2')\sinh(k_1 y)\sin(k_2 y),\end{aligned} \tag{4.10}$$

where κ_{0y}^G is the Gaussian curvature defined as

$$\kappa_{0y}^G = \frac{\kappa_{xy}^2}{4\kappa_{xx}},$$

variable y refers to the distance in the transverse direction (*i.e.* along the helix width), the k_1 and k_2 terms are defined as

$$k_1 = \sqrt{\frac{\sqrt{s_2} + s_1}{2}}, \qquad k_2 = \sqrt{\frac{\sqrt{s_2} - s_1}{2}}$$

where

$$s_1 = \frac{-\kappa_{xx}B_{21}^*}{A_{11}^* D_{22}^* + (B_{21}^*)^2}, \qquad s_2 = \frac{\kappa_{xx}^2}{A_{11}^* D_{22}^* + (B_{21}^*)^2}.$$

The remaining terms are defined as

$$C_1 = \left(\frac{\kappa^0_{yy} - D^*_{12}\Delta\kappa_{xx} + D^*_{26}\Delta\kappa_{xy}}{D^*_{22}} - \kappa^G_{0y}\right) ... \\ \left(\frac{k_1\cosh(k_1\frac{W}{2})\sin(k_2\frac{W}{2}) + k_2\sinh(k_1\frac{W}{2})\cos(k_2\frac{W}{2})}{k_1\sin(k_2\frac{W}{2})\cos(k_2\frac{W}{2}) + k_2\sinh(k_1\frac{W}{2})\cosh(k_1\frac{W}{2})}\right),$$

$$C_2 = \left(\frac{\kappa^0_{yy} - D^*_{12}\Delta\kappa_{xx} + D^*_{26}\Delta\kappa_{xy}}{D^*_{22}} - \kappa^G_{0y}\right) ... \\ \left(\frac{k_2\cosh(k_1\frac{W}{2})\sin(k_2\frac{W}{2}) - k_1\sinh(k_1\frac{W}{2})\cos(k_2\frac{W}{2})}{k_1\sin(k_2\frac{W}{2})\cos(k_2\frac{W}{2}) + k_2\sinh(k_1\frac{W}{2})\cosh(k_1\frac{W}{2})}\right),$$

$$C'_1 = \frac{\sqrt{A^*_{11}D^*_{22}}C_1 + B^*_{21}C_2}{A^*_{11}D^*_{11} + (B^*_{21})^2}, \qquad C'_2 = \frac{\sqrt{A^*_{11}D^*_{22}}C_2 - B^*_{21}C_1}{A^*_{11}D^*_{11} + (B^*_{21})^2}.$$

While the model by McHale *et al.* considers transverse curvature (κ_{yy}) effects, their lattices were manufactured by wrapping the strips around a cylindrical tool with a tool angle, θ_H, of 0° (*i.e.* $\kappa^0_{yy} = 0$) [156]. For more general lattices (*i.e.* like those in this work where the helices are wrapped on the tool at an angle, giving a non-zero manufactured transverse curvature) the manufactured transverse curvature, κ^0_{yy}, that is included in the $\boldsymbol{\Delta\kappa}$ terms must included, which is defined as

$$\kappa^0_{yy} = \frac{1}{R}\sin^2(\theta_H). \tag{4.11}$$

In addition, the Gaussian curvature, κ^G_{0y}, that is used to calculate the induced transverse curvature $\Delta\kappa_{yy}$, must be expressed in the more general way (as defined by Giomi and Mahadevan in [75]) to reflect this manufactured transverse curvature,

$$\kappa^G_{0y} = \frac{(\kappa^0_{xx}\kappa^0_{yy} - (\kappa^0_{xy})^2) + \kappa^2_{xy}}{\kappa_{xx}}. \tag{4.12}$$

This leads to an expression for the change in curvatures according to the 2D model as

$$\boldsymbol{\Delta\kappa} = \begin{bmatrix}\Delta\kappa_{xx}\\ \Delta\kappa_{yy}\\ \Delta\kappa_{xy}\end{bmatrix} = \begin{bmatrix}\frac{1}{R}\cos^2\theta_H - \kappa^0_{xx}\\ \kappa^0_{yy} + \Delta\kappa^I_{yy}\\ \frac{1}{R}\sin\theta_H\cos\theta_H - \kappa^0_{xy}\end{bmatrix}, \tag{4.13}$$

whereas the expression for the change in curvatures for the 1D model was

$$\boldsymbol{\Delta\kappa} = \begin{bmatrix}\Delta\kappa_{xx}\\ \Delta\kappa_{xy}\end{bmatrix} = \begin{bmatrix}\frac{1}{R}\cos^2\theta_H - \kappa^0_{xx}\\ \frac{1}{R}\sin\theta_H\cos\theta_H - \kappa^0_{xy}\end{bmatrix}. \tag{4.14}$$

Figure 4.9 shows comparisons of energy landscapes and force-displacement responses for our lattice design alongside predictions from the 2D model. To aid comparison of energy minima, both landscapes in Figure 4.9a are normalised with respect to each of their largest energy values. For our design it can be seen that the landscapes are similar in both predicting monostable behaviour, but the 2D model suggests that the lattice will have a much shorter length at room temperature (the energy minima is at a shorter length).

Figure 4.10 shows that for our design the 2D model provides more accurate force predictions for the range of lattice length that was investigated experimentally. While the 2D model appears to be a noticeable improvement over the 1D model (especially when predicting forces) there are still discrepancies between the temperature-length curves measured experimentally and the temperature-length curves predicted by the analytical models. This suggests that experimental factors (*i.e.* tooling, gravity loads etc.) may have influenced measurements and should be included in FE models.

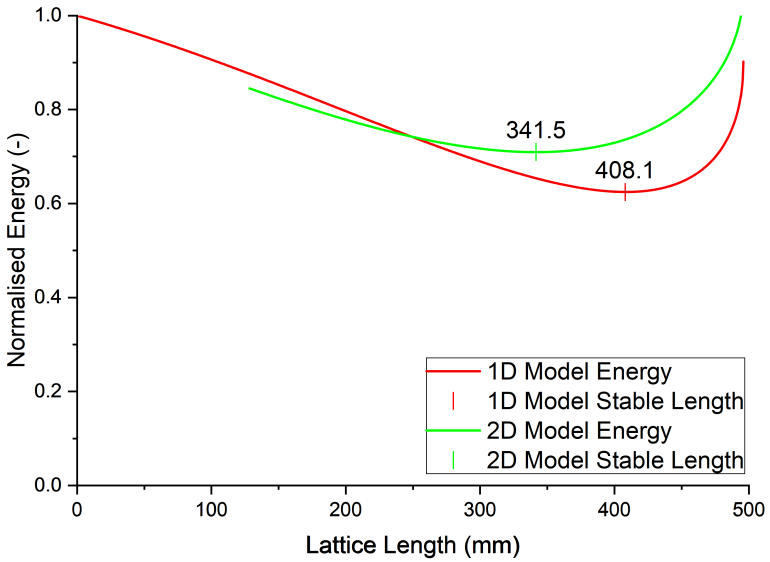

(a) *Normalised room temperature lattice energy landscapes as predicted by the 1D and 2D models*

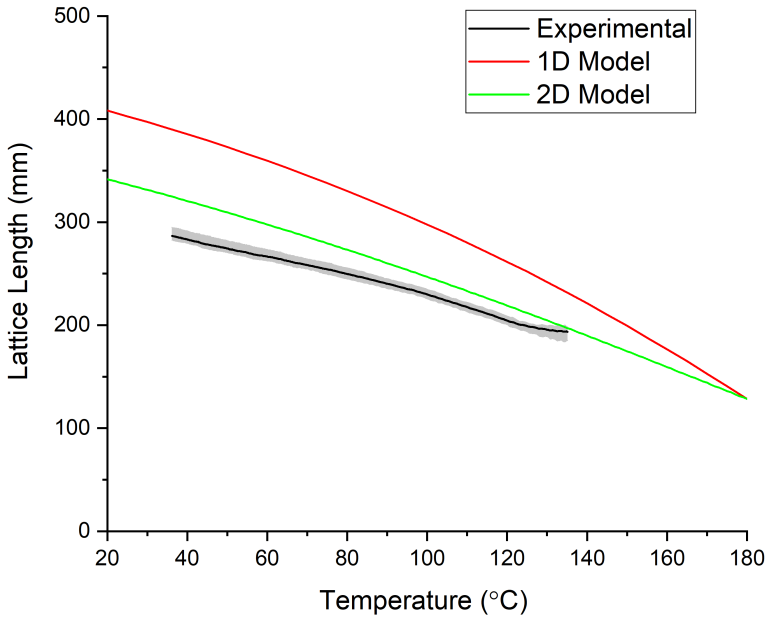

(b) *Experimental, 1D and 2D analytical temperature-extension behaviour*

Figure 4.9: *Comparison of approaches using energies and extensions from the 2D lattice model*

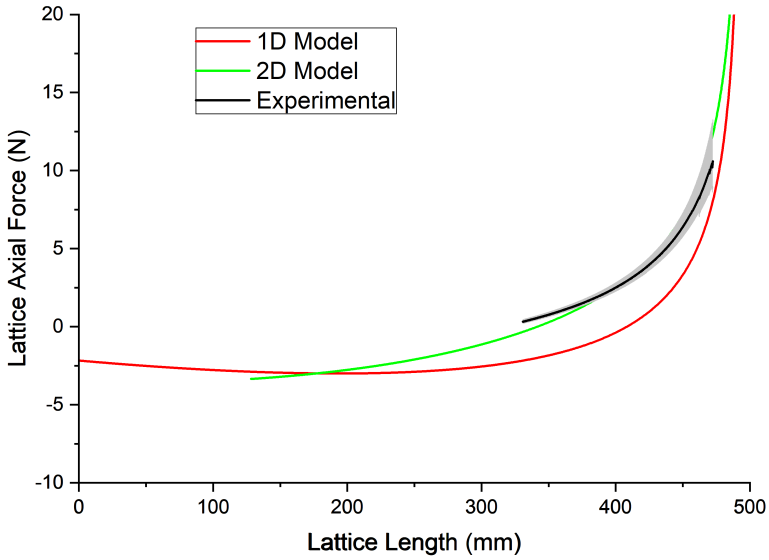

Figure 4.10: *Comparison of approaches using forces from the 2D lattice model*

4.5 Finite Element Analyses

As there appeared to be discrepancies between the analytical and experimental results, FE models of the lattices were constructed in Abaqus/Standard 2016. An advantage of using FE models is that they could be used as a virtual laboratory where experimental conditions and design parameter sensitivities could be investigated.

Helical geometries were created and partitioned at the joint locations, and cylindrical coordinate systems (aligned with the helix axes) acted as reference systems. Composite layups were applied to these geometries so that the 0° fibre direction was aligned along the helix spiral, and the strips were meshed with S4R quadrilateral shell elements. Defining the helical geometry and partitioning it so that hinge connectors and even quad meshes can be applied is not straightforward in Abaqus/Standard 2016, so the following list provides step-by-step instructions for constructing the models (without mechanical prestressing) manually in the Abaqus CAE user interface, with associated screenshots of the process shown in Figure 4.11.

1. **Create Helical Shell Geometry**. Create a part using the "3D", "'Deformable", "Shell" and "Revolution" parameters (see Figure 4.11a). Draw a line for the shell cross-section in the y-axis, at the desired radius in the x-axis. Note that the length of this line will not be the width of the helix strips unless the subsequent box "Sweep sketch normal to path" is ticked. Set the revolution angle to 360° and the extrude direction to be the desired helix pitch.

2. **Segment the Surfaces (for Meshing and Hinge-Location Purposes)**. Merge any auto-imposed edges on each side of each helix. Partition the helix

faces according to the locations of the hinges (nine on each helix, evenly spaced along the screw centre line) so that each hinge location is the meeting point of four surface segments (see Figure 4.11b). The quickest way to do this is by partitioning the faces using the shortest path between two points and making use of the automatically-marked midpoints.

3. **Apply Composite Laminate Properties and Mesh**. Define a composite material using "Lamina" elastic properties and "Orthotropic" expansion properties. A density value should also be included if gravity effects are being investigated. Define a composite layup for the part by creating a cylindrical coordinate system. Use an "Additional rotation" to ensure that the reference (*i.e.* 0° axis) aligns with the helix spiral (see Figure 4.11c). Apply a S4R shell mesh by applying a mesh seed to the edges of the desired target size (see Figure 4.11d).

4. **Align Instances in Assembly**. Once Steps 1-3 have been completed for both the left and right-handed helices, create four instances of each part in the assembly module. As each helix is one revolution, and has no mechanical prestress, they can be assembled into a lattice by translating and rotating the different instances about their individual cylindrical reference axes. The bolt locations should be aligned (see Figure 4.11e).

5. **Apply Hinge Connectors**. Create a "Hinge" connector from the "Interaction" module. This will ensure correct bolt behaviour, *i.e.* the only degree of freedom is rotations around the radial axis. Create "Wire" features from the "Interaction" module. This is done by selecting a bolt point on one helix as "Point 1" and selecting its corresponding bolt point on the other-handed helix as "Point 2". This needs to be done for every bolt location. Create "Connector Assignments" from under "Assembly". Use the "Wire" sets previously defined and ensure that a cylindrical datum axis from one of the helices is used as the connector orientation to assign the hinges to the correct places (see Figure 4.11f).

In all models hinge connectors were applied on the wires to restrict joint rotations to the radial axis. The bolt hole was defined as having a 1 mm radius and an assumed friction coefficient of 0.13 (*i.e.* dry contact between two nylon washers [218]). In addition, friction moments (based on experimental measurements) were added to the hinge behaviour to better represent the physical nuts and bolts. Mesh refinement was conducted by comparing the computed room temperature (21 °C) lattice lengths. Mesh target sizes of between 3×3 mm and 0.5×0.5 mm were considered, and a final

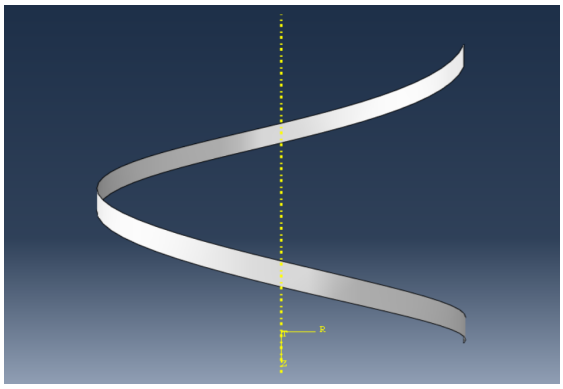

(a) *Helical shell geometry and reference cylindrical axis*

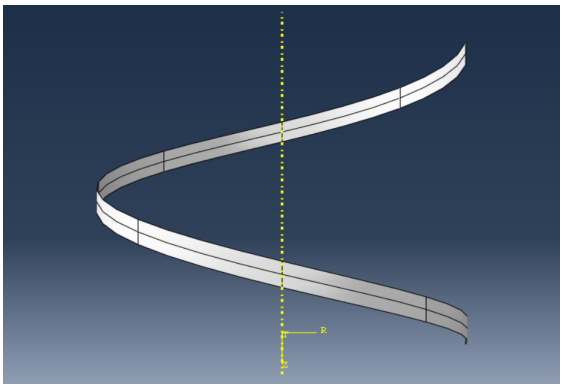

(b) *Segmented helical geometry showing bolt locations at intersections*

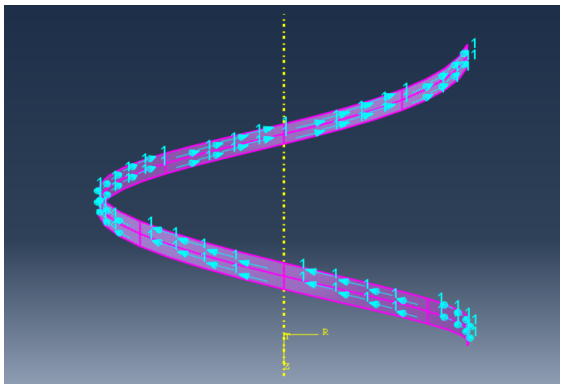

(c) *Composite material zero degree fibre reference orientation*

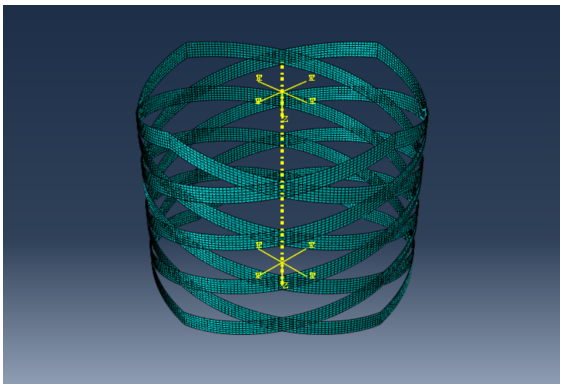

(d) *Assembled lattice showing mesh of S4R quadrilateral elements*

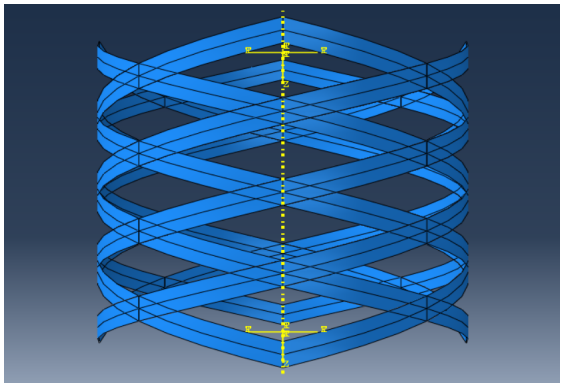

(e) *Multiple left and right helices aligned along a common cylinder axis*

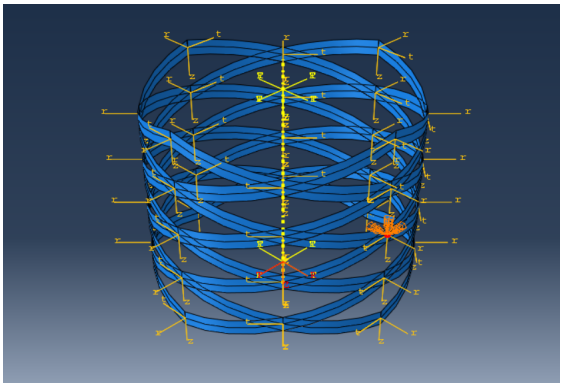

(f) *Assembled lattice showing radial hinges and encastre boundary point*

Figure 4.11: *Screenshots of the process of constructing the helical lattice models in Abaqus CAE*

mesh size of 3×3 mm was selected, as the computed length converged to 99.75% of the value from the analysis with a 0.5×0.5 mm mesh size.

The post-cure thermal actuation of the lattice was modelled using predefined ambient temperature fields with a fully-fixed boundary condition applied to a central node on one helix via geometrically nonlinear general static analyses. Other models like this were built to investigate different parameter sensitivities (*e.g.* changing the helix width or length) as well as better match experimental conditions (*e.g.* modelling the wires used to suspend the helix prototypes). The following list describes the steps, loads and boundary conditions used for each type of model:

1. Temperature-Controlled Models

   Steps: Only one step is required (after the initial) to capture the temperature-dependant extension. A nonlinear "Static, General" step with small fixed increments is often sufficient.

   Loads: A temperature "Predefined Field" should be applied across both steps, starting initially at the cure temperature and modified with a ramp down in the second step to represent the cooling.

   Boundary Conditions: A single fully-fixed node (typically in the centre of the helix) is the only boundary condition required.

2. Displacement-Controlled Models

   Steps: Three post-initial nonlinear "Static, General" steps should be created: the first to allow the lattice to cool to room temperature, the second to contract it, and the third to extend it (axial force measurements can be taken in this step).

   Loads: A gravity load should be uniformly applied across the whole model for the final extension step to reflect the experimental setup.

   Boundary Conditions: In the first step, a single fully-fixed node is sufficient. This should be deactivated in subsequent steps. For the contraction and extension steps an axial displacement condition should be applied to the four bolts on one end of the helix, while the other end of the helix has minimal conditions applied: all four bolts should be fixed in the axial direction; two should additionally be fixed in the tangential direction, and one of those should also be fixed in the radial direction.

3. Force-Controlled Models

   Steps: As per the displacement-controlled model.

Loads: As per the displacement-controlled model, but with point forces applied to the four bolts at one end of the lattice.

Boundary Conditions: As per the displacement-controlled model, but without the axial displacement condition.

This FE modelling approach differs from that used by McHale *et al.* [155, 156]: their approach modelled one helix with suitable boundary conditions that mimicked the rest of the lattice, whereas our approach models all the helices of the lattice. While more computationally expensive and complex to build, our model enables a greater range of lattice designs to be investigated such as those with different layups and amounts of prestress in each helix, as well as investigate hinge friction and experimental effects (such as potential end effects from having a finite-length lattice).

As stated in Steps 4 and 5 in the list above, individual helices were rotated and assembled so that the bolt locations overlapped correctly, and wire features were created between corresponding bolt locations on the left and right-handed helices. As the lattices in this study always had nine bolts per hinge, alternative designs with mechanical prestress could be created by shortening the helix length, effectively reducing the bolt separation distance. In these cases the FE process is more complicated as two successive modelling steps were needed to assemble the lattice. One model used kinematic constraints to align the bolt locations, and a second model (with an initial state defined as the last step of the first model) to apply the wire features. See Appendix B: Mechanically-Prestressed Helical Lattice FE Modelling for a detailed description of how to construct these mechanically-prestressed models.

4.6 Results

4.6.1 Thermal Response

Figure 4.12 shows comparisons of predicted and measured lattice behaviour across all investigative approaches, plotted in terms of absolute lattice length (Figure 4.12a) but also in terms of lattice extension from a 135 °C benchmark (Figure 4.12b). As the absolute length measurements were sensitive to handling issues it can be helpful to compare the changes in length. Figure 4.12b shows the comparisons in temperature-extension behaviour between, analytical, experimental and FE methods. Three plots of FE-modelled lattices are presented: the standard 2D shell-based approach (10 mm wide strips with no joint friction); a pseudo-1D approach (0.5 mm wide strips with no joint friction) to better match the assumptions of the 1D analytical model; and a 2D model (10 mm wide strips with no joint friction) that includes gravitational loading and fixed-length (170 mm) "wires" to better represent the experimental conditions in the oven. Modelling these wires was important because they provide a resistive axial force and lift the lattice up against gravity as it extends. A plot of the mean experimental data is also included, as well as a region bounded by the maximum and minimum lattice extension values.

Four repeat experiments were carried out on the lattice, with the average starting length of the lattice recorded as 193.4 mm, with a coefficient of variation (CV) of 3.1% (defined as the standard deviation divided by the average). This is approximately 30 mm shorter than the "wired" FE predictions at this temperature. This could be the result of a systematic error when suspending the lattice in the oven, as the prototype had very low axial stiffness and was easy to unintentionally compress or extend when handled. The average starting temperature was 135.4°C.

Firstly it can be seen that there is a small discrepancy between the 1D analytical model and the pseudo-1D FE model. While the pseudo-1D model effectively neglects transverse curvatures, it differs from the 1D analytical model by still capturing membrane strains. The 2D analytical model includes this, but additionally it includes the transverse curvature effects. Comparing the relative difference from the 1D analytical model, it can be deduced that transverse curvatures effects have a slightly greater influence on the lattice extension than the membrane strain effects.

It can be seen that the 2D analytical model matches well with the predictions of the standard FE shell model as expected, but a discrepancy between these models and the experimental data does exist. When experimental conditions are included in FE models (*i.e.* gravitational and wire suspension effects are included), it can be seen that the FE approach captures the response of the prototype well. As the prototype had low-stiffness hinges and was made with thin strips (*i.e.* the thermally-induced axial forces were small), the gravity and wire effects had a large impact on

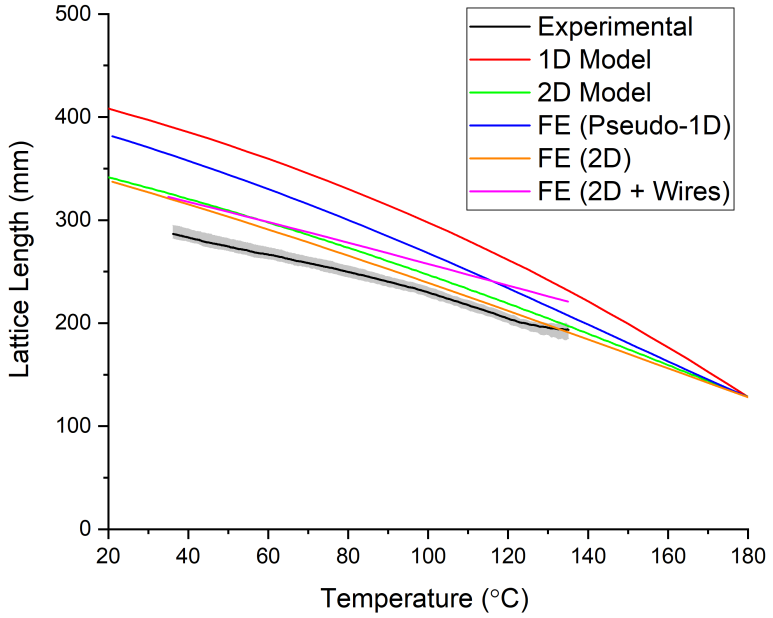

(a) *Comparison of all predicted and measured temperature-length responses*

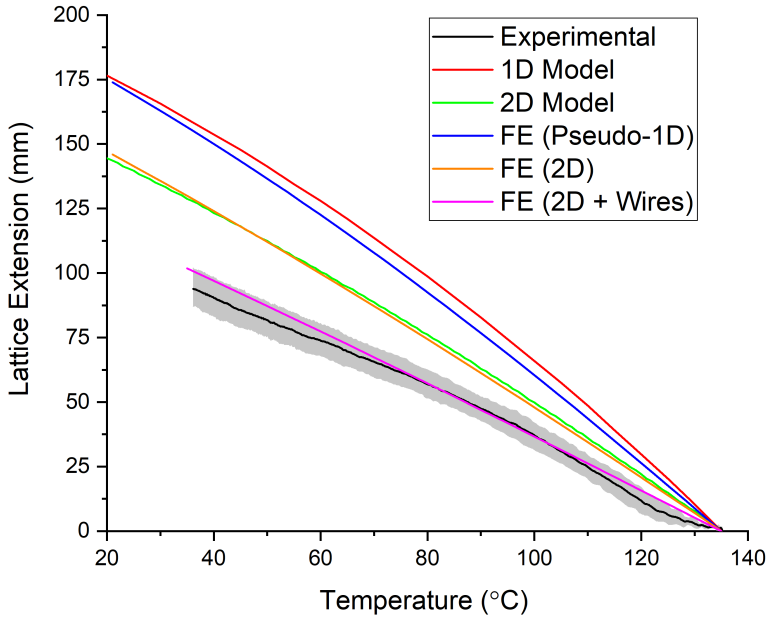

(b) *Comparison of all predicted and measured temperature-extension responses, with extension considered from the experimental 'hot' temperature (135°C)*

Figure 4.12: *Comparisons of predicted (analytical and FE) and measured lattice behaviour*

the overall prototype behaviour. Ignoring them in FE models results in large errors in predicted extension. Good agreement can also be seen between the 1D analytical model and the narrow (pseudo-1D) FE model, due to the FE model exhibiting minimal transverse curvature changes. As such it seems that the discrepancy between the original analytical model and the manufactured prototype behaviour can be attributed to a transverse effects and experimental conditions. The good match between the experiment and FE results shows that the FE models give reasonable predictions of the lattice behaviour, and can thus be used as a benchmark against the numerical models.

During experimental testing of the thermal expansion, the cylinder axial length was measured to be 286 mm at 309 °K, and 193 mm at 408 °K. This gives an effective thermal expansion coefficient for the helical structure of $-3285 \cdot 10^{-6} K^{-1}$ in terms of engineering strain, and $-3933 \cdot 10^{-6} K^{-1}$ in terms of logarithmic strain. The significance of this is clear when considering that these numbers are an order of magnitude larger than a previous benchmark extreme negative thermal expansion coefficient of $-204 \cdot 10^{-6} K^{-1}$ [39], demonstrating the potential of these tailored helical lattices to act as thermally-active structures.

4.6.2 Force-Displacement Response

Figure 4.13 shows the comparisons in force-extension behaviour between analytical, experimental and FE methods. When this lattice structure extends axially, it contracts radially. As such the cotton loops used to suspend the lattice were connected to the test machine on smooth steel rods to allow them to slide thereby minimising any unintended radial constraint. It was observed that when these mounting threads were placed vertically in the initial zero-extension state, they did not always slide along the steel rods smoothly, and slippage could occur at higher values of extension. As a result, a configuration was also tested where the threads were angled inwards at the zero-extension state to alleviate any potential slippage (see Figure 4.14). For the extension-force experiments, the average mounting thread angle was 23.8° for the angled tests and 1.7° for the vertical tests.

For the extension-force experiments with vertically-aligned mounting threads, the average zero-extension lattice length was 326 mm, with a CV of 1.3%. For the experiments with angled mounting threads, the average zero-extension lattice length was 329 mm (CV = 1.0%). For the extension-temperature experiments, the average initial (zero-extension) lattice condition was 188.5 mm (CV = 2.9%) at 135.4°C.

Good correlation can be seen between the FE and experimental results, with the vertically-aligned experimental data being closer to FE predictions. This is likely due to the angled wires exerting a radial force (not measured by the load cell) that

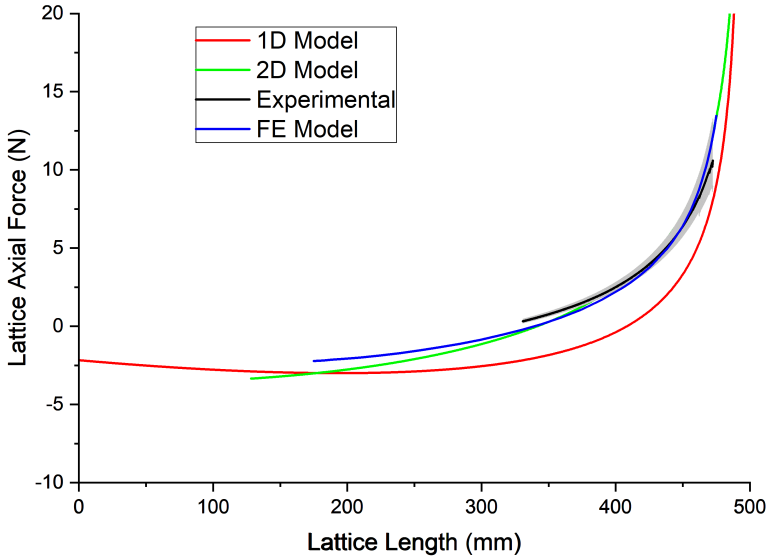

(a) *Comparison of FE predicted and vertically-measured force-extension responses*

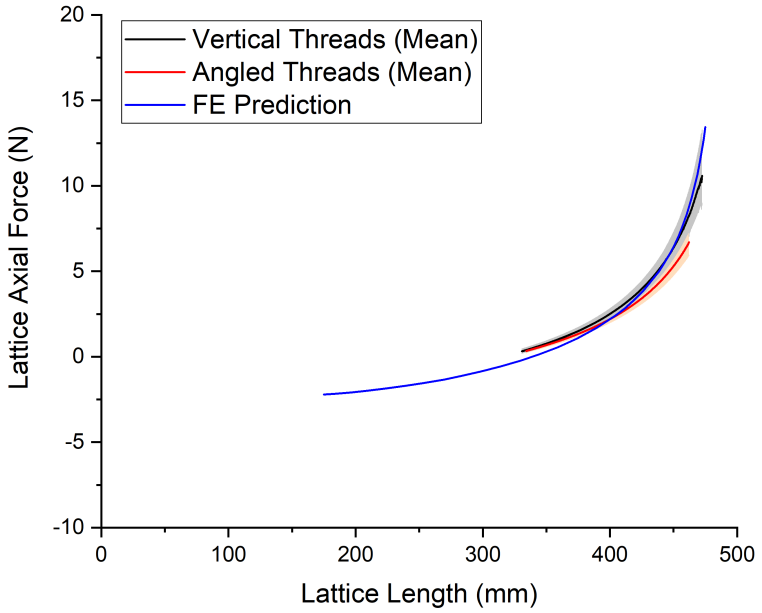

(b) *Comparison of FE predicted response with the measured force-extension responses for vertically-aligned and angled mounting threads*

Figure 4.13: *Comparison of FE and measured force-extension responses*

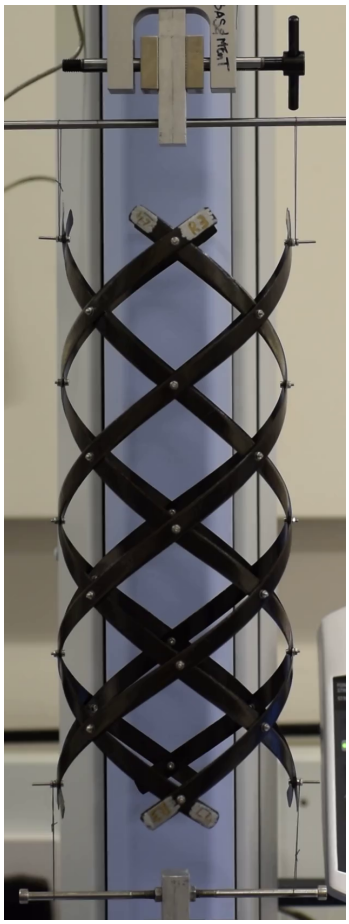

(a) *Vertical mounting threads*

(b) *Angled mounting threads*

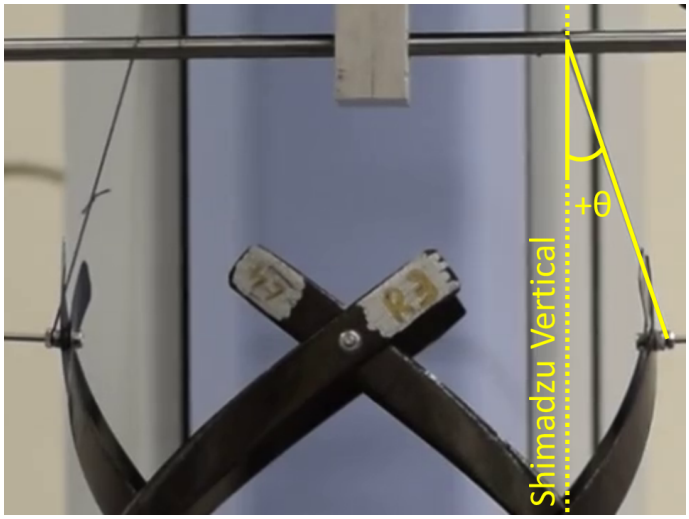

(c) *Mounting thread angle sign convention used in each test configuration*

Figure 4.14: *DSLR photos showing the test configurations used in the Shimadzu machine at their initial zero-extension states*

extends the lattice, causing the measured axial force to be reduced. The 'vertical' results are those shown in Figure 4.13a. The experimental prototype appears to be not as stiff as the FE lattice, particularly at longer lengths. The force-extension tests were conducted several days after the temperature-extension tests, potentially allowing time for moisture absorption and a reduction of the thermal prestress to have taken place in the prototype, although further characterisation of the lattice prototype's time-dependant behaviour is required to verify this discrepancy.

4.7 Parameter Sensitivities

One additional motivation for developing FE models of the lattice structures was to create a virtual environment where parameter sensitivities could be investigated without costly and time-consuming manufacturing. This allowed the investigation of effects not captured by the analytical, as well as validate assumptions around transverse curvatures in the strips and the effect of helix dimensions.

Figures 4.15 and 4.16 show comparisons of FE-predicted lattice axial lengths against temperature for variations of the optimised lattice design. Unless otherwise specified the design parameters were kept consistent throughout the sensitivity investigation, as detailed in Table 4.1. Figure 4.15a shows the effects on the temperature-extension behaviour of changing joint types and helix lengths (*i.e.* the total angle of revolution in each helix), with the lattice length reported divided by the number of revolutions in the corresponding helices (*i.e.* the 1080° lattices have three full revolutions, so the total lattice lengths are three times larger than shown in Figure 4.15a). It was observed in prototypes that the normals of the strips at the bolted connections would not longer align near the bolts at the ends of the lattice, so these models were built to investigate these "end-effects". Initially joints were modelled as hinges (*i.e.* only radial rotation was permitted), shown with the solid lines, but FE models were also built with pin joints, shown by the dashed lines (*i.e.* rotations could occur about any axis). In terms of helix lengths, an initial 360° helix of 128 mm axial length was compared to lattices with helices of double and triple length (*i.e.* two and three full rotations). Slightly larger extensions occur when modelling the joints as pins (*i.e.* where non-radial rotation is permitted), likely due to the helices being allowed to extend further via twisting, but that the difference in extension between the hinge and pinned models is not significant for most of the temperature range tested. This difference is constant across the two longer lengths, but appears greater in the shorter lattice (the 360° case), suggesting edge effects may be more dominant in lattices with helices shorter than one full rotation.

Figure 4.15b shows the effect of changing the width of the composite helices, while still maintaining a 2D structure. Values between 5 mm and 15 mm were inves-

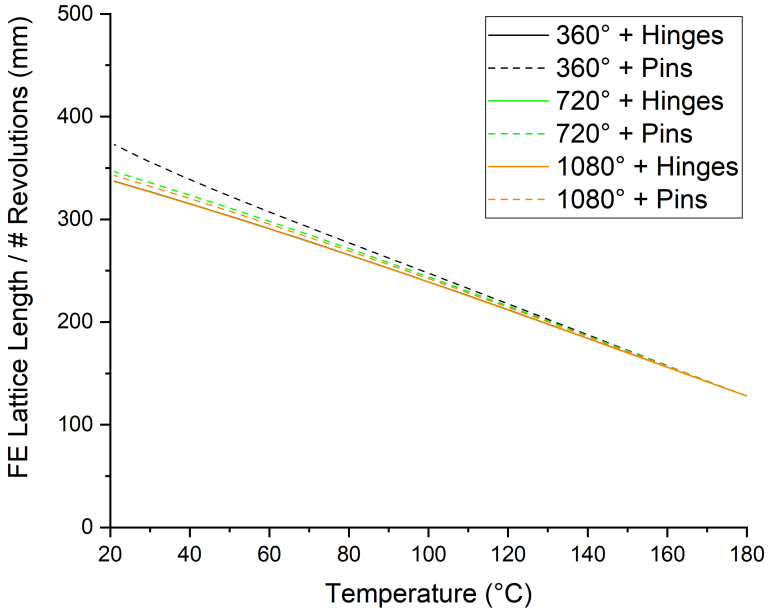

(a) *Temperature-extension response with joint types and helix lengths*

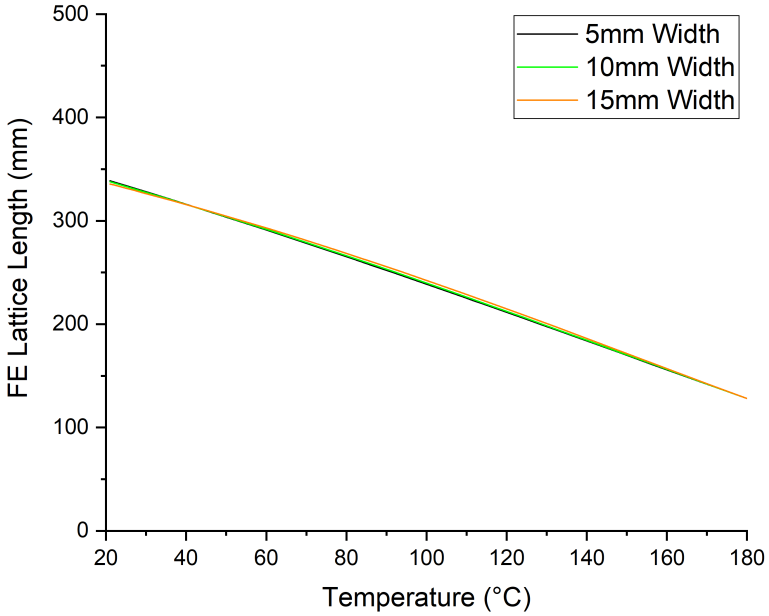

(b) *Temperature-extension response with different helix widths*

Figure 4.15: *FE temperature-extension behaviour with varying geometric parameters for the optimised lattice*

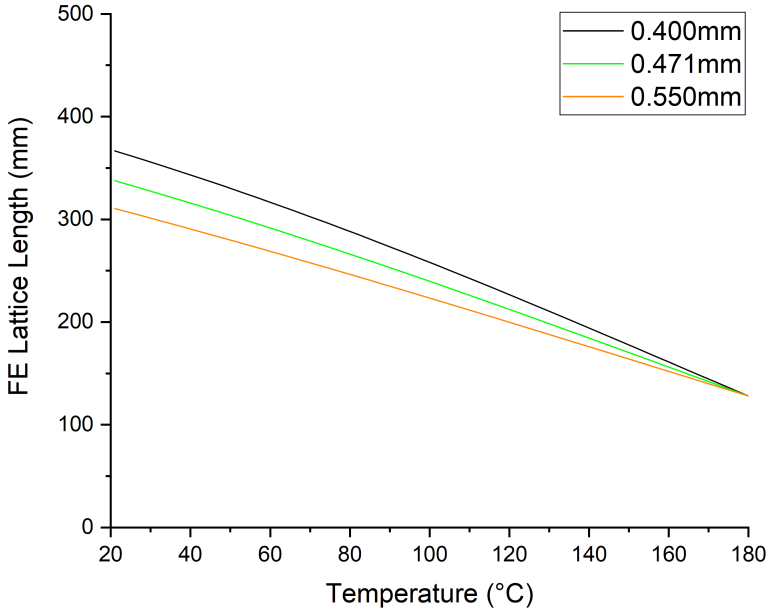

(a) *Temperature-extension response with different total ply thicknesses (assuming all constituent plies have equal thickness)*

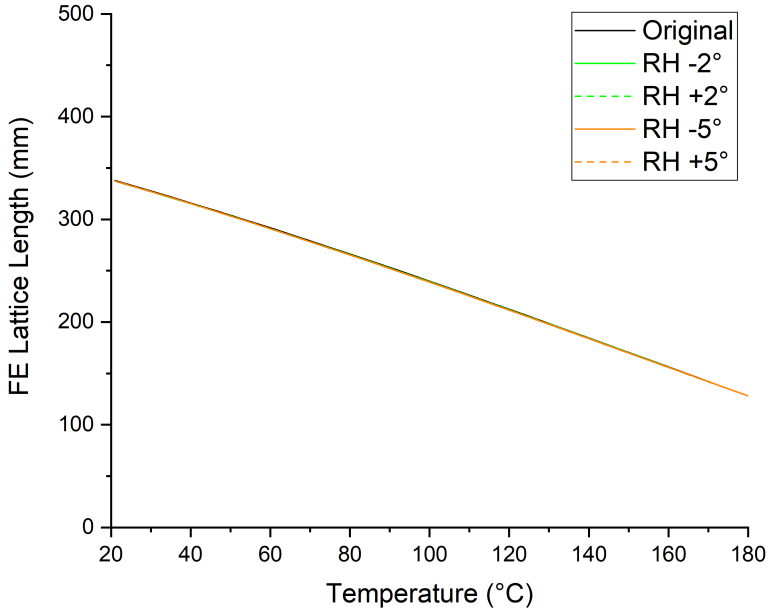

(b) *Temperature-extension response for different levels of ply misalignment*

Figure 4.16: *FE temperature-extension behaviour with manufacture-induced parameter variations for the optimised lattice*

tigated, as this range of widths could be manufactured manually without difficulty, and produce helices that has sufficiently low axial stiffness as to be handled safely. McHale *et al.* showed that for lattices $\geqslant$10 mm wide transverse curvature effects can become significant [156]. For our design it can be seen that there is only a very small reduction in total contraction for these widths, and only a slight increase in behavioural nonlinearity as the width increases. More extreme helix aspect ratios may yield greater variations in behaviour - especially for very small widths where the helices act like 1D structures - but would far more difficult to manufacture.

4.7.1 Manufacturing Effects

Figure 4.16a shows the effects of changing the ply thicknesses of the laminates. Micrograph measurements of ply cross sections revealed average prototype helix thicknesses of 117.7 μm with a standard deviation of $\pm$9.8 μm (see Appendix Helical Lattice Ply-Level Thickness Measurements). Values of total (4-ply) laminate thickness between 0.400 mm and 0.550 mm were chosen based on these ply-level measurements by uniformly changing the individual ply thicknesses. Lattice contraction can be seen to be very sensitive to laminate thickness, with almost 75 mm less contraction for only 0.150 mm additional thickness. While thickness variations of this magnitude are likely to be localised effects, and not across the entire lattice, controlling laminate total thickness should be considered one of the main manufacturing concerns when making these thin-shell structures.

Figure 4.16b shows the effects of ply misalignment - a common source of manufacturing error. Uniform orientation misalignments of $\pm2^\circ$ and $\pm5^\circ$ were added to the composite layup orientations. During skilled manual layup of thin-shell structures the standard deviation of ply misalignment is around $\pm2^\circ$ [231]. Misalignments are only likely to be of similar magnitude and direction for all plies in the laminate in the case of ply-cutter error, but this systematic error approach can model the cumulative effect of this error. In this case it can be seen that for misalignments of this magnitude the lattice structure exhibits very robust behaviour.

4.7.2 Transverse and Frictional Effects

Two key assumptions of the initial analytical model were firstly that the lattice structure is constructed of 1D beam elements (with no transverse curvature), and secondly that the joints between the helices have no size or frictional effects. Another motivation for building FE models of the lattice structures was to investigate the limits of these analytical assumptions. Figure 4.17 shows results from FE models that include transverse curvature not captured by 1D beam models, and Figure 4.18 shows results from FE models that include frictional effects (to more realistically

model the lattice hinges).

Figure 4.17a shows the changes in transverse curvature in a central section of the lattice as it is cooled from cure temperature to room temperature. These curvature changes are plotted along the width of the section, with the 0 mm distance representing the helix centre line. The transverse curvature changes are plotted for a location close to a central bolt hole, at the middle distance between two central bolt holes, and at a point a the quarter distance between two central bolt holes. It can be seen that the changes in curvature that occur during the analysis are smaller along the edges of each helical strip, and that a fairly uniform transverse curvature builds along the strip widths during cooling. The discontinuity at the transverse edges suggests the need for finer meshing to capture curvature changes here. The magnitude of curvature change also appears to be consistent between the different locations along the strip. The discontinuity on the "Bolt" plot is a numerical artefact resulting from taking a measurement from a node in close proximity to a connector.

Figure 4.17b is similar to Figure 4.17a, except that here transverse bending moments are plotted for the same locations. It shows a similar pattern to Figure 4.17a in that transverse moments remain largely consistent between different locations along the strip length. A discontinuity can also be seen when taking measurements near the bolt connector, although the magnitudes of moments appear to be consistent in this location also. Theoretically Figure 4.17b should be linearly proportional to Figure 4.17a, and this would likely occur if the edge discontinuity effect in Figure 4.17a was not present.

Figure 4.18a shows the variation of total lattice length against temperature when hinge friction moments are included, and when no hinge friction moment is included. Two values of hinge moment are included (7.29 Nmm and 1.23 Nmm) that are the maximum and minimum friction moment values measured experimentally. Including the maximum value of friction results in a reduction in extension of approximately 10 mm due to a slipping effect at the start of the lattice cool-down. It was observed in experiments that the bolts loosened after a short extension, meaning the lower value of friction is more applicable, and that the joints may behave less like 'pure' hinges in the prototypes. As such frictional effects can be considered to have a negligible effect on temperature-extension behaviour.

Figure 4.18b is similar to Figure 4.18a, except that the variation in axial reaction force is plotted against total lattice length for the range of friction moment values. A similar effect can be seen in that the lower - and more applicable - value of friction has a very small effect on the total response. If the design were revised to include locking nuts at the bolt joints then frictional effects may be significant, but in the current design configuration this is not the case.

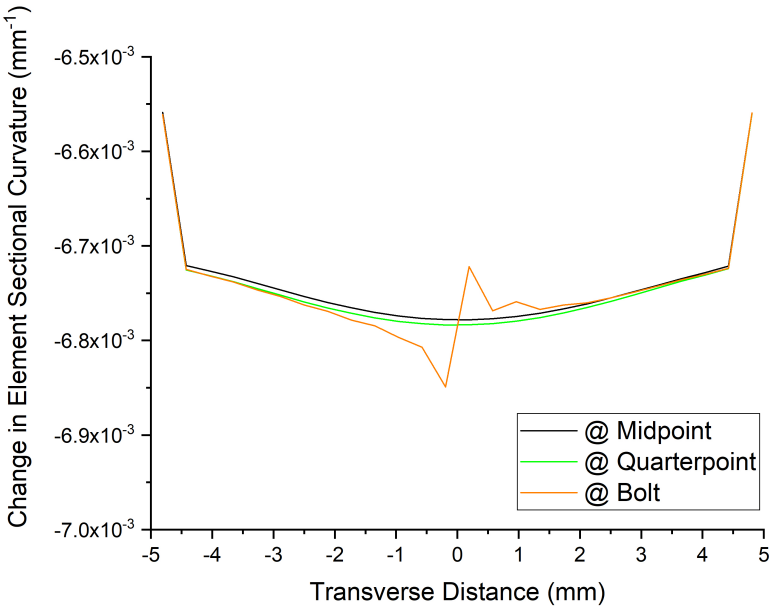

(a) *Changes in transverse curvature across helix width at different locations*

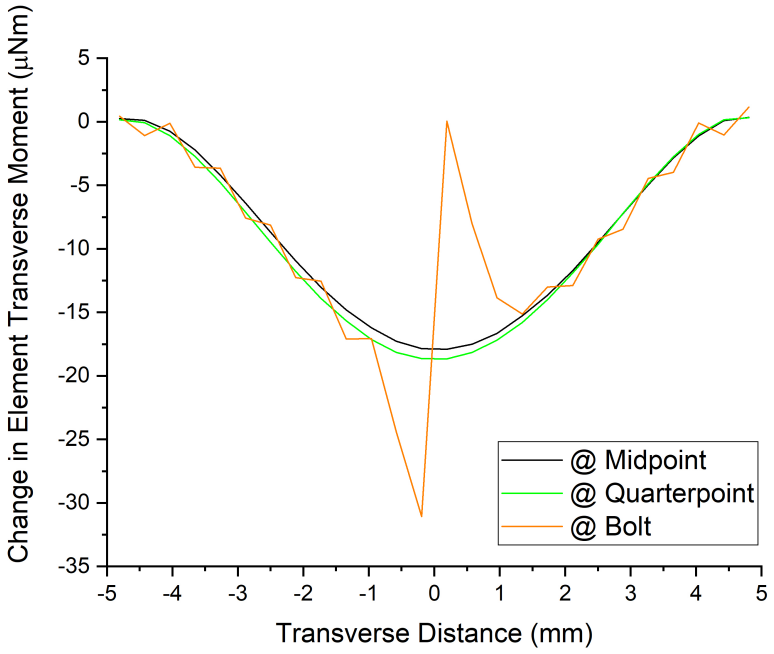

(b) *Changes in transverse moment across helix width at different locations*

Figure 4.17: *FE predictions of the transverse curvature changes and bending moment distributions*

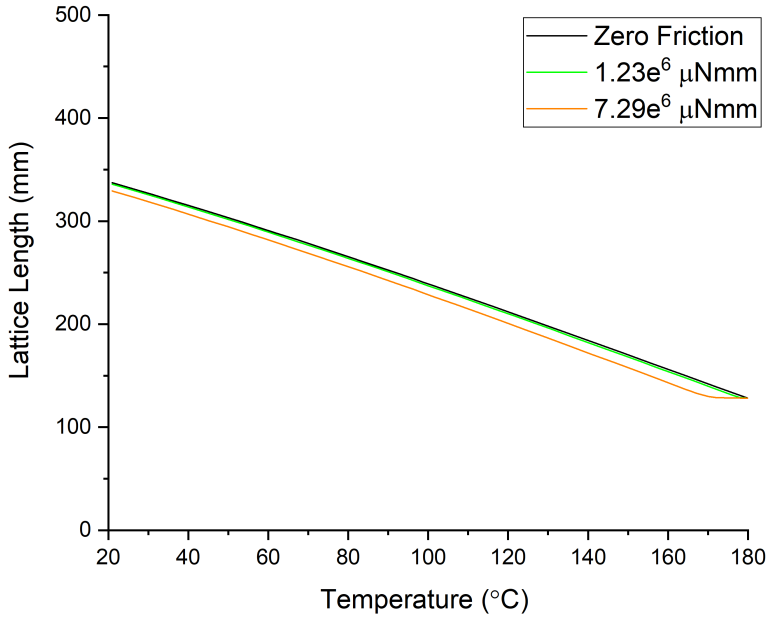

(a) *Temperature-extension behaviour for different values of hinge friction*

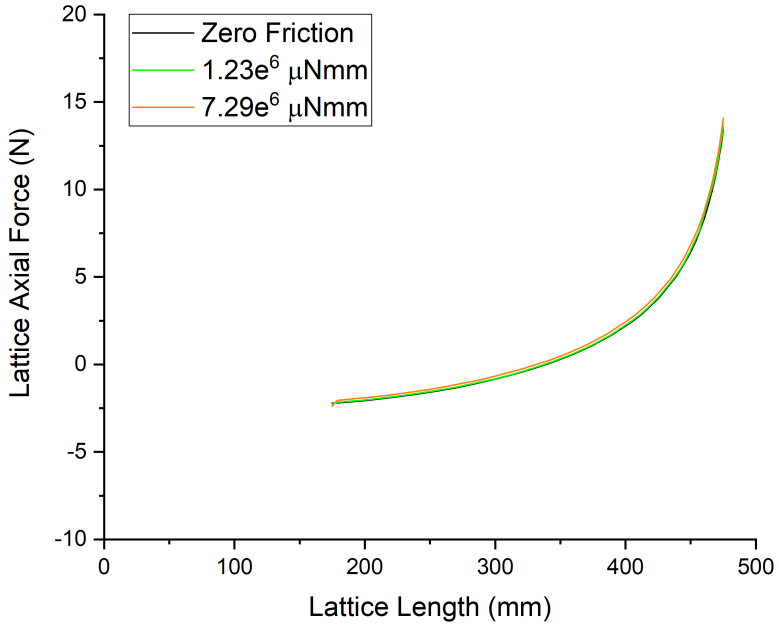

(b) *Force-extension behaviour for different values of hinge friction*

Figure 4.18: *FE predictions of frictional effects on lattice behaviour*

4.8 Alternative Lattice Designs

The work detailed in this chapter primarily focused on a proof-of-concept lattice with negative thermal expansion which was as simple to manufacture as possible. While there were challenges in correctly modelling and manufacturing the lattice, the huge negative CTE that (measured in excess of $-3000 \cdot 10^{-6} K^{-1}$) it achieved demonstrated the value in investigating prestressed composite lattices. The helical lattice structural concept can be tailored for other novel behaviours though, particularly if manufacturing constraints are eased and additional prestress can be incorporated into the design.

4.8.1 Including Mechanical Prestress

Figure 4.19 shows temperature-extension behaviour and energy landscape predictions for an alternative lattice that includes a degree of mechanical prestress. By ensuring that the assembly geometry of the helices is different to their geometry when cured, a mechanical prestress can be added to the system on top of the thermal prestress from the cure cycle. This additional prestress expands the lattice behaviour design space.

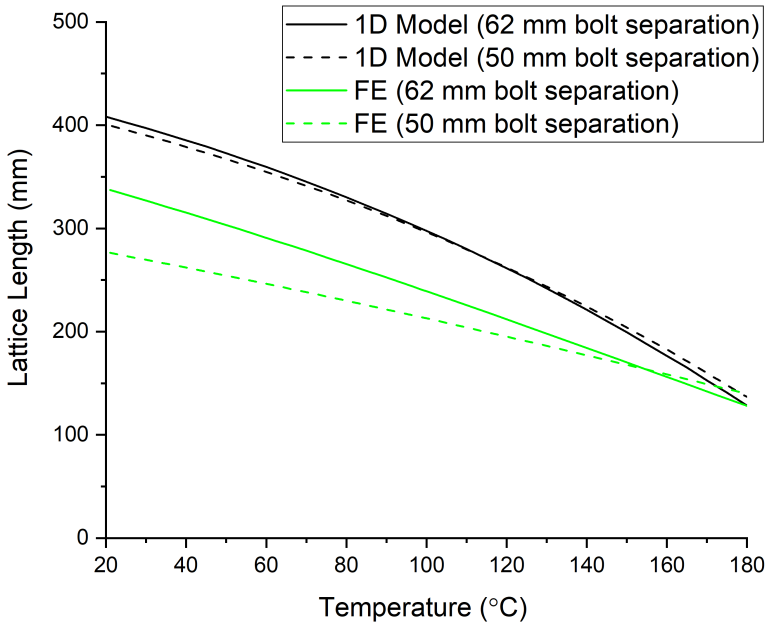

Figure 4.19: *Comparisons between the prototype helix design and an alternative helix with a reduced* 50 mm *bolt separation distance*

Figure 4.19 shows comparisons between the behavioural predictions of the prototype lattice and a mechanically-prestressed lattice where the bolt separation has been reduced from 62 mm to 50 mm. A bolt separation of 62 mm corresponds to a lattice length that, when assembled, possesses an equilibrium position that corre-

sponds to the cylindrical tool radius - *i.e.* there is no mechanical prestress. In this particular case it can be seen that reducing the bolt separation (*i.e.* constraining the helices to a smaller radius cylinder during assembly) reduces the total lattice extension. It can also be seen that the discrepancy between the 1D analytical model and the FE is greater with the reduced bolt separation (*i.e.* when a degree of mechanical prestress is present). As the 1D model has been shown to not capture transverse effects well, this suggests that this form of mechanical prestressing has a significant effect on the transverse curvatures and membrane stresses of the lattice.

Mechanical prestress can also be imparted more radically, for instance by changing the angle at which the helix strips are placed upon the tool. When using a cylindrical tool an extreme case of this involves reversing the sign of the tool angle, *i.e.* curing a right-handed helix, but assembling it as a left-handed helix. This method is difficult to manufacture without delamination as inverting the helix curvature induces high strains. Additionally it is not a trivial process to model with finite-element methods and was thus beyond the scope of this work.

4.8.2 Designing for Novel Thermal Effects

Smooth expansion and contraction is not the only lattice behaviour that can be designed for, especially when the design space has been increased with the addition of mechanical prestress. The stable states of the lattice structure can be tailored, for instance by combining mechanically-prestressed helices made with non-symmetric angle-ply laminates (that will have temperature-dependant curvatures) and anti-symmetric laminates. Figure 4.20 shows the energy landscapes obtained from FE models for designs that have been tailored with mechanical and thermal prestress to have temperature-dependant stability behaviour: bistable at low temperatures, and monostable at high temperatures. Black dots indicate stable lattice lengths, and arrows indicate the lattice deformation path when heated from 0°C.

Figure 4.20a depicts the energy landscape of a lattice comprised of non-symmetric angle-ply laminates. Designs were trialled by taking [0 90] cross-ply laminates and changing their orientation (*i.e.* adding a set angle to each ply) and degree of anisotropy (*i.e.* reducing the relative angle between the two plies). A design was found where the four right-handed helices have [0 70] layups, and the four left-handed helices have [5 65] layups, with the lattices assembled together with a 50 mm bolt separation to induce mechanical prestress (in the same manner as the lattices in Figure 4.19). It can be seen that as the lattice is heated, the stable length reduces smoothly until the lattice is fully-contracted. The fully-contracted state is stable for all temperatures within the tested range, so cooling the lattice after is has been heated will not result in an equal-and-opposite extension, *i.e.* the lattice's stabil-

ity path is dependant on its initial length and temperature, and above a certain temperature the lattice is 'locked' into a monostable state.

Figure 4.20b depicts the energy landscape of a lattice comprised of unbalanced cross-ply laminates and anti-symmetric laminates. The four right-handed helices have [0 90 90] layups, and the four left-handed helices have [-45 90 -45] laminates. The mechanical prestress is also the same as before. It can be seen that as the lattice is heated the stable length changes suddenly between fully-extended, and fully-contracted. At low temperatures the energy curves possess a small peak when the lattice is highly extended, causing its fully-extended configuration to be stable. As the rest of the energy curve has a positive slope at all temperatures, the lattice returns immediately to a fully-contracted state when the increasing temperature causes the small peak to disappear, demonstrating a novel hysteretic behaviour.

These design landscapes complement the hysteretic lattice behaviours found with the 1D model in Ref [175]. They also complement the findings of similar research that was independently published by researchers in Limerick at the same time this work was being carried out [155].

4.9 Final Remarks

Using prestressed composite materials in thin-shell structures offers unique ways to tailor their active behaviour, and this can enable design spaces for some structures that possess extreme behaviour beyond that seen in natural materials and systems. The work detailed in this chapter has demonstrated, at the macroscopic length scale, a prestressed composite cylindrical lattice structure tailored for an extreme negative thermal expansion coefficient. A prototype exhibiting the desired behaviour was manufactured and tested successfully, and it was shown that lattices with other thermally-dependant stability responses are feasible. Prototype manufacturing methods have been refined, and new ways of analysing such structures in FE environments have been presented.

As well as being realisable, these structures have also been shown to be predictable with FE models. Good correlation exists between experimental and FE approaches when comparing temperature-extension and force-extension behaviour of the negative thermal expansion lattice. While 2D analytical models that considered transverse curvature effects matched well with results from FE lattice models, it was found that prototype behaviour is sensitive to gravitational effects (due to the low joint friction and axial forces involved). A series of FE analyses have been extended to quantify discrepancies between analytical beam-based lattice models and experimental shell-based prototypes, as well as assess the parameter robustness of a particular design.

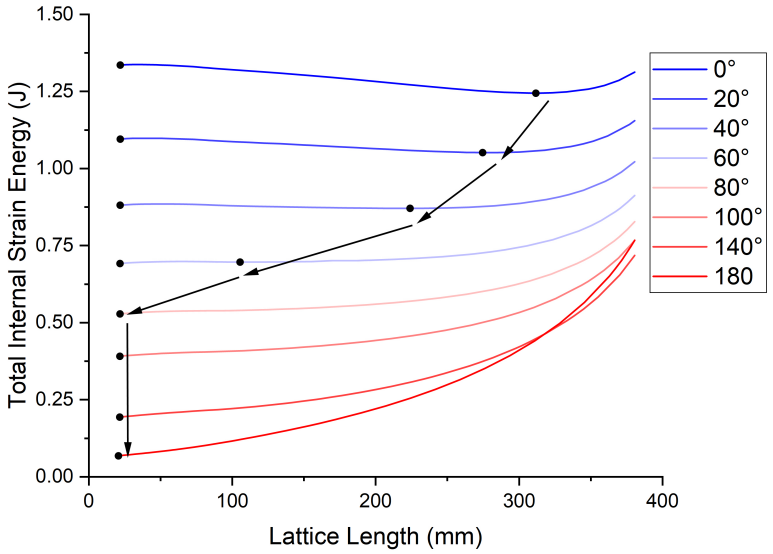

(a) *Lattice designed to be bistable at low temperatures and monostable at high temperatures, with the lattice undergoing a smooth contraction when heated*

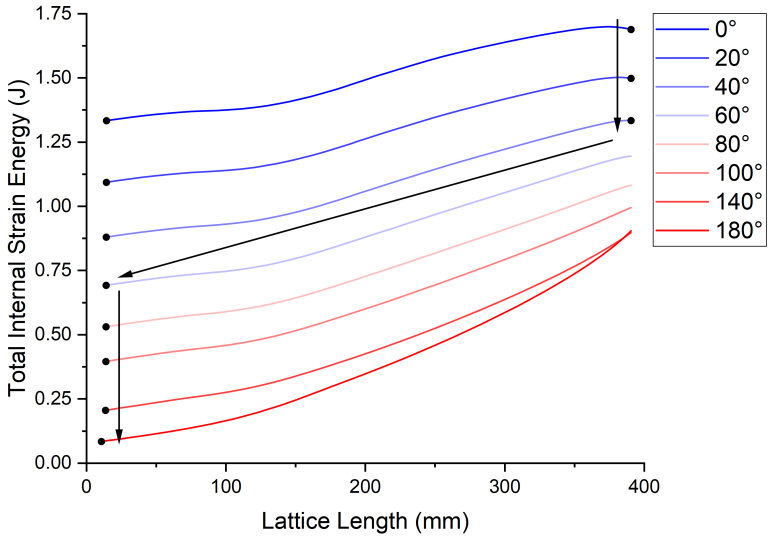

(b) *Lattice designed to be bistable at low temperatures and monostable at high temperatures, with the lattice undergoing a sharp 'snapping' contraction when heated*

Figure 4.20: *FE energy-temperature landscapes for lattices designed to exhibit thermally-dependant stability behaviours. Black dots indicate stable lattice lengths, and arrows indicate the lattice deformation path when heated from 0° C.*

A more general (*i.e.* not design-specific) study of the sensitivities of helical lattice behaviours is required if these structures (and their extreme behaviours) are to be used in deployable applications. Specifically thickness variation effects can have significant impacts on the lattice behaviours, and a more mature understanding of the expected thickness distributions and their effects on the lattice performance and failure would be valuable. This is particularly important with shell structures as small changes in the shell properties can have large behavioural effects due to the inherent high strains and nonlinearity in the deformation [164]. Further work to quantify the lattice failure limits (when assembled with high-strain mechanical prestressing) and how they affect the available behaviour design spaced would also be beneficial.

4.10 Next Steps

After assessing the thermal tailoring of a simple tape spring in the previous chapter, the work in this chapter set out to assess the feasibility of tailoring the active behaviour of a more complex composite shell structure using a combination of thermal and mechanical prestress. This combined prestress has been shown to enable extreme behaviours for the helical lattice structure, but the tailoring process itself is still reliant on the use of optimisation tools. While analytical models and FE parameter sensitivity studies provide some lattice behavioural insight to the designer, these insights are so far valid only for the design chosen. Identifying which design parameters and prestress state will give a particular behaviour is a complex question that remains largely unanswered. This leads to two design questions:

1. Is there a method for characterising the behaviour of composite shells that gives more intuitive behavioural insight to the designer than using an optimisation toolbox?

2. If so, can such a technique be applied to a general range of shell geometries to reduce reliance on the assumptions of analytical models?

The next chapter will explore the application of a robotic mechanism characterisation technique to composite shells in an attempt to improve intuitive understanding of compliant shell behaviour by considering the response of a single point of interest on the shell.

Chapter 5

Characterising Composite Shells: A Mechanisms Approach

In the previous chapter it was shown that thermal and mechanical prestress could be used to develop novel responses in a composite helical lattice structure. While the lattices are more complex structures than the tape spring mechanisms from Chapter 3, their structural responses could be determined similarly by analytically and numerically evaluating their internal strain energy states. Although this technique is valuable for compliant shell mechanisms with simple deformation modes (*e.g.* torsion of tape springs, or axial expansion of lattices), it does not necessarily give complete insight into the mechanism behaviours. It was therefore of interest to develop a technique to characterise the principal behaviours of a more general class of composite compliant shell mechanisms. To this end a collaboration with Prof. Charles Kim at Bucknell University was carried out to characterise and visualise the behaviour of generic compliant composite shells using a technique used in building block mechanism design approaches that was developed by Lipkin and Patterson [142–145, 179, 180], and extended by Leemans *et al.* [139]. In addition, a link between these concepts and the classical structural mechanics concepts of shear and twist centres is shown analytically for a simple structure.

Some work in this chapter was presented in a paper at ASME IDETC 2020 (Virtual Conference) [229], and other work presented here was first published in the journal Thin Walled Structures [226]. This chapter is based primarily on these sources where the author was the prime contributor to the literature reviews, analytical investigations and numerical modelling.

5.1 Introduction

The analysis and visualisation technique presented herein is based on the eigen-decomposition analysis framework developed by Lipkin and Patterson, which is often used in the building block method of compliant mechanism design [110]. This section will outline the important details of their decomposition, but for full details, derivations and related theorems the reader is directed to Refs. [143, 180]. In this framework, screw theory is utilised to determine the principal compliance directions (and associated magnitudes) of an elastic mechanism. This mechanism characterisation is conducted through analysis of the tangent stiffness matrix (derived from nonlinear finite element analysis) of a single point of interest (POI) lying on the mechanism. Typically the point that best represents the required deformation of the mechanism is chosen as the POI, *e.g.* an end-effector on a robotic arm. As the mechanism undergoes large, nonlinear elastic deformations, the orientations, positions and magnitudes of principal compliance directions are tracked. These may be plotted and compared throughout the mechanism's large deformation (see Ref. [139] for an example of this characterisation for isotropic shells). This method can be summarised as follows:

1. A point of interest is identified on the mechanism, the kinetic and kinematic behaviour of which is to be analysed;

2. The 6×6 tangent stiffness matrix of this point is identified, typically via a linear perturbation numerical analysis;

3. The locations, orientations and compliance magnitudes of the principal compliance directions of the point of interest are determined from this matrix;

4. Further infinitesimal perturbation analyses are conducted at multiple stages of a desired mechanism deformation;

5. The principal compliance directions are compared for each step of the deformation analysis, granting intuitive insight into the mechanism behaviour;

6. The changes in orientations and locations of the twist and wrench axes are visualised throughout the deformation of the mechanism.

The approach is advantageous in providing detailed physical insight into the behaviour of the mechanism since the different degrees of freedom of the POI can be readily interpreted with minimal knowledge of mechanism design. Each compliance axis describes a direction along which a load will induce a pure translation (or a moment induces a pure rotation) or vice versa, which makes interpretation of the mechanism response much more intuitive. Insight can be gained at any point in the

deformation of a mechanism, and for a broad variety of mechanism geometries, as it considers the response of a suitably-chosen POI. It lends itself well to the analysis of shell mechanisms, which can then form part of a mechanism library for building block mechanism design techniques. Despite these advantages, to the best of the author's knowledge, this technique has not previously been applied to anisotropic composite shells. Indeed, the use of composites in the design of any kind of compliant mechanism is currently under-utilised, with the limited previous research restricted to planar mechanisms [140, 240].

Other mechanism design and characterisation approaches exist (*e.g.* the Freedom And Constraint Topologies (FACT) and rigid-body replacement approaches reviewed in Chapter 2) but these often focus on planar (2D) mechanisms or finding suitable mechanism shapes and topologies. With composite shell mechanisms the material and prestress choices available mean that mechanisms with identical geometry can potentially exhibit radically different behaviours. As such, design approaches that search for topologies or model flexures as simple torsional springs may not fully capture the potential that composite anisotropy offers to the mechanism designer. In contrast, a building block design approach using Lipkin and Patterson's eigenscrew characterisation offers a powerful design and analysis method for composite compliant shell mechanisms.

The chapter starts firstly by explaining the theory and mathematics underpinning Lipkin and Patterson's eigenscrew characterisation, including how they are calculated from the global stiffness and compliance matrices of a compliant mechanism. Next a mathematical link is derived between eigenscrews and two classical structural mechanics concepts: shear centres and centres of twists. This link is shown for a simple structural case, and helps illustrate how to interpret the behaviour of a mechanism that is characterised using eigenscrews. Finally the eigenscrew characterisation and visualisation framework is applied to a simple tape spring mechanism, and comparisons are drawn between isotropic and anisotropic composite tape springs to demonstrate the useful insight that this framework provides into the behaviour of composite compliant shell mechanisms.

5.2 Eigenscrew Analysis

This section provides details about the nature of eigenscrews and how they relate to the global stiffness and compliance matrices of a compliant mechanism.

5.2.1 Wrenches and Twists

Lipkin and Patterson's technique builds on Chasles' Theorem [29] which states that any movement in three dimensional space can be described by a translation along a line plus a rotation about the same line. In this framework the kinetics of a body are expressed as a three-system of vectors that combine the forces and moments acting on and about a common axis. This is known as a wrench,

$$\boldsymbol{w} = \begin{bmatrix} \boldsymbol{f}_i \\ \boldsymbol{\tau}_i \end{bmatrix} = \begin{bmatrix} \boldsymbol{f}_i \\ (\boldsymbol{b}_i \times \boldsymbol{f}_i) + d_i \boldsymbol{f}_i \end{bmatrix}, \tag{5.1}$$

where $\boldsymbol{f}_i$ and $\boldsymbol{\tau}_i$ are the linear force and angular torque components of the wrench respectively, the $\boldsymbol{b}_i$ terms determine the spatial positioning, and d_i the ratios of torque and force. The subscript $i \in [1, 2, 3]$, distinguishes each orthogonal wrench axis.

Similarly, the kinematics of the body can be expressed in terms of a three-system of vectors that combine translations and rotations about a common axis. This is known as a twist,

$$\boldsymbol{T} = \begin{bmatrix} \boldsymbol{\delta}_i \\ \boldsymbol{\gamma}_i \end{bmatrix} = \begin{bmatrix} (\boldsymbol{r}_i \times \boldsymbol{\gamma}_i) + h_i \boldsymbol{\gamma}_i \\ \boldsymbol{\gamma}_i \end{bmatrix}, \tag{5.2}$$

where $\boldsymbol{\delta}_i$ and $\boldsymbol{\gamma}_i$ are the translation and rotation components of the twist, $\boldsymbol{r}_i$ the location vector (taken as the shortest (*i.e.* perpendicular) distance between the twist vector and the POI) and h_i the pitch scalar with i distinguishing between orthogonal twist axes. Figure 5.1 (reproduced from Ref. [139]) shows a visualisation of a twist axis and its terms relative to a global axis.

Typically used in the analysis of robotic systems, these wrenches and twists are scalar multiples of screws, *i.e.* scalar multiples of 6D vectors comprising the two 3D vectors of linear and angular information of a rigid body [8]. A wrench (*i.e.* a torque and/or force) applied on a POI will produce a twist (*i.e.* a translation and/or rotation). Typically these POI's are the end-effectors of robotic systems, but any class of mechanism can be analysed by considering a POI on the mechanism, as the wrenches and twists are linked by the stiffness and compliance matrices.

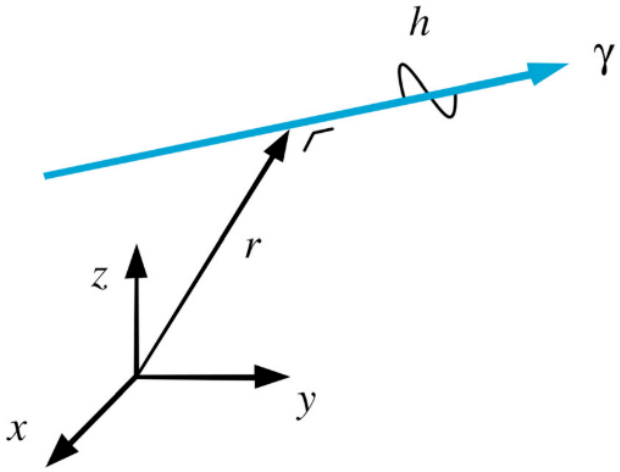

Figure 5.1: *Representation of a twist axis (in blue) in vector form. Reproduced from Ref [139].*

5.2.2 Eigenwrenches and Eigentwists

Lipkin and Patterson's decomposition produces six "eigen-screws" that characterise the principal behaviour of the POI: three pure translation screws and three pure rotation screws as well as their corresponding stiffness or compliance magnitudes. These eigenscrews are, $\boldsymbol{w}_f$, the "eigen-wrenches" (also known as wrench axes), and $\boldsymbol{T}_\gamma$, the "eigen-twists" (also known as twist axes). Applying an eigenwrench, $\boldsymbol{w}_f$, along its axis will cause a pure parallel translation of the POI (and vice versa), while applying an eigentwist, $\boldsymbol{T}_\gamma$, around its axis will cause a pure parallel moment to occur at the POI (and vice versa). This is valid for small translations and rotations, and assumes some rigid link exists between the POI and the axis where the eigentwist or eigenwrench is applied. Once derived, these eigenscrew axes can be plotted on a compliant mechanism to visualise its instantaneous behaviour, with each axis identifying a direction in which the mechanism can be loaded to induce pure translations (or rotations in the case of twist axes) and vice versa. The following subsection contains the mathematical derivation from Ref. [143] to help explain the origin of these special screws via the solution of an eigenvalue problem.

Applying a wrench to a rigid body (in a stable potential energy field) induces a twist upon that body and vice versa. We wish to identify the wrenches that induce twists of pure parallel translations and rotations, and twists that induce pure parallel forces and moments. By definition, these eigenwrenches and eigentwists would induce corresponding twists and wrenches that minimise the potential energy of the system as there is no coupling between translational and rotational response. Eigenvalues represent the stationary states of systems, and two eigenvalue problems can be generated by considering the minimum potential energy and by requiring the

wrenches and twists to have unit magnitude, *i.e.*

$$\text{Minimise} : PE = \frac{1}{2}\boldsymbol{w}^T\boldsymbol{C}_t\boldsymbol{w} \tag{5.3}$$

$$\text{Subject to} : \boldsymbol{w}^T \begin{bmatrix} \boldsymbol{I} & 0 \\ 0 & 0 \end{bmatrix} \boldsymbol{w} = 1 \tag{5.4}$$

and

$$\text{Minimise} : PE = \frac{1}{2}\boldsymbol{T}^T\boldsymbol{K}_t\boldsymbol{T} \tag{5.5}$$

$$\text{Subject to} : \boldsymbol{T}^T \begin{bmatrix} 0 & 0 \\ 0 & \boldsymbol{I} \end{bmatrix} \boldsymbol{T} = 1 \tag{5.6}$$

where PE refers to the system potential energy and $\boldsymbol{K}_t$ and $\boldsymbol{C}_t$ are the 6×6 tangent stiffness and compliance matrices for the POI respectively.

The two generalised eigenvalue problems in the form $\lambda Bx = Ax$, from Equations 5.3–5.6 can be written as

$$\boldsymbol{a}_f \begin{bmatrix} \boldsymbol{I} & 0 \\ 0 & 0 \end{bmatrix} \boldsymbol{w} = \boldsymbol{C}_t\boldsymbol{w}, \tag{5.7}$$

and

$$\boldsymbol{k}_\gamma \begin{bmatrix} 0 & 0 \\ 0 & \boldsymbol{I} \end{bmatrix} \boldsymbol{T} = \boldsymbol{K}_t\boldsymbol{T}, \tag{5.8}$$

where $\boldsymbol{a}_f$ and $\boldsymbol{k}_\gamma$ are the eigenvalues corresponding to the translational compliance of the eigenwrench and rotational stiffness of the eigentwist respectively. Note that $\boldsymbol{k}_f = 1/\boldsymbol{a}_f$ and $\boldsymbol{a}_\gamma = 1/\boldsymbol{k}_\gamma$. When $\boldsymbol{C}_t = \boldsymbol{K}_t^{-1}$ (*i.e.* the tangent matrices are non-singular) these can also be written as,

$$\boldsymbol{k}_f\boldsymbol{w} = \boldsymbol{K}_t \begin{bmatrix} \boldsymbol{I} & 0 \\ 0 & 0 \end{bmatrix} \boldsymbol{w}, \tag{5.9}$$

and

$$\boldsymbol{a}_\gamma\boldsymbol{T} = \boldsymbol{C}_t \begin{bmatrix} 0 & 0 \\ 0 & \boldsymbol{I} \end{bmatrix} \boldsymbol{T}. \tag{5.10}$$

While this decomposition is valid for cases where the tangent stiffness and compliance matrices are non-singular, Lipkin and Patterson demonstrate that decompositions also exist for singular cases, although alternative derivations and constraints may be required, and some stiffness and compliance magnitudes may become zero [143].

Solving Equation 5.7 or 5.9 subject to the constraint in Equation 5.4 gives three eigenwrenches $\boldsymbol{w}_f$ that (assuming a rigid body connection exists between the applied eigenscrews and the POI) induce pure parallel translation of the POI. Simi-

larly, solving Equation 5.8 or 5.10 subject to the constraint in Equation 5.6 gives three eigentwists $\boldsymbol{T}_\gamma$ that, under the same assumption of a rigid body connection, induce wrenches $\boldsymbol{w}_\gamma$ of pure parallel torque about the POI. The three-systems of eigenwrenches and eigentwists are orthogonal due to the fact that the translational quadrant of $\boldsymbol{C}_t$ and the rotational quadrant of $\boldsymbol{K}_t$ (*i.e.* the quadrants that determine the eigenvalues $\boldsymbol{a}_f$ and $\boldsymbol{k}_\gamma$) are symmetrical.

For the POI tangent stiffness matrix the decomposition is expressed as

$$\boldsymbol{K}_t = \begin{bmatrix} \boldsymbol{K}_1 & \boldsymbol{K}_2 \\ \boldsymbol{K}_3 & \boldsymbol{K}_4 \end{bmatrix} = \begin{bmatrix} \hat{\boldsymbol{w}}_f & \hat{\boldsymbol{w}}_\gamma \end{bmatrix} \begin{bmatrix} \boldsymbol{k}_f & 0 \\ 0 & \boldsymbol{k}_\gamma \end{bmatrix} \begin{bmatrix} \hat{\boldsymbol{w}}_f^T \\ \hat{\boldsymbol{w}}_\gamma^T \end{bmatrix}, \tag{5.11}$$

where $\hat{\boldsymbol{w}}_f$ and $\hat{\boldsymbol{w}}_\gamma$ are the normalised eigenwrenches, and $\boldsymbol{k}_f$ and $\boldsymbol{k}_\gamma$ the corresponding stiffnesses (in the directions of f and γ). For a tangent compliance matrix the decomposition is expressed as,

$$\boldsymbol{C}_t = \begin{bmatrix} \boldsymbol{C}_1 & \boldsymbol{C}_2 \\ \boldsymbol{C}_3 & \boldsymbol{C}_4 \end{bmatrix} = \begin{bmatrix} \hat{\boldsymbol{T}}_f & \hat{\boldsymbol{T}}_\gamma \end{bmatrix} \begin{bmatrix} \boldsymbol{a}_f & 0 \\ 0 & \boldsymbol{a}_\gamma \end{bmatrix} \begin{bmatrix} \hat{\boldsymbol{T}}_f^T \\ \hat{\boldsymbol{T}}_\gamma^T \end{bmatrix}, \tag{5.12}$$

where $\hat{\boldsymbol{T}}_f$ and $\hat{\boldsymbol{T}}_\gamma$ are the normalised twists, and $\boldsymbol{a}_f$ and $\boldsymbol{a}_\gamma$ the corresponding compliances (in the directions of $\boldsymbol{f}$ and $\boldsymbol{\gamma}$).

The eigenwrenches, $\boldsymbol{w}_f$, and eigentwists, $\boldsymbol{T}_\gamma$, are normalised by their respective eigenvalues to complete the decomposition *i.e.*

$$\hat{\boldsymbol{w}}_f = \frac{\boldsymbol{w}_f}{\boldsymbol{k}_f}, \tag{5.13}$$

and

$$\hat{\boldsymbol{T}}_\gamma = \frac{\boldsymbol{T}_\gamma}{\boldsymbol{a}_\gamma}. \tag{5.14}$$

These eigentwist and eigenwrench axes can be plotted on the mechanism to visualise its compliance response.

5.2.3 Computing the Decomposition

To compute the eigen-decomposition the eigenvectors ($\boldsymbol{v}_f$) and eigenvalues ($\boldsymbol{\lambda}_f$) of the upper-left (*i.e.* pure translational) quadrant ($\boldsymbol{K}_1$) of the POI's 6×6 stiffness matrix must be obtained, as well as the eigenvectors ($\boldsymbol{v}_\gamma$) and eigenvalues ($\boldsymbol{\lambda}_\gamma$) for the lower-right (*i.e.* pure rotational) quadrant ($\boldsymbol{C}_4$) of the 6×6 reduced compliance matrix. The eigenvectors correspond to the orientations of the twist and wrench axes, while the eigenvalues will give the corresponding stiffness or compliances along those axes. Note that the stiffness and compliances of the eigenwrench and eigentwist axes are found directly from the eigenvalues of the corresponding matrix quadrants,

i.e.

$$\boldsymbol{\lambda}_f = \boldsymbol{k}_f = \frac{1}{\boldsymbol{a}_f}, \tag{5.15}$$

and

$$\boldsymbol{\lambda}_\gamma = \boldsymbol{a}_\gamma = \frac{1}{\boldsymbol{k}_\gamma}. \tag{5.16}$$

Remembering that applying an eigenwrench, $\boldsymbol{w}_f$, to a system along its axis causes a pure parallel translation of the POI by inducing a twist ($\boldsymbol{T}_f$), multiplying the pure translation eigenvectors, $\boldsymbol{v}_f$, by the corresponding $\boldsymbol{K}_t$ stiffness matrix quadrants gives expressions for the eigenwrenches,

$$\boldsymbol{w}_f = \begin{bmatrix} \boldsymbol{K}_1 \\ \boldsymbol{K}_3 \end{bmatrix} \boldsymbol{v}_f. \tag{5.17}$$

Similarly, applying an eigentwist, $\boldsymbol{T}_\gamma$, to a system causes a pure parallel moment couple about the POI by inducing a wrench ($\boldsymbol{w}_\gamma$). These twist axes are expressed with the corresponding C_t compliance matrix terms and pure moment eigenvectors $\boldsymbol{v}_\gamma$ as

$$\boldsymbol{T}_\gamma = \begin{bmatrix} \boldsymbol{C}_2 \\ \boldsymbol{C}_4 \end{bmatrix} \boldsymbol{v}_\gamma. \tag{5.18}$$

In order to determine the placement of these axes in space, their position vectors, $\boldsymbol{r}_i$, relative to the POI must be found. For example, to find the twist axes' vectors, $\boldsymbol{r}_{\text{twists}}$, the following process is implemented. The twist pitch scalar is defined as

$$h_i = \boldsymbol{\delta}_i \cdot \boldsymbol{\gamma}_i, \tag{5.19}$$

with $\boldsymbol{\delta}_i$ and $\boldsymbol{\gamma}_i$ taken from the upper half and lower half of $\hat{\boldsymbol{T}}_\gamma$ respectively. The twist position vectors, $\boldsymbol{r}_{\text{twists}}$ are calculated via the vector triple product identity,

$$\boldsymbol{\gamma}_i \times (\boldsymbol{r}_{\text{twists}} \times \boldsymbol{\gamma}_i) = (\boldsymbol{\gamma}_i \cdot \boldsymbol{\gamma}_i)\boldsymbol{r}_{\text{twists}} - (\boldsymbol{\gamma}_i \cdot \boldsymbol{r}_{\text{twists}})\boldsymbol{\gamma}_i, \tag{5.20}$$

which can be simplified, noting that $\boldsymbol{r}_i$ is orthogonal to $\boldsymbol{\gamma}_i$ by its definition as the shortest distance from the POI to the twist vector,

$$-(\boldsymbol{r}_{\text{twists}} \times \boldsymbol{\gamma}_i) \times \boldsymbol{\gamma}_i = |\boldsymbol{\gamma}_i|^2 \boldsymbol{r}_{\text{twists}}, \tag{5.21}$$

and combined with the definition of $\boldsymbol{\delta}_i$ from (5.2), giving

$$\frac{-(\boldsymbol{\delta}_i - h_i\boldsymbol{\gamma}_i) \times \boldsymbol{\gamma}_i}{|\boldsymbol{\gamma}_i|^2} = \boldsymbol{r}_{\text{twists}}. \tag{5.22}$$

A similar process allows the definition of the wrench axes' vectors, $\boldsymbol{r}_{\text{wrenches}}$, using

d_i, as well as $\boldsymbol{f}_i$ and $\boldsymbol{\tau}_i$ (taken from the upper and lower half of $\hat{\boldsymbol{w}}_f$ respectively), giving

$$\frac{-(\boldsymbol{\tau}_i - d_i\boldsymbol{f}_i) \times \boldsymbol{f}_i}{|\boldsymbol{f}_i|^2} = \boldsymbol{r}_{\text{wrenches}}, \tag{5.23}$$

where

$$d_i = \boldsymbol{f}_i \cdot \boldsymbol{\tau}_i. \tag{5.24}$$

Thus the orientations ($\hat{\boldsymbol{w}}_f$ and $\hat{\boldsymbol{T}}_\gamma$), compliance magnitudes ($\boldsymbol{\lambda}_f$ and $\boldsymbol{\lambda}_\gamma$), and positions ($\boldsymbol{r}_{\text{wrenches}}$ and $\boldsymbol{r}_{\text{twists}}$) for the six principal translational and rotational axes of the POI are defined. Now that the orientations and positions of the eigenscrews have been defined these can be plotted to gain insight into the principal stiffness and compliance axes of a composite compliant shell mechanism.

5.3 Links to Classical Structural Mechanics

Before showing some examples of isotropic and anisotropic shells characterised using these eigenscrew axes, it is worth clarifying the nature of eigentwists and eigenwrenches from a structural mechanics point of view. While the concepts of eigentwists and eigenwrenches may be unfamiliar to those used to working with classical structural mechanics concepts, there exist many similarities to the 2D cross-sectional concepts of shear centre and centre of twist. In this section it is shown that for a degenerate isotropic case there is indeed a direct link between these mechanisms and structural mechanics concepts: the shear centre and centre of twist can be located and mapped using twist and wrench axes.

5.3.1 Shear Centre and Centre of Twist

In structural mechanics, the concept of the shear centre, S, is a well-known property of a prismatic cantilevered beam, derived from the shape of its cross-section. It is defined as the point through which an applied shear loading will not produce a twisting of the beam section; this point need not lie on the beam cross-section itself. Conversely, the centre of twist, T, is defined as the point on the cross-section about which the beam will purely rotate under an applied axial torque (*i.e.* torsion) [158].

For simple beam theory, the position of S and T are found to be equivalent via the Maxwell-Betti reciprocal theory [46, 158, 238]. This theorem uses the principle of superposition to state that, for a linear-elastic body, the order in which loads are applied does not affect the resulting deformations and strain energy. Consider a shear load F and torsional moment M_z applied to a cantilever beam. The reciprocal theorem shows that the deflection δ at the force application point (and parallel to load F) due to a unit applied moment M_z is equal to the rotation θ_z of the

cross-section due to a unit applied load F. If the load is applied at shear centre S, the cross-sectional rotation θ_z is zero; conversely, a torsional moment M_z thus results in no deflection δ at the shear centre, making it the instantaneous centre of twist T. In general S and T need not be coincident, but for special cases where the beam supports minimise the integral of the torsional warping function over the cross-section these boundary conditions align the two centres [238].

For more general 3D non-prismatic beams, it can be less helpful to consider the cross-sectional centres S and T, and more helpful to consider flexural axes. One such approach is that by Stodieck *et al.* who evaluated axes for loaded aircraft wings [233]. They defined a 'local' flexural axis as a loci of flexural centres, which themselves are defined as the position of a shear load on a wing cross-section which would cause zero twisting of the cross-section relative to the root. They also defined a 'global' flexural axis as the positions of a set of loads which produce zero twisting of the wing when applied simultaneously (*i.e.* the 'global' axis is load-dependant). These axes provide an intuitive insight into the decoupled torsional behaviour of the entire wing, and similarly the eigenscrew decomposition technique aims to provide insight into the decoupled translational and rotational behaviour of a compliant mechanism with a clear point of interest.

5.3.2 From Shear Centre to Eigenwrench

Centres such as S and T are used to illustrate how pure uncoupled translations and rotations can occur in a 2D beam cross-section. Eigenscrew axes are used to show the principal compliance directions for a single point on a body in 3D space. Conceptually these concepts appear to capture similar behaviours and it suggests that S and T may be identifiable from an eigen-decomposition. Centres such as S and T are only valid for simple structural cases, but the following subsection presents an analytical link between these centres and the eigenscrew axes for such a case. Establishing this link means that the analogous eigenscrew axes could be used to gain intuitive insight into more general structures such as those that include anisotropy, non-prismatic geometries, more complex boundary conditions and geometric nonlinearities [226].

Compliance Matrix Construction

A prismatic cantilevered beam of length L with a thin-walled, open, and singly-curved symmetric cross section (see Figure 5.2) may be analysed to obtain the 6×6 compliance matrix. The tape spring has a cross-section that is symmetric about the x-axis, and is cantilevered (*i.e.* all degrees of freedom are constrained at one end), with the POI at the free end. The POI is chosen to be located along the

x-axis, at a distance χ from the shear centre, S. The distance ζ is defined as the distance between the shear centre and the centroid of the cross-section, C (the point on the cross-section through which axial loading produces pure axial extension of the beam). The z-axis is defined according to the right hand rule, and moments are defined according to which axis they act around, *i.e.* M_x refers to a moment about the x-axis. The position of the shear centre relative to the centre of a tape spring arc (symmetric in the x-axis) can be calculated as

$$\zeta = \frac{2r(\sin\phi - \phi\cos\phi)}{\phi - \sin\phi\cos\phi} \tag{5.25}$$

where ϕ is equal to half of the cross-section enclosed angle and r is the arc radius [78]. As this is a cross-sectional feature, it can be shown in 3D by plotting a loci of points.

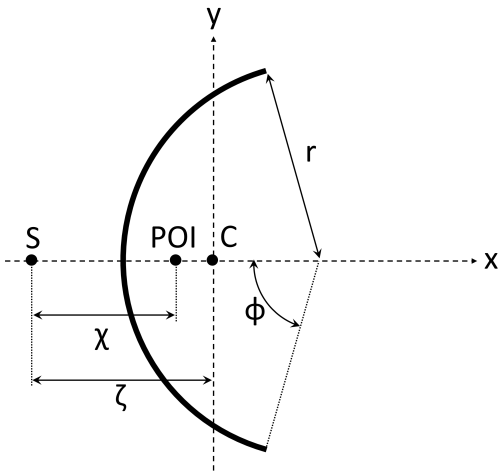

Figure 5.2: *Cross-section of the tape spring at its free end*

Using this definition of the POI, a compliance matrix can be constructed from first principles of mechanics of materials (assuming Euler-Bernoulli beam theory, and no warping of the cross-section) by considering the response of the POI when forces and moments are applied through it [159]. Terms are defined with the usual notation: second moments of area I_{xx} and I_{yy}, beam length L, Young's Modulus E, cross-sectional area A, shear modulus G and polar moment of inertia, J. Moments are defined according to the axis they act around, *i.e.* M_x refers to a moment about the x-axis. This process has been simplified by choosing cross-sectional coordinate systems to ensure $I_{xy} = 0$, at no loss of generality. The compliance matrix is

constructed as follows:

$$\left[\begin{array}{c}\delta_x\\ \delta_y\\ \delta_z\\ \hline \theta_x\\ \theta_y\\ \theta_z\end{array}\right] = \left[\begin{array}{ccc|ccc} C_{11} & 0 & C_{13} & 0 & C_{15} & 0 \\ 0 & C_{22} & 0 & C_{24} & 0 & C_{26} \\ C_{31} & 0 & C_{33} & 0 & C_{35} & 0 \\ \hline 0 & C_{42} & 0 & C_{44} & 0 & 0 \\ C_{51} & 0 & C_{53} & 0 & C_{55} & 0 \\ 0 & C_{62} & 0 & 0 & 0 & C_{66} \end{array}\right] \left[\begin{array}{c}F_x\\ F_y\\ F_z\\ \hline M_x\\ M_y\\ M_z\end{array}\right], \tag{5.26}$$

where the compliance components

$$C_{11} = \frac{L^3}{3EI_{yy}}, \quad C_{22} = \frac{L^3}{3EI_{xx}}, \quad C_{33} = \frac{L}{EA},$$

govern deflections due to applied forces, and

$$C_{44} = \frac{L}{EI_{xx}}, \quad C_{55} = \frac{L}{EI_{yy}}, \quad C_{66} = \frac{L}{GJ},$$

describe rotations due to applied moments. Deflections due to any POI offset from the centroid, C, are given by

$$C_{13} = C_{31} = \frac{(\zeta - \chi)L^2}{2EI_{yy}}.$$

The coupling between applied forces and resulting rotations (and conversely, applied moments and resulting deflections) are given by

$$C_{15} = C_{51} = \frac{L^2}{2EI_{yy}}, \quad C_{24} = C_{42} = -\frac{L^2}{2EI_{xx}},$$
$$C_{26} = C_{62} = \frac{\chi L}{GJ}, \quad C_{35} = C_{53} = \frac{(\zeta - \chi)L}{EI_{yy}},$$

where C_{62} reflects rotation around the shear centre (*i.e.* centre of twist) for a transverse load not passing through S.

This compliance matrix can be inverted to give the stiffness matrix,

$$\begin{bmatrix} \boldsymbol{K}_1 & \boldsymbol{K}_2 \\ \boldsymbol{K}_3 & \boldsymbol{K}_4 \end{bmatrix} = \begin{bmatrix} \boldsymbol{C}_1 & \boldsymbol{C}_2 \\ \boldsymbol{C}_3 & \boldsymbol{C}_4 \end{bmatrix}^{-1} \tag{5.27}$$

where the four 3×3 quadrants of the stiffness matrix ($\boldsymbol{K}_1 - \boldsymbol{K}_4$) can be found by a piece-wise inversion of the four 3x3 quadrants of the compliance matrix ($\boldsymbol{C}_1 - \boldsymbol{C}_4$) using the Schur complement approach for block matrices (also used to invert $\boldsymbol{ABD}$

matrices in composite plate theory [167]). This means

$$\boldsymbol{P}_1 = \boldsymbol{C}_1^{-1}, \qquad \boldsymbol{P}_2 = -\boldsymbol{C}_1^{-1}\boldsymbol{C}_2,$$
$$\boldsymbol{P}_3 = \boldsymbol{C}_2\boldsymbol{C}_1^{-1}, \qquad \boldsymbol{P}_4 = \boldsymbol{C}_4 - \boldsymbol{C}_2\boldsymbol{C}_1^{-1}\boldsymbol{C}_2$$

and therefore

$$\boldsymbol{K}_1 = \boldsymbol{P}_1 - \boldsymbol{P}_2\boldsymbol{P}_4^{-1}\boldsymbol{P}_3, \qquad \boldsymbol{K}_2 = \boldsymbol{P}_2\boldsymbol{P}_4^{-1},$$
$$\boldsymbol{K}_3 = -\boldsymbol{P}_4\boldsymbol{P}_3^{-1}, \qquad \boldsymbol{K}_4 = \boldsymbol{P}_4^{-1}$$

Note that $\boldsymbol{K}_2 = \boldsymbol{K}_3$ and $\boldsymbol{C}_2 = \boldsymbol{C}_3$. This gives

$$\left[\begin{array}{c} F_x \\ F_y \\ F_z \\ \hline M_x \\ M_y \\ M_z \end{array}\right] = \left[\begin{array}{ccc|ccc} K_{11} & 0 & 0 & 0 & K_{15} & 0 \\ 0 & K_{22} & 0 & K_{24} & 0 & K_{26} \\ 0 & 0 & K_{33} & 0 & K_{35} & 0 \\ \hline 0 & K_{42} & 0 & K_{44} & 0 & K_{46} \\ K_{51} & 0 & K_{53} & 0 & K_{55} & 0 \\ 0 & K_{62} & 0 & K_{64} & 0 & K_{66} \end{array}\right] \left[\begin{array}{c} \delta_x \\ \delta_y \\ \delta_z \\ \hline \theta_x \\ \theta_y \\ \theta_z \end{array}\right]. \tag{5.28}$$

where the stiffness components

$$K_{11} = \frac{12EI_{yy}}{L^3}, \quad K_{22} = \frac{12EGI_{xx}J}{L(GJL^2 - 12EI_{xx}\chi^2)},$$
$$K_{33} = \frac{EI_{yy}L}{AI_{yy}E^2 - L^2\chi^2 + 2L^2\chi\zeta - L^2\zeta^2},$$

govern forces due to applied deflections, and

$$K_{44} = \frac{4EI_{xx}(GJL^2 - 3EI_{xx}\chi^2)}{L(GJL^2 - 12EI_{xx}\chi^2)},$$
$$K_{46} = K_{64} = \frac{-(6EGI_{xx}J\chi)}{GJL^2 - 12EI_{xx}\chi^2},$$
$$K_{55} = \frac{EI_{yy}(4AI_{yy}E^2 - 3L^2\chi^2 + 6L^2\chi\zeta - 3L^2\zeta^2)}{(AI_{yy}E^2L - L^3\chi^2 + 2L^3\chi\zeta - L^3\zeta^2)},$$
$$K_{66} = \frac{G^2J^2L}{GJL^2 - 12EI_{xx}\chi^2},$$

describe moments due to applied rotations. The coupling between applied deflections and resulting moments (and conversely, applied rotations and resulting forces) are

given by

$$K_{15} = K_{51} = \frac{-(6EI_{yy})}{L^2},$$
$$K_{24} = K_{42} = -\frac{6EGI_{xx}J}{GJL^2 - 12EI_{xx}\chi^2},$$
$$K_{26} = K_{62} = \frac{-(12EGI_{xx}J\chi)}{L(GJL^2 - 12EI_{xx}\chi^2)},$$
$$K_{35} = K_{53} = \frac{EI_{yy}(L\chi - L\zeta)}{AI_{yy}E^2 - L^2\chi^2 + 2L^2\chi\zeta - L^2\zeta^2}.$$

Once both the stiffness and compliance matrices are found, the eigenscrew decomposition can be used to find the positions, orientations and magnitudes of the eigenwrench and eigentwist axes and thus show equivalence between the concepts.

5.3.3 Decomposition Results

The eigenscrew decomposition produces position vectors (relative to the POI) and orientations of the eigentwist and eigenwrench axes. Remembering that a load applied along an eigenwrench axis will describe parallel translations of the POI (and vice versa for eigentwist axes), inspecting these positions and orientations (as shown for a tape spring in Figure 5.3) shows that there are direct links between the eigenscrews and the shear centre and centre of twist.

Equations 5.29–5.31 show the position vectors $\boldsymbol{r}_w$, orientations $\boldsymbol{f}$ and stiffness magnitudes $\boldsymbol{k}_f$ respectively for the eigenwrenches $\hat{w}_1 - \hat{w}_3$, with each column corresponding to a single eigenwrench:

$$\boldsymbol{r}_{\text{wrenches}} = \begin{bmatrix} 0 & (\zeta - \chi) & -\chi \\ 0 & 0 & 0 \\ -\frac{L}{2} & 0 & -\frac{L}{2} \end{bmatrix}, \tag{5.29}$$

$$\boldsymbol{f} = \begin{bmatrix} 1 & 0 & 0 \\ 0 & 0 & 1 \\ 0 & 1 & 0 \end{bmatrix} \tag{5.30}$$

$$\boldsymbol{k}_f = \begin{bmatrix} \frac{12EI_{yy}}{L^3} & 0 & 0 \\ 0 & \frac{EI_{yy}L}{AI_{yy}E^2 - L^2\chi^2 + 2L^2\chi\zeta - L^2\zeta^2} & 0 \\ 0 & 0 & \frac{12EGI_{xx}J}{GJL^3 - 12EI_{xx}L\chi^2} \end{bmatrix} \tag{5.31}$$

It can be seen that eigenwrench W_1 exists at a distance $-L/2$ from the POI in z-axis, orientated parallel to the x-axis. This means that a force applied halfway down (and in the centre of) the tape spring in the x-direction will cause a pure translation of the POI in the x-direction, reflecting an aspect of first-order cantilever

deformation known from beam theory. Eigenwrench W_2 is located at $\zeta - \chi$ from the POI in the x-axis (*i.e.* at the centroid C), orientated parallel to the z-axis. This means a force applied along this eigenwrench axis will cause a pure translation of the POI in the z-axis, hereby demonstrating the definition of the centroid. Finally, eigenwrench W_3 exists $-L/2$ from the POI in the z-axis, $-\chi$ from the POI along the x-axis (*i.e.* at S), and is orientated parallel to the y-axis. Similarly to eigenwrench W_1, it can be seen here that a force applied along W_3 (*i.e.* through the shear centre, halfway down the tape spring) will cause pure parallel translation of the POI, linking the 2D shear centre concept to a 3D deformation.

Equations 5.32, 5.33 and 5.34 show the position vectors, orientations and compliance magnitudes respectively for the eigentwists:

$$\boldsymbol{r}_{\text{twists}} = \begin{bmatrix} 0 & (\zeta - \chi) & -\chi \\ 0 & 0 & 0 \\ -\frac{L}{2} & -\frac{L}{2} & 0 \end{bmatrix}, \tag{5.32}$$

$$\boldsymbol{\gamma} = \begin{bmatrix} 1 & 0 & 0 \\ 0 & 1 & 0 \\ 0 & 0 & 1 \end{bmatrix} \tag{5.33}$$

$$\boldsymbol{a}_{\gamma} = \begin{bmatrix} \frac{L}{EI_{xx}} & 0 & 0 \\ 0 & \frac{L}{EI_{yy}} & 0 \\ 0 & 0 & \frac{L}{GJ} \end{bmatrix} \tag{5.34}$$

Eigentwist T_1 exists at a distance $-L/2$ from the POI in z-axis, orientated parallel to the x-axis. This eigentwist is co-linear with eigenwrench W_1, and means a rotation applied around this axis will cause a pure moment about the x-axis at the POI. For an isotropic tape spring with a large enclosed angle, this will have the lowest value of compliance as usually $EI_{xx} > EI_{yy} > GJ$. Eigentwist T_2 is located at $-L/2$ from the POI in the z-axis, $\zeta - \chi$ from the POI in the x-axis (*i.e.* at the centroid C), orientated parallel to the y-axis. A rotation about this axis will cause a pure moment about the y-axis at the POI. The stiffness of this 'tape spring bending' eigentwist will increase in proportion with I_{yy} (which increases with the amount of angle enclosed by the tape spring). Finally, eigentwist T_3 exists $-\chi$ from the POI along the x-axis (*i.e.* at the shear centre, S), and is orientated parallel to the z-axis. This means a rotation applied along this axis will cause a pure moment about the z-axis at the POI, demonstrating the properties of loading through a centre of twist and illustrating that the centre of twist and the shear centre can exist at the same point, confirming reciprocal theorem. Aligning the POI with the beam centroid in a similar manner to Ciblak [32] causes some of the position vector terms to become

zero as $\chi = \zeta$, although Ciblak used Timoshenko beam theory that has more refined kinematics for the beam.

Figure 5.3 shows a plot of an isotropic, thin-walled tape spring with eigenscrews and loci of cross-sectional shear centres (dashed magenta) plotted to help illustrate the analytical link described above.

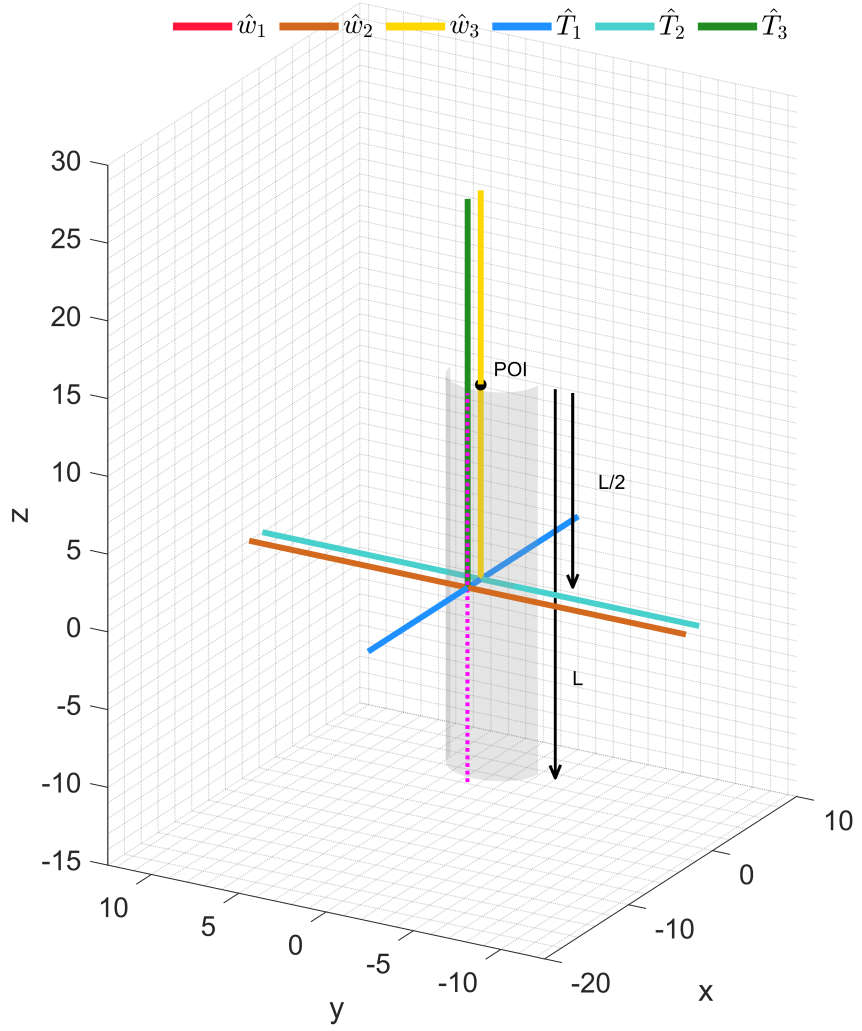

Figure 5.3: *Visualisation of undeformed eigenscrews and shear centre loci (dashed magenta line) for an isotropic tape spring of aspect ratio* 2 *and enclosed angle* 180°

For the simple case of a cantilevered beam, it can thus be shown that the well-known concepts of shear centre and centre of twist align with eigenwrench and eigentwist. This allows us to interpret the eigenscrew concepts as 'generalised shear centres' and 'axes of twist' which help to interpret the structural response for more general compliant shells.

5.4 Characterisation and Visualisation of a Tape Spring Mechanism

A series of tape spring shell mechanisms with selected anisotropic material properties are analysed to demonstrate the visualisation of the principal compliance axes for different composite lay-ups to explore the effect of material system on the principal compliance axes (see Figure 5.4). These provide a simple geometry which could be applicable to biomedical support applications by fitting around a limb or the torso. Specifically, small tape springs were investigated (chord $c = 5$ mm, total thickness $H = 0.5$ mm, and aspect ratio $a = L/c = 2$) to represent shell mechanisms for segments of finger braces or precision mechanisms. Note that these geometries are close to the limits of thin shell approximations.

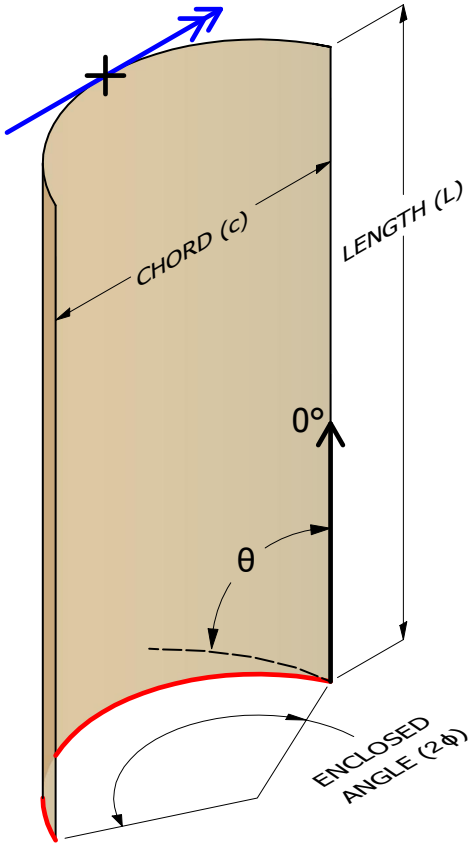

Figure 5.4: *Tape spring geometry, with location of POI (+), applied moment (blue arrow), encastre boundary condition (red edge), and fibre angle θ.*

5.4.1 Finite Element Formulation

Cantilevered tape springs subject to a follower moment acting on the POI were analysed using Abaqus/Standard 2018 using S4R shell elements. This follower moment was chosen as it reflected a finger brace load case. A mesh density of six elements per millimetre of shell chord, c, and length, L, was selected after a mesh convergence study for POI displacement. The POI is located at the centre of the tip edge, as shown in Figure 5.6a, and a "Rigid Body - Tie" constraint was applied to all tip edge nodes to ensure they displaced with the POI. The row of nodes at the base edge are constrained to be fully fixed.

The shells were incrementally loaded using a series of nonlinear static analyses, and POI stiffness matrices were extracted using a substructure analysis (see Figure 5.5 for the analysis process). Local stiffness matrices and deformed shell geometries for each loading step are subsequently post-processed via MATLAB to calculate the eigen-decomposition and produce the visualisation of shell compliance.

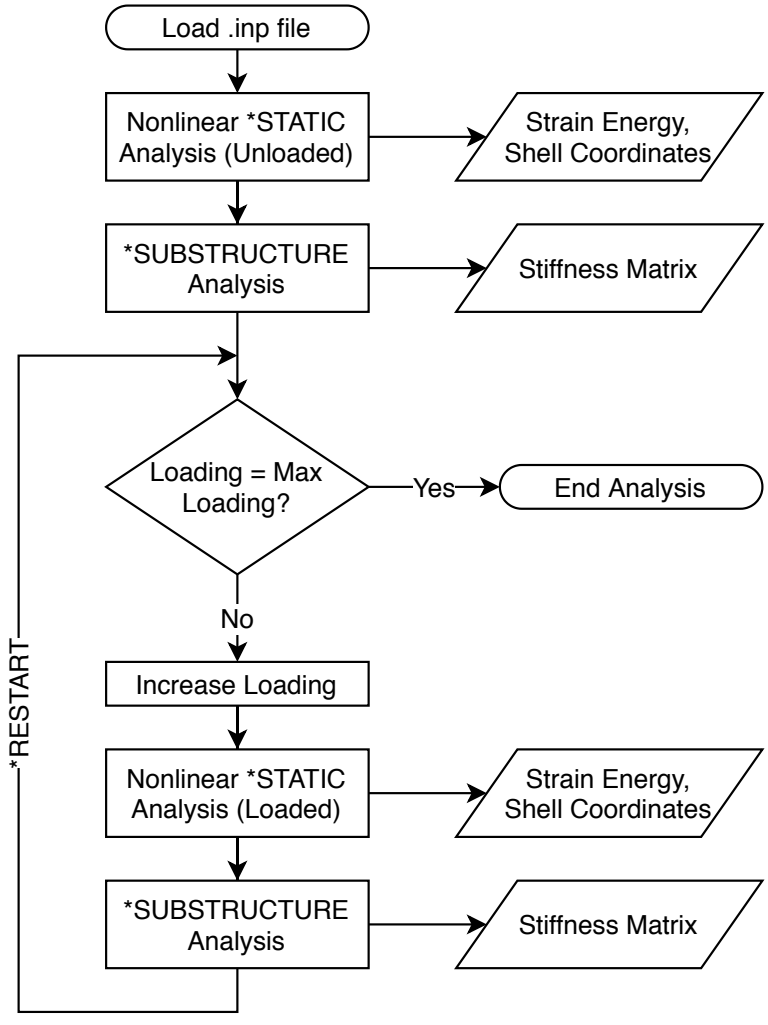

Figure 5.5: *Finite element analysis process*

Table 5.1: *Mechanism Laminates Investigated*

Cases	Layup
Isotropic benchmark	[0° -60° 60° 0° -60° 60°$_3$ −60°$_2$ 0°$_2$ -60° 0°$_2$ 60°$_2$ -60°]
Single fibres	[0°], [30°], [45°], [60°], [90°]

In order to compare behaviour for a range of anisotropic material properties, a common energetic input is enforced to limit the magnitude of the applied moment: the same work is done in all cases. A limit of 0.1 J was selected following inspection of preliminary results; this value gave appropriately large deformations without entering extreme deformation modes. No material failure was implemented, so deformations were not limited by developed stresses or strains and thus may not be physically achievable.

5.4.2 Material Model

An E-Glass/Epoxy material system was selected for investigation [37]; see Table 2.2 in Chapter 2. This material system provides a sufficient level of orthotropy ($E_{11}/E_{22} \approx 4$) to illustrate the different modes of behaviour that can be achieved when compared to an isotropic material. The ratio of stiffness along fibre E_{11} and transverse E_{22} directions dictates the relative magnitudes of deformation of the POI. This further depends on the orientation of the anisotropy, described by fibre angle θ with respect to the tape spring longitudinal axis (see Figure 5.4).

For materials such as carbon-fibre reinforced polymers with increased orthotropy ($E_{11}/E_{22} \approx 15$), this results in POI deformations that can be an order of magnitude different between the low and high compliance orientations. Although this presents a challenge when comparing responses, it highlights the potential of elastic tailoring to improve performance for fixed shell geometries. Thus, the results presented herein should not be considered the extremes of the design space.

To provide an isotropic benchmark, an eighteen-ply laminate that exhibits equivalent isotropic properties is used [245]; see Table 5.1. For this laminate $A_{16} = A_{26} = 0$, $\boldsymbol{B} = 0$ and $A_{16} = A_{26} = 0$ meaning that the fibre angles and stacking sequence cause the laminate to exhibit isotropic behaviour, in this case with equivalent in-plane and bending moduli of of 20.6 GPa. Mechanisms utilising this fully isotropic laminate were compared with those containing highly-anisotropic single-ply angle laminates (each with a single fibre angle) of the same total laminate thickness for two values of enclosed tape spring angle.

5.4.3 Visualisation

Eigenscrews can be calculated for compliant composite shell mechanisms, but in order to explore and compare the effect of this material anisotropy and geometry on the principal compliance axes, a visualisation framework has to be developed. Figures 5.6–5.8 show one such way to visualise the shell's compliance response for three anisotropic case studies. The aim is to provide an overview of the magnitudes and (re)orientation of the twist and wrench axes throughout the deformation of the compliant shell mechanisms. Combining this information helps inform the mechanism designer about the effect of parameters such as shell geometry and material anisotropy. To achieve this, each figure consists of five sub-plots:

(a) **Deformed and undeformed configurations**: a 3D representation of the shell in its original and fully-deformed state, including twist and wrench axes for the original state.

Sub-plot (a) gives the designer insight into the spatial movement of the whole shell as well as the POI, which can include bending-torsion motion in anisotropic cases. Seeing the initial (pre-deformation) positions and orientations of the twist and wrenches provides an indication of the shell's characteristics when subject to small deformation load-cases.

(b) **Wrench axes**: a polar plot shows the (re)orientation of the wrenches throughout the mechanism deformation.

(c) **Twist axes**: a polar plot shows the (re)orientation of the twists throughout the mechanism deformation.

Sub-plots (b) and (c) are polar plots that illustrate orientations of the twist and wrench vectors. The plots are akin to looking at one half of a unit sphere upon which lie traces of the axes emanating from its centre, and do not contain any information about the positions of the axes in space. The initial undeformed vector orientations together with the final values are marked to aid interpretation variation of alignment under loading. The polar-plots are included to help illustrate how the alignments of principal axes change (*i.e.* what the most and least compliant deformation paths are) as well as how they change with different laminates.

(d) **Wrench compliances**: a plot showing the variation in compliance magnitudes of the wrenches.

(e) **Twist compliances**: a plot showing the variation in compliance magnitudes of the twists.

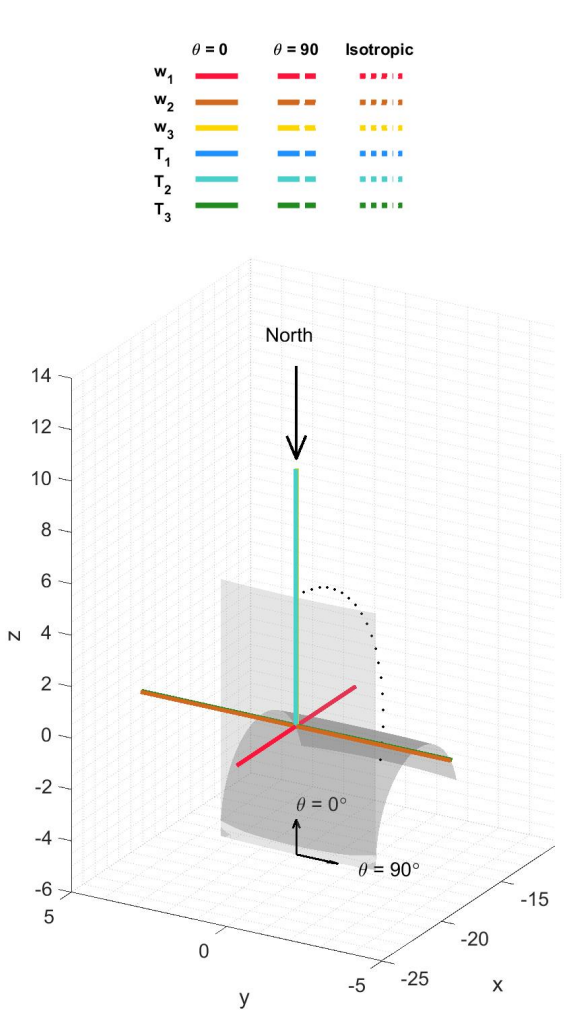

(a) *Deformed (dark) and undeformed (light) shells, POI locations (•) and undeformed twist and wrench axes. $\theta = 90°$.*

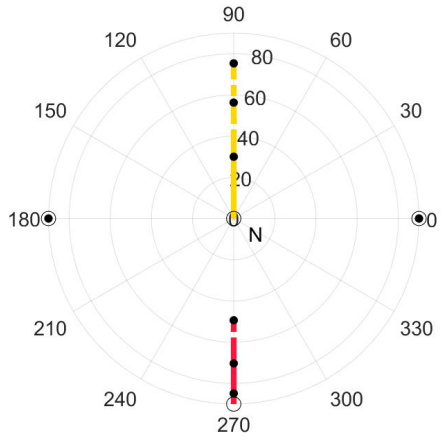

(b) *Wrench axis orientation changes, as seen from 'North' direction. Markers indicate: undeformed states (○) and fully-deformed states (•).*

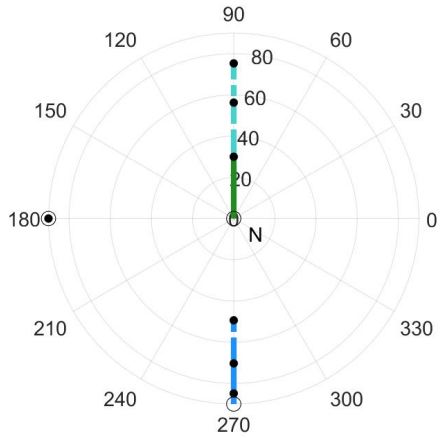

(c) *Twist axis orientation changes, as seen from 'North' direction. Markers indicate: undeformed states (○) and fully-deformed states (•).*

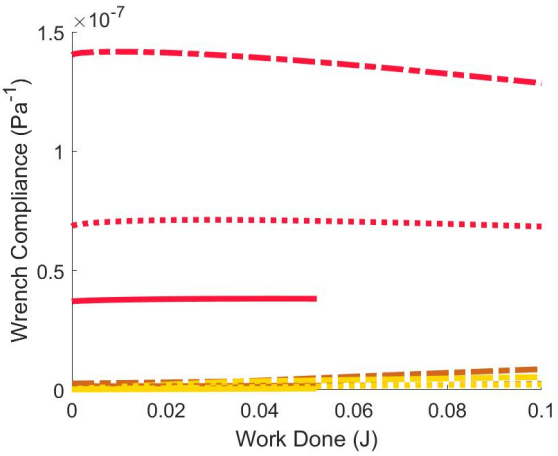

(d) *Wrench compliance magnitude changes*

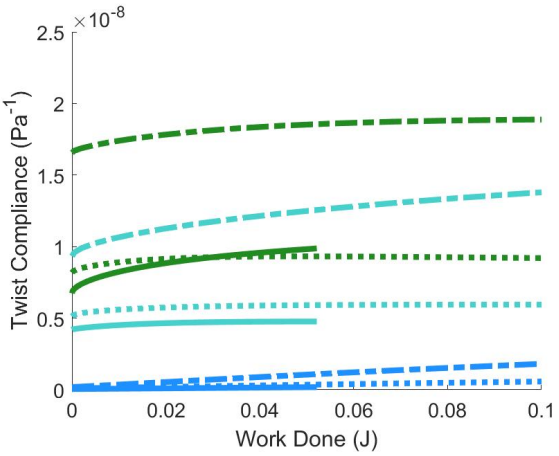

(e) *Twist compliance magnitude changes*

Figure 5.6: *Visualisation of compliance behaviour for shallow, singly-curved (enclosed angle 15°), low aspect ratio (a=2) shell mechanisms comprised of fully isotropic, $\theta = 0°$, or $\theta = 90°$ laminates.*

Subplots (d) and (e) show compliance magnitudes plotted against applied work. These plots illustrate the most compliant axes, the relative compliance between axes, and how these change throughout the mechanism deformation. This is particularly useful for the designer in cases where initial compliances between some wrenches or twists are similar, or where there are sudden changes in compliance (*e.g.* the development of a fold in a tape spring hinge).

5.4.4 Results

Figures 5.6–5.8 each compare the results for three cases with different material anisotropy. Figure 5.6 investigates a shallow tape spring (5 mm chord, enclosed angle $2\phi = 15°$) with a 0°, 90° and an isotropic laminate. Figure 5.7 compares mechanisms with the same geometry, but a 30°, 45°, and 60° laminate. Figure 5.8 replicates Figure 5.7, but for mechanisms with a larger curvature (5 mm chord, enclosed angle $2\phi = 45°$). Analysing these different cases can help illustrate the interplay between geometric and material contributions to a compliant mechanism deformation.

Case Study I: Isotropy & Aligned Anisotropy

Figure 5.6 compares the behaviour of the equivalent isotropic laminate with the most extreme form of stiffness anisotropy (*i.e.* the greatest mismatch between E_{11} and E_{22} for the shell) that can be achieved with the specified material system (0° or 90° laminates).

Figure 5.6a shows a representative shell deformation for the $\theta = 90°$ laminate. Due to the loading, geometric and material symmetry of the shell mechanism in the undeformed configuration, the twist and wrench axes are parallel to the tape spring chord and length axes. A 90° case is plotted in Figure 5.6a, and note that the twist and wrench axes overlap visually, and while parallel they do not coincide precisely: w_1 (red) overlaps with T_1 (blue), w_2 (orange) with T_3 (green), and w_3 (yellow) with T_2 (teal). They also remain parallel during deformation, as shown in Figures 5.6b–5.6c, as no geometric or material asymmetry exists.

Figures 5.6d–5.6e identify w_1 and T_3 as the most compliant wrench and twist axes, respectively, for all cases shown. For the 90° and isotropic cases, these map to a transverse load resulting in cantilever bending (w_1) and a bending mode around the global y-direction (T_3). Note that the wrench axis w_1 is not placed at the POI: a load applied there would induce both translation and rotation, whereas a load along the plotted w_1 axis only produces a translation of the POI. Conceptually, such a load would be applied to a rigid body connected to the POI, rather than to the indicated location on the shell, similar to the way off-axis loads can be applied to

beams to induce bending and torsion. The torsional T_2 twist axis passes through the shear centre of the cantilevered tape spring, as this provides the instantaneous rotation axis of the cross-section. Note that wrench w_2 is parallel to the chord axis and is applied through the shear centre of the cross-section as this will induce no torsion.

For the 0° case T_3 is still the most compliant twist, but it is now aligned with the tape spring torsion axis. In both the 0° and 90° cases T_3 aligns with the fibre direction, showing an anisotropic stiffness-dominated behaviour that favours rotation about the fibres. For cases with extreme ϕ angles (not shown here for brevity), the behaviour becomes geometry-dominated, with rotation around the tape spring torsion axis always favoured. The 0° case was only plotted up to a strain energy of approximately 0.05 J as the finite element model failed to converge when the shell was loaded beyond this point.

As all the shell cases deform, the w_1 wrench compliance gradually decreases; due to the bending of the shell mechanism, the wrench axis aligns more along the length of the deformed cantilever. As the mechanism bends, however, the shell transverse curvature decreases along the middle, which can be seen in the increase in rotational compliance of the bending twist T_2, particularly in the 90° case. This is due to Poisson's ratio effects causing the curved shell to 'open out'. Applying further work to the shell would result in a tape spring fold developing (*i.e.* this mid-spring curvature reducing to zero), characterised by a rapid increase in T_2 compliance.

For all cases, wrenches w_2 and w_3 (shear and axial loading) and twist T_1 have comparatively very low compliance and consequently have a much smaller impact on the mechanism behaviour. The ordering of the compliances does not change during the deformation of the shell.

Case Study II: Non-Aligned Anisotropy: Small Curvature

Figure 5.7 compares the compliance behaviour throughout deformation for the geometry shells as Figure 5.6, except that they now are made from composite laminates comprised of a single fibre angle. The angles of 30°, 45° and 60° were chosen to show a broad range of behaviour between the previously shown 0° and 90° cases.

Figure 5.7a shows a representative shell deformation for the $\theta = 30°$ case. It can now be seen the twist and wrench axes no longer align with the geometric axis (or with each other), as in Figure 5.6, due to the laminate's material anisotropy. In addition, only w_1 and T_1 remain parallel during deformation as shown in Figures 5.7b–5.7c as they both remain aligned with the shell normal.

Figure 5.7d–5.7e shows that, like the cases in Figure 5.6, the most compliant wrench and twist are w_1 and T_3 respectively. It can be seen that upon loading there is a brief peak in w_1 compliance, before it decreases with further loading;

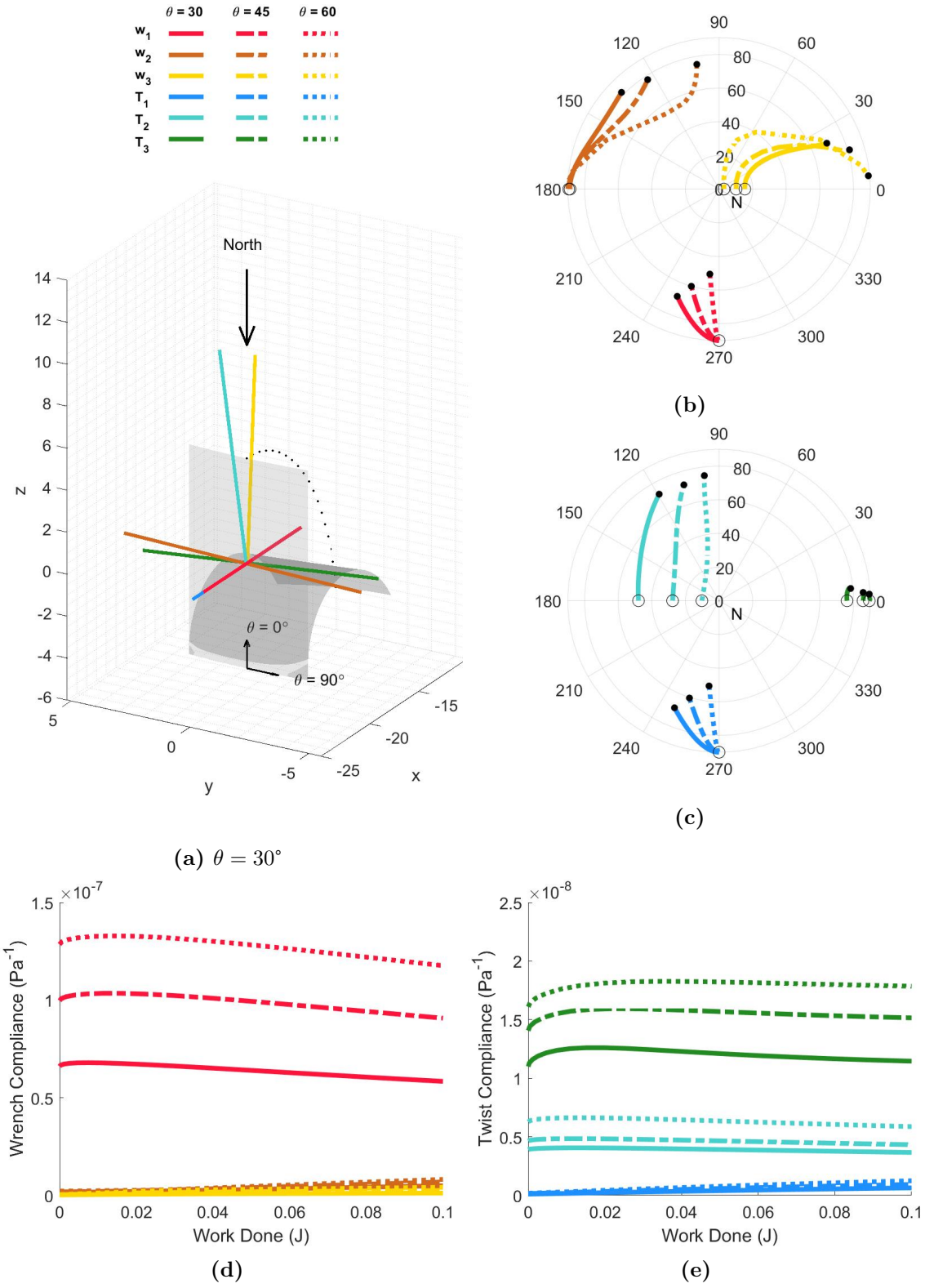

(a) $\theta = 30°$

(b)

(c)

(d)

(e)

Figure 5.7: *Visualisation of compliance behaviour for shallow, singly-curved (enclosed angle 15°), low aspect ratio (a=2) shell mechanisms comprised of fully $\theta = 30°$, $\theta = 45°$ or $\theta = 60°$ laminates.*

larger fibre angle laminates exhibit higher compliances. During deformation the mechanism undergoes a bending-torsion deformation which briefly makes w_1 more compliant, before the shell curling stiffens it. The initial orientation of T_3 favours alignment with the stiff fibres (similarly to Figure 5.6), but shell curvature and boundary effects also have an effect, so the alignment is orientated at higher angle than the fibre direction. Again, upon loading there is a brief peak in T_3 compliance (due to opening of shell curvature) before a more gradual decrease with further loading.

Unlike the 90° case in Figure 5.6e, the T_3 compliances remain always around twice as compliant as T_2. This is because T_3 is not parallel to the shell curvature, and thus the geometric stiffness does not dominate as much as for T_2 in the 90° case. The bending and torsion is not coupled in the Figure 5.6 cases, but is when there are non-aligned fibre angles, and these act to favour the coupled bending-torsion governed by T_3, illustrating a stiffness-dominated response.

In purely stiffness-dominated behaviours the initial compliance magnitudes reduce or increase depending on the axes' proximity to the fibre orientation. As the enclosed angle of the tape spring curvature increases, the geometry effects can dominate the stiffness behaviour again, and the twist axes can align much better with the classical tape spring axes, even in the presence of non-aligned material anisotropy.

Similarly to Figure 5.6, wrenches w_2 and w_3 are much less compliant than w_1, so would have little effect on the shell behaviour even though the bending-torsion deflection causes large changes in their orientations.

Case Study III: Non-Aligned Anisotropy: Large Curvature

Figure 5.8 shows the compliance behaviour for the same composite laminates as Figure 5.7, except that the enclosed angle of these tape springs has been increased to $2\phi = 45°$ to increase the effect of geometry on the structural response.

Figure 5.8a shows a representative shell deformation for the $\theta = 30°$ case, showing that the final deformation is reduced with the increased ϕ due to the geometric stiffening it provides. Figure 5.8d–5.8e shows that, like the cases in Figures 5.6–5.7, the most compliant wrench and twist are w_1 and T_3 respectively. The increase in shell curvature has reduced the peak compliance magnitudes of w_1, however, as the tape spring cross-section has a greater second moment of area and provides resistance to cantilever bending. The w_1 compliance increase during deformation is more drawn out than in Figure 5.7d, as there is more shell curvature to 'open-out'. This greater 'opening', combined with the favourable twist orientation also increases the peak compliance of T_3. The rotation of w_1 is similar, however, remaining parallel with T_1, but reflects the reduced overall deformation of the mechanism.

It can be seen that wrenches w_2 and w_3 rotate a lot for this enclosed angle. An

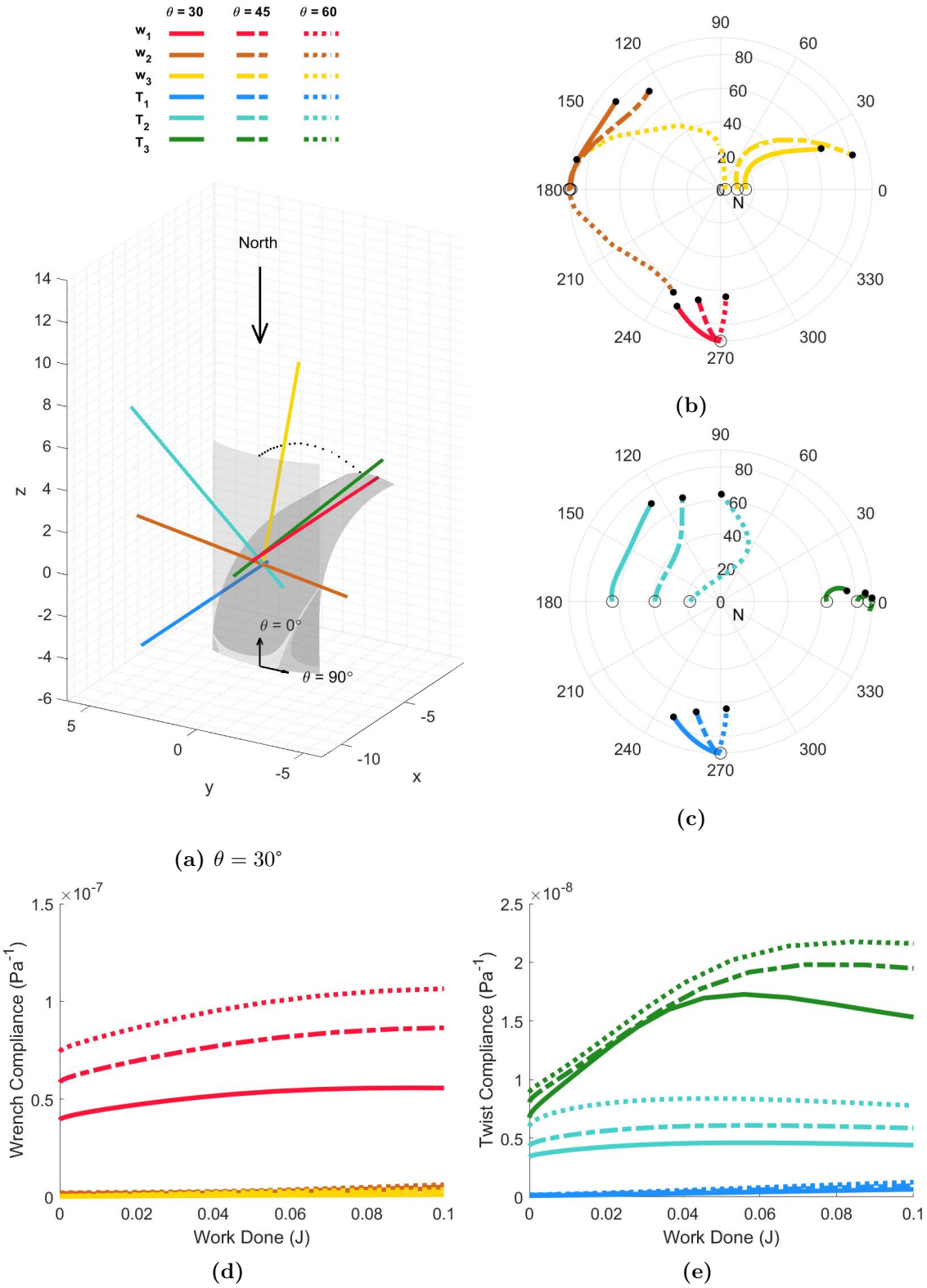

Figure 5.8: *Visualisation of compliance behaviour for deeper, singly-curved (enclosed angle 45°), low aspect ratio (a=2) shell mechanisms comprised of fully $\theta = 30°$, $\theta = 45°$ or $\theta = 60°$ laminates.*

interesting phenomena occurs when $\theta = 60°$, as the larger shell curvature causes the axes to rotate in the opposite direction during deformation. As w_2 has very low compliance, this will not affect the shell behaviour much, but it is interesting to see how the geometry and stiffness behaviour combine to produce this unexpected effect. Further work is required to identify cases where such effects can occur with more compliant axes.

The magnitudes of twists T_1 and T_2 remain similar to the $2\phi = 15°$ case, although their orientations are subtly different: T_2 rotates, then partially re-aligns throughout deformation, in another case of unusual behaviour resulting from a geometry change. The final orientations of T_2 appear similar, but not identical to, those when $2\phi = 15°$, suggesting the final deformation behaviour is more stiffness-dominated, but that initial deformations are influenced by stiffness and geometry effects: a hybrid response.

With this larger enclosed angle, more hybrid behaviours occur where initial compliance magnitudes appear to be geometry-dominated, but the axes orientations are noticeably influenced by the fibre angle. The deformation changes from classical tape spring bending, to a non-symmetric bending-torsion which is determined by the stiffness-influenced primary twist orientation. In this hybrid behaviour the primary twist compliance can actually increase as shell curvature 'opens-out'. This effect is prolonged with greater shell curvature, and higher compliance magnitudes can be achieved as rotation around the primary twist axis is more energetically favourable deformation than the classical tape spring bending.

5.5 Final Remarks

A mechanisms characterisation technique by Lipkin and Patterson [143] has for the first time been applied to shell mechanisms with material anisotropy. A visualisation method has been developed to capture the effect of material anisotropy on the magnitude and orientation of the eigen-wrenches and eigen-twists that characterise the mechanical response of a compliant shell mechanism. By applying this technique to composite tape springs the interplay between anisotropic alignment and shell geometry has been investigated, highlighting the visualisation framework's ability to capture varied response modes and provide physical insight into their mechanical response. The introduction of anisotropy is shown to offer additional modes of mechanism response, expanding the design space, which is of particular value in cases where shell geometry is highly constrained such as in medical support applications. Moreover, the visualisation framework highlighted cases where the effects of shell geometry or material anisotropy dominate, as well as when they interact.

In addition, an analytical link has been shown between the structural mechanics

concepts of shear centre and centre of twist and the mechanism design concepts of eigenwrenches and eigentwists. Eigenscrews are shown to align with shear centre and centre of twist positions for a simple isotropic cantilevered tape spring. Eigenscrew characterisations can thus be used to visualise the principal compliance behaviour of a compliant mechanism in cases where cross-sectional centres have less applicability (*e.g.* those with material anisotropy). Demonstrating the link between these concepts for the special case aids the interpretation of eigenscrew characterisations that are more appropriate for general 3D morphing structures and compliant mechanisms. Furthermore, it is hoped that the demonstrated equivalence will encourage structural engineers to consider the value of the eigenscrew characterisation used in compliant mechanism design, and thus help enable cross-fertilisation of ideas between these fields.

5.6 Next Steps

In summary, the work in this chapter set out to develop and apply an intuitive mechanism characterisation framework that would be suitable for a range of general-geometry composite compliant shell mechanisms. The analysis framework and accompanying visualisation methods were shown to offer insight into a geometrically straightforward compliant mechanism, a tape spring. The next step in demonstrating this framework is to consider a mechanism design case that is more complex than a tape spring, as the initial motivation for developing a framework was to find a characterisation technique for a broad class of mechanisms.

Therefore the next chapter will explore the application of this eigenscrew characterisation and visualisation framework to a mechanism for a scoliosis brace. Investigating this complex design case in this way will help validate the effectiveness and applicability of the framework, as well as provide an opportunity to assess the potential of using composites over isotropic materials for improving a mechanism design.

Chapter 6

Application: A Composite Scoliosis Brace

The work presented in Chapter 5 has shown that the stiffness characteristics of a simple compliant shell mechanism can be significantly tailored using fibre reinforced composites. Furthermore, these changes can be effectively visualised and interpreted using an eigenscrew decomposition of the compliant mechanism stiffness matrix. The compliant shell mechanisms investigated so far have had relatively simple geometries and well-defined analytical models, however, and it would be advantageous to consider mechanisms with more general geometries.

This chapter details a design case study for such a mechanism: a doubly-curved compliant shell structure for a scoliosis brace. The responses of braces with different geometries and layups are evaluated using the eigenscrew formulations from Chapter 5 to assess the potential benefits that inclusion of fibre reinforced composites may bring to such an application.

6.1 Introduction

Scoliosis is a condition that causes a lateral rotated curvature to develop in the spine, typically in children at or around puberty, and can compromise respiratory function of the patient in extreme cases [77]. Current understanding of the origins of the condition are unclear, meaning that non-surgical treatment techniques often focus on the correction of spinal curvature via the use of a brace worn by the patient [251]. There can be a significant negative impact on quality of life when wearing restrictive braces for prolonged periods, however, with Tones *et al.* noting in their 2006 review how psycho-social considerations have driven the search for lower-profile brace designs [239]. Furthermore, the level of treatment success has been found to link directly to how well and consistently the patient wears the brace [219].

A brace designed to minimise psychological impact on the user (*i.e.* fitting close to the body and being no more restrictive than necessary) and maximise treatment effectiveness (*i.e.* by providing sufficiently stiff support for the desired bodily degrees of freedom) is thus desirable.

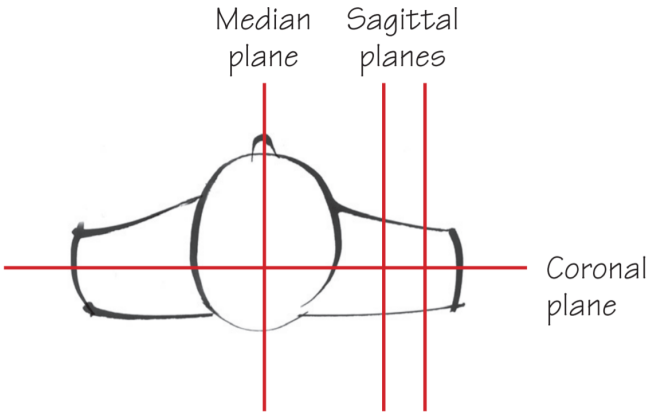

Figure 6.1: *A top-down view of the locations of the median (and parallel sagittal) and coronal anatomical planes of a human. Reproduced from Ref [58].*

To this end, work at TU Delft has been carried out to investigate braces comprised of selectively-compliant mechanisms, with the intention to find lower-profile designs that provide corrective forces to the spine while enabling the patient to retain kinematic freedom in non-critical directions. Such freedoms may include increased sagittal bending, defined as a bodily rotation parallel to a sagittal plane, and coronal torsion, defined as a bodily rotation of the coronal plane (see Figure 6.1, reproduced from [58], for an illustration of the anatomical planes). Nijssen *et al.* proposed a first iteration of a scoliosis brace by utilising multiple compliant mechanism building blocks to construct a hybrid brace [168, 170]. By considering the required 'pressure profile' of forces (and their application points) required to correct the spinal curvature, multiple isotropic shell mechanisms could be selected and connected by rigid joints to meet a series of kinetic and kinematic requirements. Figure 6.2 (reproduced from [170]) shows the final brace assembly. Strapping components under the arms and above the hips mount the brace to the patient, while selected shell mechanisms restrict movement and provide forces to the body in a manner tailored to the patient's needs. While the high level of building block selection allows for detailed matching of force profiles, the resulting brace is very complex in terms of the number of parts, and would be complex to manufacture, assemble and wear.

Subsequent brace designs by Dries and Leemans focused on the generation of a semi-rigid brace concept [51, 139]. By dividing a fully-rigid brace into two rigid sections connected by a single compliant shell mechanism they aimed to design a brace that could restore some movement freedoms (and hence improve quality of life)

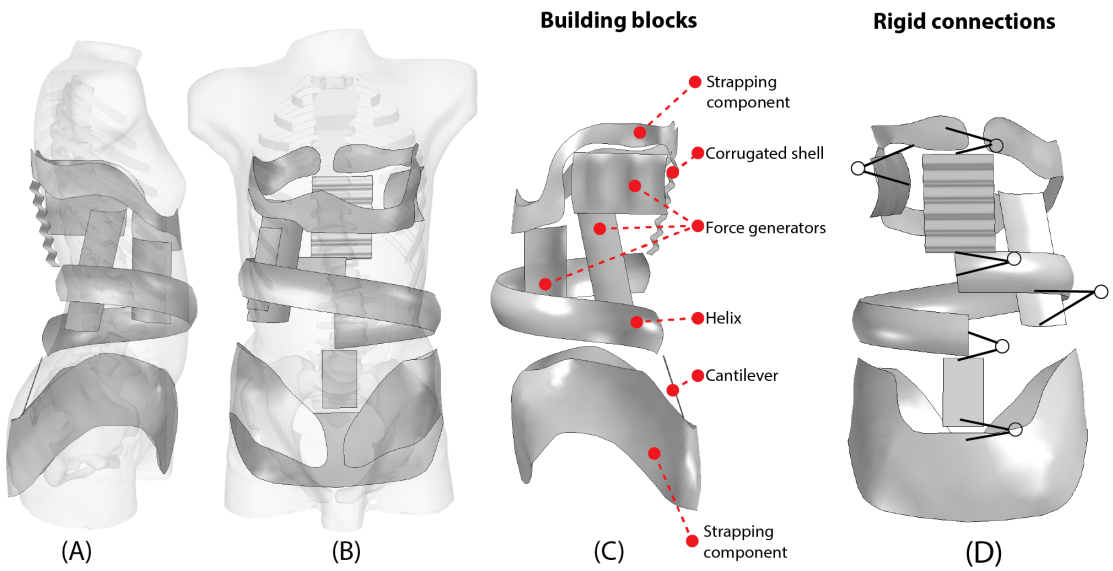

Figure 6.2: *Nijssen's building block brace design: (A) and (B) show brace views superimposed on the patient torso, while (C) and (D) show the individual mechanisms and their rigid connectors respectively. Reproduced from Ref [168].*

to the patient while still providing sufficient forces to correct spinal misalignment. By measuring spinal forces and movements they identified the kinetic requirements of the brace, and Dries proposed a compliant mechanism concept brace, shown in Figure 6.3a (reproduced from [51]).

A single-mechanism semi-rigid brace design was developed by Kooistra and Kim, who focused on identifying a compliant mechanism that would meet the kinetic requirements and permit movement in one degree of freedom that aligned with the sagittal bending axis of the patient [111, 120]. Their proposed design consists of two helical shells wrapped around the torso, each with a sinusoidal cross-sectional curvature. The helices are joined at two rigid supports worn by the patient on the upper and lower torso as shown in Figures 6.3b and 6.3c (reproduced from [120]). The idea is to increase the stiffness of all the patient's degrees of freedom, but allowing sagittal bending to remain relatively compliant.

Kim explains how the 180° sinusoidal helix enables high stiffness degrees of freedom while permitting sagittal bending [111]. A compliant eigentwist axis orthogonal to the helix central axis enables the sagittal bending, and the helix symmetry ensures that the other two eigentwists are orthogonal to the sagittal one. In addition, the cross-sectional sinusoidal curvature ensures that low stiffness sagittal behaviour becomes dominant (for an isotropic case) as the twist axes from each of the individual helix mechanisms overlap when they are joined. In Kooistra's design, the sagittal bending eigentwist was designed to be $5\times$ more compliant than then next degree of freedom, although this required that the shell cross-section (a half-sine

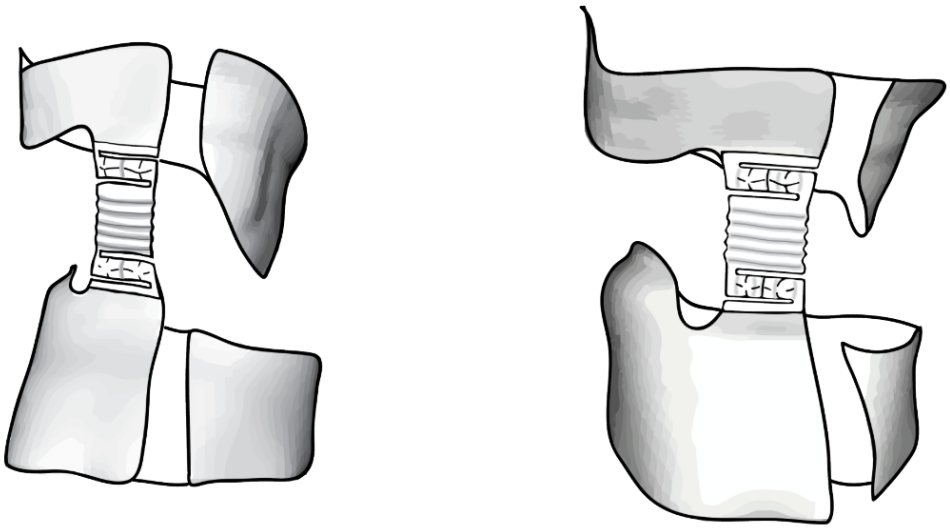

(a) *Brace designed for sagittal and lateral bending using a single corrugated compliant shell mechanism that connects two rigid support structures, reproduced from Ref [51]. The central corrugations improve the compliance and relative dominance of the sagittal bending degree of freedom, while the corrugations at the top and bottom enable lateral bending also.*

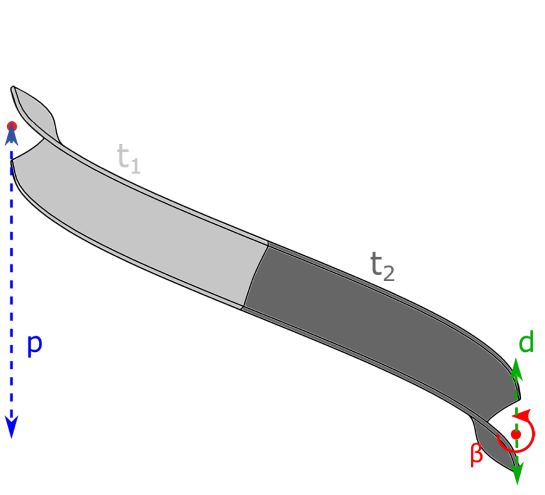

(b) *Kooistra's helical mechanism showing optimisation variables. Reproduced from Ref [120].*

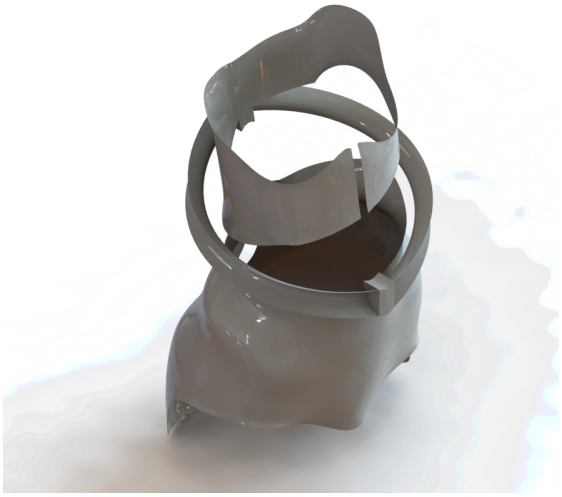

(c) *Kooistra's helical mechanism brace design with supporting structures. Reproduced from Ref [120].*

Figure 6.3: *Mechanism-based scoliosis brace designs from TU Delft that focus on replacing the midriff of a fully-rigid brace with a compliant mechanism.*

curve) had a large amplitude of 16 mm. The drawback of such a high amplitude (and thus curvature) is that the brace protrudes further from the patient body, and is therefore far more conspicuous when worn.

Kooistra used the previously-identified kinetic requirements and a path-following optimisation technique for the primary compliance vector to generate an isotropic sinusoidal helix brace mechanism with a step-change in thickness occurring at the brace mid-distance [120]. While the geometry of Kooistra's brace is more general than the tape spring mechanisms in Chapter 5 (*i.e.* a helical structure with non-zero Gaussian curvature), it still provides a clear datum line with which to align continuous fibre composites. This, and the fact that the initial design was characterised with eigenscrews, means that the brace is a suitable benchmark design case for a general-geometry composite compliant mechanism.

Inspired by this previous research, the work detailed in this chapter focuses on exploring the potential of utilising composite materials in a similar brace mechanism, with a view to matching the singular degree of freedom requirement (defined here as sagittal bending that is at least an order of magnitude more compliant than any other degree of freedom) using a composite helical mechanism with much more favourable geometry (*i.e.* a significantly reduced cross-sectional curvature that is less conspicuous). In addition the potential for using continuous fibre reinforced composites to position critical eigenscrew axes (to ensure alignment of brace and body axes) is investigated.

6.2 Unified Compliance Magnitudes

In Chapter 5 separate graphs of rotational and translational compliances were presented for the compliant mechanisms. In order to be able to directly compare the compliances of translational and rotational degrees of freedom, especially when trying to determine which type of deformation is dominant (*i.e.* least energetic), an additional step is required, namely the calculation of unification lengths. Leeman's *et al.* recognised that translational compliances, a_f, are displacements per unit force [m/N], whereas rotational compliances, a_γ, are given as angles divided by torques [rad/Nm], and introduced two methods of converting the units via the use of 'unification lengths' χ_i and ψ_i, where $i = 1, 2, 3$ and corresponds to the three twist axes [139].

The first approach is to express rotational compliances as equivalent translational compliances, $\tilde{a}_{f_i}$ ("RasT"), *i.e.*

$$\tilde{a}_{f_i} = \chi_i^2 a_\gamma, \tag{6.1}$$

while the second approach is to express translational compliances as equivalent ro-

tational compliances $\tilde{a}_{\gamma_i}$ ("TasR"), *i.e.*

$$\tilde{a}_{\gamma_i} = \frac{a_{f_i}}{\psi_i^2}. \tag{6.2}$$

Leemans' "RasT" approach has three steps to determine χ_i. Firstly, equivalent translations of the POI, δ_{eq_i}, are expressed in terms of rotation about the twist axis

$$\delta_{eq_i} = \sqrt{\delta_{r_i}^2 + \delta_{h_i}^2} = \sqrt{(|r_i|\theta_i)^2 + (h_i\theta_i)^2}, \tag{6.3}$$

where h_i are the twist pitches, r_i are the twist location vectors, δ_{r_i} are the rotational displacements of the POI around the twist axis, and δ_{h_i} are the translational displacements of the POI parallel to the twist axis. Secondly, equivalent virtual forces, F_{eq_i}, are expressed at the POI in terms of the parallel moment that corresponds to rotation about the twist axis. This is done by defining virtual forces, F_{m_i}, which act at a distance r_i to produce an equivalent moment to a pure parallel moment caused by rotation

$$F_{m_i} = \frac{M_i}{r_i}, \tag{6.4}$$

and then considering the angle, β_i, which is the angle between each equivalent force, F_{eq_i}, and corresponding virtual force, F_{m_i}, as well as between each equivalent displacement, δ_{eq_i}, and corresponding virtual displacement, $\delta_{\gamma r_i}$,

$$\beta_i = \frac{F_{m_i}}{F_{eq_i}} = \frac{\delta_{eq_i}}{\delta_{\gamma r_i}} = \frac{\sqrt{h_i^2 + |r_i|^2}\theta_i}{|r_i|\theta_i}. \tag{6.5}$$

This expression rearranges to give

$$F_{eq_i} = \frac{M_i}{\sqrt{h_i^2 + |r_i|^2}\theta_i}. \tag{6.6}$$

Finally, equivalent translational compliances, $a_{f\gamma_i}$, are calculated by dividing the previous two expressions

$$a_{f\gamma_i} = \frac{\delta_{eq_i}}{F_{eq_i}} = \chi_i^2 \frac{\theta_i}{M_i} = (h_i^2 + |r_i|^2)\frac{\theta_i}{M_i}. \tag{6.7}$$

This gives an expression for the "RasT" unification lengths

$$\chi_i = \sqrt{h_i^2 + |r_i|^2}, \tag{6.8}$$

The "TasR" approach for determining ψ_i is similar: (i) express an equivalent rotation of the POI in terms of translation parallel to the wrench axis; (ii) express an equivalent virtual moment at the POI in terms of the force that corresponds to

translation parallel to the wrench axis; and (iii) calculate an equivalent rotational compliance by dividing the previous two expressions. This gives an expression for the unification length

$$\psi_i = \sqrt{|d_i|^2 + b_i^2}, \tag{6.9}$$

where ψ_i are the "TasR" unification lengths, d_i are the wrench torque-to-force ratios and the b_i terms determine the spatial positioning. For full details of these derivations see Ref [139]. These lengths allow direct comparison of the wrench and twist compliance magnitudes as they are made to be work-equivalent.

One limitation of these unification lengths is that they are equal to zero in cases where the screw axes have zero pitch (*i.e.* $h_i = 0$ or $b_i = 0$) and the eigenscrew positions lie on the POI (*i.e.* $r_i = 0$ or $d_i = 0$) and thus cannot be used. This was the case for the tape springs in Chapter 5 as in some cases the twist and wrench axes lay along the shell surface in-line with the POI. As the scoliosis brace geometry is more complex (*i.e.* r_i and $d_i = 0$ will not be zero), the unification lengths can be used to compare twist and wrench compliances like for like.

6.3 Brace Geometry & Load Cases

For the investigations three brace geometries were investigated: a 'flat' brace with no cross-sectional curvature, and two sinusoidal braces (one with curvature matching Kooistra's brace, and one with a reduced curvature). The flat helix geometry can be expressed as

$$x = r_{\mathrm{H}} \cos(u_1), \tag{6.10}$$

$$y = r_{\mathrm{H}} e \sin(u_1), \tag{6.11}$$

and

$$z = p|u_1| + w. \tag{6.12}$$

where x, y and z are the Cartesian coordinates of the brace nodes, r is the internal radius of the helix (with e describing any radius eccentricity), u_1 refers to the revolution angle of the helix (*i.e.* for a half-revolution helix $0 \leq u_1 \leq \pi$), w refers to the range of widths specified from the helix centre-line (*i.e.* $-w/2$ to $w/2$), and p refers to the mechanism's helical pitch.

The sinusoidal helix geometry can be expressed as

$$x = r_{\mathrm{S}} \cos(u_1), \tag{6.13}$$

$$y = r_{\mathrm{S}} \sin(u_1) + (e-1) r_{\mathrm{S}}^0 \sin(u_1), \tag{6.14}$$

Table 6.1: *Scoliosis Brace Parameters Investigated*

	Flat Brace	Shallow Sinusoidal Brace	Deep Sinusoidal Brace
Helix Radius, r_{H} or r_{S}	88 mm		
Helix Angles, u_1	$0 \leq u_1 \leq \pi$ radians		
Radial Eccentricity, e	1.25		
Helix Pitch, p	$127/\pi$ mm/radian		
Helix Width, w	30 mm		
Helix Total Thickness, H	0.5 mm		
Sinusoidal Amplitude b	N/A	5 mm	10 mm
Sinusoidal Angle, u_2	N/A	N/A	$0 \leq u_1 \geq 2\pi$ radians

and

$$z = p|u_1| + w. \tag{6.15}$$

Figure 6.4 illustrates some of the key terms for the sinusoidal helix geometry. Note that for the sinusoidal length the width, w, refers to the absolute distance between one edge of the helical shell and the other, not the circumference caused by the cross-sectional curvature. Also r_{S} is a modified radius term that takes into account the cross-sectional curvature effect on the radial position of each node as

$$r_{\mathrm{S}} = r_{\mathrm{H}} - b\sin(u_2). \tag{6.16}$$

Here b refers to the amplitude of the sinusoidal curvature, u_2 refers to the sinusoidal curvature angle (*i.e.* $0 \leq u_2 \leq \pi$), and r_{S}^0 refers to the minimum value of r_{S}. Table 6.1 details the specific values used for the above terms in the models detailed in this chapter, chosen to match those used by Kooistra [121], although in that work the sinusoidal amplitude, b, was larger at 16 mm.

The POI for the helical mechanisms was located at the central node at one end of the helices, with encastre boundary conditions applied at the other end, as shown in Figures 6.5 and 6.6. For braces with composite laminates the 0° fibre datum line was taken to be the helix line as shown in Figure 6.5. Finite-element models (comprising 15 nonlinear static analysis steps to model incremental loading) were made for each brace to determine its stiffness and compliance matrices in the same manner as described in Chapter 5. Mesh convergence was based on achieving total mechanism deflection distances within 0.5%, resulting in models with 150 elements along each helix length, and 10 elements across each helix width (see Figure 6.6).

As in Chapter 5, loads were applied at the POI, as this would reflect the fact that torso loads would be applied to the compliant mechanism via the rigid support that was connected at this location. During sagittal bending, the load applied by the torso to a brace is a complex (and unknown) combination of translational force and bending moment. The objective of this work was not to model torso loads

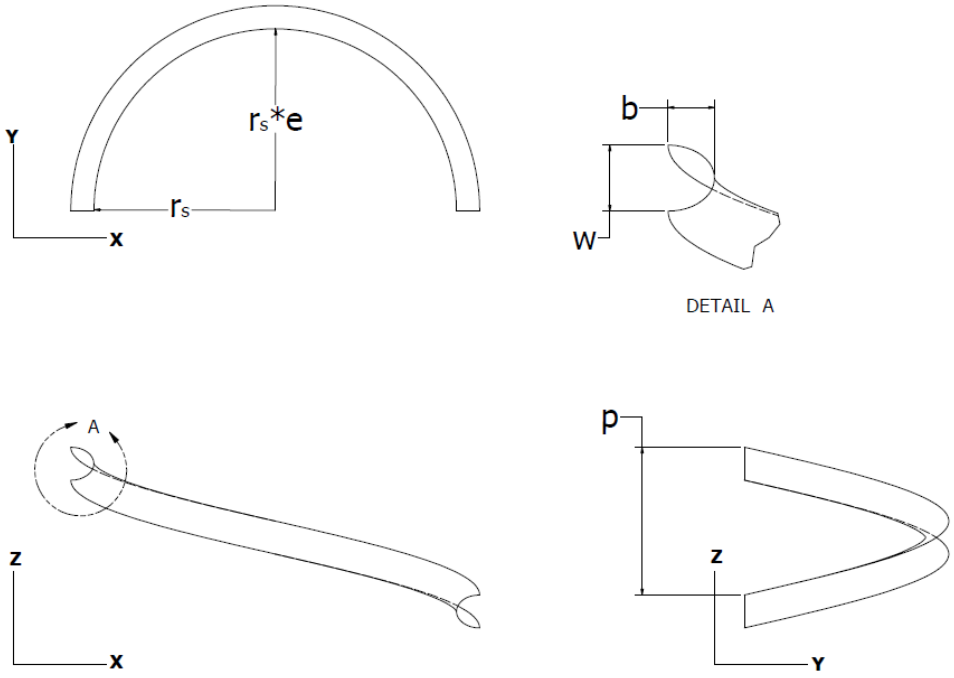

Figure 6.4: *Illustration of one half of the sinusoidal helix, highlighting key dimensions defining the geometry.*

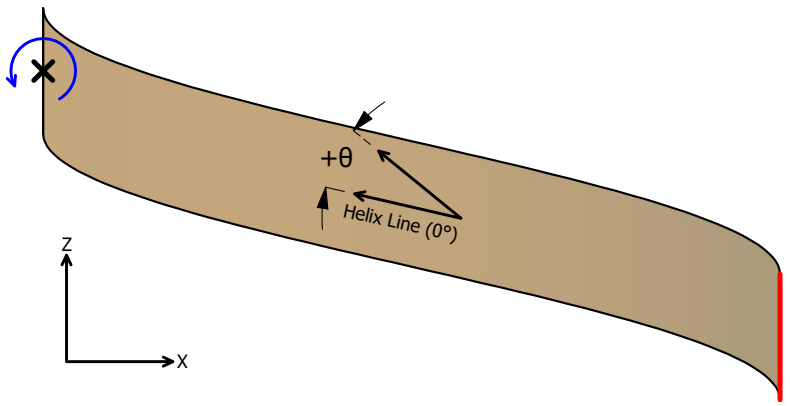

Figure 6.5: *Schematic of a flat brace showing the fibre angle datum (the helix line) and fibre angle θ, the POI at the centre of one end (cross), the fixed edge (red line) and the applied bending moment (blue arrow)*

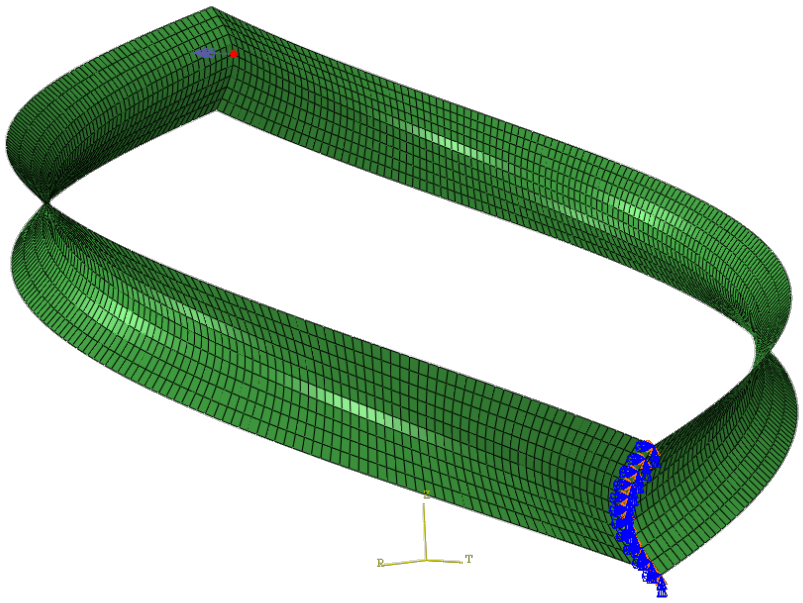

Figure 6.6: *Example finite element model for a sinusoidal brace showing the applied bending moment (purple arrow) applied to the POI (red dot) and the encastre boundary conditions (orange and blue triangles) applied at the fixed end.*

accurately, but to assess the eigenscrew characteristics of a brace mechanism, which would be dependent on the deformed shape of the mechanism; thus, for simplicity, the torso loading was assumed to be either a point-load (initially normal to the torso) or a bending moment, both of which would 'follow' the POI movement and rotation during deformation. It was observed from initial models that for these mechanisms the deformation was similar whether a follower point-load or follower bending moment was used. Consequently, to enable more direct comparisons with Kooistra's work the torso load was modelled as just a bending moment acting at the POI, with magnitude based on what would achieve broadly similar amounts of brace deformation: 100 Nmm for the flat braces and 200 Nmm for the sinusoidal braces.

6.4 Isotropic Brace

The first stage of the investigation was to explore the effects of geometry on the brace behaviour for isotropic materials before including anisotropic composite laminates. The isotropic case considered used the same material and layup as the fully-isotropic laminate described in Chapter 5, and the tables containing the material property values can be found in Chapter 2. The variables to be compared were the compliance magnitudes and positions of the eigenscrews. Of particular interest is the sagittal

bending eigentwist, where the objective was to achieve a sagittal bending compliance 10× greater than any other eigenscrew to demonstrate that enabling additional movement freedom for the patient is feasible.

6.4.1 Loaded Responses

Figures 6.7 and 6.8 show the unloaded, mid-deformation and fully-deformed shapes of the different isotropic brace designs investigated during this work. It can be seen that each type of brace undergoes a similar symmetrical deformation path, and that the orientation of the key design twist (the green $\hat{T}_3$ sagittal bending eigentwist) does not change. This symmetrical pattern of deformation was observed in all the brace designs investigated (including those with anisotropic laminates) suggesting that the brace geometry dominates the deformation pathway for this load case. As there is no re-orientation of the sagittal twist axis, twist orientation plots like those from Chapter 5 are less useful for the designer and are not shown in this chapter.

Figure 6.9 shows the changes in unified compliance magnitudes during loading for the most dominant eigenscrews of the flat and sinusoidal isotropic braces. Eigenscrew compliances $< 1 \times 10^{-6}$ are not shown so as to enable clearer comparisons of the eigenscrews where compliances are highest. As the relative differences in compliances between the different eigenscrews are more extreme in this mechanism than for the tape springs of Chapter 5, the compliance magnitudes are plotted on logarithmic scales. It can be seen from Figure 6.9a that the most dominant (*i.e.* most compliant) eigenscrew is the red $\hat{w}_1$ wrench, which corresponds to a lateral translation of the POI for the flat mechanism, while the desired green $\hat{T}_3$ sagittal bending eigentwist varies between second-most and third-most compliant. The brown $\hat{w}_2$ wrench is also very compliant, and represents a vertical translation of the POI. It can also be seen that as the brace mechanism deforms with loading, the compliance of these more dominant degrees of freedom increases slightly.

Comparing Figure 6.9a with Figure 6.9b illustrates why Kooistra chose a sinusoidal helix as opposed to a flat helix [120]: the $\hat{T}_3$ sagittal bending eigentwist is dominant for small loads and deformations, and secondary degrees of freedom (*i.e.* blue $\hat{T}_1$ and teal $\hat{T}_2$ twists, and yellow $\hat{w}_2$ wrench) have become negligibly small in comparison to this degree of freedom. Including a small cross-sectional curvature ($b = 5\,\text{mm}$) has made all the eigenscrews stiffer, but the desired sagittal bending eigentwist is now the initial preferred deformation mode for the unloaded brace. In these sinusoidal braces the red $\hat{w}_1$ wrench is still the next most dominant in terms of compliance, although it now corresponds to a vertical translation of the POI, while the brown $\hat{w}_2$ wrench corresponds to the lateral translation, which is now the third-most dominant behaviour. Increasing the curvature ($b = 10\,\text{mm}$) as shown in

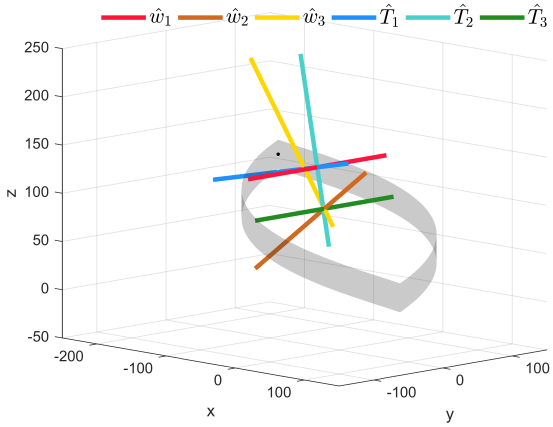

(a) *Unloaded configuration*

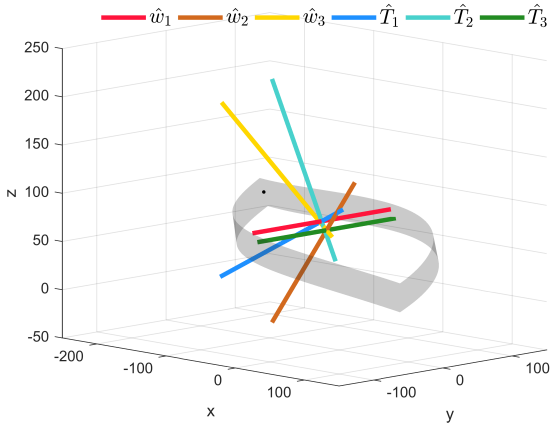

(b) *Applied follower moment of* 50 Nmm

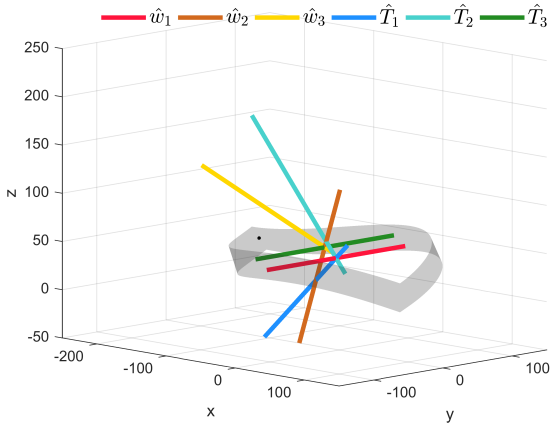

(c) *Applied follower moment of* 100 Nmm

Figure 6.7: *Deformed shapes of the flat isotropic brace mechanisms*

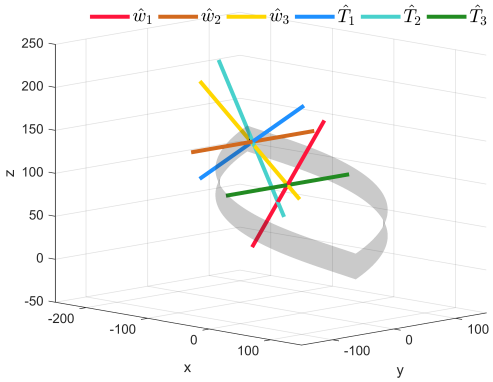

(a) $b = 5\,\text{mm}$, *unloaded configuration*

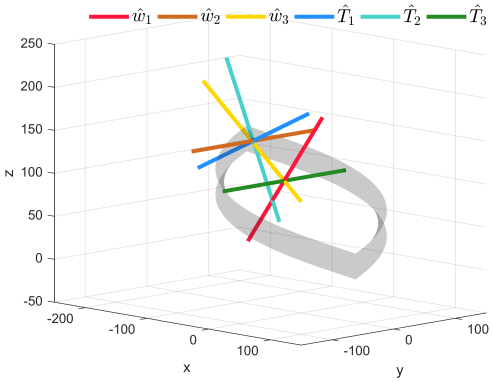

(b) $b = 10\,\text{mm}$, *unloaded configuration*

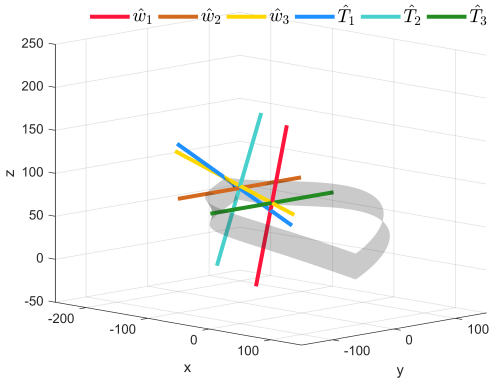

(c) $b = 5\,\text{mm}$, $M = 100\,\text{Nmm}$

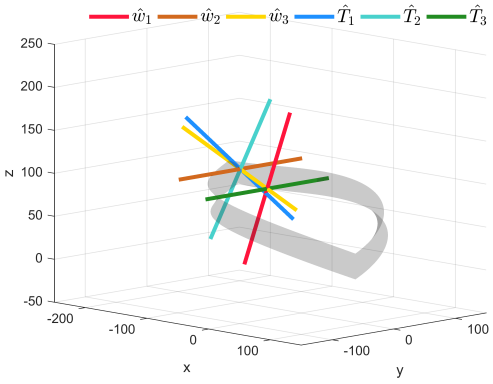

(d) $b = 10\,\text{mm}$, $M = 100\,\text{Nmm}$

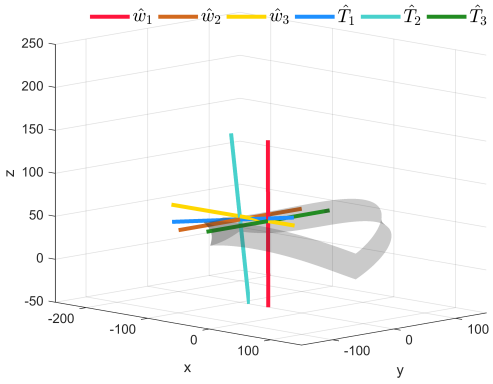

(e) $b = 5\,\text{mm}$, $M = 200\,\text{Nmm}$

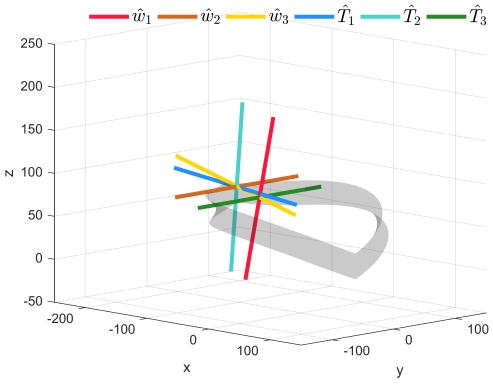

(f) $b = 10\,\text{mm}$, $M = 200\,\text{Nmm}$

Figure 6.8: *Deformed shapes of the sinusoidal isotropic brace mechanisms with different sinusoidal curvatures, b, and applied follower moments M.*

Figure 6.9c further reduces the eigenscrew compliance magnitudes, but changes the relative regions of dominance (in terms of applied load) of the $\hat{T}_3$ and $\hat{w}_1$ screws very little. That said, while these curvature have had a large impact on the compliance magnitudes and relative dominance of different twists and wrenches, they alone are insufficient to provide sagittal bending that is an order of magnitude more compliant than the next degree of freedom. Further increases in the cross-sectional curvature may help increase the $\hat{T}_3$ dominance, but this would undermine efforts to reduce the brace profile.

6.5 Single-Ply Anisotropic Brace

Before considering more tailored laminates, it is worth investigating mechanism designs comprised of one single-ply unidirectional laminate, and assessing the effects of varying that fibre angle on the eigenscrews (see Figure 6.5 for the fibre angle datum definition). Although designs are unlikely to be chosen using a single fibre direction, this approach enables an assessment of maximum potential that material anisotropy (and its orientation) has for tailoring the behaviour of the brace mechanism.

6.5.1 Effects on Initial Brace Responses

Figure 6.10 shows the changes in eigenscrew magnitudes of the unloaded flat and sinusoidal braces as a function of the fibre angle. Figure 6.10a shows that, for the flat helix the maximum sagittal bending compliance is achieved using fibres aligned at approximately $\theta = 75°$ to the helix datum line, although it is most dominant for $\theta = 0°$. It can be seen that a simple change of fibre angle can affect the eigenscrew order of dominance significantly, with the green $\hat{T}_3$ sagittal bending wrench being first, second and third most dominant depending on the fibre angle. Figures 6.10b and 6.10c show that as cross-sectional curvature is introduced the green $\hat{T}_3$ sagittal bending eigentwist becomes dominant (like in the isotropic cases). For this mechanism the greatest sagittal bending compliance is achieved when the fibres are orientated at 90° to the helix datum line, as in this orientation the bending stiffness of each helical strip is most dependant on the composite matrix, and not the fibres.

6.5.2 Effects on Unloaded Sagittal Axis Positions

Figure 6.11 shows the changes in relative position of the sagittal bending axis in the XZ plane as the fibre angle sweeps from 0° to 90°. Ensuring consistent alignment of the mechanism sagittal bending axis and the body sagittal bending axis is an important factor in designing a mechanism for a scoliosis brace, although precisely

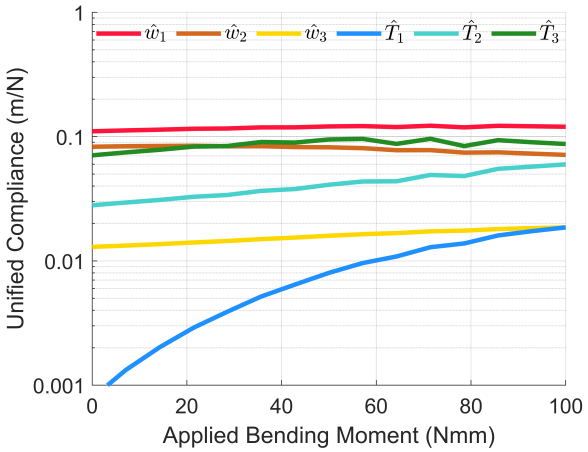

(a) *Flat isotropic brace ($b = 0$)*

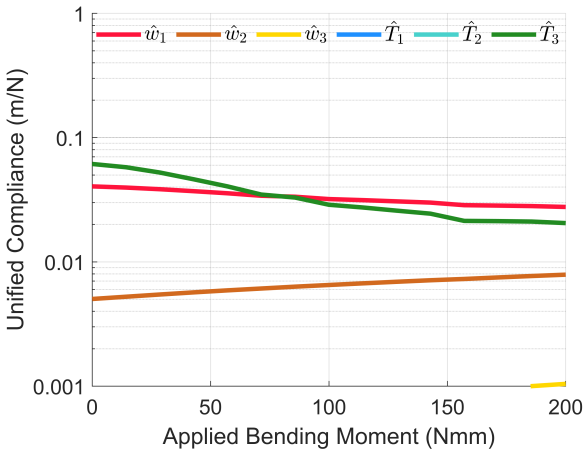

(b) *Sinusoidal isotropic brace with $b = 5\,\mathrm{mm}$*

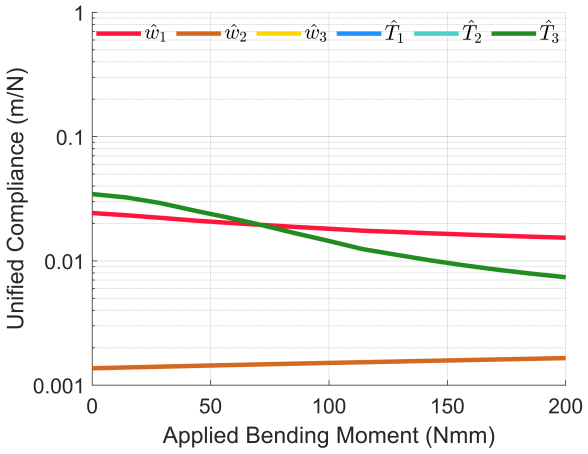

(c) *Sinusoidal isotropic brace with $b = 10\,\mathrm{mm}$*

Figure 6.9: *Unified compliance magnitudes against applied load for isotropic brace configurations*

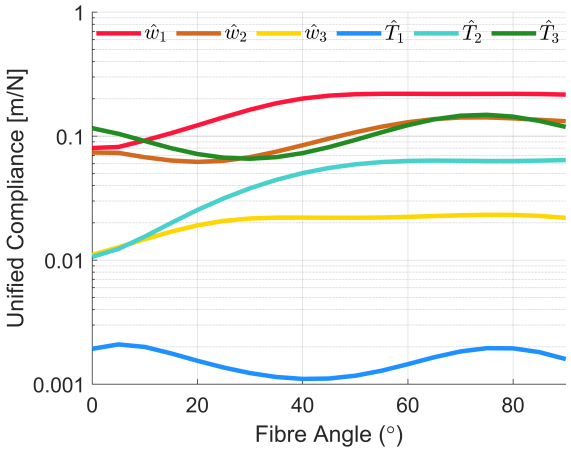

(a) *Unloaded flat braces ($b = 0$)*

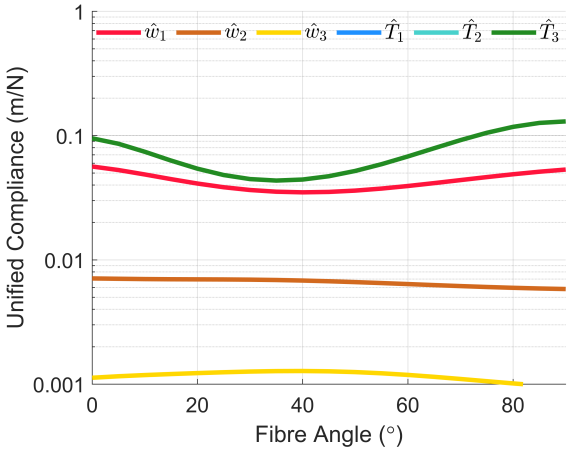

(b) *Unloaded sinusoidal braces with $b = 5\,\mathrm{mm}$*

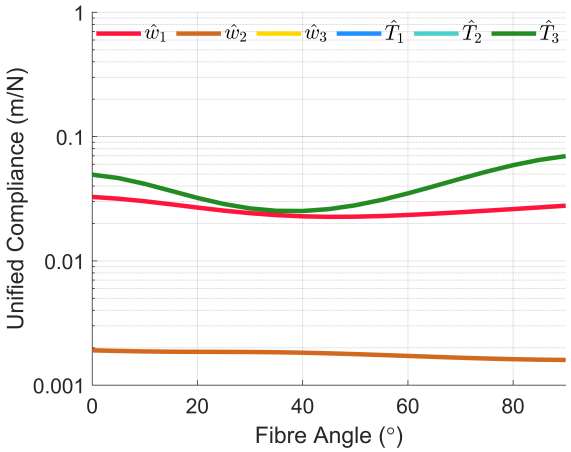

(c) *Unloaded sinusoidal braces with $b = 10\,\mathrm{mm}$*

Figure 6.10: *Fibre angle effects on the unified compliance magnitudes of unloaded braces comprised of single-ply anisotropic layups*

locating the position of the body bending axes of a patient can be difficult. As such, the relative displacement of the mechanism axis position is plotted as opposed to its absolute positions. It can be seen that although inclusion of composite anisotropy in the helical brace mechanisms does relocate the sagittal bending axis, the magnitudes of the relative changes in position are so small as to unlikely be helpful, with only a few millimetres of movement realistically possible via material orientation. Inspection of Figures 6.7 and 6.8 suggests that sagittal axis position is more dependent on the brace geometry, with the axis moving further forward as the braces deflect. Tailoring the amount of sinusoidal curvature near the central region of the mechanism may be the best way to control the position of this twist axis.

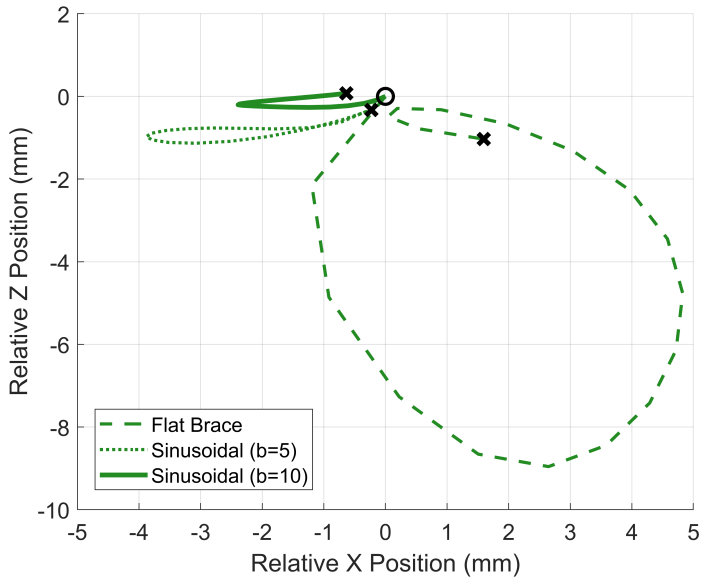

Figure 6.11: *Relative positions of the sagittal bending axis on the XZ plane as the fibres sweep from 0° (○) to 90° (×). The potential for shifting the twist axis using fibre lay-up is much reduced for geometry-dominated braces.*

6.5.3 Effects on Loaded Brace Responses

The trends in Figure 6.10 only provide insight into the effect of fibre angle on the initial response of the brace. In comparison Figure 6.12 shows the change in eigenscrew compliances during loading for flat brace mechanisms with varying fibre angles.

The results in Figure 6.12 confirm that for the flat brace the $\hat{T}_3$ sagittal bending eigentwist is only dominant for small fibre angles ($\theta = 0°$). The relative compliance of the $\hat{T}_3$ twist axis also does not change significantly or beneficially throughout loading. For all fibre angles, the $\hat{T}_2$ twist axis (body torsion axis) is seen to increase in compliance throughout loading.

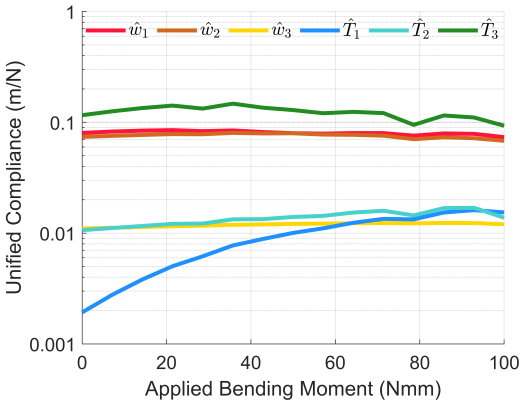

(a) *Fibre angle* $\theta = 0°$

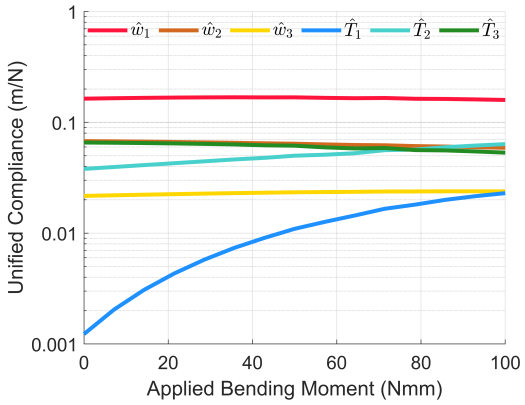

(b) *Fibre angle* $\theta = 30°$

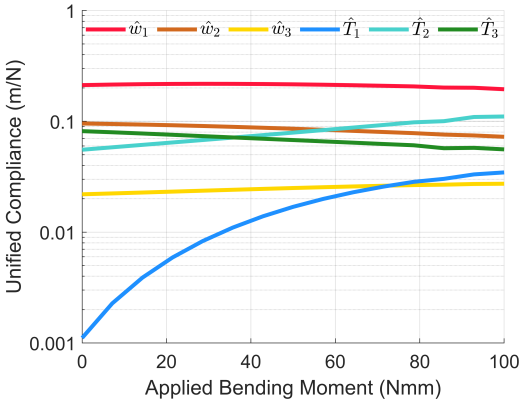

(c) *Fibre angle* $\theta = 45°$

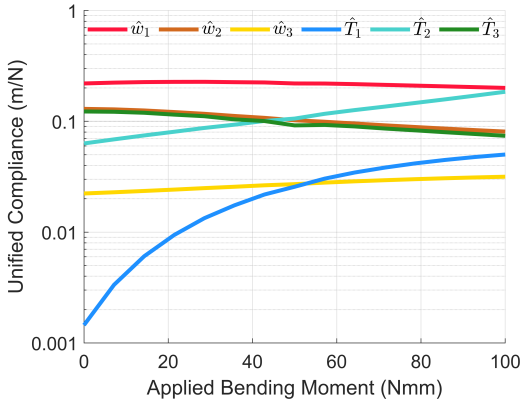

(d) *Fibre angle* $\theta = 60°$

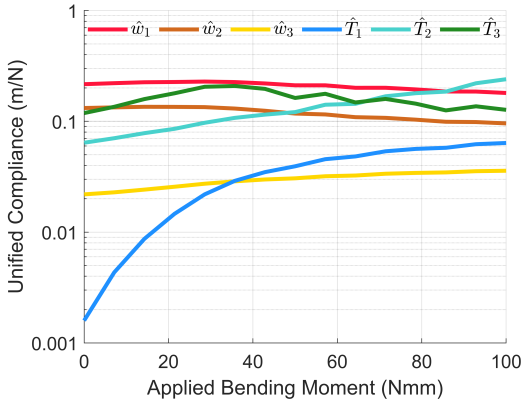

(e) *Loaded flat brace where* $\theta = 90°$

Figure 6.12: *Fibre angle effects on the unified compliance magnitudes of loaded isotropic flat* ($b = 0$) *braces comprised of single-ply anisotropic layups*

Figure 6.13 shows the eigenscrew compliances for five different sinusoidal mechanisms each with a different fibre angle. Given the similarity of the trends in Figures 6.10b and 6.10c only plots for loaded shallow sinusoidal mechanisms are shown (*i.e.* $b = 5\,\text{mm}$). The sagittal bending dominance shown in Figure 6.10b can be seen for every fibre angle case, but now the extent of the dominance (in terms of applied load) can be seen, with sagittal bending generally ceasing to be dominant between 25% and 50% of the loads applied in this study. As predicted by Figure 6.10b, maximum sagittal compliance is present in the $\theta = 90°$ case, although it is at most only $2.44\times$ as compliant as the red $\hat{w}_1$ vertical translation wrench, and this gap decreases further with even small applied loads. Overall these results show that using a single fibre angle is insufficient to achieve the desired response over the range of motion of the brace mechanism.

6.5.4 Matrix Conditioning

In Figures 6.12a and 6.12e, a degree of 'jaggedness' can be seen in plots of compliance magnitude for the flat braces. As the brace deflections appeared smooth, this jaggedness was unexpected. Further, it appeared for fibre angles close to 0° or 90°, but plots of compliance magnitudes for fibre angles between 10° and 80° were smooth, as were plots for the sinusoidal braces.

Several hypotheses were considered for the jaggedness. Increasing the number of load steps in the FE models did not reduce it, suggesting that the jaggedness is not a physical response poorly captured by overly-coarse increments of the applied load. The unification lengths were also considered as a potential issue in case r_i and d_i terms were close to zero, but plotting the non-unified compliances (in a similar manner to those Chapter 5) did not remove the jaggedness either. The double precision of the stiffness matrices generated in the FE code was also confirmed to be preserved throughout post-processing.

As no obvious problem could be found with the model setup or post-processing it is supposed that this jaggedness is due to the fact that stiffness matrices are generally poorly conditioned. The condition number of a matrix in a function gives an indication of how sensitive the function output is to variations in the function input (*e.g.* the condition number for a stiffness matrix would indicates how sensitive the output stresses are to perturbations in the input strains). The MATLAB function `rcond` was used to obtain the reciprocal condition number for the stiffness matrix [151]. A well-conditioned matrix will have a value close to 1.0, whereas a poorly conditioned matrix will have a value close to 0.0.

Figure 6.14 shows comparisons of the matrix reciprocal condition numbers for loaded flat brace mechanisms with different fibre orientations. It can be seen that

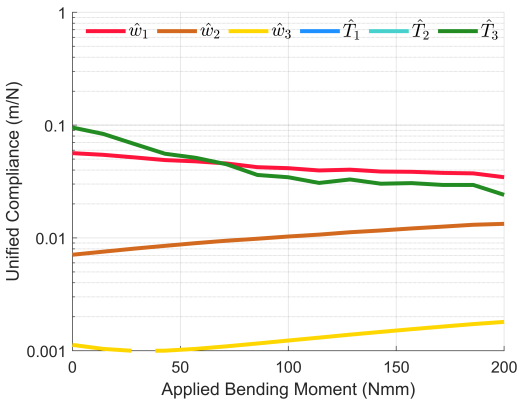

(a) *Fibre angle* $\theta = 0°$

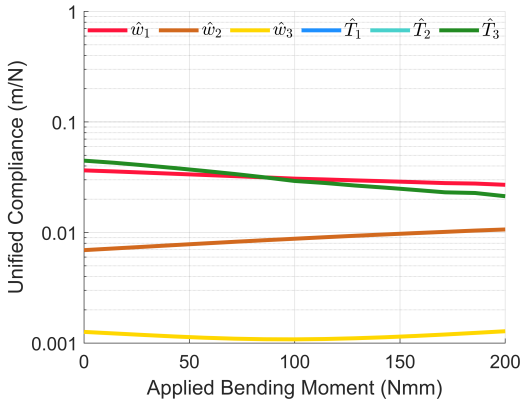

(b) *Fibre angle* $\theta = 30°$

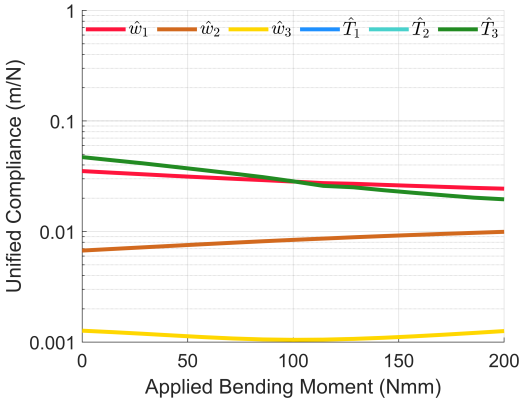

(c) *Fibre angle* $\theta = 45°$

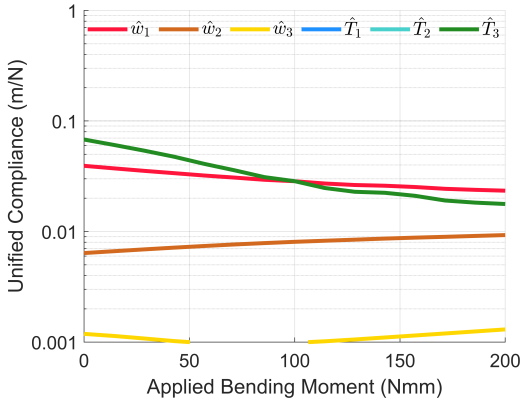

(d) *Fibre angle* $\theta = 60°$

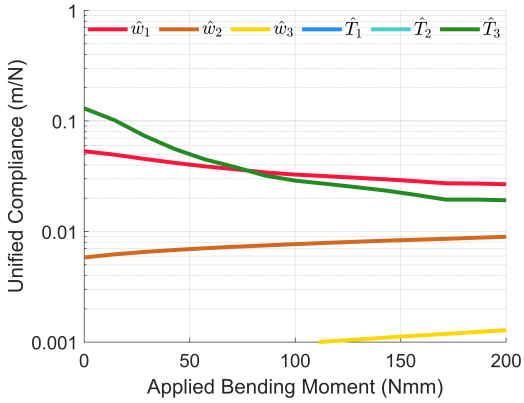

(e) *Fibre angle* $\theta = 90°$

Figure 6.13: *Fibre angle effects on the unified compliance magnitudes of loaded sinusoidal* ($b = 5\,\text{mm}$) *braces comprised of single-ply anisotropic layups*

the matrices all have very small reciprocal condition numbers and are thus poorly conditioned in all cases. This may mean that the jaggedness observed in some of the compliance magnitude plots is a result of numerical errors arising in the linear perturbation substructure analysis steps that generate the stiffness matrices in the FE model.

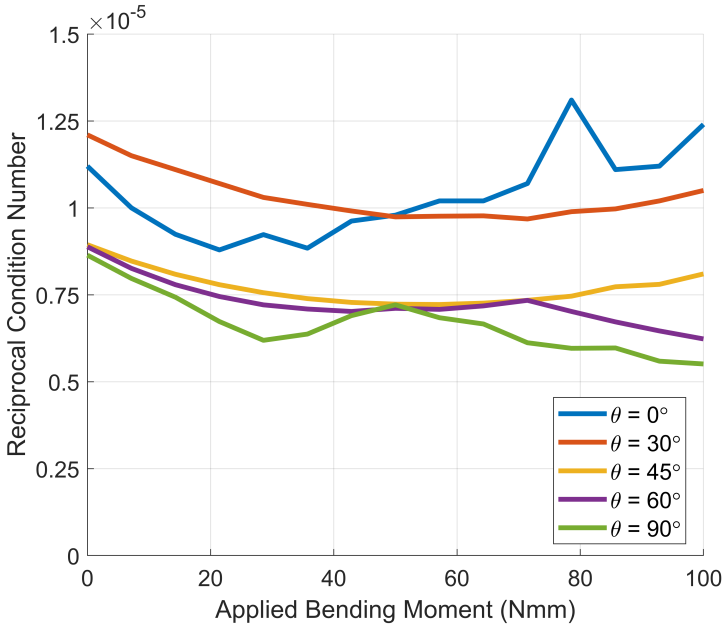

Figure 6.14: *Reciprocal condition numbers for the stiffness matrices of loaded flat brace mechanisms with different fibre angles*

Given that there have been very large differences in compliance magnitudes between the most and least compliant eigenscrews for many of these mechanism designs it is perhaps not surprising that the stiffness matrices are poorly conditioned and sensitive to input perturbations. It is worth noting that there appears to be similar levels of jaggedness for different magnitudes of condition number, so there may be other sources of error such as mesh refinement issues. Further investigation to confirm that compliance magnitude 'jaggedness' is linked to stiffness matrix conditioning or mesh definitions is recommended, as this can obscure the trends in compliance behaviour and limit the effectiveness of the eigenscrew characterisation for mechanisms with such matrices.

6.6 Segmented Brace

The response tailoring achievable using a generally orthotropic laminate (*i.e.* one fibre direction) for the entire brace has highlighted some potential benefits of introducing composite materials, but achieving a sagittal bending compliance that is an order of magnitude higher than the next degree of freedom has not been feasible. A potential solution is to tailor the layup of the helical strips to introduce desirable force-displacement couplings, *e.g.* if a section of the helix is twisting can the laminate be optimised to ensure that this also causes a desirable bending motion?

Layups could be varied across the brace to tailor the laminate properties depending on the loading or deformation in different segments. A first step in doing this is to explore the types of deformations (*e.g.* bending, torsion) across flat and sinusoidal braces with isotropic material properties to inform this selection. This is a preliminary design optimisation - full optimisation of the mechanism laminates is beyond the scope of this work.

6.6.1 Deformation Energies

Insight into the brace mechanism local deformations can be gained by calculating the shell bending and in-plane strain (membrane) energy densities for each element [22]. The bending strain energy density, U_b, is calculated for isotropic materials as

$$U_b = \frac{D}{2}\{(\kappa_{11} + \kappa_{22})^2 + 2(1-\nu)(-\kappa_{11}\kappa_{22} + (\kappa_{12})^2)\}, \tag{6.17}$$

where κ_{11} is the curvature along the helix line, κ_{22} is the curvature perpendicular to that, κ_{12} is the shell twist, ν is the isotropic Poisson's ratio and D is the material flexural stiffness defined as

$$D = \frac{EH^3}{12(1-\nu^2)}. \tag{6.18}$$

where H is the total shell thickness. The membrane energy density is calculated as

$$U_s = \frac{EH}{2(1-\nu^2)}\left\{(\epsilon_{11} + \epsilon_{22})^2 + 2(1-\nu)\left(-\epsilon_{11}\epsilon_{22} + \left(\frac{1}{2}\gamma_{12}\right)^2\right)\right\}. \tag{6.19}$$

Figures 6.15 shows the energy densities of the isotropic braces, plotted on the undeformed brace geometries. Firstly, the magnitudes of the energy densities indicate that the mechanism deflection is dominated by bending and twisting of the shell, with U_b maximum values being over an order of magnitude greater than U_s values. Secondly, this dominant shell bending predominantly occurs near the fixed end and POI end of the mechanism and is primarily a twisting of the brace, $\Delta\kappa_{12}$, as shown in Figure 6.16. Some bending about the helix line, $\Delta\kappa_{11}$, can be seen on the lower

edge of the central region (*i.e.* where the shell is in compression), and some bending perpendicular to the helix line, $\Delta\kappa_{22}$, can be seen in the region near to the POI, but these are much smaller in magnitude. This bending-dominant pattern appears in both the flat and sinusoidal cases, although the sinusoidal case involves slightly larger curvatures that are concentrated primarily in the region near the POI. Note that in Figures 6.16c and 6.16d the use of separate cylindrical axes for each half-helix causes each half-helix to appear to have opposite magnitude twisting: in reality the mechanism twisting is symmetrical and of equal magnitude in each half-helix.

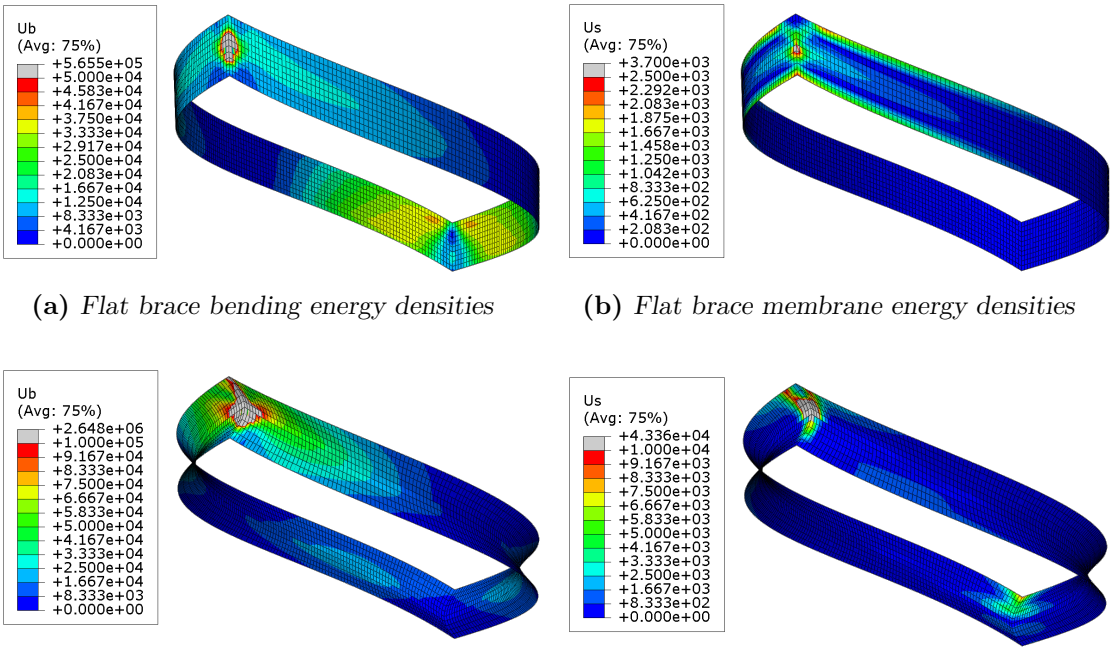

(a) *Flat brace bending energy densities* **(b)** *Flat brace membrane energy densities*

(c) *Sinusoidal brace bending energy densities* **(d)** *Sinusoidal brace membrane energy densities*

Figure 6.15: *Energy densities for flat and sinusoidal ($b = 10\,\text{mm}$) isotropic braces. Densities are taken with the follower moment applied at its maximal extent, and are plotted on the undeformed mechanism geometries.*

From these energy density plots it would seem that an optimal composite brace would be tailored to maximising the twisting of the shell near the POI and fixed ends of the mechanism. As a first step this could be done by dividing the mechanism into three equal-sized regions with laminates tailored to enhance twisting in the regions near the POI and fixed ends of the brace, and tailored to enhance global sagittal bending in the central region. Figure 6.17 shows a brace mechanism split into thirds, with the regions near the POI and fixed ends having laminates tailored to maximise twisting, and the central region (highlighted red) tailored for global bending.

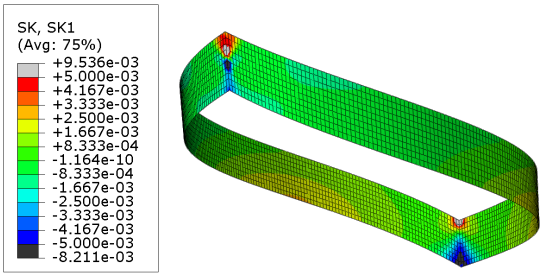

(a) *Changes in bending along the helix line,* $\Delta\kappa_{11}$*, for the flat brace*

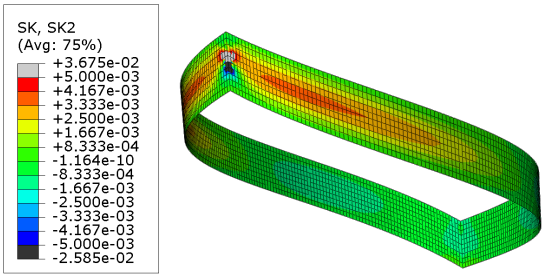

(b) *Changes in bending perpendicular to the helix line,* $\Delta\kappa_{22}$*, for the flat brace*

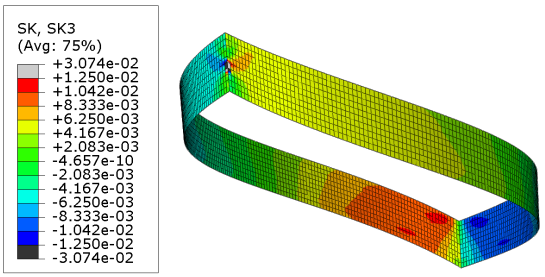

(c) *Changes in twist about the helix line,* $\Delta\kappa_{12}$*, for the flat brace*

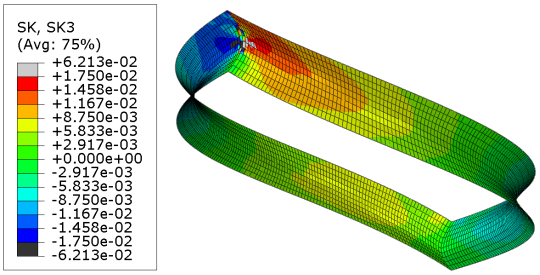

(d) *Changes in twist about the helix line,* $\Delta\kappa_{12}$*, for the sinusoidal* ($b = 10\,\text{mm}$) *brace*

Figure 6.16: *Changes in curvature* $\Delta\kappa$ *for the loaded brace mechanisms. Changes are measured with the follower moment applied at its maximal extent, and are plotted on the undeformed mechanism geometries.*

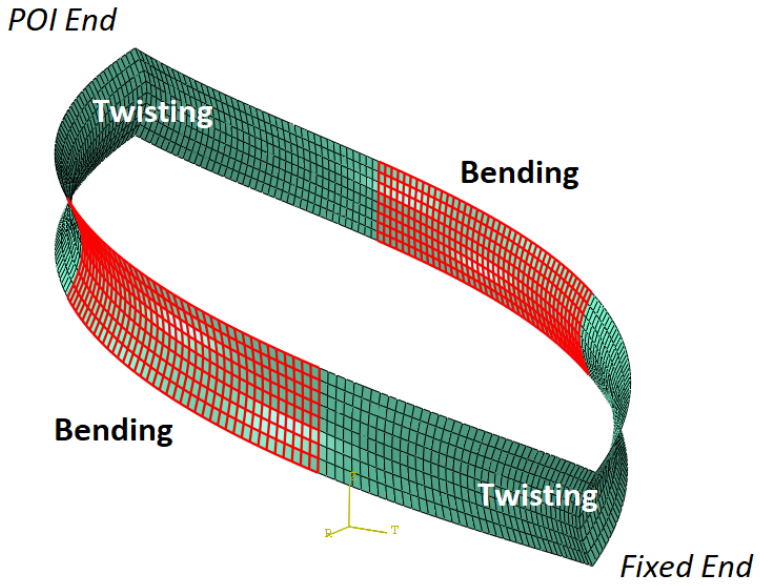

Figure 6.17: *Finite element model for a scoliosis brace split into different laminate regions. The helix cylindrical reference axis is shown inset.*

6.6.2 Laminate Selection

For a single-ply laminate, the maximum ratio of torsional compliance to bending stiffness (*i.e.* maximum D_{11}/D_{66}) is found using a 0° ply. Aligning the fibres in this way (*i.e.* with the helix line) was shown to enable sagittal bending dominance, but on its own could not make this degree of freedom an order of magnitude more compliant than the others (see Figure 6.10a). For a flat mechanism, this 0° laminate is likely to be close to the optimum laminate for initial sagittal bending compliance. Cross-ply laminates (like those in Chapter 3) are also effective at reducing torsional stiffness, and could be better for the twisting regions of a sinusoidal brace as they are more effective at resisting other deformation modes. The energy landscapes shown in Figure 6.15 suggest that the laminate choice for the central region is less important, but Figure 6.10 suggests that a 90° laminate would benefit sagittal bending in this case.

Figures 6.18 show plots of the compliance magnitudes for loaded sinusoidal brace mechanisms with the same laminate thickness, but using [90°/0°] laminates in the twisting regions (the 90° plies being on the inside of the mechanism, next to the body) and 90° fibres in the bending region (as per Figure 6.17). In addition, Figures 6.18b and 6.18d show these brace designs but with the inclusion of thermal prestress (defined as a temperature difference of $-160\,°\text{K}$ to model the cool down of a laminate from 180 °C cure to room temperature), which had been shown in Chapter 3 to further increase the torsional compliance of an open-section cylindrical shell with a cross-ply laminate.

It can be seen that for shallow curvature brace (*i.e.* $b = 5\,\text{mm}$), very little improvement is seen for the prestressed laminate, although the initial sagittal bending compliance is slightly larger than in Figure 6.13a. Including thermal prestress causes the initial unloaded state to become unstable (*i.e* a negative stiffness was observed, which cannot be plotted on a logarithmic axis) which, while this may encourage sagittal bending motion, is unsuitable for this application. Inclusion of thermal prestress in the larger curvature ($b = 10\,\text{mm}$) case does, however, show a large increase in initial sagittal bending compliance, over six times greater than the next most compliant eigenscrew: this is the greatest sagittal dominance seen in any brace investigated in this work. While not a full order of magnitude larger, this does illustrate the potential of using tailored laminates and prestressing to make a particular degree of freedom dominant in a compliant mechanism, all in a brace mechanism that has a smaller profile (*i.e.* lower cross-section sinusoidal amplitude), with $b = 5\,\text{mm}$ for this case while but $b = 16\,\text{mm}$ for Kooistra's benchmark case.

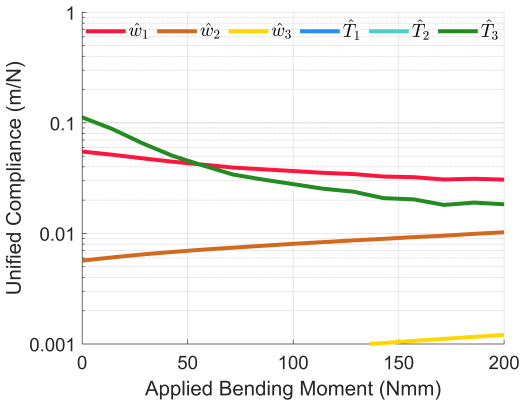

(a) *Sinusoidal brace ($b = 5\,\mathrm{mm}$)*

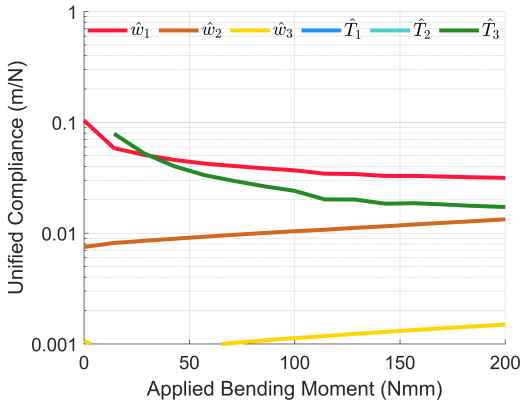

(b) *Sinusoidal brace ($b = 5\,\mathrm{mm}$) with thermal prestress*

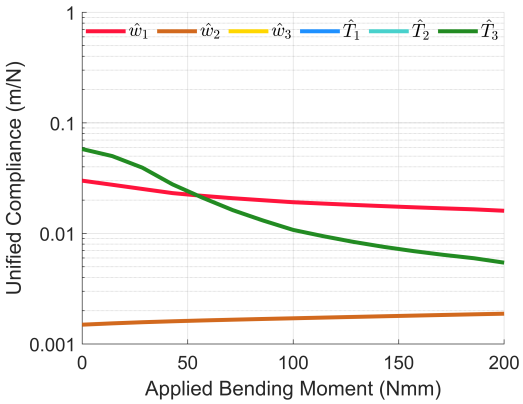

(c) *Sinusoidal brace ($b = 10\,\mathrm{mm}$)*

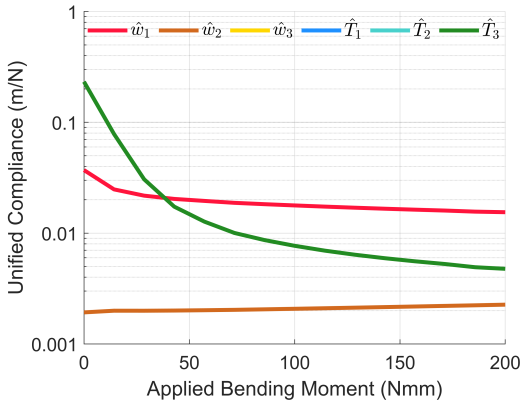

(d) *Sinusoidal brace ($b = 10\,\mathrm{mm}$) with thermal prestress*

Figure 6.18: *Unified compliance magnitudes for sinusoidal brace mechanisms utilising multiple laminates chosen to increase compliance*

6.7 Final Remarks

Eigenscrew magnitudes and positions have been investigated for a range of scoliosis brace mechanism geometries and laminate configurations. The eigenscrew characterisation framework was found to offer a convenient way of assessing the impact that inclusion of composites has on sagittal bending performance.

It has been shown that simply changing of fibre orientations can increase sagittal bending compliance, but this alone cannot achieve the desired order of magnitude dominance over other degrees of freedom. Tailoring the laminates of the mechanism to maximise local twisting has been shown to be beneficial for sagittal bending compliance (especially when coupled with inclusion of thermally-prestressed cross-ply laminates) but cannot significantly change the position of this axis. Composite mechanism designs have been found that ensure initial sagittal bending dominance, with the largest observed sagittal compliance being six times greater than the next eigenscrew, all while utilising a cross-sectional curvature that is significantly less than an isotropic benchmark and thus reduces the overall dimensions of the brace.

The work presented in this chapter represents a preliminary exploratory case study into the design of a composite compliant mechanism for a scoliosis brace, but by no means represents the design of an optimum mechanism. With a simplified set of design requirements and a limited selection of shell geometries, the design space for composite compliant scoliosis brace mechanisms remains largely unexplored. Nonetheless this case study has demonstrated the potential use of the eigenscrew characterisation technique, as well as the benefits of inclusion of composites for tailoring a mechanism response and reducing the mechanism profile.

Chapter 7

Conclusions & Future Work

7.1 Conclusions

The research presented in this thesis represents part of ongoing investigations into the stiffness tailoring of compliant shell mechanisms. These are structures designed to transmit forces and moments via large elastic deformations of the shell, and are valuable in reducing part count and maintenance requirements. Introducing composite materials to these structures offers unique ways to tailor their behaviour.

The potential for tailoring mechanism responses via use of material anisotropy alongside thermal and mechanical prestress has been assessed for several shell mechanisms including tape springs, helical lattices and a configuration of two doubly-curved parallel helices. Extensions to analytical models have been presented, as well as refined finite-element modelling and manufacturing methods.

The mechanical response of these tailored structures is often complex, nonlinear and non-intuitive. To provide further physical insight, an eigenscrew-based mechanisms characterisation framework has been applied to composite shells for the first time to calculate and visualise principal compliance axes, and analytical links have been established between this framework and classical structural mechanics concepts.

As a result of the work in this thesis the following conclusions can be drawn:

- Utilising the anisotropy of fibre reinforced composites is a promising way to expand the design spaces of compliant shell mechanisms and extend their range of novel behaviours, especially when combined with prestress introduced during the composite mechanism manufacture.

- Including thermal prestress in the internal strain energy formulations of a cross-ply tape spring was shown to increase its range of low-energy twisting compliance; this was validated using finite element simulations and physical prototypes.

- Moisture ingress was shown to significantly affect the shape and response of a thermally prestressed tape spring, highlighting the importance of environmental effects on thin-walled compliant mechanisms.

- Combined thermal and mechanical prestress were shown to enable novel negative thermal expansion behaviour in a thermally-actuated composite helical lattice structure, demonstrating extremely large values of thermal strain (in excess of $-3000 \cdot 10^{-6} K^{-1}$) for the mechanism as a whole. It was also shown analytically to enable new lattice designs exhibiting bistable and hysteretic behaviours.

- A new method for constructing finite-element models of helical lattices was presented that utilised the importing of a stress state from a previous model, thereby accurately capturing assembly-induced mechanical stresses that are essential for functionality.

- High-quality prototypes of the helical lattices were manufactured and tested, in order to assess the validity of the analytical and numerical models.

- Differences between the predicted energy states and lattice extensions between 1D and a 2D analytical models, finite-element simulations and experimental measurements of lattice behaviours were identified and explained. These highlighted the importance of accurately modelling shell mechanism manufacture and assembly, geometry and experimental loads and boundary conditions.

- A characterisation and visualisation framework for the behaviour of compliant shell mechanisms based on eigen-decomposition of stiffness matrices has been applied to composite compliant shells for the first time, enabling more intuitive insight into the physical behaviour of a loaded composite shell throughout its deformation.

- An analytical link has been demonstrated between the mechanisms and robotics concepts of eigentwists and eigenwrenches and the structural mechanics concepts of shear centre and centre of twist for a simple structural case of a cantilevered prismatic beam; this aids the interpretation of eigenscrew characterisations of the non-intuitive 3D spatial deformations of anisotropic shells.

- The effects of laminate anisotropy on shell deformations have been visualised using the eigenscrew characterisation for the first time, highlighting new deformation modes and identifying tape spring designs with geometry-dominated and material-dominated (*i.e.* stiffness dominated) behaviour, as well as a region of hybrid behaviour where material and curvature effects have similar contributions to the shell behaviour.

- Eigenscrews for a scoliosis brace mechanism were identified for representative isotropic and composite material systems. Although prestressed composite laminates were shown to make desired deformation behaviour more dominant while also reducing the brace geometric profile, the ability of prestress and anisotropy to tailor eigenscrew compliance magnitudes and positions was found to be limited, with geometric stiffness contributions still important for the behaviour of a complex compliant mechanism.

7.2 Future Work

The work presented in this thesis forms part of the ongoing development of the tailoring and characterisation of the behaviour of composite compliant shell mechanisms, and has opened up a range of possible directions for future research that could make practical composite compliant shell mechanisms more realisable.

- **Mechanism Materials and Laminate Lay-up.** The composite material systems investigated in this thesis were chosen for their ease of availability and well-documented properties. The carbon fibre epoxy or glass fibre epoxy systems used herein therefore do not necessarily represent the optimum-choice materials for effective composite compliant shell mechanisms. Different combinations of constituent fibres and matrix materials could dramatically affect the degree of stiffness anisotropy and hence mechanism behaviour, especially in cases where hygro-thermal prestress is being used. The use of hybrid laminates (*i.e.* those containing plies of different isotropic or anisotropic materials) could further expand the design space of available mechanism behaviour.

  The optimisation of the composite laminate lay-up for a compliant shell mechanisms can exploit results from the eigenscrew decomposition for the objective function. Furthermore, fibre angles can be varied continuously across the compliant shell mechanisms using recent technologies such as continuous tow shearing [108].

  Any benefits to mechanism performance will need to be traded against costs and processing complexities. Developing an optimisation framework to identify the most effective material system and composite laminate lay-up for given mechanism geometry and response requirements would be very valuable to designers.

- **Mechanism Durability.** Many compliant mechanisms are required to maintain their geometry and behaviour over many cycles (particularly in the case of medical device mechanisms). The long-term performance of large-deformation

mechanisms is also susceptible to high-strain viscoelastic effects, especially when the response relies on prestress and when polymeric fibres or matrices are used. Modelling the long-term effects on mechanism performance and identifying the expected mechanism fatigue life would be valuable for many application areas, and a first step could be to conduct fatigue life tests for representative large-deflection, high-strain composite compliant shell mechanisms. Once timescales and rates of stress relaxation were understood, research could then focus on identifying design rules and manufacturing techniques that reduce performance degradation due to stress relaxation, and increase the number of deformation cycles before failure.

- **Mechanism Robustness.** Ascertaining how sensitive a mechanism is to variations in the magnitude and position of applied loads, as well as manufacturing variability and uncertainty in material properties is necessary for realising products based on compliant shell mechanisms. While some parameter sensitivity and manufacturing variability investigations were conducted, a more comprehensive evaluation of the impact on mechanism performance and lifespan of ply misalignment, thickness variations and geometry defects would be valuable.

  In addition, the structural response should be robust to changes in environmental conditions, as hygrothermal stresses (due to changes in temperature and moisture absorption) can negatively impact the mechanism performance. Such relaxation was observed in mechanisms manufactured for the work in this thesis, necessitating their storage in sealed containers with desiccant pellets.

  Initial finite element models could be developed to input stochastic perturbations into the mechanism properties, environment and load cases (based on literature values for expected deviations, or Monte-Carlo analyses of experimental data). These could give a first indication of parameter sensitivity magnitudes for a range of mechanism types.

- **Mechanism Interaction.** While the eigenscrew decomposition technique has introduced a new framework for visualising the behaviour of composite morphing shells, information is only given for the principal degrees of freedom of the mechanism. These axes may not necessarily align with known load cases, or may exist outside of the mechanism geometry in such a way that a realistic load or deformation could not be applied to them, *i.e.* there may be no rigid body to transfer the load to the mechanism. It is thus valuable to develop understanding of how eigenscrews relate to real-world complex load cases and vice-versa, especially in medical support brace applications where this can inform how a person might best interact with a compliant shell mechanism.

Interpreting known load cases through the eigenscrew framework - either by expressing them as combinations of equivalent eigenscrews, or by simply understanding the effects of linear and angular proximity to known eigenscrews - may help to provide designers with intuitive insight into complex spatial mechanism behaviour.

The applicability of the eigenscrew framework can also be explored more generally too, for instance by investigating what insight is given in the cases of mechanisms where the behaviour is not clearly defined by a single point of interest *e.g.* a morphing wing which may require analysis of multiple points, or by assessing ways to quantitatively determine whether a mechanism is operating with material-dominated, geometry-dominated or hybrid behaviour, as opposed to just qualitatively.

Appendix A

Helical Lattice Ply-Level Thickness Measurements

Not all of the prototype helices survived being assembled into lattices. In some design cases significant flexural strains were mechanically applied to the helices to facilitate lattice assembly, and some helices exhibited catastrophic delamination failures in the vicinity of the bolt holes. As failure is dominated by localised effects in composite materials, a study of the ply-level properties of the individual helices was carried out to quantify, and subsequently minimise, the variation in local laminate properties.

A.1 Sample Measurements

Small sections of spare helices were cut up, potted and polished to produce microscope samples. These samples were viewed at 10x magnification with a Zeiss Axio Imager 2 optical microscope, and AxioVision software was used to take thickness measurements of each ply at 1mm intervals.

For each interval a 20x magnification image was taken of a ply with few polishing artefacts and fibres perpendicular to the polishing face. This was so that fibre volume fraction (FVF) could be determined using ImageJ image processing software. This method was limited in terms of its accuracy as small deviations from perpendicularity would result in higher measured fibre volume fractions due to the larger fibre cross sections, while polishing artefacts would appear like resin voids and reduce the measured fraction. Although this method is crude, when it was applied consistently across all samples it was felt to be sufficient to provide insight into the variation in fibre volume fraction across and between the samples.

It was observed that when samples were manufactured with a layer of breather fabric above the composite (a 'breather topper'), large undulations would occur. It

was speculated that these thickness variations could have a significant effect on the laminate flexural behaviour as flexural stiffness is a function of thickness to the third power. As such some 4-ply $[0\ 90]_S$ samples were made and measured that included a silicone layer between the composite and the breather with the aim of improving surface finish and thickness uniformity.

Figure A.1 shows two sample cross-sections that had been manufactured with and without a silicone layer. While the layup configuration between samples varied, it was felt acceptable to make direct comparisons between the samples as all the laminates were constructed from unidirectional plies of the same material, thus no major differences in the consolidation of the plies were expected.

Figures A.2a to A.2f show the tallies and the normal distributions assumed for each ply-level parameter with a breather topper and with a silicone topper. It can be seen that the standard deviation reduces across the board when a silicone topper is used, and that the silicone reduces thicknesses. It can also be seen that the assumption of normality of distribution is sometimes of limited validity.

A.2 Statistical Sensitivity Analysis

Once the distributions in ply-level properties were known, these were applied in a Monte Carlo simulation that used Classical Laminate Analysis [167] to calculate the $\boldsymbol{A}$, $\boldsymbol{B}$ and $\boldsymbol{D}$ stiffness matrices, as well as the reduced flexural stiffness matrix $\boldsymbol{D}^*$ (see Eqn. 2.9) ten thousand times. Two quasi-isotropic (QI) laminates and a cross-ply (XP) laminate (comprised of 0°and 90°plies) were chosen for investigation to capture the maximum and minimum levels of anisotropy achievable with fibre reinforced composites.

Table A.1 shows the mean values (μ), standard deviations (σ) and percentage coefficients of variance (CoV: defined as μ/σ) for key design parameters ($\delta_a = D^*_{66}/D^*_{11}$; $\delta_b = D^*_{16}/D^*_{11}$) calculated from this analysis. The variations used were those found for the silicone topper in Figures A.2b and A.2f, as well as a normal distribution of ply angles measured by Steeves and Pellegrino [231].

It can be seen that for typical 4-ply QI laminates there are coefficients of variation (CoV) up to almost 30%. Furthermore for these layups the variation in FVF and fibre angles do not generally increase the CoV much above those observed for just ply thickness. The only exception to this is for the flexure design parameters δ_a and δ_b (which are not affected by ply thickness) and B_{11}, although only for one QI configuration. For the XP laminate (that exhibits maximum laminate anisotropy) it can be seen that the CoV values do not increase by much either when other variations are considered, except in σ.

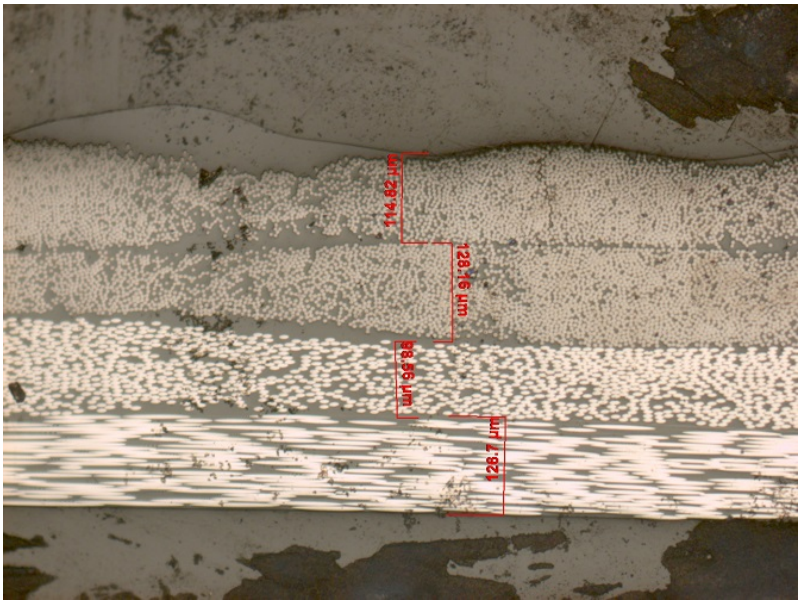

(a) *Sample with [90 -65 -25 20] layup manufactured with breather topper*

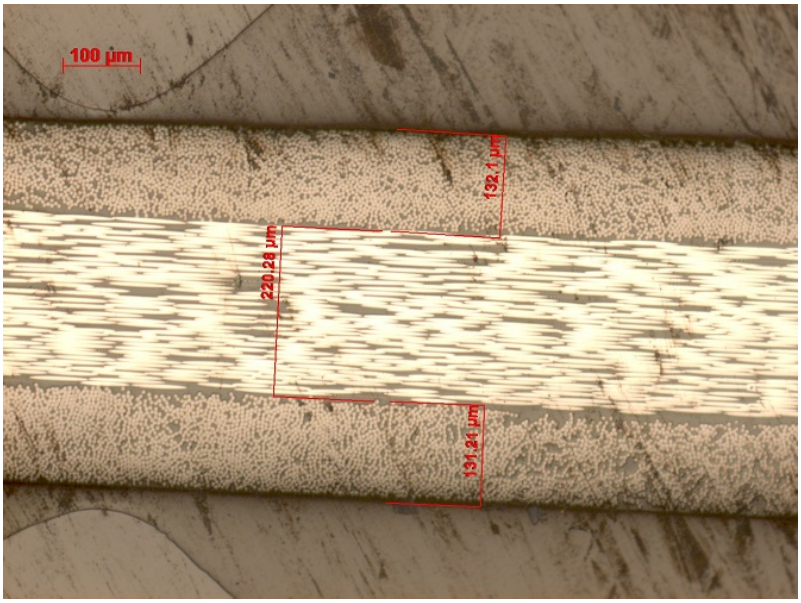

(b) *Sample with [0 90 90 0] layup manufactured with silicone topper*

Figure A.1: *Microscope images (10x magnification) showing cross-sections of two laminates made from four plies of unidirectional prepreg.*

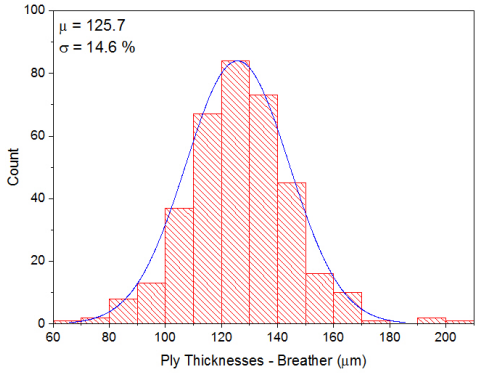

(a) *Ply thickness variation with a breather topper*

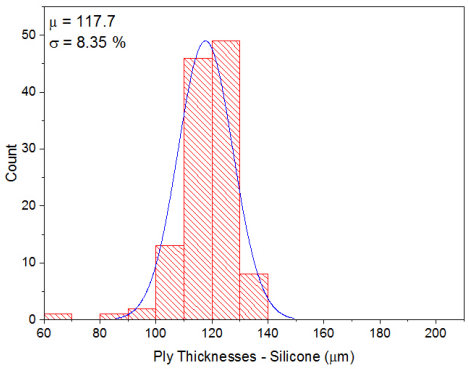

(b) *Ply thickness variation with a silicone topper*

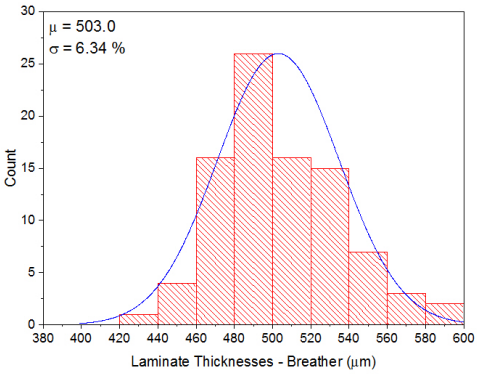

(c) *Laminate thickness variation with a breather topper*

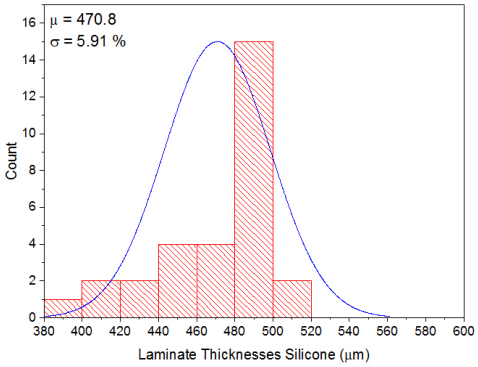

(d) *Laminate thickness variation with a silicone topper*

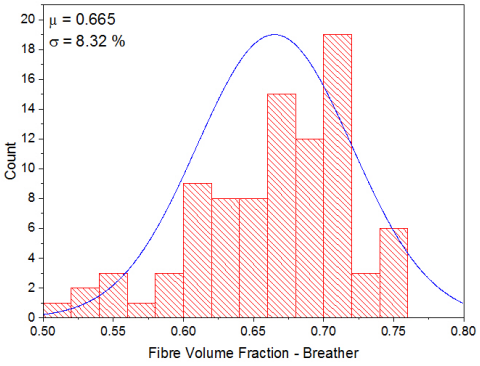

(e) *Fibre Volume Fraction variation with a breather topper*

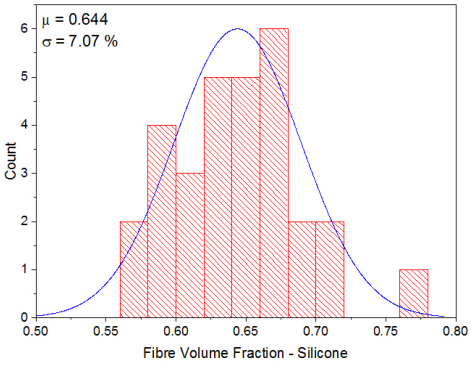

(f) *Fibre Volume Fraction variation with a silicone topper*

Figure A.2: *Histograms and normal distributions for various ply-level parameters when a breather topping material or silicone topping material is used.*

Table A.1: *Parameter mean values and standard deviations from the Monte Carlo simulation for various laminates. Underlined numbers indicate the 'tool ply' at the bottom of the laminate.*

Simulation Type	Parameter	[45 0 90 -45]			[90 45 -45 0]			[0 0 90 90]		
		μ	σ	CoV	μ	σ	CoV	μ	σ	CoV
Ply Thickness Variation	A_{11}	3.23e7	2.70e6	8.34%	3.23e7	2.71e6	8.39%	4.08e7	3.45e6	8.46%
	B_{11}	1.05e3	1.75e2	16.6%	-3.15e3	5.25e2	16.7%	4.20e3	7.06e2	16.8%
	D_{11}	4.89e-1	1.21e-1	24.8%	7.28e-1	1.82e-1	25.0%	7.70e-1	1.94e-1	25.2%
	D^*_{11}	2.23e-1	5.52e-2	24.8%	3.59e-1	8.97e-2	25.0%	3.34e-1	8.41e-2	25.2%
	δ_a	9.51e-1	0	-	2.03e-1	0	-	1.37e-1	0	-
	δ_b	-1.76e-1	0	-	1.09e-1	0	-	0	0	-
Ply Thickness & FVF Variations	A_{11}	3.47e7	3.32e6	9.57%	3.47e7	6.06e6	9.49%	4.40e7	4.17e6	9.48%
	B_{11}	1.12e3	2.36e2	21.0%	-3.37e3	6.19e2	18.4%	4.49e3	7.91e2	17.6%
	D_{11}	5.23e-1	1.33e-1	25.4%	7.87e-1	2.02e-1	25.6%	8.31e-1	2.12e-1	25.5%
	D^*_{11}	2.39e-1	6.09e-2	25.5%	3.92e-1	9.94e-2	25.4%	3.68e-1	9.34e-2	25.4%
	δ_a	9.54e-1	1.09e-2	1.14%	1.94e-1	8.84e-3	4.55%	1.25e-1	6.74e-3	5.38%
	δ_b	-1.72e-1	1.49e-2	8.64%	1.06e-1	5.43e-3	5.14%	0	0	-
All Variations	A_{11}	3.47e7	3.27e6	9.42%	3.47e7	3.34e6	9.61%	4.39e7	4.17e6	9.49%
	B_{11}	1.12e3	3.32e3	29.7%	-3.36e3	6.26e2	18.6%	4.48e3	7.89e2	17.6%
	D_{11}	5.24e-1	1.31e-1	25.0%	7.86e-1	2.04e-1	26.0%	8.29e-1	2.11e-1	25.4%
	D^*_{11}	2.40e-1	6.03e-2	25.1%	3.91e-1	1.01e-1	25.9%	3.67e-1	9.28e-2	25.3%
	δ_a	9.49e-1	4.84e-2	5.10%	1.97e-1	2.06e-2	10.5%	1.27e-1	7.22e-3	5.67%
	δ_b	-1.69e-1	4.34e-2	25.6%	1.05e-1	3.00e-2	28.6%	0	2.49e-2	-

A.3 Discussion & Conclusion

In terms of the Monte Carlo analysis, the predicted CoV values seemed very high. Up to 30% deviation in the flexural properties of a laminate should have a significant effect on the theoretical geometries of the helices. When manufacturing the lattice prototypes there was negligible geometric variation between the helices, suggesting that these flexural property variations are very localised and average-out across the structure.

Even if these are localised effects, there is reason to believe that the current Monte Carlo analysis is simply too conservative. Each parameter is currently treated independently meaning that, for example, it is possible for all the plies to exist with large thicknesses. It was often observed in the microscope images however, that generally where one ply is thicker, the adjacent plies are thinner, and the overall laminate thickness is uniform throughout. In this case the thickness parameters are not independent of each other as some ply compaction from adjacent plies is observed. Figure A.3 shows a plot of individual ply thicknesses with the corresponding laminate thickness, and it can be seen that a slight positive correlation exists between the these two values for a $[0\ 90]_S$ laminate. This correlation suggests that parameter independence should not be assumed, and that a deeper understanding of the interplay between ply-level parameters is required for greater accuracy.

Furthermore the distributions assumed for the ply-level properties may not be truly representative. While normality seems appropriate for individual ply thicknesses (see Figures A.2a and A.2b), the assumption of normality does not look as

appropriate for laminate thicknesses and FVFs (see Figures A.2c to A.2f). Fitness tests (e.g. Chi squared or Anderson-Darling) should be carried out at 5% and 10% levels of significance to check these assumptions, and alternative distributions applied if necessary.

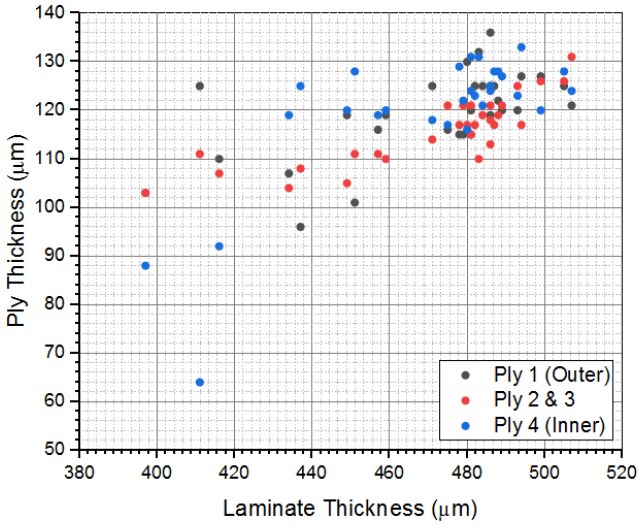

Figure A.3: *Individual ply thicknesses for each layer plotted against their corresponding total laminate thickness. Plies 2 and 3 were assumed to be equal thickness as their boundary was not identifiable under the microscope due to their identical fibre angle.*

Results of this analysis suggest that large local variations in stiffness properties can exist, and future work should focus on how to correctly model these and understand their effect on failure modes. The use of thin-ply technologies to expand the lattice design space and reduce delamination vulnerability should also be considered.

Appendix B

Mechanically-Prestressed Helical Lattice FE Modelling

The following appendix describes the steps used to construct FE models of the mechanically-pressed lattices in Chapter 4 using Abaqus/Standard 2016 CAE.

Due to the complexity of applying mechanical prestress this is multi-model process where the helices are deformed into their assembly configurations, and the deformed geometries and stress states from these are imported into a final model for assembly. This is because modelling the prestressing deformation is the easiest way to accurately obtain the state of mechanical prestress, and connectors cannot then be added in the same model after this has taken place.

Mechanical prestress typically takes two forms: 1) assembling the helices into a lattice with a different radius to the manufactured state, and 2) reversing the handedness of the helices (*i.e.* helices placed on the tool as right-handed are assembled into the lattice by bending them back to become left-handed).

B.1 Model 1 - Including Radial Prestress

Follow Steps 1-4 for the simple lattice, although different lengths of helices or bolt separations will mean that the bolt locations will not align currently. After this coupling constrains are applied to the bolt locations and rotated to cause the helices to 'twist-in' thereby changing the radius for assembly.

1. **Create the coupling constraints**

   (a) Create "Reference Points" (RPs) on the helix axis that align with the bolt locations, *i.e.* there should be one RP for every four bolt nodes

   (b) Define kinematic "Coupling" constraints for each set of four bolt nodes: the RPs should act as the control points, and the bolt nodes as the surface

points. Radial translation should be left unconstrained. This should look like a series of bicycle spokes.

2. **Create the Step**

   (a) One nonlinear "Static, General" step should be sufficient for this model.

   (b) A "Restart Request" must be selected from the "Output" tab to enable the final state to be imported into the assembly model.

3. **Apply Boundary Conditions**

   (a) The four bolt nodes at one end of the lattice need to remain stationary in space, but allowed to rotate and translate along the radial axis.

   (b) Apply rotational boundary conditions to each RP, fixing everything except axial translation, and defining the required axial rotation increments to ensure correct 'twist-in' and alignment of the bolt nodes.

A predefined temperature field can also be applied in Model 1 to include states of thermal prestress.

B.2 Model 2 - Reversing the Helix Directions

This model applies the next stage of mechanical prestress using the imported geometry and stress state from Model 1.

1. **Import Previous Model State**

   (a) Make a copy of Model 1 to be the base of Model 2.

   (b) Delete all previous constraints and boundary conditions.

   (c) In the initial step apply an "Initial State" predefined field to the entire model. Type the name of the previous job with the output request, use the last step and frame and be sure to update the reference configuration.

2. **Create the Step**

   (a) As per Model 1 (including the restart request)

3. **Apply Boundary Conditions**

   (a) The four bolt nodes at one end of the lattice need to be fully-fixed.

   (b) Each set of four bolt holes needs to have similar boundary conditions applies, except that an axial displacement must be included that will cause the lattice to align in its correct, 'bent-back' configuration.

B.3 Model 3 - Assembling and Testing the Helix

Once the helices in Model 2 are aligned properly (*i.e.* all bolt locations match up) then Model 3 can be created. Using a copy of Model 2 to make Model 3, remove unnecessary boundary conditions then define an "Initial State" predefined field to import the 'bent-back' geometry and stress state. Once this is done "Wire" features and "Hinge" connectors can be applied to complete the assembly as before with the simpler helix models. Model 3 can then become a temperature, displacement or force-controlled model as described previously.

B.4 Modelling Experimental Effects

Steel wires were used to suspend the lattices in an oven while they were heated. The effect of these can be added by including a gravity load (as previously described) and two "Wire" features. Datum points and RPs can be used to set the fixed positions of the wires in space, and a "Join" connector can be used to attach the wires to two bolt locations to mimic the experiments. Fully-fixed boundary conditions then need to be applied to the other end of the two wires when the lattice is at the room temperature length.

Bibliography

[1] B.D. Agarwal and L.J. Broutman. Expansion coefficients and transport properties. In *Analysis and performance of fiber composites*. John Wiley & Sons Inc., 1990.

[2] S.H. Ahn, K.T. Lee, H.J. Kim, R. Wu, J.S. Kim, and S.H. Song. Smart Soft Composite: An Integrated 3D Soft Morphing Structure Using Bend-twist Coupling of Anisotropic Materials. *International Journal of Precision Engineering and Manufacturing*, 13(4):631–634, 2012.

[3] T.M. Allred. *Compliant Mechanism Suspensions*. Masters thesis, Brigham Young University, 2006.

[4] R. Amacher, J. Cugnoni, J. Botsis, L. Sorensen, W. Smith, and C. Dransfeld. Thin ply composites: Experimental characterization and modeling of size-effects. *Composites Science and Technology*, 101:121–132, 2014.

[5] Y. Arao, J. Koyanagi, S. Takeda, S. Utsunomiya, and H. Kawada. Geometrical stability of CFRP laminate considering ply angle misalignment. In *ICCM International Conferences on Composite Materials*, pages 1–3, 2011.

[6] Y. Arao, J. Koyanagi, S. Utsunomiya, and H. Kawada. Effect of ply angle misalignment on out-of-plane deformation of symmetrical cross-ply CFRP laminates: Accuracy of the ply angle alignment. *Composite Structures*, 93(4):1225–1230, 2011.

[7] C. Aza, A. Pirrera, and M. Schenk. Multistable morphing of nonlinear springs. *Journal of Mechanisms and Robotics*, 11(5), 2019.

[8] R.S. Ball. *A Treatise on the Theory of Screws*. Cambridge University Press, London, 1900.

[9] R. Barents, M. Schenk, W.D. van Dorsser, B.M. Wisse, and J.L. Herder. Spring-to-Spring Balancing as Energy-Free Adjustment Method in Gravity Equilibrators. *Journal of Mechanical Design*, 133(June 2011):061010, 2011.

[10] J.M. Berthelot. Effect of Fiber Misalignment on the Elastic Properties of Oriented Discontinuous Fiber Composites. *Fibre Science & Technology*, 17(1):25–39, 1982.

[11] D.N. Betts, A.I.T. Salo, C.R. Bowen, and H.A. Kim. Characterisation and modelling of the cured shapes of arbitrary layup bistable composite laminates. *Composite Structures*, 92(7):1694–1700, 2010.

[12] O. Bilgen, K.B. Kochersberger, D.J. Inman, and O.J. Ohanian. Novel, bidirectional, variable-camber airfoil via macro-fiber composite actuators. *Journal of Aircraft*, 47(1):303–314, 2010.

[13] C.J. Brampton, D.N. Betts, C.R. Bowen, and H.A. Kim. Sensitivity of bistable laminates to uncertainties in material properties, geometry and environmental conditions. *Composite Structures*, 102:276–286, 2013.

[14] A. Brinkmeyer, S. Pellegrino, and P.M. Weaver. Effects of Long-Term Stowage on the Deployment of Bistable Tape Springs. *Journal of Applied Mechanics*, 83(1):011008, 2015.

[15] A. Brinkmeyer, A. Pirrera, M. Santer, and P.M. Weaver. Pseudo-bistable pre-stressed morphing composite panels. *International Journal of Solids and Structures*, 50(7-8):1033–1043, 2013.

[16] A. Brinkmeyer, A. Pirrera, P.M. Weaver, and M. Santer. Pseudo-Bistable Morphing Composites. In *53rd AIAA/ASME/ASCE/AHS/ASC Structures, Structural Dynamics and Materials Conference 20th AIAA/ASME/AHS Adaptive Structures Conference 14th AIAA*, 2012.

[17] A. Brinkmeyer, M. Santer, A. Pirrera, and P.M. Weaver. Pseudo-bistable self-actuated domes for morphing applications. *International Journal of Solids and Structures*, 49(9):1077–1087, 2012.

[18] D. Brown. Tracker Video Analysis and Modeling Tool. `https://physlets.org/tracker/`, 2018.

[19] T.E. Bruns and D.A. Tortorelli. Topology optimization of non-linear elastic structures and compliant mechanisms. *Computer Methods in Applied Mechanics and Engineering*, 190(26-27):3443–3459, 2001.

[20] T. Buhl, C. Pedersen, and O. Sigmund. Stiffness Design of Geometrically Nonlinear Structures Using Topology Optimization. *Structural and Multidisciplinary Optimization*, 19:93–104, 2000.

[21] C.J. Burgoyne and K.G.N.C. Alwis. Visco-elasticity of aramid fibres. *Journal of Materials Science*, 43(22):7091–7101, 2008.

[22] C.R. Calladine. *Theory of Shell Structures*. Cambridge University Press, New York, 1983.

[23] C.R. Calladine and K.A. Seffen. Folding the Carpenter's Tape: Boundary Layer Effects. *Journal of Applied Mechanics*, 87(1):1–5, 2020.

[24] P.P. Camanho, P. Maimí, and C.G. Dávila. Prediction of size effects in notched laminates using continuum damage mechanics. *Composites Science and Technology*, 67(13):2715–2727, 2007.

[25] B.R. Cannon, T.D. Lillian, S.P. Magleby, L.L. Howell, and M.R. Linford. A compliant end-effector for microscribing. *Precision Engineering*, 29:86–94, 2005.

[26] L. Cappello, X. Lachenal, A. Pirrera, F. Mattioni, P.M. Weaver, and L. Masia. Design, characterization and stability test of a multistable composite compliant actuator for exoskeletons. In *5th IEEE RAS/EMBS International Conference on Biomedical Robotics and Biomechatronics*, pages 1051–1056, 2014.

[27] S. Carey, C. McHale, V. Oliveri, and Paul M. Weaver. Reconfigurable Multi-Stable Helical Lattice. In *ASME 2020 Conference on Smart Materials, Adaptive Structures and Intelligent Systems Conference*, Irvine, CA, 2020. ASME.

[28] S. Carey, R. Telford, V. Oliveri, C. McHale, and P.M. Weaver. Bistable composite helices with thermal effects. *Proceedings of the Royal Society A: Mathematical, Physical and Engineering Sciences*, 475:20190295, 2019.

[29] M. Chasles. Note Sur Les Propriétés Générales du Système de Deux Corps Semblables Entr'eux et Placés D'un Manière Quelconque Dans L'espace; et Sur le Déplacement Fini, ou Infiniment Petit, D'un Corps Solide Libre. *Bulletin Des Sciences Mathématiques, Astronomiques, Physiques et Chimiques*, 14:321–326, 1831.

[30] V.S.C. Chillara and M.J. Dapino. Mechanically-prestressed bistable composite laminates with weakly coupled equilibrium shapes. *Composites Part B: Engineering*, 111:251–260, 2017.

[31] V.S.C. Chillara, L.M. Headings, and M.J. Dapino. Multifunctional composites with intrinsic pressure actuation and prestress for morphing structures. *Composite Structures*, 157:265–274, 2016.

[32] N. Ciblak. *Analysis of Cartesian Stiffness And Compliance With Applications*. PhD thesis, Georgia Institute of Technology, 1998.

[33] J. Costantine, Y. Tawk, C.G. Christodoulou, J. Banik, and S. Lane. CubeSat Deployable Antenna Using Bistable Composite Tape-Springs. *IEEE Antennas and Wireless Propagation Letters*, 11:285–288, 2012.

[34] Y. Cui and M. Santer. Highly multistable composite surfaces. *Composite Structures*, 124:44–45, 2015.

[35] Y. Cui and M. Santer. Characterisation of tessellated bistable composite laminates. *Composite Structures*, 137:93–104, 2016.

[36] F. Dai, H. Li, and S. Du. A multi-stable lattice structure and its snap-through behavior among multiple states. *Composite Structures*, 97:56–63, 2013.

[37] I.M. Daniel and O. Ishai. *Engineering Mechanics of Composite Materials*. Oxford University Press, Oxford, second edition, 2006.

[38] M.L. Dano and M.W. Hyer. Snap-through of unsymmetric fiber-reinforced composite laminates. *International Journal of Solids and Structures*, 39(1):175–198, 2002.

[39] D. Das, T. Jacobs, and L.J. Barbour. Exceptionally large positive and negative anisotropic thermal expansion of an organic crystalline material. *Nature Materials*, 9(1):36–39, 2010.

[40] A.J. Daton-Lovett. Extendible Member, US Patent No. 6,217,975, 2001.

[41] S. Daynes, C.G. Diaconu, K.D. Potter, and P.M. Weaver. Bistable Prestressed Symmetric Laminates. *Journal of Composite Materials*, 44(9):1119–1137, 2010.

[42] S. Daynes, K.D. Potter, and P.M. Weaver. Bistable prestressed buckled laminates. *Composites Science and Technology*, 68(15-16):3431–3437, 2008.

[43] S. Daynes and P.M. Weaver. Analysis of unsymmetric CFRP-metal hybrid laminates for use in adaptive structures. *Composites Part A: Applied Science and Manufacturing*, 41(11):1712–1718, 2010.

[44] S. Daynes and P.M. Weaver. Stiffness tailoring using prestress in adaptive composite structures. *Composite Structures*, 106:282–287, 2013.

[45] S. Daynes, P.M. Weaver, and J.A. Trevarthen. A morphing composite air inlet with multiple stable shapes. *Journal of Intelligent Material Systems and Structures*, 22(9):961–973, 2011.

[46] J.P. den Hartog. *Advanced Strength of Materials*. McGraw-Hill, 1952.

[47] C.G. Diaconu and H. Sekine. Erratum on "Flexural Characteristics and Layup Optimization of Laminated Composite Plates Under Hygrothermal Conditions Using Lamination Parameters". *Journal of Thermal Stresses*, 27(12):1213–1216, 2004.

[48] C.G. Diaconu, P.M. Weaver, and F. Mattioni. Concepts for morphing airfoil sections using bi-stable laminated composite structures. *Thin-Walled Structures*, 46(6):689–701, 2008.

[49] M.D.X. Dixon, M.P. O'Donnell, A. Pirrera, and I.V. Chenchiah. Bespoke extensional elasticity through helical lattice systems. *Proceedings of the Royal Society A: Mathematical, Physical and Engineering Sciences*, 475:20190547, 2019.

[50] B. Doornenbal. *Zero stiffness composite shells: Using thermal prestress*. Masters thesis, Delft University of Technology, 2018.

[51] T. Dries. *A biomechanical characterization of spinal motion data for the design of a compliant scoliosis brace*. PhD thesis, TU Delft, 2018.

[52] E. Eckstein, A. Pirrera, and P.M. Weaver. Morphing high-temperature composite plates utilizing thermal gradients. *Composite Structures*, 100:363–372, 2013.

[53] E. Eckstein, A. Pirrera, and P.M. Weaver. Multi-mode morphing using initially curved composite plates. *Composite Structures*, 109(1):240–245, 2014.

[54] E. Eckstein, A. Pirrera, and P.M. Weaver. Thermally driven morphing with hybrid laminates and metal matrix composites. In *56th AIAA/ASCE/AHS/ASC Structures, Structural Dynamics, and Materials Conference*, 2015.

[55] E. Eckstein, A. Pirrera, and P.M. Weaver. Thermally Driven Morphing and Snap-Through Behavior of Hybrid Laminate Shells. *AIAA Journal*, 54(5):1778–1788, 2016.

[56] M. Elseifi, M. Khalessi, H.-Z. Lin, G. Rogers, and T. Torng. Probabilistic analysis of thick composite plates with manufacturing and material uncertainties. In *19th AIAA Applied Aerodynamics Conference*, pages AIAA–2001–1612, 2001.

[57] J. Etches, K.D. Potter, P.M. Weaver, and I. Bond. Environmental effects on thermally induced multistability in unsymmetric composite laminates. *Composites Part A: Applied Science and Manufacturing*, 40(8):1240–1247, 2009.

[58] O. Faiz, S. Blackburn, and D.B. Moffat. *Anatomy at a glance*. Wiley-Blackwell, Chichester, UK, 3rd edition, 2011.

[59] W. Falk and R.D. James. Elasticity theory for self-assembled protein lattices with application to the martensitic phase transition in bacteriophage T4 tail sheath. *Physical Review E - Statistical, Nonlinear, and Soft Matter Physics*, 73(1):1–23, 2006.

[60] K.S. Fancey. Prestressed polymeric composites produced by viscoelastically strained nylon 6,6 fibre reinforcement, 2000.

[61] K.S. Fancey. Viscoelastically prestressed polymeric matrix composites - Potential for useful life and impact protection. *Composites Part B: Engineering*, 41(6):454–461, 2010.

[62] K.S. Fancey and A. Fazal. Prestressed polymeric matrix composites: Longevity aspects. *Polymer Composites*, 37(7):2092–2097, 2016.

[63] K.S. Fancey and J.W.C. Pang. The flexural stiffness characteristics of viscoelastically prestressed polymeric matrix composites. *Composites Part A: Applied Science and Manufacturing*, 40(6-7):784–790, 2009.

[64] M. Farshad. *Design and Analysis of Shell Structures*. Springer Science & Business Media B.V., Dordrecht, NL, 1992.

[65] P. Feraboli, T. Cleveland, P. Stickler, and J. Halpin. Stochastic laminate analogy for simulating the variability in modulus of discontinuous composite materials. *Composites Part A: Applied Science and Manufacturing*, 41(4):557–570, 2010.

[66] J.M. Fernandez, A. Viquerat, V.J. Lappas, and A.J. Daton-Lovett. Bistable Over the Whole Length (BOWL) CFRP Booms for Solar Sails. In M. MacDonald, editor, *Advances in Solar Sailing*, pages 609–628. Springer Berlin Heidelberg, 2014.

[67] Y. Forterre and J. Dumais. Generating Helices in Nature. *Science*, 333(6050):1715–1716, 2011.

[68] M.I. Frecker, G.K. Ananthasuresh, S. Nishiwaki, N. Kikuchi, and S. Kota. Topological synthesis of compliant mechanisms using multi-criteria optimization. *Journal of Mechanical Design*, 119(2):238–245, 1997.

[69] H. Fukunaga. A solution procedure for determining laminate configurations from lamination parameters. *Advanced Composite Materials*, 1(3):209–224, 1991.

[70] H. Fukunaga and G.N. Vanderplaats. Stiffness optimization of orthotropic laminated composites using lamination parameters. *AIAA Journal*, 29(4):641–646, 1991.

[71] J.A. Gallego and J.L. Herder. Synthesis Methods in Compliant Mechanisms: An Overview. In *Proceedings of the ASME 2009 International Design Engineering Technical Conferences & Computers and Information in Engineering Conference*, pages 193–214. ASME, 2009.

[72] D.A. Galletly and S.D. Guest. Bistable composite slit tubes. I. A beam model. *International Journal of Solids and Structures*, 41(16-17):4517–4533, 2004.

[73] D.A. Galletly and S.D. Guest. Bistable composite slit tubes. II. A shell model. *International Journal of Solids and Structures*, 41(16-17):4503–4516, 2004.

[74] P.F. Giddings, C.R. Bowen, A.I.T. Salo, H.A. Kim, and A. Ive. Bistable composite laminates: Effects of laminate composition on cured shape and response to thermal load. *Composite Structures*, 92(9):2220–2225, 2010.

[75] L. Giomi and L. Mahadevan. Multi-stability of free spontaneously curved anisotropic strips. *Proceedings of the Royal Society A: Mathematical, Physical and Engineering Sciences*, 468(2138):511–530, 2012.

[76] D. Girardeau-Montaut. CloudCompare Project. `http://www.danielgm.net/cc/`.

[77] C.J. Goldberg, D.P. Moore, E.E. Fogarty, and F.E. Dowling. Scoliosis: A review. *Pediatric Surgery International*, 24(2):129–144, 2008.

[78] B.J. Goodno and J.M. Gere. *Mechanics of Materials*. Cengage Learning, Boston MA, 9th edition, 2018.

[79] R.M.J. Groh and A. Pirrera. A general computational framework for designing morphing structures. In *21st International Conference on Composite Materials*, Xi'an, 2017.

[80] R.M.J. Groh and A. Pirrera. Extreme mechanics in laminated shells: New insights. *Extreme Mechanics Letters*, 23:17–23, 2018.

[81] S.D. Guest, E. Kebadze, and S. Pellegrino. A zero-stiffness elastic shell structure. *Journal of Mechanics of Materials and Structures*, 6(1-4):203–212, 2011.

[82] S.D. Guest and S. Pellegrino. Analytical models for bistable cylindrical shells. *Proceedings of the Royal Society A: Mathematical, Physical and Engineering Sciences*, 462(2067):839–854, 2006.

[83] Q. Guo, A.K. Mehta, M.A. Grover, W. Chen, D.G. Lynn, and Z. Chen. Shape selection and multi-stability in helical ribbons. *Applied Physics Letters*, 104(21), 2014.

[84] W. Hamouche, C. Maurini, S. Vidoli, and A. Vincenti. Multi-parameter actuation of a neutrally stable shell: A flexible gear-less motor. *Proceedings of the Royal Society A: Mathematical, Physical and Engineering Sciences*, 473(2204), 2017.

[85] W. Hamouche, C. Maurini, A. Vincenti, and S. Vidoli. Basic criteria to design and produce multistable shells. *Meccanica*, 51(10):2305–2320, 2016.

[86] M.W. Han, H. Rodrigue, S. Cho, S.H. Song, W. Wang, W.S. Chu, and S.H. Ahn. Woven type smart soft composite for soft morphing car spoiler. *Composites Part B: Engineering*, 86:285–298, 2016.

[87] Hexcel. HexPly® 8552 Data Sheet. Technical report, Hexcel, 2016.

[88] K. Hoetmer, J.L. Herder, and C.J. Kim. A Building Block Approach for the Design of Statically Balanced Compliant Mechanisms. In *Proceedings of the ASME 2009 International Design Engineering Technical Conferences & Computers and Information in Engineering Conference*, pages 313–323, San Diego CA, USA, 2010.

[89] K. Hoetmer, G. Woo, C.J. Kim, and J. Herder. Negative stiffness building blocks for statically balanced compliant mechanisms: Design and testing. *Journal of Mechanisms and Robotics*, 2(4):041007, 2010.

[90] J.B. Hopkins. *Design of Parallel Flexure Systems via Freedom and Constraint Topologies (FACT)*. PhD thesis, Massachusetts Institute of Technology, 2007.

[91] J.B. Hopkins and M.L. Culpepper. Synthesis of multi-degree of freedom, parallel flexure system concepts via Freedom and Constraint Topology (FACT) - Part I: Principles. *Precision Engineering*, 34(2):259–270, 2010.

[92] J.B. Hopkins and M.L. Culpepper. Synthesis of multi-degree of freedom, parallel flexure system concepts via freedom and constraint topology (FACT). Part II: Practice. *Precision Engineering*, 34(2):271–278, 2010.

[93] J.B. Hopkins and M.L. Culpepper. Synthesis of precision serial flexure systems using freedom and constraint topologies (FACT). *Precision Engineering*, 35(4):638–649, 2011.

[94] J.B. Hopkins, K.J. Lange, and C.M. Spadaccini. Designing microstructural architectures with thermally actuated properties using freedom, actuation, and constraint topologies. *Journal of Mechanical Design*, 135(6), 2013.

[95] L.L. Howell. *Compliant Mechanisms*. John Wiley & Sons Inc., New York, 2001.

[96] L.L. Howell and A. Midha. A method for the design of compliant mechanisms with small-length flexural pivots. *Journal of Mechanical Design*, 116(1):280–290, 1994.

[97] S. Huang and J.M. Schimmels. Achieving an arbitrary spatial stiffness with springs connected in parallel. *Journal of Mechanical Design*, 120(4):520–526, 1998.

[98] S. Huang and J.M. Schimmels. The eigenscrew decomposition of spatial stiffness matrices. *IEEE Transactions on Robotics and Automation*, 16(2):146–156, 2000.

[99] X. Huang, Y. Li, S.W. Zhou, and Y.M. Xie. Topology optimization of compliant mechanisms with desired structural stiffness. *Engineering Structures*, 79:13–21, 2014.

[100] M.W. Hyer. Calculations of the Room-Temperature Shapes of Unsymmetric Laminates. *Journal of Composite Materials*, 15(July):296–310, 1981.

[101] K. Iqbal and S. Pellegrino. Bi-stable composite shells. In *41st Structures, Structural Dynamics, and Materials Conference and Exhibit*, 2000.

[102] S.K. Jeon and T.W. Murphey. Design and analysis of a meter-class CubeSat boom with a motor-less deployment by bi-stable tape springs. In *52nd AIAA/ASME/ASCE/AHS/ASC Structures, Structural Dynamics and Materials Conference*, 2011.

[103] W. Johannisson, R. Harnden, D. Zenkert, and G. Lindbergh. Shape-morphing carbon fiber composite using electrochemical actuation. *Proceedings of the National Academy of Sciences of the United States of America*, 117(14):7658–7664, 2020.

[104] R.M. Jones. *Mechanics of Composite Materials*. Taylor & Frances, 2rd edition, 1999.

[105] M. Kameyama and H. Fukunaga. Optimum design of composite plate wings for aeroelastic characteristics using lamination parameters. *Computers & Structures*, 85(3-4), 2007.

[106] E. Kebadze, S.D. Guest, and S. Pellegrino. Bistable prestressed shell structures. *International Journal of Solids and Structures*, 41(11-12):2801–2820, 2004.

[107] A. Khani, S.T. Ijsselmuiden, M.M. Abdalla, and Z. Gürdal. Design of variable stiffness panels for maximum strength using lamination parameters. *Composites Part B: Engineering*, 42(3), 2011.

[108] B.C. Kim, K. Potter, and P.M. Weaver. Continuous tow shearing for manufacturing variable angle tow composites. *Composites Part A: Applied Science and Manufacturing*, 43(8):1347–1356, 2012.

[109] C.J. Kim. *A conceptual approach to the computational synthesis of compliant mechanisms*. PhD thesis, University of Michigan, 2005.

[110] C.J. Kim. Functional characterization of compliant building blocks utilizing eigentwists and eigenwrenches. In *Proceedings of the ASME 2008 International Design Engineering Technical Conferences & Computers and Information in Engineering Conference*, Brooklyn NY, USA, 2008.

[111] C.J. Kim. On the geometry of stiffness and compliance under concatenation. *Journal of Mechanisms and Robotics*, 12(2):021113, 2020.

[112] C.J. Kim, S. Kota, and Y.M. Moon. An Instant Center Approach Toward the Conceptual Design of Compliant Mechanisms. *Journal of Mechanical Design*, 128(3):542, 2006.

[113] C.J. Kim, Y.M. Moon, and S. Kota. A Building Block Approach to the Conceptual Synthesis of Compliant Mechanisms Utilizing Compliance and Stiffness Ellipsoids. *Journal of Mechanical Design*, 130(2):022308, 2008.

[114] H.I. Kim, M.W. Han, S.H. Song, and S.H. Ahn. Soft morphing hand driven by SMA tendon wire. *Composites Part B: Engineering*, 105:138–148, 2016.

[115] C. Kimball and L.W. Tsai. Modeling of flexural beams subjected to arbitrary end loads. *Journal of Mechanical Design*, 124(2):223–235, 2002.

[116] R.H. Knibbs and J.B. Morris. The effects of fibre orientation on the physical properties of composites. *Composites*, 5(5):209–218, 1974.

[117] G. Knott. *New forms of bistable composite slit tube*. Phd thesis, University of Surrey, 2018.

[118] G. Knott and A. Viquerat. Helical bistable composite slit tubes. *Composite Structures*, 207(September 2018):711–726, 2019.

[119] K.B. Kochersberger, D. Landmark, J.L. Player, and K.W. Hyde. Evaluation of the Wright 1902 glider using full-scale wind-tunnel data. *Journal of Aircraft*, 42(3):710–717, 2005.

[120] H. Kooistra. *Scoliosis Brace Design: Utilizing Compliant Shell Mechanisms and Primary Compliance Vector Path Optimization.* Master thesis, TU Delft, 2019.

[121] H. Kooistra, C.J. Kim, W.W.P.J. van de Sande, and J.L. Herder. Shape optimization framework for the path of the primary compliance vector in compliant mechanisms. In *Proceedings of the ASME 2019 International Design Engineering Technical Conferences and Computers and Information in Engineering Conference*, volume V05AT07A00, Anaheim, CA, 2019. ASME.

[122] S. Kota, J. Joo, Z. Li, S.M. Rodgers, and J. Sniegowski. Design of compliant mechanisms: Applications to MEMS. *Analog Integrated Circuits and Signal Processing*, 29(1-2):7–15, 2001.

[123] G. Krishnan, C.J. Kim, and S. Kota. An Intrinsic Geometric Framework for the Building Block Synthesis of Single Point Compliant Mechanisms. *Journal of Mechanisms and Robotics*, 3(1):011001, 2011.

[124] I.K. Kuder, A.F. Arrieta, M. Rist, and P. Ermanni. Aeroelastic response of a selectively compliant morphing aerofoil featuring integrated variable stiffness bi-stable laminates. *Journal of Intelligent Material Systems and Structures*, 27(14):1949–1966, 2016.

[125] I.K. Kuder, U. Fasel, P. Ermanni, and A.F. Arrieta. Concurrent design of a morphing aerofoil with variable stiffness bi-stable laminates. *Smart Materials and Structures*, 25(11), 2016.

[126] X. Lachenal. *Concepts for Morphing Composite Structures using Non-Linear Stiffness Tailoring.* PhD thesis, University of Bristol, 2013.

[127] X. Lachenal, S. Daynes, and P.M. Weaver. A zero torsional stiffness twist morphing blade as a wind turbine load alleviation device. *Smart Materials and Structures*, 22(6):065016, 2013.

[128] X. Lachenal, S. Daynes, and P.M. Weaver. Review of morphing concepts and materials for wind turbine blade applications. *Wind Energy*, 16(2):283–307, 2013.

[129] X. Lachenal, S. Daynes, and P.M. Weaver. A non-linear stiffness composite twisting I-beam. *Journal of Intelligent Material Systems and Structures*, 25(6):744–754, 2014.

[130] X. Lachenal, P.M. Weaver, and S. Daynes. Multi-stable composite twisting structure for morphing applications. *Proceedings of the Royal Society A: Mathematical, Physical and Engineering Sciences*, 468(2141):1230–1251, 2012.

[131] X. Lachenal, P.M. Weaver, and S. Daynes. Influence of transverse curvature on the stability of pre-stressed helical structures. *International Journal of Solids and Structures*, 51(13):2479–2490, 2014.

[132] X. Lachenal, P.M. Weaver, and A. Pirrera. Concept for a Deployable Wing. In *Proceedings of the ASME 2014 Conference on Smart Materials, Adaptive Structures and Intelligent Systems*, pages SMASIS2014–7428, 2014.

[133] E. Lamacchia, E. Eckstein, A. Pirrera, and P.M. Weaver. Morphing structures: non-linear composite shells with irregular planforms. In *56th AIAA/ASCE/AHS/ASC Structures, Structural Dynamics, and Materials Conference*, 2015.

[134] E. Lamacchia, A. Pirrera, I.V. Chenchiah, and P.M. Weaver. Morphing shell structures: A generalised modelling approach. *Composite Structures*, 131:1017–1027, 2015.

[135] A.J. Lee, A. Moosavian, and D.J. Inman. Control and characterization of a bistable laminate generated with piezoelectricity, 2017.

[136] J. Lee, J. Ryu, and M. Cho. Evaluation of Initial Curvature Effect on the Snap- through Load of Bi-stable Composites. In *55th AIAA/ASME/ASCE/AHS/ASC Structures, Structural Dynamics, and Materials Conference*, pages 1–8, National Harbour, MD, 2014.

[137] J.R. Leemans. *Characterization of non-linear compliant shell mechanisms To enhance the design process of a compliant scoliosis brace.* PhD thesis, TU Delft, 2018.

[138] J.R. Leemans, C.J. Kim, W.W.P.J. van de Sande, and J.L. Herder. Unified Rotational and Translational Stiffness Characterization of Compliant Shell Mechanisms. In *Proceedings of the ASME 2018 International Design Engineering Technical Conferences and Computers and Information in Engineering Conference*, page V05AT07A003, 2018.

[139] J.R. Leemans, C.J. Kim, W.W.P.J. van de Sande, and J.L. Herder. Unified Stiffness Characterization of Nonlinear Compliant Shell Mechanisms. *Journal of Mechanisms and Robotics*, 11(1):011011, 2018.

[140] D. Li, X. Zhang, Y. Guan, and H. Zhang. Topology optimization of compliant mechanisms with anisotropic composite materials. In *2010 IEEE International Conference on Mechatronics and Automation, ICMA 2010*, pages 416–421, Xi'an, China, 2010. IEEE.

[141] D. Liaw, S. Singhal, P. Murthy, and C. CHamis. Quantification of Uncertainties in Composites. In *34th Structures, Structural Dynamics and Materials Conference*, pages 1163 – 1173, 1993.

[142] H. Lipkin and T. Patterson. Generalized center of compliance and stiffness. In *Proceedings - IEEE International Conference on Robotics and Automation*, volume 2, pages 1251–1256, 1992.

[143] H. Lipkin and T. Patterson. Geometrical Properties of Modelled Robot Elasticity: Part I - Decomposition. In *Proceedings of the ASME Design Technical Conferences*, pages 179–185, Scottsdale AZ, 1992.

[144] H. Lipkin and T. Patterson. Geometrical Properties of Modelled Robot Elasticity: Part II - Center of Elasticity. In *Proceedings of the ASME Design Technical Conferences*, pages 187–193, Scottsdale AZ, 1992.

[145] H. Lipkin and T. Patterson. Geometrical Decomposition of Robot Elasticity. In *Proceedings of the 9th CISM-IFToMM Symposium on Theory and Practice of Robots and Manipulators*, pages 101–110, 1993.

[146] Z. Luo, L. Tong, M.Y. Wang, and S. Wang. Shape and topology optimization of compliant mechanisms using a parameterization level set method. *Journal of Computational Physics*, 227(1):680–705, 2007.

[147] H.M.Y.C. Mallikarachchi and S. Pellegrino. Design of Ultrathin Composite Self-Deployable Booms. *Journal of Spacecraft and Rockets*, 51(6):1811–1821, 2014.

[148] G.W. Marks, M.T. Reilly, and R.L. Huff. The Lightweight Deployable Antenna for the MARSIS Experiment on the Mars Express Spacecraft. In *36th Aerospace Mechanisms Symposium, Glenn Research Center*, 2002.

[149] L. Masia, L. Cappello, P. Morasso, X. Lachenal, A. Pirrera, P.M. Weaver, and F. Mattioni. CARAPACE: A novel composite advanced robotic actu-

ator powering assistive compliant exoskeleton preliminary design. In *IEEE International Conference on Rehabilitation Robotics*, Seattle, WA, 2013.

[150] MathWorks. MATLAB Optimization Toolbox Documentation. `https://uk.mathworks.com/help/optim/`.

[151] MathWorks. MATLAB Reciprocal condition number documentation. `https://uk.mathworks.com/help/matlab/ref/rcond.html`.

[152] F. Mattioni, P.M. Weaver, K.D. Potter, and M.I. Friswell. Analysis of thermally induced multistable composites. *International Journal of Solids and Structures*, 45(2):657–675, 2008.

[153] C.A. Mattson, L.L. Howell, and S.P. Magleby. Development of Commercially Viable Compliant Mechanisms Using the Pseudo-Rigid-Body Model: Case Studies of Parallel Mechanisms. *Journal of Intelligent Material Systems and Structures*, 15(3):195–202, 2004.

[154] E. McEwen, R.L. Miller, and C.A. Bergman. Early Bow Design and Construction The most effective tool of hunter and warrior that reflect the functional requirements of their users. *Scientific American*, 264(6):76–83, 1991.

[155] C. McHale, S. Carey, D.A. Hadjiloizi, and P.M. Weaver. Morphing Composite Cylindrical Lattices : Thermal Effects and Actuation. In *AIAA Scitech Forum*, Orlando, FL, 2020.

[156] C. McHale, D.A. Hadjiloizi, R. Telford, and P.M. Weaver. Morphing composite cylindrical lattices : Enhanced modelling and experiments. *Journal of the Mechanics and Physics of Solids*, 135:1–15, 2020.

[157] C. McHale, R. Telford, and P.M. Weaver. Compact Telescopic Morphing Lattice Boom. In *Proceedings of the ASME 2019 Conference on Smart Materials, Adaptive Structures and Intelligent Systems*, Louisville, KY, 2019. ASME.

[158] T.H.G. Megson. *Introduction to Aircraft Structural Analysis*. Butterworth-Heinemann, Amsterdam, NL, 3rd edition, 2018.

[159] T.H.G. Megson. *Structural and Stress Analysis*. Butterworth-Heinemann, Amsterdam, NL, 4th edition, 2019.

[160] T.S. Mesogitis, A.A. Skordos, and A.C. Long. Uncertainty in the manufacturing of fibrous thermosetting composites: A review. *Composites Part A: Applied Science and Manufacturing*, 57:67–75, 2014.

[161] A. Midha, L.L. Howell, and T.W. Norton. Limit positions of compliant mechanisms using the pseudo-rigid-body model concept. *Mechanism and Machine Theory*, 35(1):99–115, 2000.

[162] M. Miki and Y. Sugiyama. Optimum design of laminated composite plates using lamination parameters. *AIAA Journal*, 31(5), 1993.

[163] F.M. Morsch and J.L. Herder. Design of a Generic Zero Stiffness Compliant Joint. In *Proceedings of the ASME 2010 International Design Engineering Technical Conferences & Computers and Information in Engineering Conference*, 2010.

[164] T.W. Murphey, W. Francis, B. Davis, and J.M. Mejia-Ariza. High Strain Composites. In *2nd AIAA Spacecraft Structures Conference*, 2015.

[165] T.W. Murphey, S.K. Jeon, A. Biskner, and G.E. Sanford. Deployable Booms and Antennas Using Bi-stable Tape-springs. In *24th Annual AIAA/USU Conference on Small Satellites*, 2010.

[166] T.W. Murphey and S. Pellegrino. A Novel Actuated Composite Tape-Spring for Deployable Structures. In *45th AIAA/ASME/ASCE/AHS/ASC Structures, Structural Dynamics & Materials Conference*, pages 1–11, Reston, Virigina, 2004. AIAA.

[167] A.T. Nettles. Basic mechanics of laminated composite plates. Technical Report October 1994, NASA Marshall Spaceflight Centre, 1994.

[168] J.P.A. Nijssen. *A Type Synthesis Approach to Compliant Shell Mechanisms*. Masters thesis, Delft University of Technology, 2016.

[169] J.P.A. Nijssen, G. Radaelli, J.L. Herder, and C.J. Kim. Overview and Kinetostatic Characterization of Compliant Shell Mechanism Building Blocks. *Journal of Mechanisms and Robotics*, 12(December):061009, 2020.

[170] J.P.A. Nijssen, G. Radaelli, J.L. Herder, C.J. Kim, and J.B. Ring. Design and analysis of a shell mechanism based two-fold force controlled scoliosis brace. In *Proceedings of the ASME 2017 International Design Engineering Technical Conferences and Computers and Information in Engineering Conference*, Cleveland, OH, 2017.

[171] J.P.A. Nijssen, G. Radaelli, J.L. Herder, J.B. Ring, and C.J. Kim. Spatial Concept Synthesis of Compliant Mechanisms Utilizing Non-Linear Eigentwist

Characterization. In *Proceedings of the ASME 2018 International Design Engineering Technical Conferences and Computers and Information in Engineering Conference*, Québec City, Canada, 2018.

[172] S. Nishiwaki, M.I. Frecker, S. Min, and N. Kikuchi. Topology Optimization of Compliant Mechanisms Using the Homogenization Method. *International Journal for Numerical Methods in Engineering*, 42:535–559, 1998.

[173] A.D. Norman, K.A. Seffen, and S.D. Guest. Multistable corrugated shells. *Proceedings of the Royal Society A: Mathematical, Physical and Engineering Sciences*, 464(2095):1653–1672, 2008.

[174] G. Noselli, M. Arroyo, and A. DeSimone. Smart helical structures inspired by the pellicle of euglenids. *Journal of the Mechanics and Physics of Solids*, 123:234–246, 2018.

[175] M.P. O'Donnell, J.P. Stacey, I.V. Chenchiah, and A. Pirrera. Multiscale tailoring of helical lattice systems for bespoke thermoelasticity. *Journal of the Mechanics and Physics of Solids*, 133:103704, 2019.

[176] M.P. O'Donnell, P.M. Weaver, and A. Pirrera. Can tailored non-linearity of hierarchical structures inform future material development? *Extreme Mechanics Letters*, 7:1–9, 2016.

[177] G.M. Olson, S. Pellegrino, J. Banik, and J. Constantine. Deployable helical antennas for cubesats. In *54th AIAA/ASME/ASCE/AHS/ASC Structures, Structural Dynamics, and Materials Conference*, Boston MA, 2013.

[178] A.S. Panesar and P.M. Weaver. Optimisation of blended bistable laminates for a morphing flap. *Composite Structures*, 94(10):3092–3105, 2012.

[179] T. Patterson and H. Lipkin. A Classification of Robot Compliance. *Journal of Mechanical Design*, 115(3):581–584, 1993.

[180] T. Patterson and H. Lipkin. Structure of Robot Compliance. *Journal of Mechanical Design*, 115(3):576–580, 1993.

[181] C.B.W. Pedersen, T. Buhl, and O. Sigmund. Topology synthesis of large-displacement compliant mechanisms. *International Journal for Numerical Methods in Engineering*, 50(12):2683–2705, 2001.

[182] X. Pei, J. Yu, G. Zong, and S. Bi. An effective pseudo-rigid-body method for beam-based compliant mechanisms. *Precision Engineering*, 34(3):634–639, 2010.

[183] S. Pellegrino. Bistable Shell Structures. In *46AIAA/ASME/ASCE/AHS/ASC Structures, Structural Dynamics, and Materials ConferenceA-IAA/ASME/ASCE/AHS/ASC Structures, Structural Dynamics, and Materials Conference*, 2005.

[184] S. Pellegrino and J.C.H. Yee. Foldable composite structures. In *Proceedings of the IASS-APCS*, volume 2, pages 1–12, 2003.

[185] A. Pirrera. *Bistable Structures for Morphing Applications Using Anisotropic Shells*. PhD thesis, University of Bristol, 2011.

[186] A. Pirrera, D. Avitabile, and P.M. Weaver. Bistable plates for morphing structures: A refined analytical approach with high-order polynomials. *International Journal of Solids and Structures*, 47(25-26):3412–3425, 2010.

[187] A. Pirrera, X. Lachenal, S. Daynes, P.M. Weaver, and I.V. Chenchiah. Multistable cylindrical lattices. *Journal of the Mechanics and Physics of Solids*, 61(11):2087–2107, 2013.

[188] E.L. Pollard, T.W. Murphey, and G.E. Sanford. Experimental and Numerical Analysis of a DECSMAR Structure's Deployment and Deployed Performance. In *48th AIAA/ASME/ASCE/AHS/ASC Structures, Structural Dynamics, and Materials Conference*, 2007.

[189] P. Portela, P. Camanho, P.M. Weaver, and I.P. Bond. Analysis of morphing, multi stable structures actuated by piezoelectric patches, 2008.

[190] K. Potter. Measurements of the snap-through behaviour and snap-through fatigue performance of bistable unsymmetric composite structures. In *3rd international conference on composite testing and model identification*, Porto, Portugal, 2006.

[191] K. Potter, B. Khan, M.R. Wisnom, T. Bell, and J. Stevens. Variability, fibre waviness and misalignment in the determination of the properties of composite materials and structures. *Composites Part A: Applied Science and Manufacturing*, 39(9):1343–1354, 2008.

[192] G. Radaelli, R. Buskermolen, R. Barents, and J.L. Herder. Static balancing of an inverted pendulum with prestressed torsion bars. In *13th World Congress in Mechanisms and Machine Science*, 2011.

[193] G. Radaelli and J.L. Herder. Isogeometric Shape Optimization for Compliant Mechanisms With Prescribed Load Paths. In *Proceedings of the ASME*

2014 International Design Engineering Technical Conferences & Computers and Information in Engineering Conference, 2014.

[194] G. Radaelli and J.L. Herder. A monolithic compliant large-range gravity balancer. *Mechanism and Machine Theory*, 102:55–67, 2016.

[195] G. Radaelli and J.L. Herder. Gravity balanced compliant shell mechanisms. *International Journal of Solids and Structures*, 118-119:1339–1351, 2017.

[196] D.W. Radford and T.S. Rennick. Separating Sources of Manufacturing Distortion in Lamnianted Composites. *Journal of Plastics and Composites*, 19(08):621–641, 2000.

[197] J.G. Ratcliffe, M.W. Czabaj, and T.K. O'Brien. Characterizing Delamination Migration in Carbon/Epoxy Tape Laminates. In *27th American Society for Composites Technical Conference*, Arlington, TX, 2012.

[198] F.J.P. Rimrott. Storable tubular extendible member: a unique machine element. *Machine Design*, 37(28):156–165, 1965.

[199] H. Rodrigue, W. Wang, B. Bhandari, M.W. Han, and S.H. Ahn. Cross-shaped twisting structure using SMA-based smart soft composite. *International Journal of Precision Engineering and Manufacturing - Green Technology*, 1(2):153–156, 2014.

[200] E.J. Rosenberg, G. Radaelli, and J.L. Herder. An energy approach to a 2DOF compliant parallel mechanism with self-guiding statically-balanced straight-line behavior. In *Proceedings of the ASME 2010 International Design Engineering Technical Conferences & Computers and Information in Engineering Conference*, 2010.

[201] M.T. Saad, S.G. Miller, and T. Marunda. Thermal characterization of IM7/8552-1 carbon-epoxy composites. In *Proceedings of the ASME 2014 International Mechanical Engineering Congress and Exposition*, pages IMECE2014–40030, Montreal, Canada, 2014.

[202] M. Sakovsky. *Design and Characterization of Dual-Matrix Composite Deployable Space Structures*. Phd thesis, California Institute of Technology, 2018.

[203] M. Sakovsky, S. Pellegrino, and H.M.Y.C. Mallikarachchi. Folding and Deployment of Closed Cross-Section Dual-Matrix Composite Booms. In *3rd AIAA Spacecraft Structures Conference*, 2016.

[204] B.A. Salamon. *Mechanical Advantage Aspects in Compliant Mechanisms Design*. Masters thesis, Purdue University, 1989.

[205] B.I. Sandor. The Rise and Decline of the Tutankhamun-Class Chariot. *Oxford Journal of Archaeology*, 23(2):153–175, 2004.

[206] M. Schenk and S.D. Guest. On zero stiffness. *Proceedings of the Institution of Mechanical Engineers, Part C: Journal of Mechanical Engineering Science*, 228(10):1701–1714, 2014.

[207] M. Schenk, S.D. Guest, and J.L. Herder. Zero stiffness tensegrity structures. *International Journal of Solids and Structures*, 44(20):6569–6583, 2007.

[208] R. Schnabel, R. Wahl, and R. Klein. Efficient RANSAC for point-cloud shape detection. *Computer Graphics Forum*, 26(2):214–226, 2007.

[209] M.R. Schultz, M.J. Hulse, P.N. Keller, and D. Turse. Neutrally stable behavior in fiber-reinforced composite tape springs. *Composites Part A: Applied Science and Manufacturing*, 39(6):1012–1017, 2008.

[210] M.R. Schultz, W.K. Wilkie, and R.G. Bryant. Investigation of Self-Resetting Active Multistable Laminates. *Journal of Aircraft*, 44(4):1069–1076, 2007.

[211] V.R. Seereeram and K.A. Seffen. Confirming inextensional theory. *International Journal of Solids and Structures*, 51(19-20):3439–3448, 2014.

[212] K.A. Seffen. On the behavior of folded tape-springs. *Journal of Applied Mechanics, Transactions ASME*, 68(3):369–375, 2001.

[213] K.A. Seffen. 'Morphing' bistable orthotropic elliptical shallow shells. *Proceedings of the Royal Society A: Mathematical, Physical and Engineering Sciences*, 463(2077):67–83, 2007.

[214] K.A. Seffen. Compliant shell mechanisms. *Philosophical Transactions of the Royal Society A: Mathematical, Physical and Engineering Sciences*, 370(1965):2010–2026, 2012.

[215] K.A. Seffen and S.D. Guest. Prestressed Morphing Bistable and Neutrally Stable Shells. *Journal of Applied Mechanics*, 78(1):011002, 2011.

[216] K.A. Seffen and S. Pellegrino. Deployment dynamics of tape springs. *Proceedings of the Royal Society A: Mathematical, Physical and Engineering Sciences*, 455:1003–1048, 1999.

[217] K.A. Seffen, Z. You, and S. Pellegrino. Folding and deployment of curved tape springs. *International Journal of Mechanical Sciences*, 42(10):2055–2073, 2000.

[218] J.F. Shackelford, Y.H. Han, S. Kim, and S.H. Kwon. *CRC Materials Science and Engineering Handbook*. CRC Press, Boca Ranton, FL, fourth edition, 2016.

[219] W.J. Shaughnessy. Advances in Scoliosis Brace Treatment for Adolescent Idiopathic Scoliosis. *Orthopedic Clinics of North America*, 38(4):469–475, 2007.

[220] O. Sigmund. On the design of compliant mechanisms using topology optimization. *Mechanics of Structures and Machines*, 25(4):493–524, 1997.

[221] S. Sihn, R.Y. Kim, K. Kawabe, and S.W. Tsai. Experimental studies of thin-ply laminated composites. *Composites Science and Technology*, 67(6):996–1008, 2007.

[222] S.H. Song, H. Lee, J.G. Lee, J.Y. Lee, M. Cho, and S.H. Ahn. Design and analysis of a smart soft composite structure for various modes of actuation. *Composites Part B: Engineering*, 95:155–165, 2016.

[223] S. Sriramula and M.K. Chryssanthopoulos. Quantification of uncertainty modelling in stochastic analysis of FRP composites. *Composites Part A: Applied Science and Manufacturing*, 40(11):1673–1684, 2009.

[224] J.P. Stacey. Bristol Composites Institute PhD projects: 2016 Cohort. "Stiffness tailoring of compliant prestressed composite shells". `http://www.bristol.ac.uk/composites/cdt/research-projects/phd/2016/`.

[225] J.P. Stacey. Stiffness Tailoring of Composite Shells via Thermal Prestress. Technical report, University of Bristol (Internal Unpublished Document), 2016.

[226] J.P. Stacey, M.P. O'Donnell, C.J. Kim, and M. Schenk. From shear centre to eigenwrenches. *Thin-Walled Structures*, 161:107478, 2021.

[227] J.P. Stacey, M.P. O'Donnell, and M. Schenk. Thermal Prestress in Composite Compliant Shell Mechanisms. In *Proceedings of the ASME 2018 International Design Engineering Technical Conferences and Computers and Information in Engineering Conference*, page V05AT07A012, Québec City, 2018. ASME.

[228] J.P. Stacey, M.P. O'Donnell, and M. Schenk. Thermal Prestress in Composite Compliant Shell Mechanisms. *Journal of Mechanisms and Robotics*, 11(2):020908, 2019.

[229] J.P. Stacey, M.P. O'Donnell, M. Schenk, and C.J. Kim. Visualising Compliance of Composite Shell Mechanisms. In *Proceedings of the ASME 2020*

International Design Engineering Technical Conferences and Computers and Information in Engineering Conference. ASME, 2020.

[230] J. Steeves, M. Laslandes, S. Pellegrino, D. Redding, S.C. Bradford, J.K. Wallace, and T. Barbee. Design, fabrication and testing of active carbon shell mirrors for space telescope applications. *SPIE - The International Society for Optical Engineering*, 9151, 2014.

[231] J. Steeves and S. Pellegrino. Post-cure shape errors of ultra-thin symmetric CFRP laminates: Effect of ply-level imperfections. *Composite Structures*, 164:237–247, 2017.

[232] P. Steutel, G.A. Kragten, and J.L. Herder. Design of an underactuated finger with a monolithic structure and largely distributed compliance. In *Proceedings of the ASME 2010 Design Engineering Technical Conference & Computers and Information in Engineering Conference*, 2010.

[233] O. Stodieck, J.E. Cooper, and P.M. Weaver. Interpretation of bending/torsion coupling for swept, nonhomogenous wings. *Journal of Aircraft*, 53(4):892–899, 2016.

[234] T. Tarnai. Zero stiffness elastic structures. *International Journal of Mechanical Sciences*, 45(3):425–431, 2003.

[235] R. Telford. *Hygro-thermal Residual Stresses in Unsymmetrical Multi-Stable Composite Laminates*. PhD thesis, University of Limerick, 2014.

[236] R. Telford, K.B. Katnam, and T.M. Young. The effect of moisture ingress on through-thickness residual stresses in unsymmetric composite laminates: A combined experimental-numerical analysis. *Composite Structures*, 107:502–511, 2014.

[237] C. Thill, J. Etches, I. Bond, K. Potter, and P.M. Weaver. Morphing skins. *Aeronautical Journal*, 112(1129):117–139, 2008.

[238] S. Timoshenko and J.N. Goodier. *Theory of Elasticity*. McGraw-Hill, New York, 3rd edition, 1970.

[239] M. Tones, N. Moss, and D.W. Polly. A review of quality of life and psychosocial issues in scoliosis. *Spine*, 31(26):3027–3038, 2006.

[240] X. Tong, W. Ge, and Y. Zhang. Topology optimization of compliant mechanisms with curvilinear fiber path laminated composites. *Proceedings of the Institution of Mechanical Engineers, Part C: Journal of Mechanical Engineering Science*, 230(17):3101–3110, 2016.

[241] S.W. Tsai. *Introduction to Composite Materials*. Technomic Publishing, Westport, CT, 1981.

[242] S.W. Tsai, S. Sihn, and R.Y. Kim. Thin Ply Composites. In *46th AIAA/ASME/ASCE/AHS/ASC Structures, Structural Dynamics & Materials Conference*, 2005.

[243] W.W.P.J. van de Sande and J.L. Herder. Analysis of parasitic motion in compliant mechanisms using eigenwrenches and eigentwists. *Proceedings of the ASME Design Engineering Technical Conference*, 5A-2018:1–9, 2018.

[244] G. Van Vinckenroy and W.P. de Wilde. The use of Monte Carlo techniques in statistical finite element methods for the determination of the structural behaviour of composite materials structural components. *Composite Structures*, 32(1-4):247–253, 1995.

[245] P. Vannucci and G. Verchery. A new method for generating fully isotropic laminates. *Composite Structures*, 58(1):75–82, 2002.

[246] S. Vidoli and C. Maurini. Tristability of thin orthotropic shells with uniform initial curvature. *Proceedings of the Royal Society A: Mathematical, Physical and Engineering Sciences*, 464(2099):2949–2966, 2008.

[247] B. Wang, C. Ge, and K.S. Fancey. Snap-through behaviour of a bistable structure based on viscoelastically generated prestress. *Composites Part B: Engineering*, 114:23–33, 2017.

[248] B. Wang, K.A. Seffen, and S.D. Guest. Folding of a Bistable Tape-Spring Structure Based on Plain-Woven Composite. In *International Conference on Composites/Nano Engineering*, 2018.

[249] B. Wang, K.A. Seffen, and S.D. Guest. Folding of Bistable Composite Tape-Springs. Technical report, University of Cambridge, 2019.

[250] P.M. Weaver. Anisotropic Laminates That Resist Warping During Manufacture. *ICCM15 - 15th International Conference on Composite Materials*, pages 3–4, 2005.

[251] S.L. Weinstein, L.A. Dolan, J.C.Y. Cheng, A. Danielsson, and J.A. Morcuende. Adolescent idiopathic scoliosis. *The Lancet*, 371:1527–1537, 2008.

[252] S.M. Yang, J.H. Han, and I. Lee. Characteristics of smart composite wing with SMA actuators and optical fiber sensors. *International Journal of Applied Electromagnetics and Mechanics*, 23(3-4):177–186, 2006.

[253] Z. Yang, Q. Liu, and B. Zhang. Influence of Layup Sequence on the Surface Accuracy of Carbon Fiber Composite Space Mirrors. *Applied Composite Materials*, 2018.

[254] G. Yanjin, S. Sheng, Z. Guoqun, and L. Yiguo. Finite element modeling of laser bending of pre-loaded sheet metals. *Journal of Materials Processing Technology*, 142(2):400–407, 2003.

[255] J.C.H. Yee and S. Pellegrino. Folding of woven composite structures. *Composites Part A: Applied Science and Manufacturing*, 36(2 SPEC. ISS.):273–278, 2005.

[256] J.C.H. Yee, O. Soykasap, and S. Pellegrino. Carbon Fibre Reinforced Plastic Tape Springs. In *45th AIAA Structures, Structural Dynamics & Materials Conference*, pages 1–9, 2004.

[257] J. Yu, S. Li, X. Pei, S. Bi, and G. Zong. A unified approach to type synthesis of both rigid and flexure parallel mechanisms. *Science China Technological Sciences*, 54(5):1206–1219, 2011.

[258] J. Yu, D. Lu, and G. Hao. Design and analysis of a compliant parallel pan-tilt platform. *Meccanica*, 51(7):1559–1570, 2016.

[259] Z. Zhang, G. Ye, H. Wu, H. Wu, D. Chen, and G. Chai. Thermal effect and active control on bistable behaviour of anti-symmetric composite shells with temperature-dependent properties. *Composite Structures*, 124:263–271, 2015.

Laus Deo Semper